STUDY THE REGULATORY ROLES OF HUMAN MITOCHONDRIAL DNA G-QUADRUPLEX STRUCTURES WITH TARGET-SPECIFIC FLUORESCENT LIGANDS

ZHENG BOXIN

PhD

The Hong Kong Polytechnic University

2025

The Hong Kong Polytechnic University

Department of Applied Biology and Chemical Technology

Study the regulatory roles of human mitochondrial DNA G-quadruplex structures with target-specific fluorescent ligands

ZHENG Boxin

A thesis submitted in partial fulfilment of the
requirements for the degree of Doctor of Philosophy

June 2025

CERTIFICATE OF ORIGINALITY

I hereby declare that this thesis is my own work and that, to the best of my knowledge and belief, it reproduces no material previously published or written, nor material that has been accepted for the award of any other degree or diploma, except where due acknowledgement has been made in the text.

_____ (signed)

ZHENG Boxin (Name of student)

Abstract

Cancer is the second leading cause of death in humans, following cardiovascular and cerebrovascular diseases, and poses a critical threat in human health. Despite many new treatments have been proposed, the development of effective and safe cancer therapy remains a challenge. Mitochondria are known to take crucial roles in different biological processes, such as energy metabolism, proliferation and apoptosis, and they also have a close relationship with cancer development and progression. Thus, mitochondria are regarded as promising targets for cancer therapy. In recent years, many studies have shown that certain regions of human genes with guanine (G)-rich sequences may form a four-stranded structure containing two or more stacked G-tetrad planes of four guanines connected by a network of Hoogsteen hydrogen bonding, known as G-quadruplex structure (G4). It has been reported that tumor cells often overexpress G4s. Increasing evidence shows that G4s may play important roles in gene transcription and translation processes. In the mitochondrial genome, approximately 170 mitochondrial gene sequences are capable of forming G4s, which have been known closely associated with mitochondrial DNA deletions, energy metabolism, mitochondria-related diseases, and cancer progression. However, the regulatory function of mitochondrial DNA G-quadruplexes (G4-mtDNAs) is still unclear. This hinders the use of G4-mtDNA as a potential target for the development of new anticancer strategies. To understand the regulatory function of G4-mtDNAs, target-selective and cell-permeable small-molecule ligands are needed. Thus, the design and synthesis of small-molecule fluorescent ligands specifically targeting G4-mtDNAs in living cells is critical important. In this study, the primary objective is to design, synthesize, and isolate a series of G4-mtDNAs-targeting ligands and understand how these ligands could regulate the mitochondrial functions for anticancer therapy. In addition, the *in vivo* antitumor efficiency and biosafety of the potent and G4-mtDNA-targeting ligands screened are evaluated with human tumor xenograft mouse models.

In the thesis, Chapter 1 summarizes the recent development of targeting G4-structures including G4-mtDNAs as the potential drug target of small molecules for anticancer study. An overview of research methods tailored for this study to achieve the objectives is given in Chapter 2. In Chapter 3 and Chapter 4, a comprehensive investigation of a small-sized benzoindole-benzothiazole ligand

BYB, capable of targeting mitochondria and their G4-DNA structures, for antitumor study is discussed. The experimental results show that **BYB** is selectively targeting G4-mtDNAs, capable of stabilizing the structure of G4-mtDNAs upon interaction. **BYB** could also bind to G4-mtDNA targets to generate fluorescent signal for imaging and visualization in living human cancer cells. Moreover, **BYB** was found to be able to inhibit the proliferation of a panel of human cancer cells, including human cervical cancer cell HeLa. The anticancer mechanism of **BYB** targeting G4-mtDNAs was investigated in HeLa cells. The results suggest that **BYB** could inhibit the replication and transcription of mtDNAs, resulting in the downregulation of mitochondrial respiratory chain complexes. More importantly, the intracellular interaction of **BYB** with G4-mtDNAs could induce mitochondrial calcium overload in cancer cells. Calcium overload in mitochondria triggers a series of cellular events, including mitochondrial dysfunction, inhibition of ATP production, and elevated mtROS production, as well as the induction of mitophagy, ferroptosis, mtDNA and nuclear DNA damage, and apoptosis. To the best of our knowledge, this is the first study revealing that G4-mtDNA-targeting ligand induces mitochondrial calcium overload and then causes nuclear DNA damage and cell death. Moreover, the *in vivo* antitumor efficacy of **BYB** in a HeLa cell xenograft tumor model was validated. A 64.6% reduction in tumor weight was achieved with **BYB** in the *in vivo* study.

The molecular design and synthesis of a series of small-sized di-cationic lipophilic ligands capable of targeting G4-mtDNAs and their anticancer mechanism are discussed in Chapter 5 and Chapter 6. To the best of our knowledge, this series of G4-mtDNA-targeting di-cationic ligands is first reported by us. Through different screening assays, ligand **9** is identified as a highly G4-mtDNA-selective ligand and exhibits potent antiproliferation activity against human colorectal cancer cell HCT116. The anticancer mechanism of the ligand was investigated in HCT116 cells. It was found that ligand **9** was specifically localized in mitochondria and significantly inhibited the expression of mitochondrial genes and then induced a series of cellular events, including mitochondrial dysfunction, ROS production, DNA damage, cellular senescence, and apoptosis. Furthermore, ligand **9** shows high antitumor efficacy in HCT116 tumor xenograft mouse model. A 70% reduction in tumor weight is achieved after the treatment with the ligand.

Taken together, this study provides new insights into the design of G4-mtDNA-targeting ligands for chemical biology and new anticancer drug discovery. In addition, we revealed the possible antitumor mechanisms of targeting G4-mtDNAs with ligands. Particularly, the induction of mitochondrial calcium overload by G4-mtDNA-targeting ligands is reported for the first time. Due to targeting mitochondrial calcium signaling has the potential to reduce resistance induced by conventional chemical therapy, this new anticancer strategy targeting mitochondrial DNA G4s may provide a new opportunity to develop potent drug against drug-resistant cancers.

Publications

1. **Zheng, B. X.**; Long, W.; Zeng, Y. X.; She, M. T.; Zheng, Y. Y.; Zheng, W. D.; Wang, Y. K.; Chan, K. H.; Leung, S. L.; Chan, C. M.; Lu, Y. J.; Wong, W. L., A Mitochondria-Targeting and G-Quadruplex Structure-Binding Ligand Inducing Calcium Overload and Ferroptosis in Human Cancer Cells. *Brit. J. Pharmacol.* **2025**, 182 (16), 3923-3951.
2. **Zheng, B. X.**; Long, W.; Zheng, W. D.; Zeng, Y. X.; Guo, X. C.; Chan, K. H.; She, M. T.; Leung, S. L.; Lu, Y. J.; Wong, W. L., Mitochondria-selective dicationic small-molecule ligand targeting G-quadruplex structures for human colorectal cancer therapy. *J. Med. Chem.* **2024**, 67 (8), 6292-6312.
3. **Zheng, B. X.**; Long, W.; She, M. T.; Wang, Y. K.; Zhao, D.; Yu, J.; Leung, S. L.; Chan, K. H.; Hou, J. Q.; Lu, Y. J.; Wong, W. L., A Cytoplasm-Specific Fluorescent Ligand for Selective Imaging of RNA G-Quadruplexes in Live Cancer Cells. *Chem-Eur. J.* **2023**, 29 (34), e202300705.
4. **Zheng, B. X.**; Yu, J.; Long, W.; Chan, K. H.; Leung, S. L.; Wong, W. L., Structurally diverse G-quadruplexes as the noncanonical nucleic acid drug target for live cell imaging and antibacterial study. *Chem. Commun.* **2023**, 59 (11), 1415-1433. (Co-first author)
5. Chan, K. H.; **Zheng B. X.**; Leung, S. L.; Long, W.; Zhao, Y. C.; Zheng, Y. Y.; Wong, W. L., A NRAS mRNA G-quadruplex structure-targeting small-molecule ligand reactivating DNA damage response in human cancer cells for combination therapy with clinical PI3K inhibitors. *Int. J. Biol. Macromol.* **2024**, 279 (3), 135308.
6. Long, W.; Zeng, Y. X.; **Zheng, B. X.**; Li, Y. B.; Wang, Y. K.; Chan, K. H.; She, M. T.; Lu, Y. J.; Cao, C. Y.; Wong, W. L., Targeting hTERT promoter G-quadruplex DNA structures with small-molecule ligand to downregulate hTERT expression for triple-negative breast cancer therapy. *J. Med. Chem.* **2024**, 67 (15), 13363-1338.
7. Chan, K. H.; Wang, Y. K.; **Zheng, B. X.**; Long, W.; Feng, X. X.; Wong, W. L., RNA-Selective Small-Molecule Ligands: Recent Advances in Live-Cell Imaging and Drug Discovery. *ChemMedChem*, **2023**, 18 (19), e202300271. (Co-first author)

Acknowledgement

As time passes, the three-year journey of PhD study is coming to an end. Looking back on these three years, there are too many people to thank, and it is because of their encouragement and support that I can overcome all the difficulties and successfully complete my thesis.

First of all, I would like to express my deepest gratitude to my chief supervisor, Prof. W. L. Wong, for providing me with a superior learning and research environment. In scientific research, he always guided me patiently, never gave up on me, and gave me great encouragement and support. In addition, I am more grateful to him for guiding my life and learning the ability to solve problems independently. I firmly believe that the skills learned in these three years will benefit me for the rest of my life.

Secondly, I would like to thank my co-supervisor, Prof. K. Y. Wong, for his support during these three years of study, as he always can give me valuable advice and help me solve the difficulties I encountered. Besides, I would like to thank Prof. X. Y. Li, Dr. W. Long, Dr. Alan S. L. Leung and Dr. S. F. Chung, for their kind assistance in my studies. I am also truly grateful to my groupmates in Y1313, Y1124 and Y727 for their mutual encouragement and support in our studies, which has led to the formation of valuable friendships. On the other hand, I would like to express my appreciation to all the scientific officers in the University Research Facility in Life Sciences and department of Applied Biology and Chemical Technology for their assistance in the equipment training.

Furthermore, I am very grateful to the Department of Applied Biology and Chemical Technology, the State Key Laboratory of Chemical Biology and Drug Discovery, and the Research Committee of the Hong Kong Polytechnic University for their support in my PhD study.

Last but not least, I want to express my gratitude to my family and friends for their love and support. Their unconditional support has enabled me to fully dedicate myself to my research and studies over the past three years.

Table of Content

Chapter 1. Introduction

Nucleic acids are critically important biomolecules in organisms as they are the core components of deoxyribonucleic acid (DNA) and ribonucleic acid (RNA) for storing and transmitting genetic information. They also determine the genetic characteristics and functions of organisms. In addition, nucleic acids play an indispensable role in the regulation of gene expression, cell signaling and protein synthesis, and have become an important pillar of life activities.

In physiological environments, nucleic acids can form a variety of conformations through base interactions. Among them, the B-type double helix structure of DNA and the single-stranded structure of RNA are the most common. However, in addition to these structures, a series of non-classical secondary structures exist, such as the A- or Z-type double helix of DNA, the triplex of DNA and RNA, G-quadruplex (G4) and the *i*-motif. There is a complex competition and transformation between these secondary structures, which are formed and exist to adapt and respond to different biological processes and functional requirements, and to support the normal life cycle and function of the organism.

Among the non-classical secondary structures, G4-structures have attracted much attention because of their unique biofunctions. The G4-structure consists of guanine-rich DNA or RNA sequences, which form a stable planar tetrameric structure (known as G-tetrad or G-quartet) through hydrogen bonding and ionic interactions and further stack of two or more G-tetrads to form a G4-structure. Numerous studies have demonstrated that G4s are widely distributed in chromatin DNA and RNA, and they involve in the key biological processes, such as telomere protection, gene expression and genome stability. Therefore, the regulation of G4-structures may directly affect these biological processes and thus regulate the life cycle and proliferation of cells. In view of this, the development of potent G4-targeting ligands is regarded as a potential strategy for anticancer drug discovery and development because G4-structures are often found overexpressed in tumor cells.

1.1 The structure and distribution of G-quadruplexes

1.1.1 Structural characteristics of G-quadruplexes

As early as 1920, studies have shown that guanylate derivatives can self-aggregate at high concentrations and spontaneously form micelles.[1] About 50 years later, Gellert et al. demonstrated by *X*-ray diffraction that guanines can polymerize to form a planar structure and proposed the G-quartet model (G-quartet). The model consists of four guanine bases with atoms at the N1, N7, O6, and N2 positions connected by Hoogsteen hydrogen bonds to form a planar structure. Two or more layers of G-quartets can further form G-quadruplex by stacking (**Figure 1.1**).[2]

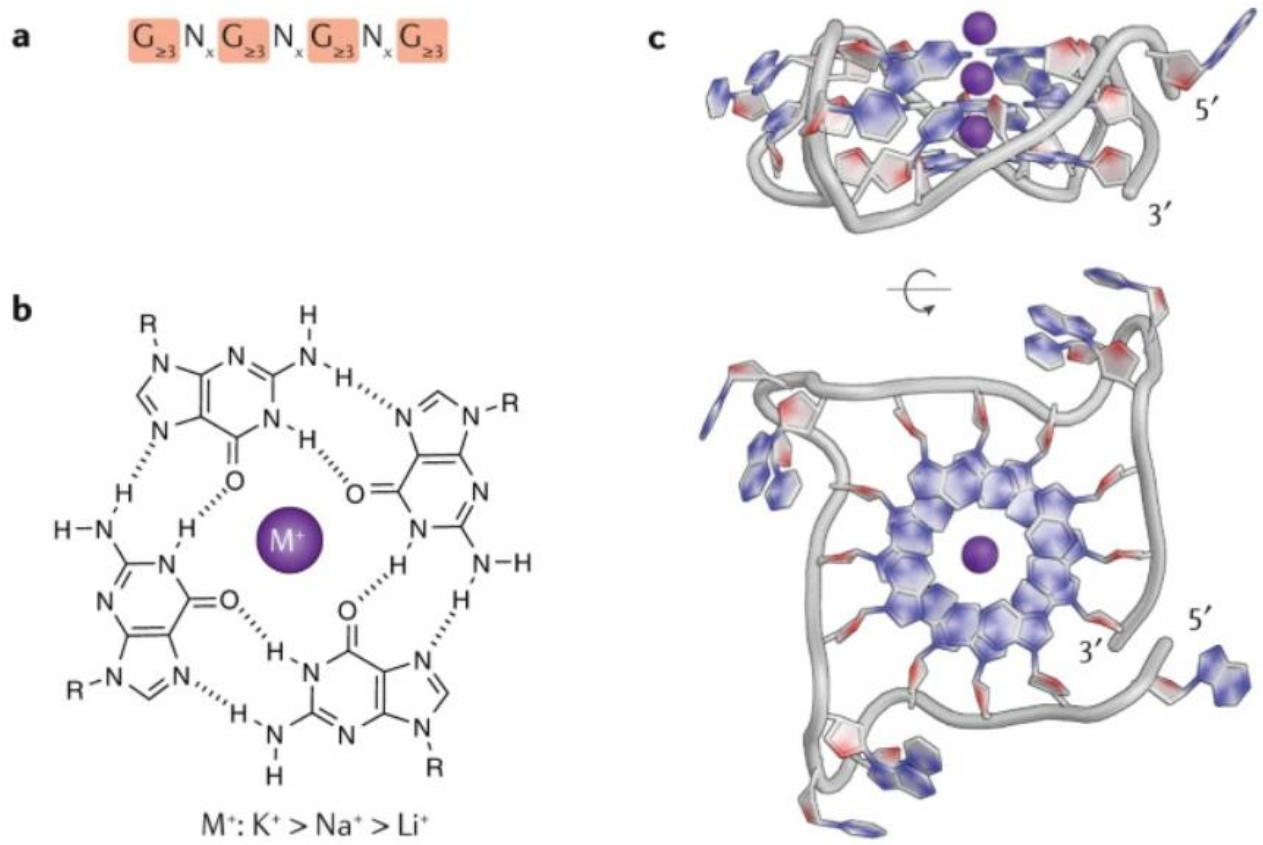

Figure 1.1. The formation of G-quadruplex structures. (a) The G-quadruplex consensus sequence. x denotes the number of nucleotides in the loops. (b) A guanine tetrad is stabilized by Hoogsteen base-pairing and by a central cation (M^+), with a preference for monovalent cations in the order of potassium (K^+) > sodium (Na^+) > lithium (Li^+). (c) *X*-ray crystal structure of an intramolecular, parallel G4 from a human telomere sequence.[3]

In addition to the G-quartet, the structure of G4 includes key components such as a central ion channel, a groove, and a loop (**Figure 1.2**). The ion channel is a negatively charged region formed by the six carbonyl oxygens of the four guanine's pointing to the center, which selectively chelates positively charged metal cations, thus significantly enhancing the stability of the G4 structure. The precise position of the cation between G-quartet depends on the ionic species. It has been reported that Na^+ is mainly located in the plane of the G-quartet and between two neighboring G-quartets, whereas K^+ is distributed at equidistant intervals between the planes of each G-quartet and forms a symmetric tetragonal bipyramidal configuration with eight oxygen atoms. Due to the abundance of K^+ in the cellular environment, buffers containing K^+ ion as the stabilizer are often used for *in vitro* study of G4s. In addition, other metal ions such as Pb^{2+} and Sr^{2+} also can bind to the channel and play a role in stabilizing the structure of G4s.[4, 5]

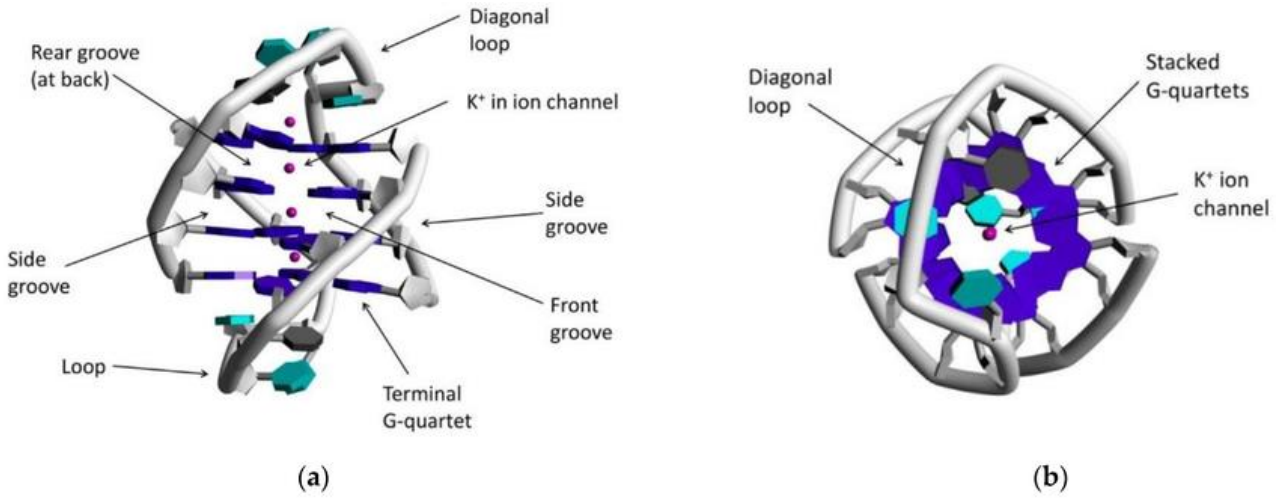

Figure 1.2. The constituent elements of a G-quadruplex structure. (a) A side-view and (b) a top-view of the structure.

Grooves in G4s are specific cavities formed on the surface of the DNA or RNA backbone with unique spatial structure and chemical properties. They can be categorized as wide, medium, or narrow based on their width. In contrast, loops are noncontiguous, loose regions formed by unpaired or partially paired bases in the G4 structure, usually consisting of one to seven bases. The conformation and thermal stability of G4s are largely influenced by the structure of loops. Specifically, longer loops tend to cause sequences to form stable non-parallel topologies, while shorter loops are more likely to lead to the formation of less stable parallel topologies.[6] Moreover, the length of the loop affects the binding of proteins to the G4. For example, nucleolin prefers to bind to a G4 with a longer loop structure.[7] Therefore, the loop is of great research value as a potential site for realizing ligand-

specific targeting of G4. It has been reported that specific recognition and binding of a G4 can be achieved by direct targeting of the loop.[8] This discovery provides an important idea for the development of novel G4-specific ligands and a new strategy for the development of G4-targeting anticancer drugs.

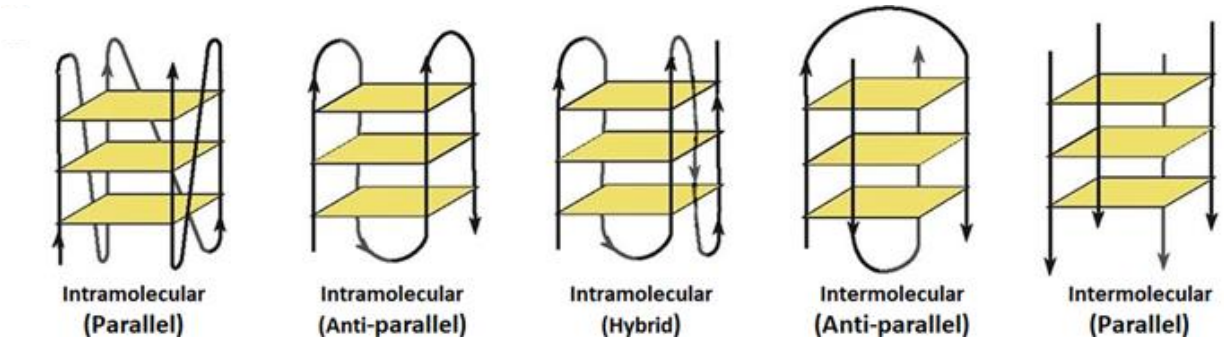

Figure 1.3. Topology of G-quadruplex structures.[13]

G4s exhibit diverse structural patterns due to their rich characterization. G4s can be categorized into various types based on different classification criteria (**Figure 1.3**). First, based on the number of nucleic acid strands involved, G4s can be divided into two categories: intramolecular G4 and intermolecular G4. Intramolecular G4 is formed by the folding of a single G-rich sequence through intramolecular interactions, whereas intermolecular G4 is composed of two or more G-rich sequences through intermolecular interactions, and is further subdivided into bimolecular, trimolecular, and tetramolecular G4, depending on the number of G-rich sequences involved in G4 formation.[9] Second, based on the loop of G4 and the orientation of the nucleic acid chains, its conformation can be categorized into parallel, antiparallel, and hybrid types. In parallel G4, the backbones of the four strands have the same orientation and show a parallel arrangement. The anti-parallel G4 contains two nucleic acid strands with the same orientation and two others with opposite orientations. The hybrid G4, on the other hand, has three chains in the same direction and one chain in the opposite direction.[10] It is worth noting that the conformation of G4 is not fixed, but dynamically changes by environmental conditions such as ion concentration, solvent pH, temperature, etc. For example, in Na^+ solution, the human telomere G4 sequence is more inclined to form an antiparallel conformation, whereas in K^+ solution it is more inclined to form a mixed conformation.[11, 12] Finally, based on the type of nucleic acid, G4 can also be categorized as DNA G4, RNA G4, and DNA-RNA hybrid G4. Different ways of categorization help us to understand more deeply the roles of G4 structures in different biological systems and functions and provide an important basis for related drug design and research.

1.1.2 Distribution of G-quadruplexes

1.1.2.1 G-quadruplexes in the human genome

Early computational studies of the human genome showed that there are many potential G-quadruplex sequences (pG4s) in the genome, which conform to the general formula $G_{3+}N_{1-7}G_{3+}N_{1-7}G_{3+}N_{1-7}G_{3+}N_{1-7}G_{3+}$. Two independent studies using different algorithms come to a similar conclusion that there are approximately 370,000 such potential G4 sequences in the genome.[14, 15] In addition to algorithmic predictions, high-throughput sequencing technology has verified the presence of G4 and its distribution in the human genome. In 2016, Shankar Balasubramanian and his team analyzed the binding of the specific G4 antibody BG4 to endogenous DNA sequences by ChIP-seq, and their findings showed that human chromatin contains approximately 10,000 pG4s.[16] Subsequently, Simon J Elsässer et al. applied the CUT&Tag technique with higher resolution and lower background noise to characterize cellular endogenous G4s and found that G4s were enriched in active promoters and enhancers.[17]

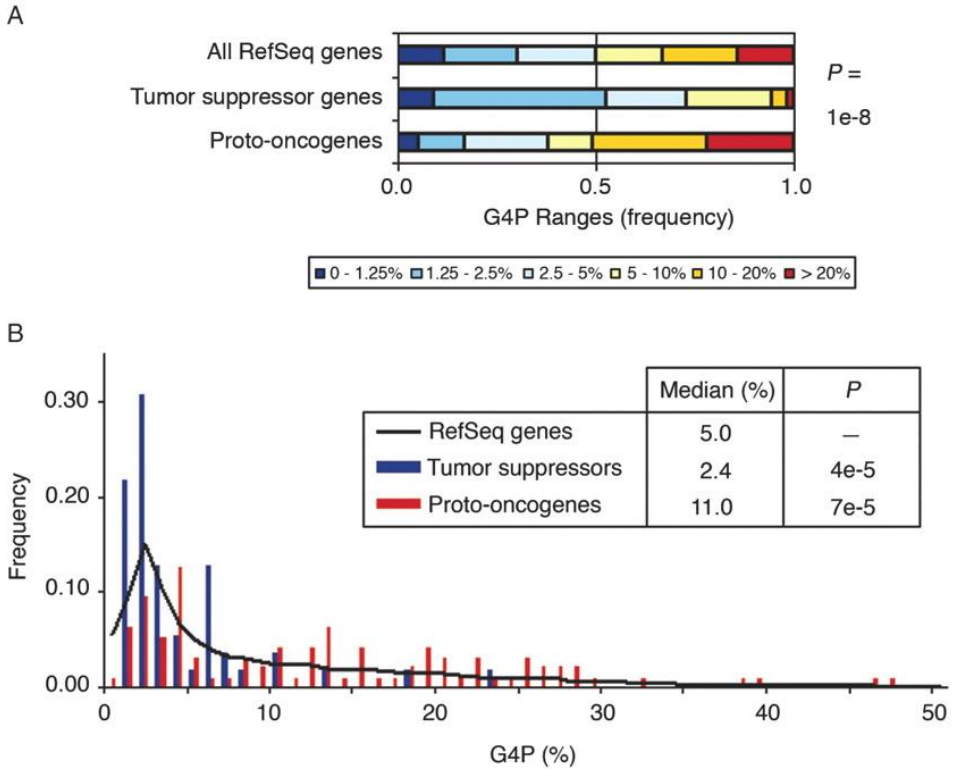

Figure 1.4. Contrasting G-quadruplex of tumor suppressor genes and proto-oncogenes. (A) Ranges of G4P for 55 tumor suppressor genes, 95 proto-oncogenes and all 16,654 RefSeq genes. (B) Distribution of tumor suppressor genes and proto-oncogenes across G-quadruplex.[18]

Moreover, although pG4s are widely distributed in the genome, they are not randomly disordered. They are mainly clustered in the key functional regions of genes, such as telomere ends, promoters and enhancers of the Transcription Start Site (TSS), and intron and exon regions of the untranslated

region (UTR) of mRNA. This finding emphasizes the important role of G4s in living organisms. Further algorithmic analysis revealed that most pG4s are located in the promoter regions of proto-oncogenes, such as *c-MYC*, *BCL-2*, and *KRAS*, while relatively few were found in oncogenes (**Figure 1.4**).[18] In addition, pG4s in the human genome are highly conserved and have remained largely unchanged during evolution, which is one of their distinguishing features.[19] Compared to DNA G4, the G4 structure formed by RNA sequences is thermodynamically more stable because the U in RNA replaces the T, which makes G4 more stable within the loop.[20] Interestingly, G-rich RNA sequences are prevalent in the 5'-UTR region of mRNA, long stranded non-coding RNA (lncRNA), and microRNA (miRNA), and are relatively rare in rRNA and tRNA, hinting at their uniqueness in terms of biological functions.[21] In addition to bioinformatics predictions and genomics studies, the presence of DNA and RNA G4s has been confirmed in the human genome and transcriptome by methods such as biochemical and optical imaging.

1.1.2.2 G-quadruplexes in other species

Studies have shown that the G4s are not only present in the human genome but are also widely distributed in the genomes of other species. In animal genomes, G4s are also widespread and play a key role in regulating gene expression as well as chromatin structure. Compared with animals, the distribution of G4s in plant genomes is more generalized, and it is closely related to plant growth and development, hormone regulation, and response to environmental stresses.[22, 23] In addition, numerous bacterial pathogens, such as Streptococcus pneumoniae and Mycobacterium tuberculosis, are also rich in G4s, which play important roles in transcriptional regulatory mechanisms.[24] Although G4s exhibit a wide distribution in the genomes of all types of species, there are differences in the regions of enrichment. In the genomes of organisms such as humans, mice and trypanosomes, G4s are predominantly enriched in the promoter region and the 5'-UTR, suggesting an important role in the regulation of gene expression. However, in other eukaryotes, such as Cryptobranchus Showyi, Zebrafish or Drosophila, the distribution of G4s is relatively low, being more enriched in non-coding RNAs (ncRNAs), microRNAs (miRNAs), or long-stranded non-coding RNAs (lncRNAs). This difference in distribution may be related to the specificity of gene regulatory mechanisms and expression in different organisms.[25] Studying the distribution and function of G4s in different species not only helps us to gain a deeper understanding of the gene regulatory networks of these organisms, but also reveals the mechanisms of their adaptive evolutionary processes. Therefore, the study of G4s in different species has great scientific importance.

1.2 Biological function of G-quadruplexes

The biofunction of the G4s has not been fully understood currently. It is generally believed that G4s may play crucial roles in cellular regulation. The formation and disassembly of G4s control gene replication, transcription, and translation, and then regulate physiological processes such as cell proliferation, cell growth, and cell apoptosis. Therefore, it is a feasible anti-tumor strategy to stabilize the G4 structures through small molecule ligands, and then regulate the transcription and expression of oncogenes to affect the progress of its downstream events, so as to inhibit the proliferation of cancer cells or promote their apoptosis. This section will introduce the biological functions of the G4s from the following aspects: The relationship between G4s and genome stability and the role of G4s in gene expression.

1.2.1 G-quadruplexes and genome stability

1.2.1.1 G-quadruplexes and replication

DNA replication is a crucial step in cell division, which refers to the process of copying one DNA molecule into two identical DNA molecules. DNA replication is the basis for the transmission of genetic information in living organisms, ensuring that each new cell retains its genetic information intact.[26] The process of DNA replication consists of three main steps: unwinding, replication, and ligation. Unwinding refers to the unwinding of double-stranded DNA by DNA helicases to form two single-stranded DNAs. Replication refers to the synthesis of new complementary strands on the template strand of each single strand of DNA according to the principle of complementary base pairing. Since DNA polymerase is only capable of synthesizing in one direction, DNA replication is an asymmetric process in which one strand is known as the leading strand and the other as the lagging strand. After replication is complete, the RNA and DNA fragments are enzymatically excised, and the missing bases are filled in by DNA polymerase to join the two strands together.[27, 28]

During DNA replication, the formation of single-stranded DNA provides for the appearance of G4-structures. However, the presence of G4s may impede the DNA replication process, leading to interruption of DNA replication or the occurrence of errors. *In vitro* experiments have shown that G4s can inhibit the activity of DNA polymerase, thus hindering the process of DNA replication.[29] Numerous studies have shown that replication arrest occurs in cells treated with G4s targeting ligands, accompanied by micronucleus formation and telomere instability.[30-32] In addition, some studies

suggested G4 structures may perform specific functions at specific stages of DNA replication. For example, when replication forks are stalled or damaged, G4 structures may be associated with repair mechanisms involved in the repair of DNA damage and the restart of replication forks.[33] This suggested the complexity and diversity of the role of G4s in DNA replication.

Furthermore, G4s are related to genome stability. Genomic stability refers to the absence of heritable mutations or errors in the DNA sequence in the genome.[26] The presence of G4s induces DNA double-strand breaks (DSBs), and DSBs cannot be repaired in a timely manner can lead to DNA sequence recombination and mutation.[34, 35] This means that excessive formation of G4s in the genome may increase the risk of genomic instability and mutation. These mutations and instabilities may lead to genetic diseases, cancers and neurodegenerative diseases.[36]

In summary, G4s play important regulatory roles in DNA replication. It affects the speed and accuracy of DNA replication to a certain extent and influences the stability of the genome. Therefore, an in-depth study of the role of G4s is of great significance for understanding the replication mechanism of the genome, maintaining its stability, and exploring issues related to gene mutation and genome instability.

1.2.1.2 G-quadruplexes and telomere

At the end of chromosomes, there is a special structure called telomere, which is composed of two parts: telomeric DNA sequences and telomere-binding proteins. Telomeres protect the integrity of chromosomes and control the cell division cycle.[37, 38] The structure of telomeric DNA is very special (**Figure 1.5**).[39] Their DNA sequences consist of the G-rich repeating unit TTAGGG, including a double-stranded region of about 10 to 15 kb and a single-stranded overhanging region of 100 to 300 bp. The single-stranded overhang of telomeric DNA is able to hybridize with the double-stranded region by means of strand invasion to form a stable T-loop structure, which interacts with telomere repeat binding factor 1 (TRF1), telomere repeat binding factor 2 (TRF2), Repressor Activator Protein 1 (RAP1), TRF1-interacting Nuclear Factor 2 (TIN2), Tripeptidyl Peptidase 1 (TPP1) and Protection of Telomeres 1 (POT1) proteins interact to form the Shelterin complex. Also, telomere repeat-containing RNA (TERRA), a 200 bp r(UUAGGG)$_n$ repeat sequence obtained by transcribing telomeric DNA as a template, is an important component of telomere structure.

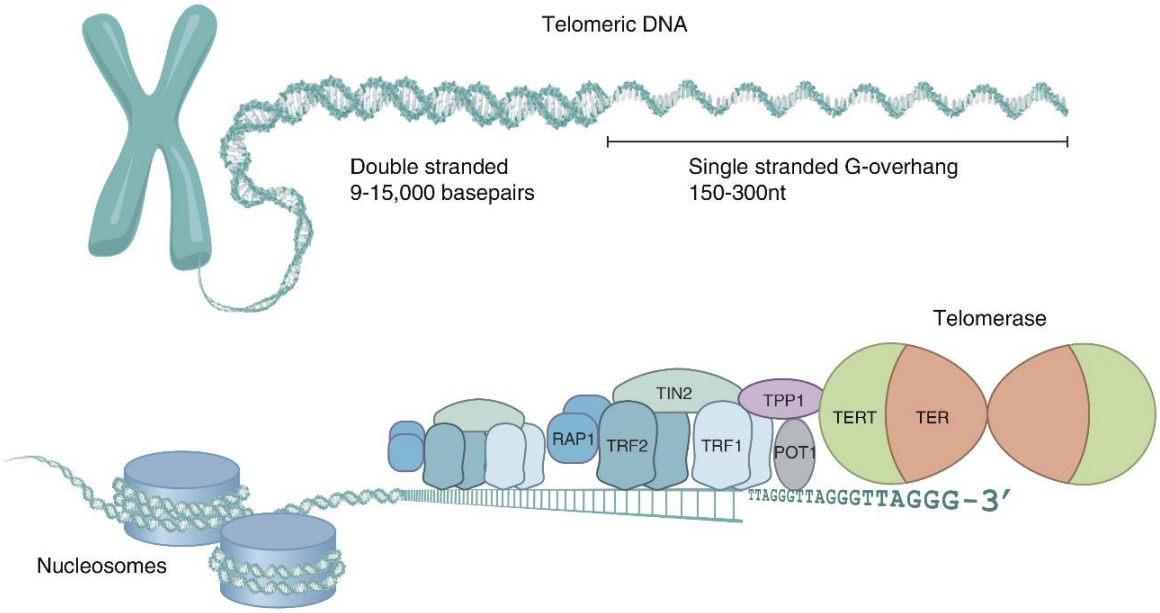

Figure 1.5. Structure of human telomere.[39]

Telomere is known as the "clock of life" and is involved in many key physiological processes such as cancer, aging, inflammation, epigenetics, etc.[40, 41] It is well-known that normal cells cannot divide indefinitely. It is because when the number of divisions increases, the length of telomere will gradually shorten. When it shortens to a certain extent, the cell will enter the stage of aging and apoptosis. Studies have shown that telomere length is directly related to the activity of telomerase. Telomerase is a reverse transcriptase composed of human telomere RNA template (hTR), human telomerase reverse transcriptase (hTERT), and telomerase-associated protein (TAP1). Telomerase can synthesize the telomeric repeat sequence TTAGGG. In this process, it uses its own RNA complementary to the telomeric repeat as a template and then uses the 3'-overhanging single-stranded region as a primer. In normal cells, the expression of telomerase is low or not expressed, the activity is very low, and the telomere structure cannot be synthesized by reverse transcription. Therefore, with the number of cell divisions increasing, the length of telomere will gradually shorten, and eventually enter the stage of aging and apoptosis.[42, 43] However, compared with normal cells, most tumor cells can overexpress telomerases that have higher activity.[44, 45] Thus, tumor cells can rely on telomerase to synthesize telomere structures, maintain the length of telomeres, and achieve unlimited proliferation.[46] Approximately 85% of tumor cells achieve telomere elongation through the activation of telomerase-dependent mechanisms, and thus telomerase is considered an important target for antitumor therapy. In addition, another 15% of tumor cells achieve telomere elongation through the Alternative Lengthening of Telomeres (ALT) pathway, a process that involves DNA recombination, single-stranded structural transitions, DNA synthesis, and repair, and relies on key

proteins of the homologous recombination repair pathway, such as single-stranded binding proteins and helicases.[47]

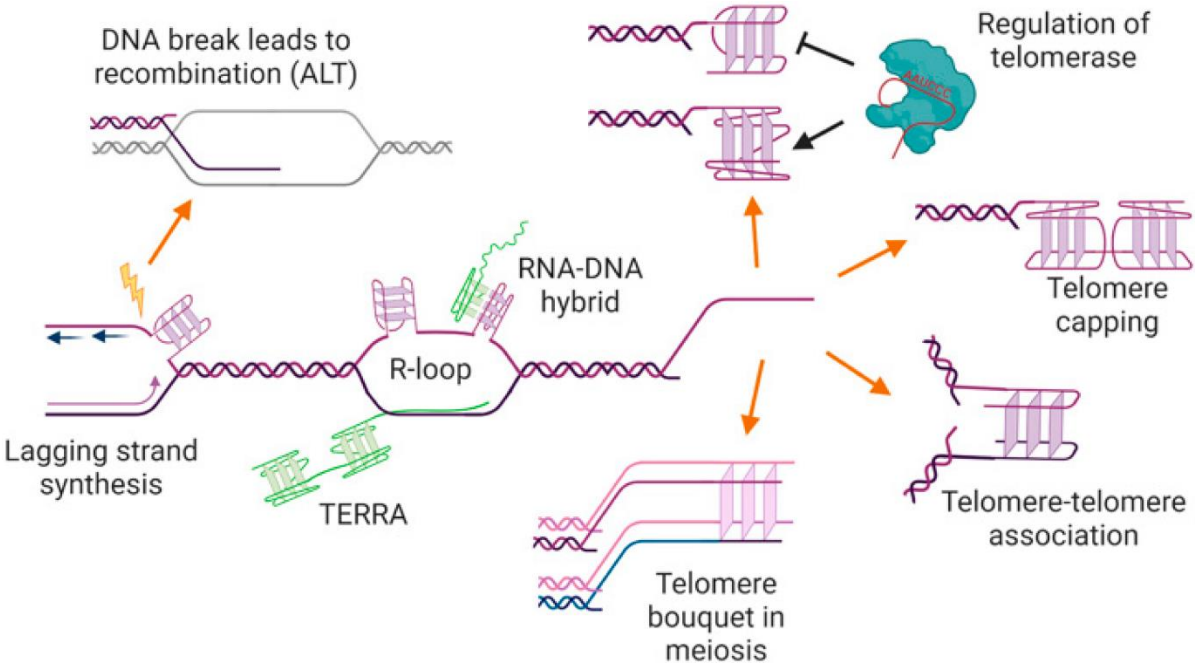

Figure 1.6. The biofunctions of G-quadruplex at telomeres.[49]

Since telomeric DNA sequences consist of TTAGGG repeat units, multiple G4 structures may be formed at telomeres. G4s may play crucial regulatory roles in the structure and function of telomeres (**Figure 1.6**). Firstly, the formation of telomeric G4s affects the function of the Shelterin complex. When G4s are formed, they may block the interaction between TRF2 and POT1, leading to the abnormal localization of TRF2, which makes the Shelterin complex unable to effectively protect telomeric DNAs, triggering the telomere damage response and ultimately leading to cell death.[31] In this case, the formation of telomeric G4s exacerbates telomere disruption and adversely affects cellular stability. Secondly, telomeric G4s are also involved in regulating the telomere lengthening process. Some studies have found that the formation of telomeric G4s can inhibit the binding of telomerase to telomeric DNAs, thereby inhibiting telomerase activity and hindering telomere extension.[48]

In summary, telomeric G4s have been a new target for the development of anticancer drugs. Small molecule ligands are applied to induce and/or stabilize the formation of telomeric G4s. As a result, telomerase cannot perform reverse transcription, leading to the impairment of the division ability of cancer cells.

1.2.2 G-quadruplexes and their biofunction in the regulation of gene expression

1.2.2.1 G-quadruplexes and transcription

Transcription is an important process in biology that serves to transcribe genetic information DNA into RNA, which can translate that information into proteins. The transcription process consists of three major steps: initiation, extension, and termination. The initiation step is when RNA polymerase binds to the promoter region of DNA, unwinding the double-strand DNA and synthesizing RNA from the 3' end of the DNA template strand. The extension step is where RNA polymerase synthesizes the RNA strand by adding complementary bases to the DNA template. The product of transcription is a strand of RNA, also known as a transcript. The transcript is further processed and modified and then transported to the ribosomes in the cytoplasm for protein synthesis. The regulation of transcription plays an important role in the normal growth and development of organisms, and abnormal regulation of transcription is closely related to the occurrence of many human diseases.

As mentioned earlier, pG4s are enriched in the TSS region of genes, and their effect on transcription is closely related to their location. When G4s are located in the promoter region of a gene (upstream of the TSS), they may prevent the binding of RNA polymerase II as well as transcription factors to the promoter DNA, thereby inhibiting gene transcription. Moreover, if pG4s are located downstream of the TSS, G4 also blocks the advance of RNA polymerase II, leading to transcription arrest or even termination, which reduces the expression of related genes.[50, 51] In addition, pG4s located on non-template strands may form relatively stable DNA/RNA hybrid G4s with RNA, a structure also known as the R-loop. R-loop formation may inhibit the advance of RNA polymerase II, leading to termination or interruption of transcription, and may also lead to increased DNA vulnerability, which in turn affects gene stability and expression.[52, 53]

Bioinformatics analysis shows that many nucleic acid sequences present in the promoter regions of proto-oncogenes can form G4s *in vitro*, such as *c-MYC*, *BCL-2*, *H-RAS*, *K-RAS*, *VEGF*, *c-KIT*, etc. Among the many proto-oncogenes, *c-MYC* is the most widely concerned by scientists.[54-57] The oncoprotein encoded by *c-MYC* has important regulatory functions. It participates in various physiological processes such as cell cycle regulation, cell apoptosis, protein synthesis, and cell adhesion.[58] Studies have shown that *c-MYC* is overexpressed in about 70% of human cancer cells, such as breast cancer, colon cancer, cervical cancer, osteosarcoma and glioma.[59-61] Based on the

pervasive role of the *c-MYC* in cancer biology, achieving *c-MYC* downregulation has become an attractive strategy for cancer therapy. Moreover, c-MYC has a short half-life, and it lacks binding sites on its surface.[62, 63] These properties make it difficult to be targeted directly with small molecule ligands or drugs. Therefore, other therapeutic strategies have been further explored to inhibit the function of *c-MYC* genes by suppressing their transcription, translation or signaling pathways and thereby inhibiting their function. Currently, a range of potential therapeutic approaches have been developed. Among them, the downregulation of *c-MYC* by transcriptional repression shows a good anti-tumor effect.

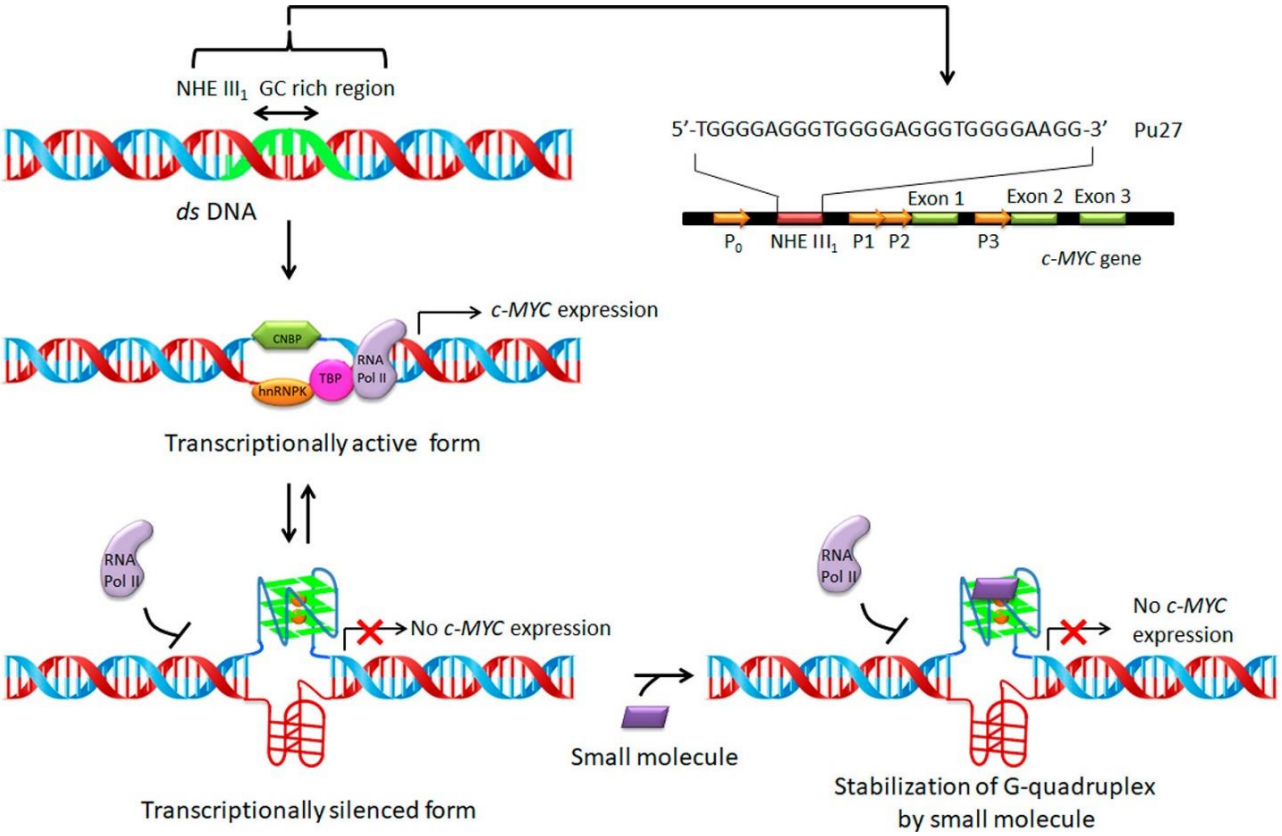

Figure 1.7. G-quadruplex mediated transcriptional regulation of *c-MYC*.[63]

Approximately 85%-90% of the transcriptional activity of the *c-MYC* is controlled by a Nuclease Hypersensitive Element III1 (NHEIII1) located upstream of the P1 promoter.[64-66] The region where NHEIII1 is located is rich in guanines and can form G4 structures. Intracellularly, a series of G4-binding proteins, including nucleolin, ADAR1, and BLM, achieve fine regulation of endogenous *c-MYC* G4s through specific interactions with *c-MYC* G4s. These G4-binding proteins work by altering the stability or conformation of G4 structures, which in turn affects its dynamic homeostasis within the cell as well as the transcriptional activity of *c-MYC* genes.[67] It was found that the transcriptional activity of *c-MYC* gene could be significantly inhibited by inducing the formation of

the *c-MYC* DNA G4 structures with potent ligands (**Figure 1.7**). This finding provides a new strategy for cancer treatment.[68-70] A variety of small molecule ligands capable of targeting *c-MYC* DNA G4s have been developed, which effectively affect the stability of G4 structures by interacting with it, thereby decreasing the expression level of the *c-MYC* gene and showing significant effects in cancer therapy.

In addition to *c-MYC*, oncogenes including *K-RAS*,[71] *BCL-2*,[72] *c-KIT*,[73] *VEGF*,[74] and *H-RAS* [75] have been reported to regulate the transcription process through the associated G4 ligands. These findings suggest that G4s play an important role in the regulation of gene expression and provide potential opportunities for the development of novel therapeutic targets.

1.2.2.2 G-quadruplexes and translation

Translation is an important process in living organisms that converts information on mRNA into proteins. The translation process takes place primarily in the ribosome and consists of three major steps: initiation, extension, and termination. Translation is initiated by a ribosomal subunit that binds to a start codon (usually is AUG) on the mRNA. This start codon is recognized by and paired with a special tRNA called the initiation tRNA. During the extension phase, a tRNA coding for a specific amino acid is paired with the next codon on the mRNA. The ribosome then forms a peptide bond that attaches the amino acid on the tRNA to the already formed peptide chain. This process is repeated until the stop codon is reached. When translation reaches a stop codon (UGA, UAA, UAG), it induces the ribosome to release the protein and terminate the translation process. The termination process also involves many termination factors that help the ribosome release of the protein.[21]

RNA produced during transcription is more flexible relative to double-helix DNA and therefore more likely to form G4 structures. It has been shown that the 5'-UTR regions of mRNAs are enriched with many G4 structures, and pG4s are present in the 5'-UTRs of approximately 3000 genes.[76] The presence of these G4 structures in the 5'-UTR has a significant effect on translation efficiency, both by facilitating and inhibiting translation. Most of the 5'-UTRs of mRNAs containing G4 structures show translation impairment. For example, G4 structures close to the cap position (*N-RAS* [77]) or close to the AUG start codon (*BCL-2* [78]) can repress translation. This inhibition may be due to a large spatial barrier caused by the G4 structures, which prevents the recruitment and binding of the

eIF4F complex or 40S or disrupts the scanning of the complex to the AUG translation start codon. However, when G4s are located at the Internal Ribosome Entry Site (IRES), the translation process will start in a cap-independent manner (**Figure 1.8**). During this process, G4 can enhance the translation efficiency of mRNAs by promoting ribosome recruitment. This mechanism has been validated in several genes, such as *FGF* and *VEGF* [79, 80]. Therefore, the position of the G4s in the 5'UTR of mRNAs plays an important role in the regulation of translation, which also provides a new perspective for us to deeply understand the mechanism of translation regulation.

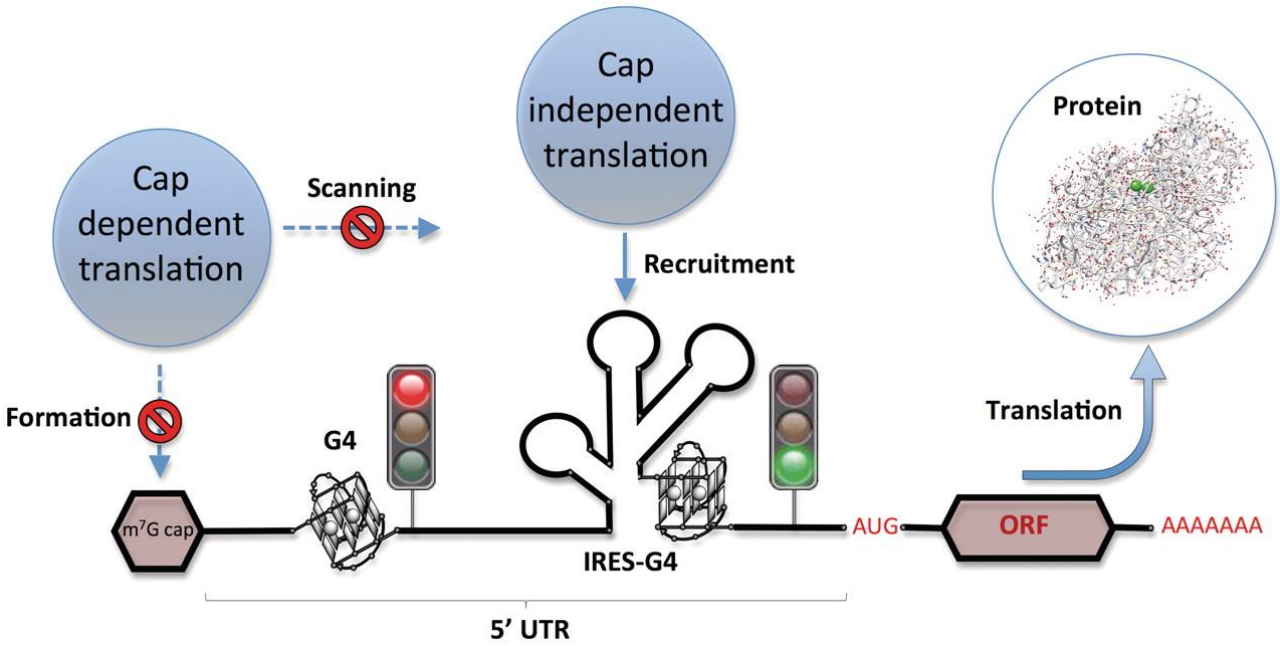

Figure 1.8. Schematic illustration of the possible roles of 5'-UTR RNA G-quadruplex formation in cap-dependent and cap-independent regulation of translation initiation.[21]

1.3 Mitochondrial DNA G-quadruplexes and their biological functions

Mitochondrion is a highly specialized double-membrane organelle in eukaryotic cells. As the "energy factory" of the cell, mitochondria synthesize adenosine triphosphate (ATP) through the oxidative phosphorylation (OXPHOS) system, which provides about 90% of the energy for cellular activities. Apart from energy metabolism, mitochondria are involved in key biological processes such as the regulation of cell cycle, proliferation, apoptosis, reactive oxygen species (ROS) generation, calcium signaling and lipid synthesis. In addition to their key role in cellular energy production, abnormalities in mitochondrial function have been closely associated with a wide range of human diseases, especially in metabolic diseases, neurodegenerative diseases, and cancer.[81-83]

In neurodegenerative diseases, neuronal mitochondria in patients with Alzheimer's disease and

Parkinson's disease often show reduced electron transport chain activity, excessive accumulation of ROS, and defective mitochondrial autophagy, which accelerates apoptosis.[84, 85] In addition, imbalances in mitochondrial dynamics (fusion/disintegration abnormalities) and dysregulated calcium signaling can induce cardiovascular disease, whereas the release of mitochondrial DNA into the cytoplasm also activates inflammatory vesicles involved in autoimmune disease processes.[86, 87] On the other hand, it has been found that abnormal mitochondrial function is closely related to tumor development in recent years.[88-91] Cancer cells often exhibit the "Warburg effect", they preferentially supply energy through glycolysis under aerobic conditions, which may be related to the reorganization of mitochondrial metabolism, the accumulation of mtDNA mutations and the dysregulation of ROS signaling.[92-95] Given the important role of mitochondria in disease, especially in cancer, it has become an emerging research direction in cancer therapy.

Apart from nuclear DNA, mitochondrial DNA also has many putative G4-forming sequences. Human mtDNA has approximately 170 sequences that can form G4s, but it is poorly understood by humans compared to G4s in the nucleus.[96-98] Studies have shown that G4-mtDNAs may be associated with the deletion of mtDNAs, and may also interfere with the replication, transcription, and expression of mtDNAs, which may lead to the development of various diseases as well as cancer.[99-102] Although most believe that G4-mtDNAs play important regulatory roles, there is currently little supporting evidence, which may be related to the lack of tools to study G4-mtDNAs, especially the small molecules that can specifically recognize and bind G4-mtDNAs are relatively few. Therefore, the development of small molecules that can specifically target and bind G4-mtDNAs is of great significance for the study of its biological functions. Besides, some studies have also shown that targeting G4-mtDNAs by specific ligands can inhibit tumor cell growth and induce apoptosis,[103-107] suggesting that G4-mtDNAs are expected to be a new anti-tumor target.

In summary, G4-mtDNAs have important biological functions as well as being a potential anti-tumor target, but the current research has been slowed by the limited number of tools available to study G4-mtDNAs, especially the low number of small molecule fluorescent ligands that can specifically target G4-mtDNAs. Consequently, the development of small-molecule fluorescent ligands that can specifically target G4-mtDNAs is important for the study of the distribution, formation, and unwinding process of G4s in mitochondria, which provides a powerful tool to investigate the

regulatory function of G4-mtDNAs. Meanwhile, the developed small-molecule ligands of G4-mtDNAs are expected to be used as anti-tumor lead drugs, and the corresponding anti-tumor mechanism is expected to provide ideas for the design of drugs targeting G4-mtDNAs.

1.3.1 The biofunction of mitochondrial G-quadruplexes in replication and transcription

In human cells, mitochondrial DNA (mtDNA) is circular double-stranded, with a total of 16,569 bp, of which the outer circular single-stranded DNA is called the heavy chain, because this chain contains more guanine (G) and less cytosine (C), Guanine has a greater mass than cytosine, which results in a larger DNA mass throughout the outer loop. In contrast, the inner circular single-stranded DNA is called the light chain because it contains more cytosine (C) and less guanine (G). The mitochondrial genome encodes mitochondrial 16S and 12S ribosomal RNAs, 22 mitochondrial tRNAs, and 13 respiratory chain-associated proteins (**Figure 1.9**).[108, 109]

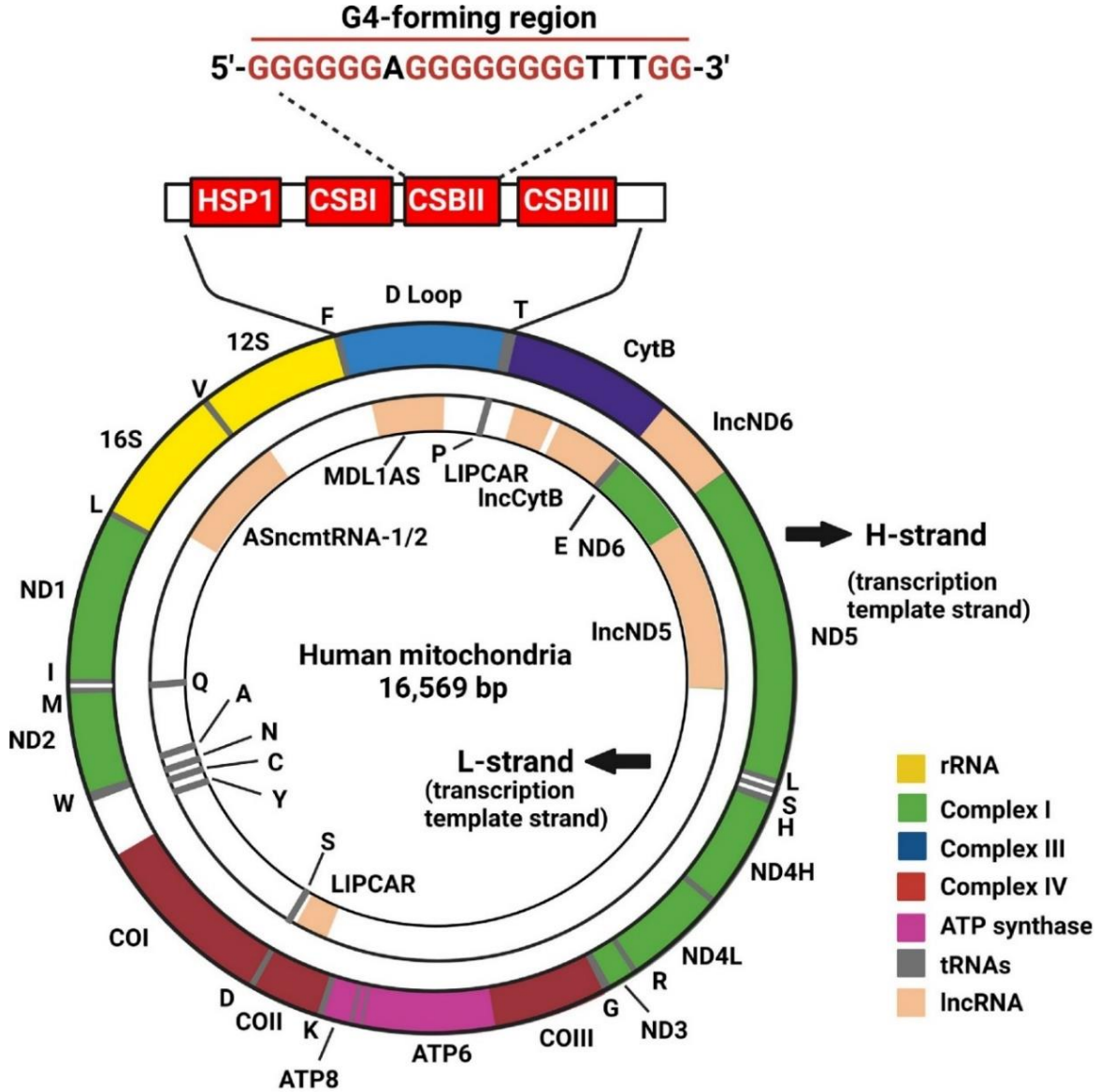

Figure 1.9. Human mitochondrial DNA composition.[97]

Compared with G4s in the nucleus, G4-mtDNAs have been less studied, but more and more evidence show that G4-mtDNAs may have regulatory roles in important biological functions. Biological studies have shown that about 170 G4-forming sequences exist in the mitochondrial genome, most of them located in the heavy chain.[96-98] Mitochondrial replication is a slow process, taking approximately 2 hours. During this period, the single-stranded G-rich heavy strand has a significant chance to form G4 structures.[110] In addition, the potassium ion concentration of the mitochondrial internal environment is as high as 150 mM,[111, 112] and the mitochondrial genome does not contain introns and protective histones, which are conducive to the formation of G4 structures of the mitochondrial genome.[96]

In mammals, mtDNA replicates differently from nuclear DNA. Due to its circular structure, there can be collisions between transcription and replication machinery, potentially negatively impacting mtDNA gene expression.[102, 113] Mitochondrial RNA polymerase (mitoRNAP) is responsible for transcribing mtDNA and generating primers for replication, while the mitochondrial transcription elongation factor, TEFM, plays a crucial role in the interplay between replication and transcription.[102] Human mtDNA transcription is initiated by two promoters: the light-strand promoter (LSP) and the heavy-strand promoter (HSP), which are located on opposite strands of mtDNA. This arrangement results in polycistronic transcripts that undergo extensive processing, ultimately terminating at the CSBII site. The termination of transcription occurs through the formation of R-loops and is more efficient when the Conserved Sequence Box II (CSBII) region contains a higher number of G tracts in G6AG8, compared to the less common variant G5AG7, indicating a potential influence of G4 structures on transcription (**Figure 1.10**).[102] The presence of G4 formations contributes to genomic instability and plays a significant role in various cancers and genetic disorders.[114, 115] G4 sequences are not randomly distributed within the genome; they often coincide with chromosomal breakpoints, underlining their significance.[114] Given that mitochondria contain a higher frequency of potential G4 sequences, these structures may significantly contribute to mtDNA instability. Mitochondrial deletions are prevalent in cancer and genetic diseases and are also implicated in the aging process.[116, 117] The presence of G4 sequences can stall mitochondrial replication machinery during DNA synthesis, serving as a major source of instability in the mitochondrial genome.[100]

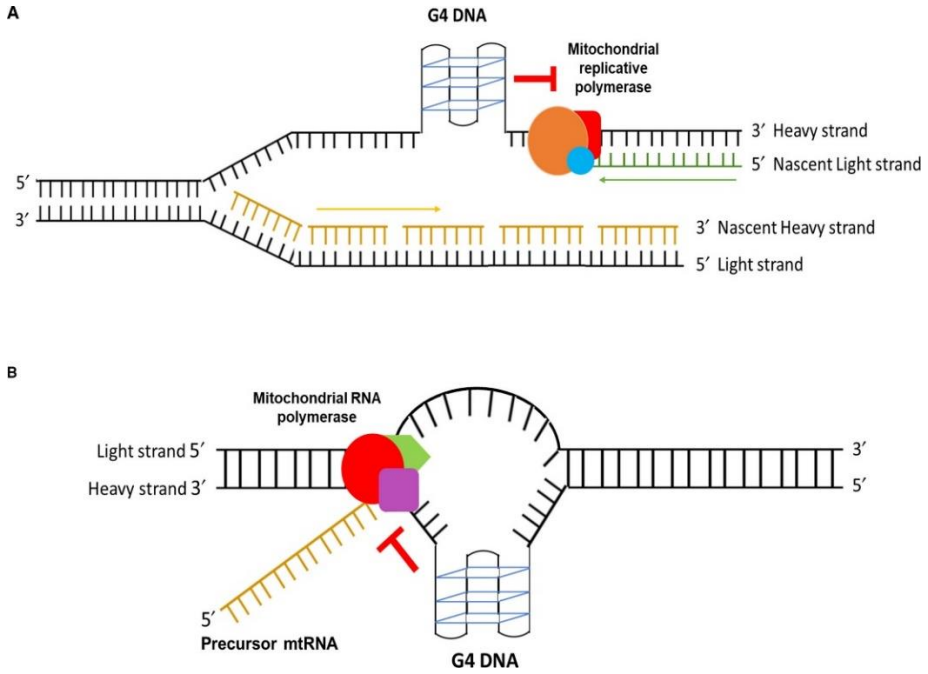

Figure 1.10. G-quadruplex is involved in mitochondrial DNA replication and transcription.[118]

1.3.2 The biofunction of mitochondrial G-quadruplexes in energy metabolism

Mitochondria play an important role as energy factories in providing the energy needed for cell survival.[119, 120] As mentioned earlier, the mitochondrial genome encodes 13 proteins that are closely related to the respiratory chain and serve as subunits of the five complexes that make up the mitochondrial electron transport chain, ensuring the proper transfer of electrons.[121, 122] Twelve of these genes are located in the heavy chain of mtDNA and are characterized by sequences rich in guanine.[97] In the environment of high mitochondrial potassium ion concentration, these sequences are likely to form G4s, which inhibit the replication and transcription of these genes, thereby blocking their expression and affecting the assembly of electron transport chain complexes, resulting in mitochondrial dysfunction or impairment.[123, 124]

In hypoxic conditions, many cancer cells primarily rely on glycolysis for energy, a shift believed to result from metabolic reprogramming.[126] During this process, G4-mtDNAs may play a crucial regulatory role in mediating the switch between oxidative phosphorylation and glycolysis, although the underlying mechanism remains unclear. Some studies showed that the stabilization of G4-mtDNAs could cause glycolysis-related gene activation in cancer cells, resulting in down-regulation of mitochondrial oxidative phosphorylation and up-regulation of glycolysis, which revealed that G4-mtDNAs could have a close relationship with glycolysis. Moreover, recent research has identified the JAK/STAT3 pathway as a key regulator of G4-mtDNAs dynamics in cancer cells under low oxygen

levels. When the JAK/STAT3 pathway is activated, it facilitates the movement of RelA, an NF-κB family member, to the mitochondria. Then, RelA binds to G4-mtDNAs and enhances mtDNA folding, which results in an increased mtDNA instability and the inhibition of mtDNA transcription, leading to mitochondrial dysfunction. This cascade of events ultimately disturbs energy metabolism homeostasis and promotes a metabolic shift towards glycolysis (**Figure 1.11**).[125]

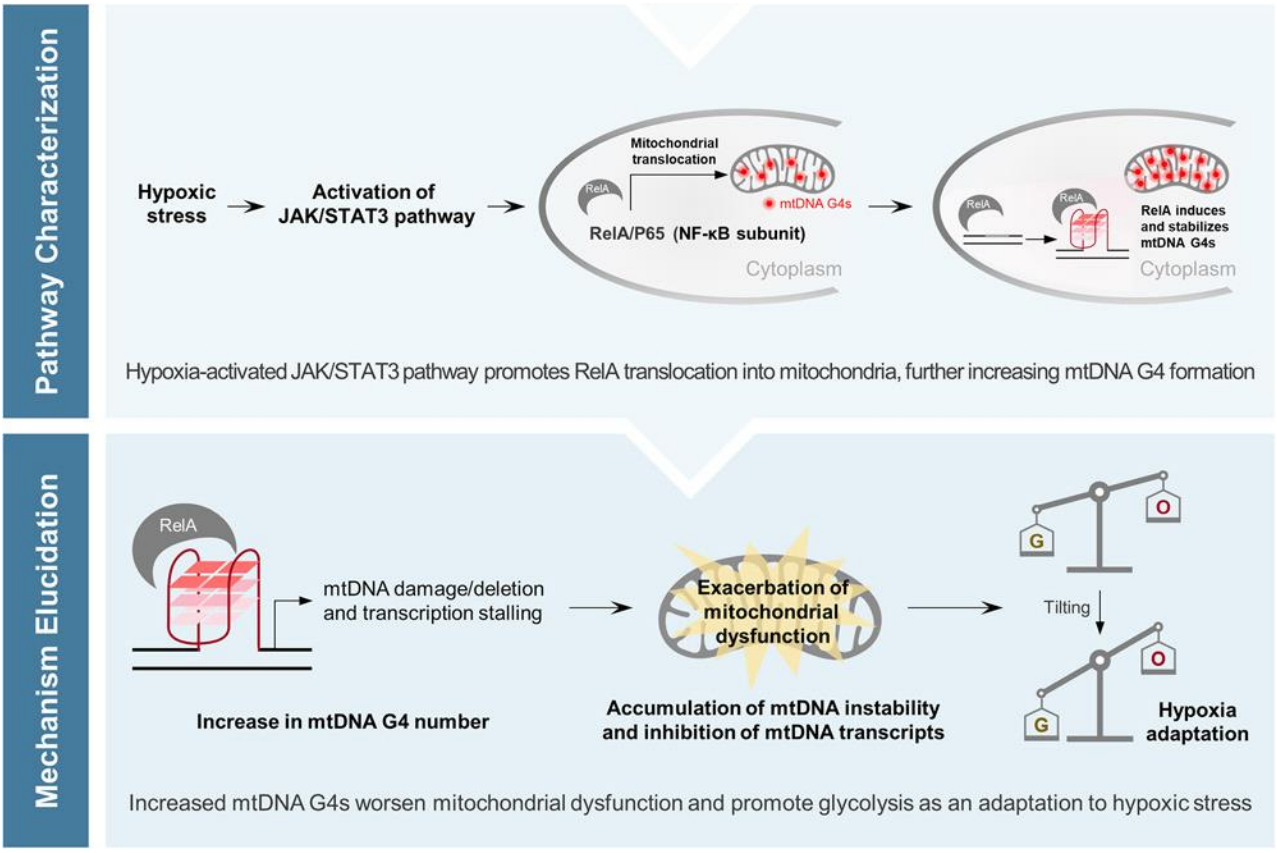

Figure 1.11. The relationship between mitochondrial DNA G-quadruplexes and reprogramming of mitochondrial energy production.[125]

Given the important role of G4-mtDNAs in the regulation of mitochondrial energy in cancer cells, the study of relevant mechanisms using appropriate tools will contribute to the development of new cancer therapeutics targeting G4-mtDNAs.

1.3.3 Control and regulation of mitochondrial G-quadruplexes

Within cells, G4 structure is tightly regulated by G4-binding proteins (G4BPs), which can either promote or impair G4 formation, thereby affecting biological processes such as transcription, translation, and genome stability.[127] Various techniques using G4 bait and mass spectrometry have successfully identified many proteins that interact with G4s in cells.[128, 129] Studies have shown that most G4BPs belong to helicases, such as DEAH-box helicase (DHX36),[130] RecQ class

(BLM),[131] and Werner's syndrome protein (WRN).[132] Although most studies on G4BPs have focused on the nucleus and cytoplasm, more and more studies have revealed that G4BPs have important regulatory roles on mitochondrial G4.

Pif1 is an evolutionarily conserved DNA helicase that exists in bacteria, yeast and mammals, which displays 5'-3' helicase activity on both DNA/DNA and DNA/RNA hybrids.[133, 134] It has been proven to have strong G4 unwinding activity, which plays an important role in inhibiting the formation of G4-mtDNAs. The G4 is a large secondary structure for the cell, and in the cells lacking Pif1 helicases, DNA replication is impeded due to the obstruction caused by the formation of G4s, thus resulting in the formation of DNA breakpoints, which in turn lead to the deletion of gene fragments.[134-136] Apart form Pif1 helicases, the RECQL4 helicases in the RECQ family have also been shown to exist in mitochondria and are found to play an important role in regulating the structure of G4-mtDNAs. The loss of RECQL4 helicases can alter mitochondrial integrity. Studies have shown that RECQL4 helicase is associated with Rothmund-Thomson syndrome (RTS), a very rare autosomal recessive disorder characterized by premature aging, genomic instability, and susceptibility to cancer. Q-PCR amplification of mtDNAs showed that the RECQL4 helicase deletion resulted in mtDNA damage in cells.[137] In addition, an *in vitro* study confirmed that the mtDNA-binding protein TFAM is a G-quadruplex-binding protein with the ability to bind to G4s, suggesting that the G-quadruplex structure may be present in mitochondria, but no evidence has been found for TFAM binding to the G4 structures in mammalian cells.[138] In addition to DNA, the mitochondrial RNA-binding protein GRSF1 exhibits a strong affinity for mitochondrial noncoding RNA sequences that are thought to potentially form G4s.[139] These G4BPs are believed to have the ability to control the stability and dynamic processes of mitochondrial G4s *in vivo*. They also have excellent specificity for specific G4s. The determination of G4 unwinding activities of G4BPs is essential for understanding the effects of G4s on mitochondrial function.

1.4 Research progress of G-quadruplex-targeting small molecule ligands

G4s play important roles in gene replication, transcription, translation and maintenance of genome stability. G4-selective small-molecule fluorescent ligands provide reliable tools to study the distribution, formation, and unwinding processes of G4s *in vivo*, which contributes to the study of G4 regulatory functions. At the same time, G4 also has an impact on the occurrence and development of

many diseases, including cancer and neurodegenerative diseases. Some G4 ligands have also been evaluated in clinical trials (**Table 1-1**). Therefore, it is important to develop ligands that can specifically bind to G4s and effectively regulate their biofunctions in living cells. This section will focus on the reported classical G4 ligands.

Table 1-1. G-quadruplex ligands studied in clinical trials.

Ligand	Clinical Number	Phase	Indications	Clinical state
CX-3543	NCT00955786	I	Advanced Solid Tumor, Lymphoma	Completed
	NCT00955292	I	Advanced Solid Tumor, Lymphoma	Terminated
	NCT00780663	II	Neuroendocrine Tumor, Carcinoid Tumor	Completed
	NCT00485966	II	B-cell Chronic Lymphocytic Leukemia	Withdrawal
CX-5461	NCT02719977	I	Solid Tumor	Completed
	NCT04890613	I	Advanced Solid Tumor	Recruiting
APTO-253	NCT02267863	I	Acute Myeloid Leukemia, Myelodysplastic Syndromes	Terminated
SOP1812	NCT06086522	I	Solid Tumor	Recruiting

1.4.1 Small-molecule ligands targeting telomeric DNA G-quadruplexes

As mentioned above, the telomere is closely related to the division ability of cancer cells. As the first target of G4s, researchers have developed many small-molecule ligands targeting telomeric G4-DNAs. The basic principle of these ligands to treat cancer is to induce or stabilize G4 structures at the end of the chromosome so that the activity of telomerase is inhibited. Then, the tumor cells enter the stage of senescence and apoptosis. Among many reported small-molecule ligands of telomeric G4-DNAs, BRACO19,[140] Telomestatin,[141] TMPyP4,[142] PDS,[143] Phen-DC3 [144] and 360A [145] are more classic ligands (**Figure 1.12**). Some studies have shown that these ligands can bind to telomeric G4-DNAs, which can lead to the impairment of telomere function and apoptosis of cancer cells.

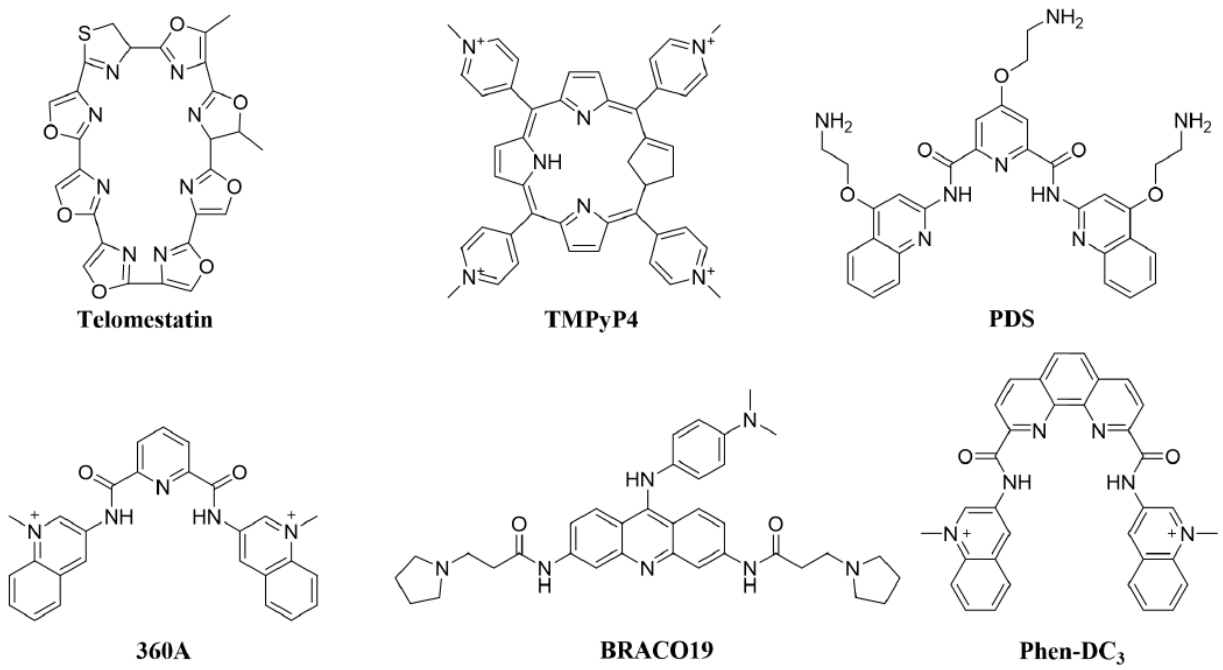

Figure 1.12. Some examples of typical telomere G-quadruplex ligands.

BRACO19 is a 3,6,9-trisubstituted acridine compound reported by Neidle et al. in 2005.[140] It is quite special in structure, in which the 3rd and 6th positions are respectively amide side chains, and the 9th position is an arylamine side chain. These side chains extend to the groove when BRACO19 interacts with G4-DNAs. At the same time, the aromatic amine at the 9th position of BRACO19 is an electron-donating group. The introduction of this group can enhance the electron cloud density of the pyridine nitrogen atom, resulting in greater basicity, which will be protonated in the physiological buffer and carry positive charges. Then, it can bind more tightly to G4-DNAs through electrostatic interaction. Studies have shown that BRACO19 has better G4 specificity and its affinity for G4-DNAs is 30 times as that of double-stranded DNAs. In the test of telomerase activity, its inhibitory effect is remarkable, and the half-inhibitory concentration (IC_{50}) value reaches 0.06 μM. In addition, in terms of anti-tumor, BRACO19 significantly inhibits the growth of tumors. For example, in human glioma cells, BRACO19 destroys the telomere structure by binding to G4-DNAs, exposing chromosomes, leading to DNA damage, and finally causing cell senescence and apoptosis.[146]

1.4.2 Small-molecule ligands targeting promoter DNA G-quadruplexes

In addition to telomere, proto-oncogene promoters are also potential G4-forming regions. Unlike telomeric G4-DNAs, G4s in promoter regions are mainly involved in the transcription of genes. Decreasing the expression of certain oncogenes by inducing or stabilizing the promoter G4-DNAs

with small-molecule ligands is an emerging anti-tumor strategy. Therefore, small-molecule ligands targeting G4-DNAs of proto-oncogene promoters have been developed rapidly in recent years.

c-MYC is a well-known anticancer drug target, but it is difficult to be targeted with small-molecule drugs. In recent years, researchers have synthesized many small-molecule ligands targeting *c-MYC* G4-DNAs to suppress c-MYC expression at transcriptional level. CX-3543, also known as Quarfloxin, is a fluoroquinolone derivative and the first G4 stabilizer to enter clinical trials (NCT00955786). The compound is rationally designed from norfloxacin and the fluoroquinolone G4 ligand QQ5863 by optimizing the planar core and adding a side chain that binds to the G4 loop for improving the selectivity for G4s.[147] In a breast cancer xenograft mouse model, CX-3543 exhibited *in vivo* antitumor activity and had minimal effect on animal body weight.[148] Initially, CX-3543 was thought to be a specific stabilizer of *c-MYC* G4-DNAs, but subsequent studies found that its interaction with ribosomal DNAs (rDNAs) interfered with the original interaction of G4s with nucleolin, thereby inhibiting RNA polymerase I transcription and inducing apoptosis in cancer cells.[148] In a phase II clinical trial (NCT00485966), CX-3543 showed good biological activity and tolerability with relatively low toxicity. However, CX-3543 has attracted attention due to its unique pharmacokinetic properties, manifested by its wide distribution in organisms and high accumulation levels in neural crest tissues, a feature that has raised concerns. Given the drug properties of CX-3543, especially the problems in bioavailability, its clinical application was significantly limited, which ultimately led to the withdrawal of the drug from phase II clinical trials.[149]

In addition to *c-MYC* G4-DNAs, the development of small-molecule ligands targeting *c-KIT*, *BCL2*, *K-RAS*, and other promoters has also received extensive attention. In 2017, Huang et al. designed and synthesized a series of 5,6-dihydrobenzo[*c*]acridine derivatives, and demonstrated in subsequent evaluations that these derivatives could effectively bind to *c-KIT* G4-DNAs. In addition, RT-PCR and Western-blot analyses showed that 2b was able to repress the transcription and translation of the *c-KIT* gene in K562 cells, which is consistent with the nature of the G-quadruplex-binding ligand targeting the *c-KIT* oncogene promoter. Further biological evaluation showed that compound 2b induced apoptosis by activating the caspase-3 cascade pathway.[150] In 2018, Cruz et al. synthesized a series of acridine orange derivatives (C3-C8), among which derivative C8 has a high affinity binding to *KRAS* G4-DNAs (K_D=10^{-7} M). Moreover, in the study of imaging of human cervical cancer

cells (HeLa), C8 was found specifically localized in the nucleus. Meanwhile, this derivative showed strong inhibitory effects on HeLa cells and was able to reduce the transcription of oncogenes without affecting non-cancer genes.[151] In 2020, Saha et al. designed and synthesized a series of carbazole derivatives. Studies have shown that the ligand 3ap could significantly increase the melting point of *BCL2* G4-DNAs. Subsequently, qRT-PCR and Western blotting analysis revealed that the ligand 3ap could downregulate the expression of the *BCL2* gene in HeLa and B95.8 cells, and induced apoptosis in a dose-dependent manner *in vitro*.[152]

1.4.3 Small-molecule ligands targeting mitochondrial DNA G-quadruplexes

Mitochondria in cells are the home of cellular metabolisms. G4-mtDNAs also plays vital roles in regulating mitochondrial gene functions. Although several fluorescent probes selectively recognizing and imaging G4-mtDNAs have been reported, compared to nuclear G4-DNAs, the ligand system targeting G4-mtDNAs developed thus far is very limited (**Figure 1.13**).[13]

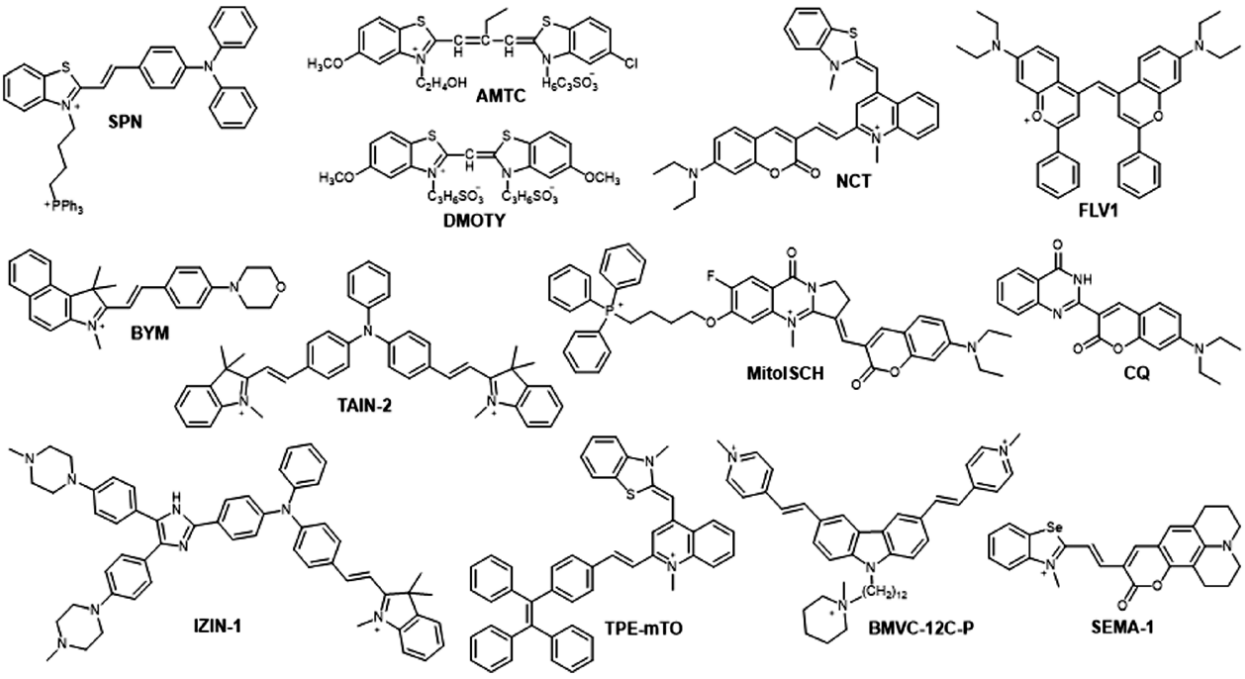

Figure 1.13. Fluorescent ligands with high selectivity toward G4-mtDNAs against other nucleic acid structures *in vitro* and in live cells.[13]

In 2013, Yao et al. reported that two G-quadruplex DNA-binding ligands (TMPyP4 and DODC) promote the release of cytochrome c, which in turn leads to mitochondrial dysfunction, and apoptosis. However, these ligands are not selective and cannot be specifically localized to mitochondria because the ligands are also enriched in the nucleus and then interact with G-quadruplex DNA to affect these

genes.[107] In 2015, Huang et al. provided the first evidence that the G4 structure exists in the mtDNA of living cells. The research group successfully synthesized a carbazole derivative BMVC-12C-P. This ligand mainly targets the mitochondrial genome and induces cancer cell death without damaging normal cells. G4-mtDNAs can also be visualized with the ligand by fluorescence lifetime imaging microscopy. At the same time, BMVC-12C-P can interact with G4-mtDNAs, stabilize the G4 structures in mtDNA, inhibit the expression of mitochondrial genes, and eventually lead to cell death.[103] In 2019, Yu et al. reported a thiazole orange derivative NCT. The ligand specifically targets G4-mtDNAs.[153] In 2021, Huang et al. reported a coumarin-quinazolinone conjugate compound CQ. Studies have shown that CQ has a mitochondrial localization function. CQ is a fluorescent probe and binds to G4-mtDNAs in living cells. Thus, it can be used for imaging G4-mtDNAs in cells.[154] To enhance the organelle specificity of the ligand, a lipophilic and cationic triphenylphosphonium (TPP) moiety that is known to drive the accumulation of organic molecules into mitochondria in response to the membrane potential is integrated into the design of G4-mtDNA-selective ligands. MitoISCH is synthesized by incorporating TPP with a coumarin–quinazolinone conjugate and is demonstrated to be a G4-mtDNA-selective fluorescent probe. The cellular location of MitoISCH in mitochondria is verified with the colocalization study using MitoTracker Green and LysoTracker Green in live HeLa cells. To characterize the specificity of MitoISCH targeting G4-mtDNAs, competition assays with MitoISCH and RHPS4 (a G4-selective ligand) were conducted in HeLa cells. The results suggest that MitoISCH is selective to G4-mtDNAs. The cytotoxicity of the ligand was examined and the IC_{50} value against HeLa cells was found to be greater than 20 μM for 3 h treatment. In addition, the ligand was utilized to investigate the relationship between G4-mtDNA formation and glycolysis levels in HepG2 cells. The results reveal that an upregulation of glycolysis by hypoxia may cause an increase in the quantity of intracellular G4-mtDNAs.[124] The probe may provide a useful chemical tool for investigating the role of G4-mtDNAs in cancer cell metabolism.

1.4.4 Small-molecule ligands targeting RNA G-quadruplexes

Compared with G4-DNAs, G4-RNAs are more widely distributed in cells and play important regulatory roles. But so far, due to the lack of real-time detection of G4-RNAs folding and unfolding methods, many studies on G4-RNAs have been carried out *in vitro*, which has led to the inability to truly understand its regulatory mechanism *in vivo*. Therefore, the development of fluorescent ligands that specifically target the G4-RNAs will help solve this dilemma and understand more about their

special structures and functions in cells. It is because G4-RNAs and G4-DNAs are similar in structure, achieving ligand-specific binding to G4-RNAs is challenging.

The research group of Huang Zhishu has reported a lot of work on the development of G4-RNA-targeting fluorescent ligands. In 2016, they designed a GTFH fluorescent probe ISCH-nras1 (**Figure 1.14**). The ligand specifically targets the G-quadruplex formed by the 5'-UTR regions of *N-RAS* mRNA. ISCH-nras1 is a hybridization probe with a very special design. Its structure consists of two parts: the first part is for the G-quadruplex fluorophore, and the second part is a nucleic acid sequence, which is complementary to the sequence located in the 5'-UTR regions of *N-RAS* mRNA. These two parts are combined by an azide reaction. Further experiments showed that ISCH-nras1 could precisely target *N-RAS* G4-RNAs for fluorescence visualization both *in vitro* and *in vivo*. Therefore, ISCH-nras1 is a useful tool to directly study the structure of G4-RNAs. It also provides a new reference for the design of G4-RNA-targeting probes.[155] In 2018, they reported a new red fluorescent probe QUMA-1, which was formed by condensation of *N*-methylated quinoline and coumarin aldehyde. Cell imaging experiments show that QUMA-1 selectively binds to G4-RNAs in HeLa cells and displays the dynamic folding process of G4-RNAs in real-time, which is beneficial to reveal the biological function of G4-RNAs.[156] In 2020, they synthesized a series of benzothiazole derivatives. Among these ligands, BEDO-3 has excellent ability to bind to G4-RNAs *in vitro*, and selectively binds to G4-RNAs in HeLa cells.[157] In 2023, they developed a cell-based approach for large-scale screening of *NRAS* G4-RNAs ligands using a G-quadruplex-triggered fluorogenic hybridization probe. Through this method, they found Octenidine, a clinically used agent, as a strong NRAS repressor. Octenidine inhibited NRAS translation, disrupted the MAPK and PI3K-AKT signaling pathways, and induced cell cycle arrest, apoptosis, and autophagy. Octenidine demonstrated superior antiproliferative effects compared to existing clinical antimelanoma treatments and effectively inhibited the growth of NRAS-mutant melanoma in a xenograft mouse model, indicating that Octenidine could be a promising treatment for NRAS-mutant melanoma.[158] In 2024, they structurally modified QUMA-1 and found that compound 15a demonstrated remarkable ability in stabilizing *KRAS* G4-RNAs, leading to suppressed KRAS translation and subsequent modulation of the MAPK and PI3K-AKT pathways. It caused cell cycle arrest and apoptosis in cancer cells driven by KRAS mutations, and significantly reduced tumor growth in a KRAS mutant xenograft model.[159]

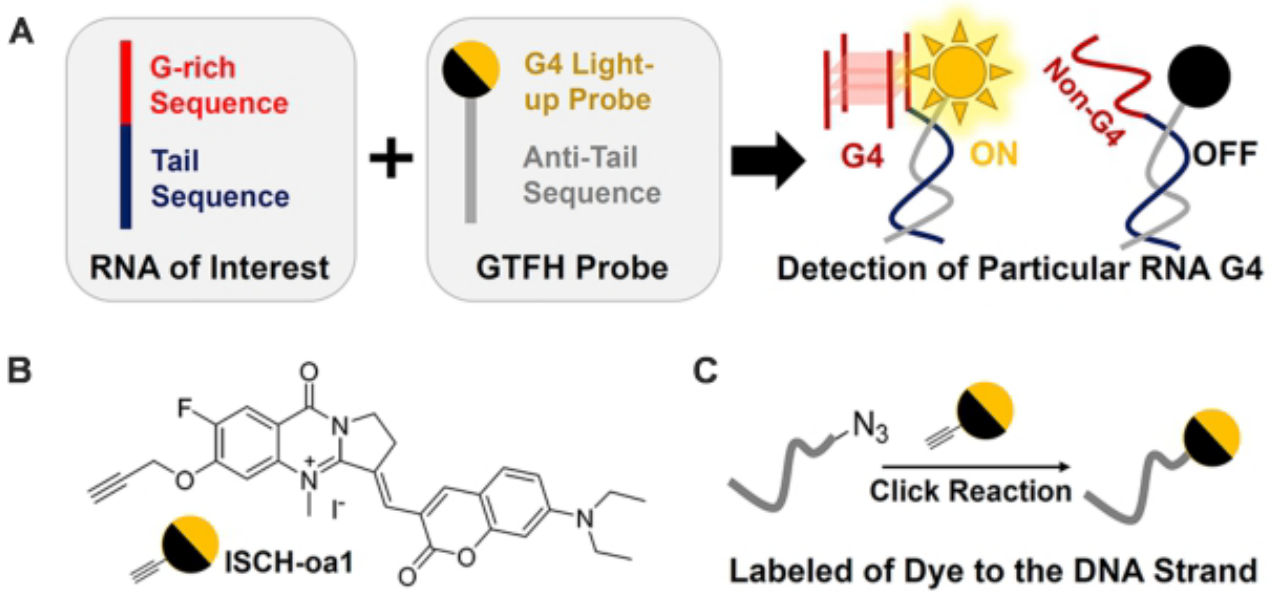

Figure 1.14. Illustration of GTFH probe: (A) GTFH probe design principle. (B) Chemical structure of ISCH-oa1. (C) GTFH probe preparation.[155]

1.5 G-quadruplexes and cancer therapy

Cancer is the second leading cause of death in the world. The latest statistics released by the National Cancer Center in February 2024 show that there are about 4.8 million new cases of cancer in China in 2022.[160] Despite the great progress made in cancer treatment in the past few years, this number is still alarming. Therefore, it is essential to strengthen research on the causes of cancer development as well as to improve diagnosis and anti-tumor treatment protocols. A number of promising therapeutic strategies have been identified through the identification of genetic and epigenetic abnormalities in tumor cells as well as oncogenes that promote tumor growth.[161, 162] One of these novel strategies is the modulation of G4 formation in DNA, which in turn affects biological processes and genomic stability.

In recent years, G4 ligands have been considered as a potential therapeutic tool against tumor cells. Researchers have also successfully developed G4 ligands with potent antitumor activity. These G4-targeting ligands mainly exert their anticancer effects by inhibiting oncogene expression, inducing genomic instability in cancer cells and disrupting telomere maintenance (**Figure 1.15**).[36]

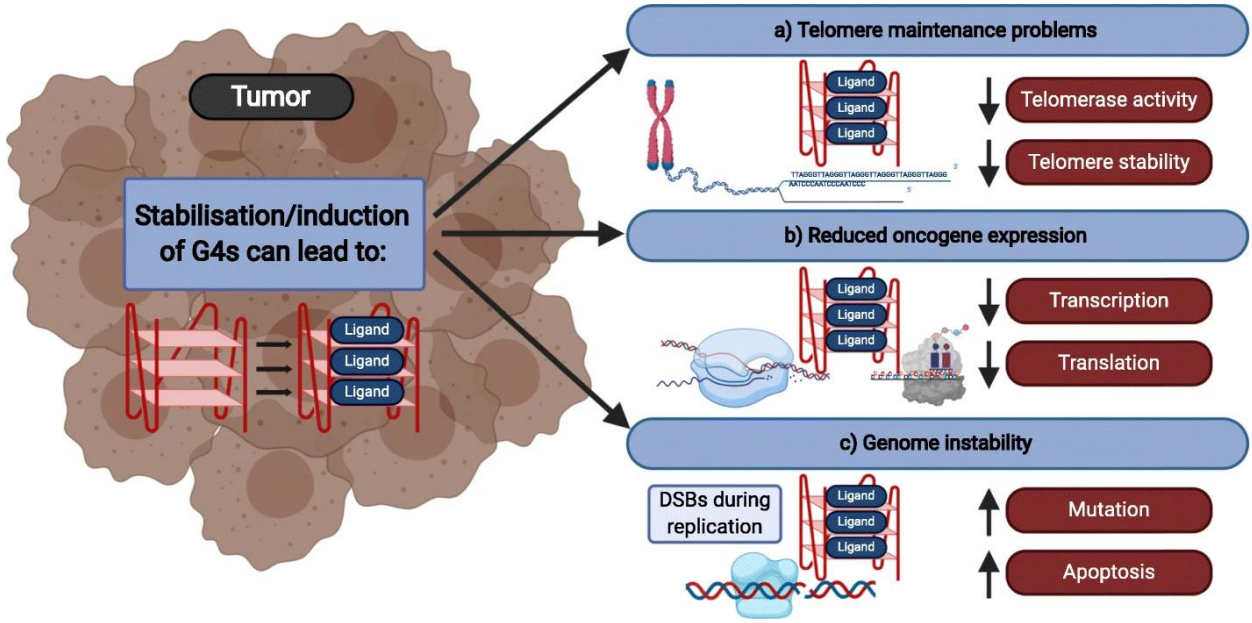

Figure 1.15. Effects of G4 ligands on cancer cells.[36]

1.5.1 G-quadruplexes-targeting ligands for melanoma treatment

Melanoma is a malignant skin tumor which usually occurs in melanocytes. The 5-year overall survival rate for limited melanoma is about 99%, while the 5-year overall survival rate for metastatic melanoma is only about 25%. Although the development of targeted therapies and immunotherapies has significantly improved survival rates, many patients still unfortunately pass away.[163, 164] Melanomas are often considered highly mutated types of cancers with genomes that frequently have mutations in different proteins, such as TP53,[165] RHOJ,[166] and RSK [167]. These mutations block DNA damage-induced apoptosis. Many studies have used different melanoma cell lines to test the effect of G4 structural stabilization on melanoma cell growth. For example, the imidazole-benzothiazole coupling IZTZ-1 inhibits melanoma cell growth. It targets *c-MYC* DNA G4s and stabilizes the G4s causing a decrease in c-MYC protein expression.[168] In addition, a porphyrin-like G4 ligand TMPyP4 retarded melanoma growth and prolonged survival in mice.[169]

1.5.2 G-quadruplex-targeting ligands for pancreatic cancer treatment

Pancreatic cancer, a malignant tumor that originates in the pancreatic tissue, has a 5-year survival rate of only 9%, and once the tumor cannot be surgically removed, its treatment options become very limited. RAS genes (including *K-RAS*, *N-RAS* and *H-RAS*) are the most mutated oncogenes in pancreatic cancer. Mutations in the oncogene *K-RAS* are essential for the initiation of Pancreatic Ductal Adenocarcinoma (PDCA). Since *K-RAS* plays a key role in the pathogenesis of pancreatic cancer, down-regulation of *K-RAS* expression could be an effective strategy for pancreatic cancer

treatment. Studies have shown that there are three G4 motifs in the *K-RAS* promoter, which are located in the nuclease hypersensitivity element upstream of the transcription start site. It has been reported that the transcription factors MAZ, HNRNPA1 and HMGB1 can regulate *KRAS* expression by binding to the G4 structures within *K-RAS*. Meanwhile, the formation of the G4 structure itself silences *K-RAS* expression. These findings further illustrate the possibility of using G4s within the promoter of the *K-RAS* gene as a potential drug target.

Several studies applying G4 ligands for pancreatic cancer therapy have been reported. For example, TMPyP4 induced tumor cell death when co-incubated with pancreatic cancer cells MIA PaCa-2, while it has no effects on normal cells.[170] In addition, porphyrin derivatives Tetrakis and Octaacetyl were able to inhibit the proliferation of Ehrlich Ascites Carcinoma (EAC) solid tumors by stabilizing *K-RAS* G4s and reducing *K-RAS* gene expression.[171]

1.5.3 G-quadruplex-targeting ligands for leukemia treatment

Leukemia is a malignant disease caused by abnormally proliferating blood cells, primarily affecting the stem cells that produce blood cells in the bone marrow and lymphoid tissue. Depending on the rate of growth and maturity of the leukemia cells, it can be classified into two types: acute and chronic. Acute Myeloid Leukemia (AML) is the most common acute leukemia in adults and is characterized by a relatively small number of mutations.[172] Over the past two decades, a variety of G4 ligands such as SYUIQ-5,[173] APTO-253 [174] and TMPyP4 [175] have studied for their inhibitory effects on leukemia cell growth. It has been reported that these ligands could stabilize the G4 structure and are found effectively inhibiting leukemia cell growth *in vitro* and *in vivo* and affecting oncogene expression and telomerase function. For example, AML cells after being treated with SYUIQ-5 showed telomere shortening and senescence.[173] In addition, computer simulations reveal that about 70% of the re-arranged genes in leukemia contain G4 motifs, suggesting that G4s may promote tumor genomic instability.[176]

1.5.4 G-quadruplexes targeting ligands for activating antitumor immunity

Significant advances have been made in tumor treatment with immunotherapy, which uses immune checkpoint inhibitors, CAR-T cells, or bispecific antibodies to enhance T-cell responses.[177, 178] However, these treatments are ineffective for many tumors or become ineffective after tumor recurrence, suggesting the need to explore novel mechanisms and molecules to optimize

immunotherapy strategies.[179] The G4 ligands PDS and PhenDC3 were found to accumulate micronuclei at non-cytotoxic concentrations, thereby activating the innate immune response in cancer cells. These micronuclei can be recognized by specific receptors, which in turn activate the cGAS-STING pathway, thereby promoting the expression of immune genes (**Figure 1.16**).[180] These findings strongly support the potential of G4 ligands in stimulating antitumor immunity, particularly in promoting immunotherapeutic activity.

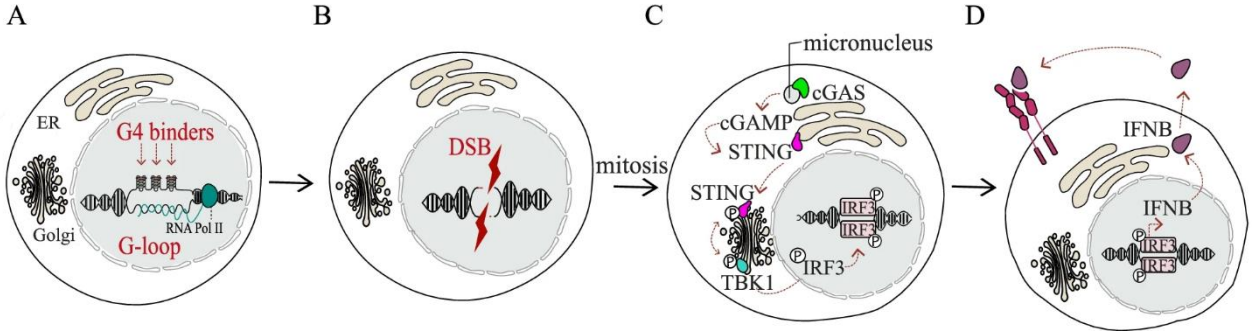

Figure 1.16. G4 ligands stimulate antitumor immunity.[181]

Taken together, G4 ligands have potential therapeutic effects for many types of cancers, but the specific mechanism and the expansion of G4-ligand diversity still need to be further investigated. Through molecular design and other drug screening strategies, it is believed that more and more G4-specific and potent ligands can be developed for antitumor therapy.

1.6 Summary and limitations of existing research

Through the literature review, this chapter concentratedly describes the structure, distribution, and major biological functions of G4s, as well as summarizes the progress of current research development on G4-targeting small-molecule ligands and their potential applications in cancer therapy. We found that most of the current studies on G4-DNAs focus on nuclear G4s, while the studies on G4-mtDNAs are just few. A summary of the limitation is listed as follows:

(i) Most evidence for G4-mtDNA comes from *in vitro* experiments. Whether these structures truly exist within living cells under physiological conditions remains to be fully confirmed.

(ii) A few small-molecule fluorescent ligands reported can specifically target G4-mtDNAs at present. Further advancing the existing ligands and novel design of G4-mtDNA targeting ligands are needed to differentiate intracellular mitochondrial and nuclear G4-DNAs, but this task remains a challenge.

(iii) It has been shown that there are multiple sequences that can form G4s in the heavy strand of mtDNA. These G4 structures formed may affect the replication and transcription of the corresponding genes. However, the specific regulatory mechanism is not well understood, which is related to the lack of appropriate research tools, especially fluorescent small molecules that can specifically target G4-mtDNAs in live-cells.

(iv) The regulation of mitochondrial function by G4-mtDNAs, especially in the regulation of energy production, calcium homeostasis, and ROS production, has not been well studied. Currently, it is not clear whether small-molecule ligands of G4-mtDNAs could regulate these important mitochondrial functions.

(v) Currently, most G4 ligands used for anti-tumor purposes target telomeres, promoters and 5'-UTR G4s, while very few target G4-mtDNAs. Although some studies have shown that small-molecule ligands targeting G4-mtDNAs may inhibit tumor cell growth and induce apoptosis, the specific anticancer mechanism needs to be further investigated.

Based on the above reasons, we believe that the regulatory mechanism of G4-mtDNAs, the effect of G4-mtDNAs on mitochondrial functions, and the anti-tumor mechanism of small-molecule ligands targeting G4-mtDNAs need to be further explored. Therefore, it is important to develop novel small-molecule fluorescent ligands that can specifically target G4-mtDNAs in live-cells for mechanistic and chemical biology studies against cancers and other mitochondria-related diseases.

1.7 Research questions and hypotheses

To better understand the regulatory role of G4-mtDNAs and its feasibility as an antitumor target, we raise the following research questions and corresponding hypotheses:

Question (i): Whether obtain fluorescent small molecules capable of specifically targeting G4-mtDNAs intracellularly and not to interfere with nuclear G4-DNAs by rational structural design approach.

Question (ii): Whether increasing the G4-mtDNAs stability by the ligands affects mtDNAs replication and transcription and whether there is any difference between cancer and non-cancer (or normal) cells.

Question (iii): Whether small-molecule ligands specifically targeting G4-mtDNAs affect the energy metabolism of mitochondria in cancer cells, causing mitochondrial dysfunction and ultimately leading to apoptosis or necrosis of cancer cells.

Question (iv): Whether small molecules specifically targeting G4-mtDNAs exhibit anticancer efficacy and biosafety in a tumor-baring mice model.

Corresponding hypotheses:
Hypotheses (i): Small-molecule fluorescent ligands that can specifically target G4-mtDNAs in cells without interfering with nuclear G4-DNAs can be obtained by rational structural design.

Hypotheses (ii): By specifically targeting small molecule ligands to G4-mtDNAs, the structure of G4-mtDNAs can be induced or stabilized, which in turn inhibits the replication and transcription of the corresponding gene.

Hypotheses (iii): Due to the stabilization of G4-mtDNAs by small-molecule ligands, the assembly of the mitochondrial respiratory chain complex is blocked, which results in changes in oxidative phosphorylation and glycolysis and may lead to impaired mitochondrial function and ultimately apoptosis of cancer cells.

Hypotheses (iv): Targeting small molecules of G4-mtDNAs can inhibit the growth of tumors in a tumor-baring mice model, showing some anti-tumor ability.

1.8 Objectives of the project

As mentioned above, it is important to develop novel anti-tumor tools that target mitochondria and their G4-mtDNAs because these structures are potential drug targets for anticancer study. However, the regulatory mechanism of G4-mtDNAs is not well understood at present due to the lack of small-

molecule fluorescent probes specifically targeting G4-mtDNAs, which poses a certain impediment to the development of antitumor drugs targeting G4-mtDNAs. To discover the roles G4-mtDNAs play in cellular activities, we design a series of small-molecule ligands to target G4-mtDNAs in living cells for in-depth investigations. The main objectives of the project are listed below:

(i) To develop novel G4-mtDNAs specific fluorescent ligands for the investigation of interaction mechanism.

(ii) To understand the regulatory role of G4 structures in mitochondria with the target-specific ligands and the ability of the ligands to regulate the mitochondrial functions.

(iii) To study the inhibitory effects of the ligands in anticancer targeting mitochondrial respiratory chain and understand the mechanism of apoptosis or necrosis induced by the G4-mtDNA target-specific ligands.

(iv) To investigate *in vivo* anti-cancer effects and biosafety of ligands in tumor-baring mouse models.

1.9 References

[1] I. Bang, Untersuchungen über die Guanylsäure, Biochem. Z 26 (1910) 293-311.

[2] M. Gellert, M.N. Lipsett, D.R. Davies, Helix formation by guanylic acid, Proceedings of the National Academy of Sciences 48(12) (1962) 2013-2018.

[3] D. Varshney, J. Spiegel, K. Zyner, D. Tannahill, S. Balasubramanian, The regulation and functions of DNA and RNA G-quadruplexes, Nature Reviews Molecular Cell Biology 21(8) (2020) 459-474.

[4] B.I. Kankia, L.A. Marky, Folding of the thrombin aptamer into a G-quadruplex with Sr2+: stability, heat, and hydration, Journal of the American Chemical Society 123(44) (2001) 10799-10804.

[5] W. Liu, H. Zhu, B. Zheng, S. Cheng, Y. Fu, W. Li, T.-C. Lau, H. Liang, Kinetics and mechanism of G-quadruplex formation and conformational switch in a G-quadruplex of PS2. M induced by Pb2+, Nucleic Acids Research 40(9) (2012) 4229-4236.

[6] M. Cheng, Y. Cheng, J. Hao, G. Jia, J. Zhou, J.-L. Mergny, C. Li, Loop permutation affects the topology and stability of G-quadruplexes, Nucleic acids research 46(18) (2018) 9264-9275.

[7] S. Lago, E. Tosoni, M. Nadai, M. Palumbo, S.N. Richter, The cellular protein nucleolin preferentially binds long-looped G-quadruplex nucleic acids, Biochimica et Biophysica Acta (BBA)-

General Subjects 1861(5) (2017) 1371-1381.

[8] A.-J. Guan, E.-X. Zhang, J.-F. Xiang, Q. Li, Q.-F. Yang, L. Li, Y.-L. Tang, M.-X. Wang, Effects of loops and nucleotides in G-quadruplexes on their interaction with an azacalixarene, methylazacalix [6] pyridine, The Journal of Physical Chemistry B 115(43) (2011) 12584-12590.

[9] Y. Chen, D. Yang, Sequence, stability, and structure of G‐quadruplexes and their interactions with drugs, Current protocols in nucleic acid chemistry 50(1) (2012) 17.5. 1-17.5. 17.

[10] S. Burge, G.N. Parkinson, P. Hazel, A.K. Todd, S. Neidle, Quadruplex DNA: sequence, topology and structure, Nucleic acids research 34(19) (2006) 5402-5415.

[11] A. Ambrus, D. Chen, J. Dai, T. Bialis, R.A. Jones, D. Yang, Human telomeric sequence forms a hybrid-type intramolecular G-quadruplex structure with mixed parallel/antiparallel strands in potassium solution, Nucleic acids research 34(9) (2006) 2723-2735.

[12] Y. Wang, D.J. Patel, Solution structure of the human telomeric repeat d [AG3 (T2AG3) 3] G-tetraplex, Structure 1(4) (1993) 263-282.

[13] B.-X. Zheng, J. Yu, W. Long, K.H. Chan, A.S.-L. Leung, W.-L. Wong, Structurally diverse G-quadruplexes as the noncanonical nucleic acid drug target for live cell imaging and antibacterial study, Chemical Communications 59(11) (2023) 1415-1433.

[14] J.L. Huppert, S. Balasubramanian, Prevalence of quadruplexes in the human genome, Nucleic acids research 33(9) (2005) 2908-2916.

[15] A.K. Todd, M. Johnston, S. Neidle, Highly prevalent putative quadruplex sequence motifs in human DNA, Nucleic acids research 33(9) (2005) 2901-2907.

[16] R. Hänsel-Hertsch, D. Beraldi, S.V. Lensing, G. Marsico, K. Zyner, A. Parry, M. Di Antonio, J. Pike, H. Kimura, M. Narita, G-quadruplex structures mark human regulatory chromatin, Nature genetics 48(10) (2016) 1267-1272.

[17] J. Lyu, R. Shao, P.Y. Kwong Yung, S.J. Elsässer, Genome-wide mapping of G-quadruplex structures with CUT&Tag, Nucleic acids research 50(3) (2022) e13-e13.

[18] J. Eddy, N. Maizels, Gene function correlates with potential for G4 DNA formation in the human genome, Nucleic acids research 34(14) (2006) 3887-3896.

[19] J.L. Huppert, S. Balasubramanian, G-quadruplexes in promoters throughout the human genome, Nucleic acids research 35(2) (2007) 406-413.

[20] B. Sacca, L. Lacroix, J.-L. Mergny, The effect of chemical modifications on the thermal stability of different G-quadruplex-forming oligonucleotides, Nucleic acids research 33(4) (2005) 1182-1192.

[21] A. Bugaut, S. Balasubramanian, 5′ -UTR RNA G-quadruplexes: translation regulation and targeting, Nucleic acids research 40(11) (2012) 4727-4741.

[22] B.D. Griffin, H.W. Bass, Plant G-quadruplex (G4) motifs in DNA and RNA; abundant, intriguing sequences of unknown function, Plant Science 269 (2018) 143-147.

[23] V. Yadav, n. Hemansi, N. Kim, N. Tuteja, P. Yadav, G quadruplex in plants: a ubiquitous regulatory element and its biological relevance, Frontiers in Plant Science 8 (2017) 1163.

[24] P. Yadav, N. Kim, M. Kumari, S. Verma, T.K. Sharma, V. Yadav, A. Kumar, G-quadruplex structures in bacteria: biological relevance and potential as an antimicrobial target, Journal of Bacteriology 203(13) (2021) 10.1128/jb. 00577-20.

[25] G. Marsico, V.S. Chambers, A.B. Sahakyan, P. McCauley, J.M. Boutell, M.D. Antonio, S. Balasubramanian, Whole genome experimental maps of DNA G-quadruplexes in multiple species, Nucleic acids research 47(8) (2019) 3862-3874.

[26] H. Masai, S. Matsumoto, Z. You, N. Yoshizawa-Sugata, M. Oda, Eukaryotic chromosome DNA replication: where, when, and how?, Annual review of biochemistry 79(1) (2010) 89-130.

[27] J.A. Patel, H. Kim, The TIMELESS effort for timely DNA replication and protection, Cellular and Molecular Life Sciences 80(4) (2023) 84.

[28] B. Ekundayo, F. Bleichert, Origins of DNA replication, PLoS genetics 15(9) (2019) e1008320.

[29] M.N. Weitzmann, K.J. Woodford, K. Usdin, The development and use of a DNA polymerase arrest assay for the evaluation of parameters affecting intrastrand tetraplex formation, Journal of Biological Chemistry 271(34) (1996) 20958-20964.

[30] A. De Magis, S.G. Manzo, M. Russo, J. Marinello, R. Morigi, O. Sordet, G. Capranico, DNA damage and genome instability by G-quadruplex ligands are mediated by R loops in human cancer cells, Proceedings of the National Academy of Sciences 116(3) (2019) 816-825.

[31] R. Rodriguez, S. Müller, J.A. Yeoman, C. Trentesaux, J.-F. Riou, S. Balasubramanian, A novel small molecule that alters shelterin integrity and triggers a DNA-damage response at telomeres, Journal of the American Chemical Society 130(47) (2008) 15758-15759.

[32] J.-B. Vannier, V. Pavicic-Kaltenbrunner, M.I. Petalcorin, H. Ding, S.J. Boulton, RTEL1 dismantles T loops and counteracts telomeric G4-DNA to maintain telomere integrity, Cell 149(4) (2012) 795-806.

[33] R. Linke, M. Limmer, S.A. Juranek, A. Heine, K. Paeschke, The relevance of G-quadruplexes for DNA repair, International journal of molecular sciences 22(22) (2021) 12599.

[34] Z. Yang, K.K. Takai, C.A. Lovejoy, T. de Lange, Break-induced replication promotes fragile telomere formation, Genes & development 34(19-20) (2020) 1392-1405.

[35] K.I. McLuckie, M. Di Antonio, H. Zecchini, J. Xian, C. Caldas, B.-F. Krippendorff, D. Tannahill, C. Lowe, S. Balasubramanian, G-quadruplex DNA as a molecular target for induced synthetic lethality in cancer cells, Journal of the American Chemical Society 135(26) (2013) 9640-9643.

[36] N. Kosiol, S. Juranek, P. Brossart, A. Heine, K. Paeschke, G-quadruplexes: a promising target for cancer therapy, Molecular Cancer 20 (2021) 1-18.

[37] J. Meyne, R.L. Ratliff, R.K. MoYzIs, Conservation of the human telomere sequence (TTAGGG) n among vertebrates, Proceedings of the National Academy of Sciences 86(18) (1989) 7049-7053.

[38] D. Hanahan, R.A. Weinberg, The hallmarks of cancer, cell 100(1) (2000) 57-70.

[39] S. Sandin, D. Rhodes, Telomerase structure, Current Opinion in Structural Biology 25 (2014) 104-110.

[40] E.H. Blackburn, Structure and function of telomeres, Nature 350(6319) (1991) 569-73.

[41] E.H. Blackburn, Switching and signaling at the telomere, Cell 106(6) (2001) 661-73.

[42] K. Damm, U. Hemmann, P. Garin-Chesa, N. Hauel, I. Kauffmann, H. Priepke, C. Niestroj, C. Daiber, B. Enenkel, B. Guilliard, I. Lauritsch, E. Müller, E. Pascolo, G. Sauter, M. Pantic, U.M. Martens, C. Wenz, J. Lingner, N. Kraut, W.J. Rettig, A. Schnapp, A highly selective telomerase inhibitor limiting human cancer cell proliferation, Embo j 20(24) (2001) 6958-68.

[43] R. Salama, M. Sadaie, M. Hoare, M. Narita, Cellular senescence and its effector programs, Genes Dev 28(2) (2014) 99-114.

[44] N.W. Kim, M.A. Piatyszek, K.R. Prowse, C.B. Harley, M.D. West, P.L. Ho, G.M. Coviello, W.E. Wright, S.L. Weinrich, J.W. Shay, Specific association of human telomerase activity with immortal cells and cancer, Science 266(5193) (1994) 2011-5.

[45] C. Autexier, N.F. Lue, The structure and function of telomerase reverse transcriptase, Annu Rev Biochem 75 (2006) 493-517.

[46] S.A. Stewart, R.A. Weinberg, Telomeres: cancer to human aging, Annu Rev Cell Dev Biol 22 (2006) 531-57.

[47] M. De Vitis, F. Berardinelli, A. Sgura, Telomere Length Maintenance in Cancer: At the Crossroad between Telomerase and Alternative Lengthening of Telomeres (ALT), Int J Mol Sci 19(2) (2018).

[48] T.M. Bryan, G-Quadruplexes at Telomeres: Friend or Foe?, Molecules 25(16) (2020).

[49] J. Gao, H.A. Pickett, Targeting telomeres: advances in telomere maintenance mechanism-

specific cancer therapies, Nat Rev Cancer 22(9) (2022) 515-532.
[50] N. Kim, The Interplay between G-quadruplex and Transcription, Curr Med Chem 26(16) (2019) 2898-2917.
[51] B.P. Belotserkovskii, J.H. Soo Shin, P.C. Hanawalt, Strong transcription blockage mediated by R-loop formation within a G-rich homopurine-homopyrimidine sequence localized in the vicinity of the promoter, Nucleic Acids Res 45(11) (2017) 6589-6599.
[52] B.P. Belotserkovskii, R. Liu, S. Tornaletti, M.M. Krasilnikova, S.M. Mirkin, P.C. Hanawalt, Mechanisms and implications of transcription blockage by guanine-rich DNA sequences, Proc Natl Acad Sci U S A 107(29) (2010) 12816-21.
[53] K.W. Zheng, S. Xiao, J.Q. Liu, J.Y. Zhang, Y.H. Hao, Z. Tan, Co-transcriptional formation of DNA:RNA hybrid G-quadruplex and potential function as constitutional cis element for transcription control, Nucleic Acids Res 41(10) (2013) 5533-41.
[54] J. Dai, D. Chen, R.A. Jones, L.H. Hurley, D. Yang, NMR solution structure of the major G-quadruplex structure formed in the human BCL2 promoter region, Nucleic Acids Res 34(18) (2006) 5133-44.
[55] R.I. Mathad, E. Hatzakis, J. Dai, D. Yang, c-MYC promoter G-quadruplex formed at the 5'-end of NHE III1 element: insights into biological relevance and parallel-stranded G-quadruplex stability, Nucleic Acids Res 39(20) (2011) 9023-33.
[56] P. Agrawal, E. Hatzakis, K. Guo, M. Carver, D. Yang, Solution structure of the major G-quadruplex formed in the human VEGF promoter in K+: insights into loop interactions of the parallel G-quadruplexes, Nucleic Acids Res 41(22) (2013) 10584-92.
[57] F. Wang, C. Wang, Y. Liu, W. Lan, H. Han, R. Wang, S. Huang, C. Cao, Colchicine selective interaction with oncogene RET G-quadruplex revealed by NMR, Chem Commun (Camb) 56(14) (2020) 2099-2102.
[58] E.V. Schmidt, The role of c-myc in cellular growth control, Oncogene 18(19) (1999) 2988-96.
[59] D.M. Miller, S.D. Thomas, A. Islam, D. Muench, K. Sedoris, c-Myc and cancer metabolism, Clin Cancer Res 18(20) (2012) 5546-53.
[60] K. Daigo, A. Takano, P.M. Thang, Y. Yoshitake, M. Shinohara, I. Tohnai, Y. Murakami, J. Maegawa, Y. Daigo, Characterization of KIF11 as a novel prognostic biomarker and therapeutic target for oral cancer, Int J Oncol 52(1) (2018) 155-165.
[61] T.A. Brooks, L.H. Hurley, The role of supercoiling in transcriptional control of MYC and its

importance in molecular therapeutics, Nat Rev Cancer 9(12) (2009) 849-61.
[62] R. Rodriguez, S. Müller, J.A. Yeoman, C. Trentesaux, J.F. Riou, S. Balasubramanian, A novel small molecule that alters shelterin integrity and triggers a DNA-damage response at telomeres, J Am Chem Soc 130(47) (2008) 15758-9.
[63] R. Chaudhuri, S. Bhattacharya, J. Dash, S. Bhattacharya, Recent Update on Targeting c-MYC G-Quadruplexes by Small Molecules for Anticancer Therapeutics, J Med Chem 64(1) (2021) 42-70.
[64] E.H. Postel, S.E. Mango, S.J. Flint, A nuclease-hypersensitive element of the human c-myc promoter interacts with a transcription initiation factor, Mol Cell Biol 9(11) (1989) 5123-33.
[65] T.L. Davis, A.B. Firulli, A.J. Kinniburgh, Ribonucleoprotein and protein factors bind to an H-DNA-forming c-myc DNA element: possible regulators of the c-myc gene, Proc Natl Acad Sci U S A 86(24) (1989) 9682-6.
[66] T. Simonsson, P. Pecinka, M. Kubista, DNA tetraplex formation in the control region of c-myc, Nucleic Acids Res 26(5) (1998) 1167-72.
[67] W. Wang, S. Hu, Y. Gu, Y. Yan, D.B. Stovall, D. Li, G. Sui, Human MYC G-quadruplex: From discovery to a cancer therapeutic target, Biochim Biophys Acta Rev Cancer 1874(2) (2020) 188410.
[68] S. Jiang, A. Awadasseid, S. Narva, S. Cao, Y. Tanaka, Y. Wu, W. Fu, X. Zhao, C. Wei, W. Zhang, Anti-cancer activity of benzoxazinone derivatives via targeting c-Myc G-quadruplex structure, Life Sci 258 (2020) 118252.
[69] J.-L. Qin, Q.-P. Qin, Z.-Z. Wei, Y.-C. Yu, T. Meng, C.-X. Wu, Y.-L. Liang, H. Liang, Z.-F. Chen, Stabilization of c-myc G-Quadruplex DNA, inhibition of telomerase activity, disruption of mitochondrial functions and tumor cell apoptosis by platinum(II) complex with 9-amino-oxoisoaporphine, European Journal of Medicinal Chemistry 124 (2016) 417-427.
[70] R. Yao, Y. Zhang, Y. Zeng, Y. Zhang, L. Liu, J. Gao, Novel c-Myc G4 stabilizer EP12 promotes myeloma cytotoxicity by disturbing NF-κB signaling, Exp Cell Res 431(1) (2023) 113759.
[71] S. Cogoi, L.E. Xodo, G-quadruplex formation within the promoter of the KRAS proto-oncogene and its effect on transcription, Nucleic Acids Res 34(9) (2006) 2536-49.
[72] P. Sengupta, S. Chattopadhyay, S. Chatterjee, G-Quadruplex surveillance in BCL-2 gene: a promising therapeutic intervention in cancer treatment, Drug Discov Today 22(8) (2017) 1165-1186.
[73] Y. Yang, Y. Yang, S. Wang, H. Li, D.D.Y. Chen, Detecting the formation of human c-KIT oncogene promoter G-Quadruplex by Taylor dispersion analysis, Talanta 233 (2021) 122533.
[74] Y. Wu, L.P. Zan, X.D. Wang, Y.J. Lu, T.M. Ou, J. Lin, Z.S. Huang, L.Q. Gu, Stabilization of

VEGF G-quadruplex and inhibition of angiogenesis by quindoline derivatives, Biochim Biophys Acta 1840(9) (2014) 2970-7.
[75] A. Membrino, S. Cogoi, E.B. Pedersen, L.E. Xodo, G4-DNA formation in the HRAS promoter and rational design of decoy oligonucleotides for cancer therapy, PLoS One 6(9) (2011) e24421.
[76] S. Kumari, A. Bugaut, J.L. Huppert, S. Balasubramanian, An RNA G-quadruplex in the 5' UTR of the NRAS proto-oncogene modulates translation, Nat Chem Biol 3(4) (2007) 218-21.
[77] R. Shahid, A. Bugaut, S. Balasubramanian, The BCL-2 5' untranslated region contains an RNA G-quadruplex-forming motif that modulates protein expression, Biochemistry 49(38) (2010) 8300-6.
[78] S. Kumari, A. Bugaut, S. Balasubramanian, Position and stability are determining factors for translation repression by an RNA G-quadruplex-forming sequence within the 5' UTR of the NRAS proto-oncogene, Biochemistry 47(48) (2008) 12664-9.
[79] M.J. Morris, Y. Negishi, C. Pazsint, J.D. Schonhoft, S. Basu, An RNA G-quadruplex is essential for cap-independent translation initiation in human VEGF IRES, J Am Chem Soc 132(50) (2010) 17831-9.
[80] S. Bonnal, C. Schaeffer, L. Créancier, S. Clamens, H. Moine, A.C. Prats, S. Vagner, A single internal ribosome entry site containing a G quartet RNA structure drives fibroblast growth factor 2 gene expression at four alternative translation initiation codons, J Biol Chem 278(41) (2003) 39330-6.
[81] T. Eleftheriadis, G. Pissas, V. Liakopoulos, I. Stefanidis, Cytochrome c as a Potentially Clinical Useful Marker of Mitochondrial and Cellular Damage, Front Immunol 7 (2016) 279.
[82] A.H. Schapira, Mitochondrial disease, Lancet 368(9529) (2006) 70-82.
[83] J. Nunnari, A. Suomalainen, Mitochondria: in sickness and in health, Cell 148(6) (2012) 1145-59.
[84] A. Johri, M.F. Beal, Mitochondrial dysfunction in neurodegenerative diseases, J Pharmacol Exp Ther 342(3) (2012) 619-30.
[85] K. Meng, H. Jia, X. Hou, Z. Zhu, Y. Lu, Y. Feng, J. Feng, Y. Xia, R. Tan, F. Cui, J. Yuan, Mitochondrial Dysfunction in Neurodegenerative Diseases: Mechanisms and Corresponding Therapeutic Strategies, Biomedicines 13(2) (2025).
[86] W. Chen, H. Zhao, Y. Li, Mitochondrial dynamics in health and disease: mechanisms and potential targets, Signal Transduction and Targeted Therapy 8(1) (2023) 333.
[87] S. Chen, Q. Li, H. Shi, F. Li, Y. Duan, Q. Guo, New insights into the role of mitochondrial dynamics in oxidative stress-induced diseases, Biomedicine & Pharmacotherapy 178 (2024) 117084.

[88] B. Yang, Y. Lin, Y.-Q. Shen, Correcting abnormal mitochondrial dynamics to facilitate tumor treatment, Mitochondrial Communications 1 (2023) 35-47.

[89] Y. Zong, H. Li, P. Liao, L. Chen, Y. Pan, Y. Zheng, C. Zhang, D. Liu, M. Zheng, J. Gao, Mitochondrial dysfunction: mechanisms and advances in therapy, Signal Transduction and Targeted Therapy 9(1) (2024) 124.

[90] M.P. Rossmann, S.M. Dubois, S. Agarwal, L.I. Zon, Mitochondrial function in development and disease, Dis Model Mech 14(6) (2021).

[91] S. Srinivasan, M. Guha, A. Kashina, N.G. Avadhani, Mitochondrial dysfunction and mitochondrial dynamics-The cancer connection, Biochim Biophys Acta Bioenerg 1858(8) (2017) 602-614.

[92] M.V. Liberti, J.W. Locasale, The Warburg Effect: How Does it Benefit Cancer Cells?, Trends Biochem Sci 41(3) (2016) 211-218.

[93] M. Tufail, C.-H. Jiang, N. Li, Altered metabolism in cancer: insights into energy pathways and therapeutic targets, Molecular Cancer 23(1) (2024) 203.

[94] Y. Yu, Y. Jiang, C. Glandorff, M. Sun, Exploring the mystery of tumor metabolism: Warburg effect and mitochondrial metabolism fighting side by side, Cellular Signalling 120 (2024) 111239.

[95] T. Epstein, R.A. Gatenby, J.S. Brown, The Warburg effect as an adaptation of cancer cells to rapid fluctuations in energy demand, PLoS One 12(9) (2017) e0185085.

[96] M. Falabella, R.J. Fernandez, F.B. Johnson, B.A. Kaufman, Potential Roles for G-Quadruplexes in Mitochondria, Curr Med Chem 26(16) (2019) 2918-2932.

[97] V.J. Sahayasheela, Z. Yu, T. Hidaka, G.N. Pandian, H. Sugiyama, Mitochondria and G-quadruplex evolution: an intertwined relationship, Trends Genet 39(1) (2023) 15-30.

[98] A. Bedrat, L. Lacroix, J.L. Mergny, Re-evaluation of G-quadruplex propensity with G4Hunter, Nucleic Acids Res 44(4) (2016) 1746-59.

[99] D.W. Dong, F. Pereira, S.P. Barrett, J.E. Kolesar, K. Cao, J. Damas, L.A. Yatsunyk, F.B. Johnson, B.A. Kaufman, Association of G-quadruplex forming sequences with human mtDNA deletion breakpoints, BMC Genomics 15(1) (2014) 677.

[100] S.K. Bharti, J.A. Sommers, J. Zhou, D.L. Kaplan, J.N. Spelbrink, J.L. Mergny, R.M. Brosh, Jr., DNA sequences proximal to human mitochondrial DNA deletion breakpoints prevalent in human disease form G-quadruplexes, a class of DNA structures inefficiently unwound by the mitochondrial replicative Twinkle helicase, J Biol Chem 289(43) (2014) 29975-93.

[101] M. Doimo, N. Chaudhari, S. Abrahamsson, V. L'Hôte, T.V.H. Nguyen, A. Berner, M. Ndi, A. Abrahamsson, R.N. Das, K. Aasumets, S. Goffart, J.L.O. Pohjoismäki, M.D. López, E. Chorell, S. Wanrooij, Enhanced mitochondrial G-quadruplex formation impedes replication fork progression leading to mtDNA loss in human cells, Nucleic Acids Res 51(14) (2023) 7392-7408.

[102] K. Agaronyan, Y.I. Morozov, M. Anikin, D. Temiakov, Replication-transcription switch in human mitochondria, Science 347(6221) (2015) 548-551.

[103] W.-C. Huang, T.-Y. Tseng, Y.-T. Chen, C.-C. Chang, Z.-F. Wang, C.-L. Wang, T.-N. Hsu, P.-T. Li, C.-T. Chen, J.-J. Lin, P.-J. Lou, T.-C. Chang, Direct evidence of mitochondrial G-quadruplex DNA by using fluorescent anti-cancer agents, Nucleic Acids Research 43(21) (2015) 10102-10113.

[104] Z. Wang, J. Zhou, L. Lin, M.H. Hu, Discovery of a far-red carbazole-benzoindolium fluorescent ligand that selectively targets mitochondrial DNA and suppresses breast cancer growth, Eur J Med Chem 264 (2024) 116046.

[105] X.D. Wang, Y.S. Liu, M.D. Chen, M.H. Hu, Discovery of a triphenylamine-based ligand that targets mitochondrial DNA G-quadruplexes and activates the cGAS-STING immunomodulatory pathway, Eur J Med Chem 269 (2024) 116361.

[106] M. Falabella, J.E. Kolesar, C. Wallace, D. de Jesus, L. Sun, Y.V. Taguchi, C. Wang, T. Wang, I.M. Xiang, J.K. Alder, R. Maheshan, W. Horne, J. Turek-Herman, P.J. Pagano, C.M. St. Croix, N. Sondheimer, L.A. Yatsunyk, F.B. Johnson, B.A. Kaufman, G-quadruplex dynamics contribute to regulation of mitochondrial gene expression, Scientific Reports 9(1) (2019) 5605.

[107] X.Y. Zhuang, Y.G. Yao, Mitochondrial dysfunction and nuclear-mitochondrial shuttling of TERT are involved in cell proliferation arrest induced by G-quadruplex ligands, FEBS Lett 587(11) (2013) 1656-62.

[108] S. Anderson, A.T. Bankier, B.G. Barrell, M.H. de Bruijn, A.R. Coulson, J. Drouin, I.C. Eperon, D.P. Nierlich, B.A. Roe, F. Sanger, P.H. Schreier, A.J. Smith, R. Staden, I.G. Young, Sequence and organization of the human mitochondrial genome, Nature 290(5806) (1981) 457-65.

[109] R.W. Taylor, D.M. Turnbull, Mitochondrial DNA mutations in human disease, Nat Rev Genet 6(5) (2005) 389-402.

[110] D.A. Clayton, Replication of animal mitochondrial DNA, Cell 28(4) (1982) 693-705.

[111] A. Kaasik, D. Safiulina, A. Zharkovsky, V. Veksler, Regulation of mitochondrial matrix volume, Am J Physiol Cell Physiol 292(1) (2007) C157-63.

[112] K.D. Garlid, Cation transport in mitochondria — The potassium cycle, Biochimica et

Biophysica Acta (BBA) - Bioenergetics 1275(1) (1996) 123-126.

[113] R.T. Pomerantz, M. O'Donnell, What happens when replication and transcription complexes collide?, Cell Cycle 9(13) (2010) 2537-43.

[114] J. Zhao, A. Bacolla, G. Wang, K.M. Vasquez, Non-B DNA structure-induced genetic instability and evolution, Cell Mol Life Sci 67(1) (2010) 43-62.

[115] Y. Wang, J. Yang, A.T. Wild, W.H. Wu, R. Shah, C. Danussi, G.J. Riggins, K. Kannan, E.P. Sulman, T.A. Chan, J.T. Huse, G-quadruplex DNA drives genomic instability and represents a targetable molecular abnormality in ATRX-deficient malignant glioma, Nat Commun 10(1) (2019) 943.

[116] J.Y. Jang, A. Blum, J. Liu, T. Finkel, The role of mitochondria in aging, J Clin Invest 128(9) (2018) 3662-3670.

[117] S. Vyas, E. Zaganjor, M.C. Haigis, Mitochondria and Cancer, Cell 166(3) (2016) 555-566.

[118] S. Sarkar, M. Nambiar, G-quadruplexes in the mitochondrial genome - a cause for instability, Febs j 289(1) (2022) 117-120.

[119] Focusing on mitochondrial form and function, Nature Cell Biology 20(7) (2018) 735-735.

[120] A. Suomalainen, J. Nunnari, Mitochondria at the crossroads of health and disease, Cell 187(11) (2024) 2601-2627.

[121] R.Z. Zhao, S. Jiang, L. Zhang, Z.B. Yu, Mitochondrial electron transport chain, ROS generation and uncoupling (Review), Int J Mol Med 44(1) (2019) 3-15.

[122] S. Cogliati, I. Lorenzi, G. Rigoni, F. Caicci, M.E. Soriano, Regulation of Mitochondrial Electron Transport Chain Assembly, Journal of Molecular Biology 430(24) (2018) 4849-4873.

[123] L. Dumas, S. Shin, Q. Rigaud, M. Cargnello, B. Hernández-Suárez, P. Herviou, N. Saint-Laurent, M. Leduc, M. Le Gall, D. Monchaud, E. Dassi, A. Cammas, S. Millevoi, RNA G-quadruplexes control mitochondria-localized mRNA translation and energy metabolism, Nat Commun 16(1) (2025) 3292.

[124] X.-C. Chen, G.-X. Tang, W.-H. Luo, W. Shao, J. Dai, S.-T. Zeng, Z.-S. Huang, S.-B. Chen, J.-H. Tan, Monitoring and Modulating mtDNA G-Quadruplex Dynamics Reveal Its Close Relationship to Cell Glycolysis, Journal of the American Chemical Society 143(49) (2021) 20779-20791.

[125] G.-X. Tang, M.-L. Li, C. Zhou, Z.-S. Huang, S.-B. Chen, X.-C. Chen, J.-H. Tan, Mitochondrial RelA empowers mtDNA G-quadruplex formation for hypoxia adaptation in cancer cells, Cell Chemical Biology 31(10) (2024) 1800-1814.e7.

[126] Z. Chen, F. Han, Y. Du, H. Shi, W. Zhou, Hypoxic microenvironment in cancer: molecular mechanisms and therapeutic interventions, Signal Transduction and Targeted Therapy 8(1) (2023) 70.
[127] V. Meier-Stephenson, G4-quadruplex-binding proteins: review and insights into selectivity, Biophys Rev 14(3) (2022) 635-654.
[128] M.M. Makowski, C. Gräwe, B.M. Foster, N.V. Nguyen, T. Bartke, M. Vermeulen, Global profiling of protein–DNA and protein–nucleosome binding affinities using quantitative mass spectrometry, Nature Communications 9(1) (2018) 1653.
[129] X. Zhang, J. Spiegel, S. Martínez Cuesta, S. Adhikari, S. Balasubramanian, Chemical profiling of DNA G-quadruplex-interacting proteins in live cells, Nature Chemistry 13(7) (2021) 626-633.
[130] M.C. Chen, R. Tippana, N.A. Demeshkina, P. Murat, S. Balasubramanian, S. Myong, A.R. Ferré-D'Amaré, Structural basis of G-quadruplex unfolding by the DEAH/RHA helicase DHX36, Nature 558(7710) (2018) 465-469.
[131] P. Mohaghegh, J.K. Karow, R.M. Brosh, Jr., V.A. Bohr, I.D. Hickson, The Bloom's and Werner's syndrome proteins are DNA structure-specific helicases, Nucleic Acids Res 29(13) (2001) 2843-9.
[132] I.D. Hickson, S.L. Davies, J.L. Li, N.C. Levitt, P. Mohaghegh, P.S. North, L. Wu, Role of the Bloom's syndrome helicase in maintenance of genome stability, Biochem Soc Trans 29(Pt 2) (2001) 201-4.
[133] M.L. Bochman, Roles of DNA helicases in the maintenance of genome integrity, Mol Cell Oncol 1(3) (2014) e963429.
[134] K. Futami, A. Shimamoto, Y. Furuichi, Mitochondrial and nuclear localization of human Pif1 helicase, Biol Pharm Bull 30(9) (2007) 1685-92.
[135] J.B. Boulé, V.A. Zakian, Roles of Pif1-like helicases in the maintenance of genomic stability, Nucleic Acids Res 34(15) (2006) 4147-53.
[136] N. Sabouri, The functions of the multi-tasking Pfh1(Pif1) helicase, Curr Genet 63(4) (2017) 621-626.
[137] D.L. Croteau, M.L. Rossi, C. Canugovi, J. Tian, P. Sykora, M. Ramamoorthy, Z.M. Wang, D.K. Singh, M. Akbari, R. Kasiviswanathan, W.C. Copeland, V.A. Bohr, RECQL4 localizes to mitochondria and preserves mitochondrial DNA integrity, Aging Cell 11(3) (2012) 456-66.
[138] S. Lyonnais, A. Tarrés-Solé, A. Rubio-Cosials, A. Cuppari, R. Brito, J. Jaumot, R. Gargallo, M. Vilaseca, C. Silva, A. Granzhan, M.P. Teulade-Fichou, R. Eritja, M. Solà, The human mitochondrial transcription factor A is a versatile G-quadruplex binding protein, Sci Rep 7 (2017) 43992.

[139] H. Antonicka, F. Sasarman, T. Nishimura, V. Paupe, Eric A. Shoubridge, The Mitochondrial RNA-Binding Protein GRSF1 Localizes to RNA Granules and Is Required for Posttranscriptional Mitochondrial Gene Expression, Cell Metabolism 17(3) (2013) 386-398.

[140] A.M. Burger, F. Dai, C.M. Schultes, A.P. Reszka, M.J. Moore, J.A. Double, S. Neidle, The G-quadruplex-interactive molecule BRACO-19 inhibits tumor growth, consistent with telomere targeting and interference with telomerase function, Cancer Res 65(4) (2005) 1489-96.

[141] M.Y. Kim, H. Vankayalapati, K. Shin-Ya, K. Wierzba, L.H. Hurley, Telomestatin, a potent telomerase inhibitor that interacts quite specifically with the human telomeric intramolecular g-quadruplex, J Am Chem Soc 124(10) (2002) 2098-9.

[142] H. Han, D.R. Langley, A. Rangan, L.H. Hurley, Selective interactions of cationic porphyrins with G-quadruplex structures, J Am Chem Soc 123(37) (2001) 8902-13.

[143] J. Birch, R.K. Anderson, C. Correia-Melo, D. Jurk, G. Hewitt, F.M. Marques, N.J. Green, E. Moisey, M.A. Birrell, M.G. Belvisi, F. Black, J.J. Taylor, A.J. Fisher, A. De Soyza, J.F. Passos, DNA damage response at telomeres contributes to lung aging and chronic obstructive pulmonary disease, Am J Physiol Lung Cell Mol Physiol 309(10) (2015) L1124-37.

[144] A. De Cian, E. DeLemos, J.-L. Mergny, M.-P. Teulade-Fichou, D. Monchaud, Highly Efficient G-Quadruplex Recognition by Bisquinolinium Compounds, Journal of the American Chemical Society 129(7) (2007) 1856-1857.

[145] G. Pennarun, C. Granotier, L.R. Gauthier, D. Gomez, F. Hoffschir, E. Mandine, J.F. Riou, J.L. Mergny, P. Mailliet, F.D. Boussin, Apoptosis related to telomere instability and cell cycle alterations in human glioma cells treated by new highly selective G-quadruplex ligands, Oncogene 24(18) (2005) 2917-28.

[146] C.M. Incles, C.M. Schultes, H. Kempski, H. Koehler, L.R. Kelland, S. Neidle, A G-quadruplex telomere targeting agent produces p16-associated senescence and chromosomal fusions in human prostate cancer cells, Mol Cancer Ther 3(10) (2004) 1201-6.

[147] T.A. Brooks, L.H. Hurley, Targeting MYC Expression through G-Quadruplexes, Genes Cancer 1(6) (2010) 641-649.

[148] D. Drygin, A. Siddiqui-Jain, S. O'Brien, M. Schwaebe, A. Lin, J. Bliesath, C.B. Ho, C. Proffitt, K. Trent, J.P. Whitten, J.K. Lim, D. Von Hoff, K. Anderes, W.G. Rice, Anticancer activity of CX-3543: a direct inhibitor of rRNA biogenesis, Cancer Res 69(19) (2009) 7653-61.

[149] S. Balasubramanian, L.H. Hurley, S. Neidle, Targeting G-quadruplexes in gene promoters: a

novel anticancer strategy?, Nat Rev Drug Discov 10(4) (2011) 261-75.

[150] Q.L. Guo, H.F. Su, N. Wang, S.R. Liao, Y.T. Lu, T.M. Ou, J.H. Tan, D. Li, Z.S. Huang, Synthesis and evaluation of 7-substituted-5,6-dihydrobenzo[c]acridine derivatives as new c-KIT promoter G-quadruplex binding ligands, Eur J Med Chem 130 (2017) 458-471.

[151] J. Carvalho, E. Pereira, J. Marquevielle, M.P.C. Campello, J.L. Mergny, A. Paulo, G.F. Salgado, J.A. Queiroz, C. Cruz, Fluorescent light-up acridine orange derivatives bind and stabilize KRAS-22RT G-quadruplex, Biochimie 144 (2018) 144-152.

[152] P. Saha, D. Panda, D. Müller, A. Maity, H. Schwalbe, J. Dash, In situ formation of transcriptional modulators using non-canonical DNA i-motifs, Chemical Science 11(8) (2020) 2058-2067.

[153] L.-L. Li, H.-R. Xu, K. Li, Q. Yang, S.-L. Pan, X.-Q. Yu, Mitochondrial G-quadruplex targeting probe with near-infrared fluorescence emission, Sensors and Actuators B: Chemical 286 (2019) 575-582.

[154] S. Liu, L. Bu, Y. Zhang, J. Yan, L. Li, G. Li, Z. Song, J. Huang, Subtle Structural Changes of Dyes Lead to Distinctly Different Fluorescent Behaviors in Cellular Context: The Role of G-Quadruplex DNA Interaction Using Coumarin–Quinazolinone Conjugates as a Case Study, Analytical Chemistry 93(12) (2021) 5267-5276.

[155] S.-B. Chen, M.-H. Hu, G.-C. Liu, J. Wang, T.-M. Ou, L.-Q. Gu, Z.-S. Huang, J.-H. Tan, Visualization of NRAS RNA G-Quadruplex Structures in Cells with an Engineered Fluorogenic Hybridization Probe, Journal of the American Chemical Society 138(33) (2016) 10382-10385.

[156] X.C. Chen, S.B. Chen, J. Dai, J.H. Yuan, T.M. Ou, Z.S. Huang, J.H. Tan, Tracking the Dynamic Folding and Unfolding of RNA G-Quadruplexes in Live Cells, Angew Chem Int Ed Engl 57(17) (2018) 4702-4706.

[157] Z.-Y. Yu, W.-H. Luo, X.-C. Chen, S.-B. Chen, Z. Huang, J.-H. Tan, Efficient and rational development of a new fluorescent probe specific for RNA G-quadruplex imaging in cells, Sensors and Actuators B-chemical 324 (2020) 128770.

[158] X.-C. Chen, G.-X. Tang, J. Dai, L.-T. Dai, T.-Y. Wu, W.-W. Li, T.-M. Ou, Z.-S. Huang, J.-H. Tan, S.-B. Chen, Discovery of Clinically Used Octenidine as NRAS Repressor That Effectively Inhibits NRAS-Mutant Melanoma, Journal of Medicinal Chemistry 66(7) (2023) 5171-5184.

[159] M.-L. Li, L.-T. Dai, Z.-Y. Gao, J.-T. Yan, S.-M. Xu, J.-H. Tan, Z.-S. Huang, S.-B. Chen, X.-C. Chen, Discovery of Novel Coumarin-quinolinium Derivatives as Pan-KRAS Translation Inhibitors

by Targeting 5′-UTR RNA G-Quadruplexes, Journal of Medicinal Chemistry 67(3) (2024) 1961-1981.

[160] B. Han, R. Zheng, H. Zeng, S. Wang, K. Sun, R. Chen, L. Li, W. Wei, J. He, Cancer incidence and mortality in China, 2022, Journal of the National Cancer Center 4(1) (2024) 47-53.

[161] W. Sun, Q. Shi, H. Zhang, K. Yang, Y. Ke, Y. Wang, L. Qiao, Advances in the techniques and methodologies of cancer gene therapy, Discov Med 27(146) (2019) 45-55.

[162] A. Klinakis, D. Karagiannis, T. Rampias, Targeting DNA repair in cancer: current state and novel approaches, Cell Mol Life Sci 77(4) (2020) 677-703.

[163] K.T. Flaherty, C. Robert, P. Hersey, P. Nathan, C. Garbe, M. Milhem, L.V. Demidov, J.C. Hassel, P. Rutkowski, P. Mohr, R. Dummer, U. Trefzer, J.M. Larkin, J. Utikal, B. Dreno, M. Nyakas, M.R. Middleton, J.C. Becker, M. Casey, L.J. Sherman, F.S. Wu, D. Ouellet, A.M. Martin, K. Patel, D. Schadendorf, Improved survival with MEK inhibition in BRAF-mutated melanoma, N Engl J Med 367(2) (2012) 107-14.

[164] J.D. Wolchok, V. Chiarion-Sileni, R. Gonzalez, P. Rutkowski, J.J. Grob, C.L. Cowey, C.D. Lao, J. Wagstaff, D. Schadendorf, P.F. Ferrucci, M. Smylie, R. Dummer, A. Hill, D. Hogg, J. Haanen, M.S. Carlino, O. Bechter, M. Maio, I. Marquez-Rodas, M. Guidoboni, G. McArthur, C. Lebbé, P.A. Ascierto, G.V. Long, J. Cebon, J. Sosman, M.A. Postow, M.K. Callahan, D. Walker, L. Rollin, R. Bhore, F.S. Hodi, J. Larkin, Overall Survival with Combined Nivolumab and Ipilimumab in Advanced Melanoma, N Engl J Med 377(14) (2017) 1345-1356.

[165] C. Monnerat, A. Chompret, C. Kannengiesser, M.F. Avril, N. Janin, A. Spatz, J.M. Guinebretière, C. Marian, M. Barrois, F. Boitier, G.M. Lenoir, B. Bressac-de Paillerets, BRCA1, BRCA2, TP53, and CDKN2A germline mutations in patients with breast cancer and cutaneous melanoma, Fam Cancer 6(4) (2007) 453-61.

[166] H. Ho, J. Aruri, R. Kapadia, H. Mehr, M.A. White, A.K. Ganesan, RhoJ regulates melanoma chemoresistance by suppressing pathways that sense DNA damage, Cancer Res 72(21) (2012) 5516-28.

[167] H. Ray-David, Y. Romeo, G. Lavoie, P. Déléris, J. Tcherkezian, J.A. Galan, P.P. Roux, RSK promotes G2 DNA damage checkpoint silencing and participates in melanoma chemoresistance, Oncogene 32(38) (2013) 4480-4489.

[168] T.Y. Wu, Q. Huang, Z.S. Huang, M.H. Hu, J.H. Tan, A drug-like imidazole-benzothiazole conjugate inhibits malignant melanoma by stabilizing the c-MYC G-quadruplex, Bioorg Chem 99

(2020) 103866.

[169] V. Rapozzi, S. Zorzet, M. Zacchigna, E. Della Pietra, S. Cogoi, L.E. Xodo, Anticancer activity of cationic porphyrins in melanoma tumour-bearing mice and mechanistic in vitro studies, Molecular Cancer 13(1) (2014) 75.

[170] S.Y. Rha, E. Izbicka, R. Lawrence, K. Davidson, D. Sun, M.P. Moyer, G.D. Roodman, L. Hurley, D. Von Hoff, Effect of telomere and telomerase interactive agents on human tumor and normal cell lines, Clin Cancer Res 6(3) (2000) 987-93.

[171] R. Pattanayak, A. Barua, A. Das, T. Chatterjee, A. Pathak, P. Choudhury, S. Sen, P. Saha, M. Bhattacharyya, Porphyrins to restrict progression of pancreatic cancer by stabilizing KRAS G-quadruplex: In silico, in vitro and in vivo validation of anticancer strategy, Eur J Pharm Sci 125 (2018) 39-53.

[172] J.C. Castle, M. Uduman, S. Pabla, R.B. Stein, J.S. Buell, Mutation-Derived Neoantigens for Cancer Immunotherapy, Front Immunol 10 (2019) 1856.

[173] J.N. Liu, R. Deng, J.F. Guo, J.M. Zhou, G.K. Feng, Z.S. Huang, L.Q. Gu, Y.X. Zeng, X.F. Zhu, Inhibition of myc promoter and telomerase activity and induction of delayed apoptosis by SYUIQ-5, a novel G-quadruplex interactive agent in leukemia cells, Leukemia 21(6) (2007) 1300-1302.

[174] A. Local, H. Zhang, K.D. Benbatoul, P. Folger, X. Sheng, C.Y. Tsai, S.B. Howell, W.G. Rice, APTO-253 Stabilizes G-quadruplex DNA, Inhibits MYC Expression, and Induces DNA Damage in Acute Myeloid Leukemia Cells, Mol Cancer Ther 17(6) (2018) 1177-1186.

[175] S.G. Zidanloo, A. Hosseinzadeh Colagar, H. Ayatollahi, J.B. Raoof, Downregulation of the WT1 gene expression via TMPyP4 stabilization of promoter G-quadruplexes in leukemia cells, Tumour Biol 37(7) (2016) 9967-77.

[176] V.K. Katapadi, M. Nambiar, S.C. Raghavan, Potential G-quadruplex formation at breakpoint regions of chromosomal translocations in cancer may explain their fragility, Genomics 100(2) (2012) 72-80.

[177] G. Morad, B.A. Helmink, P. Sharma, J.A. Wargo, Hallmarks of response, resistance, and toxicity to immune checkpoint blockade, Cell 184(21) (2021) 5309-5337.

[178] R.S. Riley, C.H. June, R. Langer, M.J. Mitchell, Delivery technologies for cancer immunotherapy, Nat Rev Drug Discov 18(3) (2019) 175-196.

[179] F.R. Greten, S.I. Grivennikov, Inflammation and Cancer: Triggers, Mechanisms, and Consequences, Immunity 51(1) (2019) 27-41.

[180] G. Miglietta, M. Russo, R.C. Duardo, G. Capranico, G-quadruplex binders as cytostatic modulators of innate immune genes in cancer cells, Nucleic Acids Res 49(12) (2021) 6673-6686.
[181] G. Miglietta, J. Marinello, M. Russo, G. Capranico, Ligands stimulating antitumour immunity as the next G-quadruplex challenge, Mol Cancer 21(1) (2022) 180.

Chapter 2. Research methods

Given that G4s play an important role in the process of gene replication, transcription, translation, and maintenance of genome stability. At the same time, G4s are also closely related to the occurrence and development of many major diseases, including cancer and neurodegenerative diseases. Therefore, it is important to study and develop specific ligands that can bind and effectively regulate G4 formation. To comprehensively evaluate the interaction of G4 ligands with G4s, various evaluation methods are used in the study, including fluorescence spectroscopy, nuclear magnetic resonance, immunoblotting, and so on. This chapter will focus on the commonly used G4 ligands evaluation methods and describe the experimental design of the project to obtain supportive results.

2.1 Overview of evaluation methods for G-quadruplexes targeting ligands

The interaction between G4 ligands and G4s involves several aspects, including the binding ability of ligands for G4s, stabilizing effects, binding modes, and intracellular interactions. Firstly, the binding ability of a ligand often determines its biological activity. In general, a ligand with a high affinity for G4-interaction is likely to exhibit stronger regulation effects on the G4-function. Secondly, the stabilizing effect of ligands on G4s affects G4-related biological processes, leading to changes in the regulatory function of G4s. Thirdly, the binding modes of different ligands interacting with G4s can affect its specificity and activity, which can provide guidance for the design and synthesis of G4-targeting ligands. As for the ability of G4 ligands to interact with G4s in the cell, it can affect cell survival, proliferation and differentiation, which provides a reference for whether the ligand could be a lead compound for anticancer study. Therefore, a systematic understanding of the molecular interaction of a ligand with G4s can provide important clues for resolving their biological functions and guide the development of G4-structure targeting therapies. Common methods for evaluating the different properties of G4 ligands are described in **Table 2-1**.

Table 2-1. Common methods for the study of interaction between ligands and G-quadruplexes.

Purpose	Methods	Features
Binding ability	Fluorescence spectrometry	Real-time monitoring, high sensitivity, low sample requirements, easy to operate;
	Surface plasmon resonance, SPR	Real-time data collection with high efficiency and sensitivity and low sample requirements;
	Isothermal titration calorimetry	High precision, larger sample volume requirements, and better water solubility of the sample required.
Stabilizing ability	Circular dichroism, CD [1]	Low cost, time-consuming and low sample requirements;
	Fluorescence resonance energy transfer, FRET [2]	High throughput, simple operation, low sample requirements, and ability to monitor signals in real time.
Binding mode	Nuclear magnetic resonance, NMR [3, 4]	Does not damage the sample and provides high-resolution structural information;
	X-ray crystal	Precise determination of ligand binding sites;
	Molecular docking	High-throughput screening to predict the binding mode of ligand to G4.
Intracellular interactions	Polymerase chain reaction, PCR	Detection of the effect of G4 ligands on the study of gene replication;
	Reverse transcription Quantitative real-time PCR, RT-qPCR	Detection of the effect of G4 ligands on studying gene transcription;
	Western blotting, WB	Detection of the effect of G4 ligands on protein expression of studied genes.
Anti-tumor ability	Wound healing assay	Detection of the effect of ligands on the migration and proliferation of cancer cells;
	Colony formation assay	Detection of the effect of ligands on the proliferation and viability of cancer cells;
	MTT assay	Detection of the effect of ligands on the proliferation and viability of cancer cells;
	Xenograft tumor model	Transplantation of human cancer cell lines into immunodeficient mice to study tumor growth, metastasis and response to therapy.

2.2 Experimental design for this project

After a brief introduction of commonly used methods for G4-ligand interaction study, we conducted a rational experimental design based on the research objectives of this project (**Figure 2.1**).

In the literature review, we found that only a few fluorescent ligands have been reported to specifically target G4-mtDNAs, which limits the study of the regulatory role of G4-mtDNAs. Therefore, we will design and synthesize a series of ligands based on the structural features of mitochondria and G4, as well as those of published G4 ligands. Methods for evaluation of ligand-G4-mtDNA interactions will be established to screen fluorescent ligands that can specifically target G4-mtDNAs and be used for more in-depth studies. In this section, fluorescence spectroscopy, CD, SPR, ITC, NMR, and other methods will be used to assess the ability of the ligand to bind to G4-mtDNAs.

The ligand with superior performance obtained from the above screening will be used as fluorescent probe, and experimental methods such as co-localization of mitochondrial commercial dyes, ligand displacement, enzymatic digestion and transfection were employed to detect the ability of the ligand to specifically recognize G4-mtDNAs in living cells with the aid of laser confocal fluorescence microscopy cell imaging technology. Once the ligand has been determined to specifically recognize G4-mtDNAs in living cells, we will investigate the effect of the ligand on mtDNAs replication and transcription. Since mitochondrial DNA encodes 13 genes related to the respiratory chain complex, the ligand binding to G4-mtDNAs may affect the function of the mitochondrial respiratory chain, which may lead to mitochondrial disorders. Therefore, we will examine mitochondrial functions, including oxidative phosphorylation, glycolysis, membrane potential, calcium homeostasis, and ROS production in human cancer cells.

If a ligand binding to G4-mtDNAs affects mitochondrial functions, we will explore the feasibility of G4-mtDNAs as an anti-tumor target and the specific mechanisms involved. Specifically, we will investigate whether a ligand targeting G4-mtDNAs could show inhibitory effects on cell migration, repair, and proliferation capabilities of different cancer cells. On the other hand, mitochondria have important regulatory roles in cellular senescence, apoptosis or necrosis, and iron death. The ligand targeting G4-mtDNAs may induce the above events. Therefore, we will investigate the effect of ligands targeting G4-mtDNAs on cancer cell senescence, apoptosis, and iron death, and elucidate the

possible mechanisms. Finally, the *in vivo* efficacy of the G4-mtDNA-targeting ligands in inhibiting tumor growth is evaluated in a tumor xenograft mouse model.

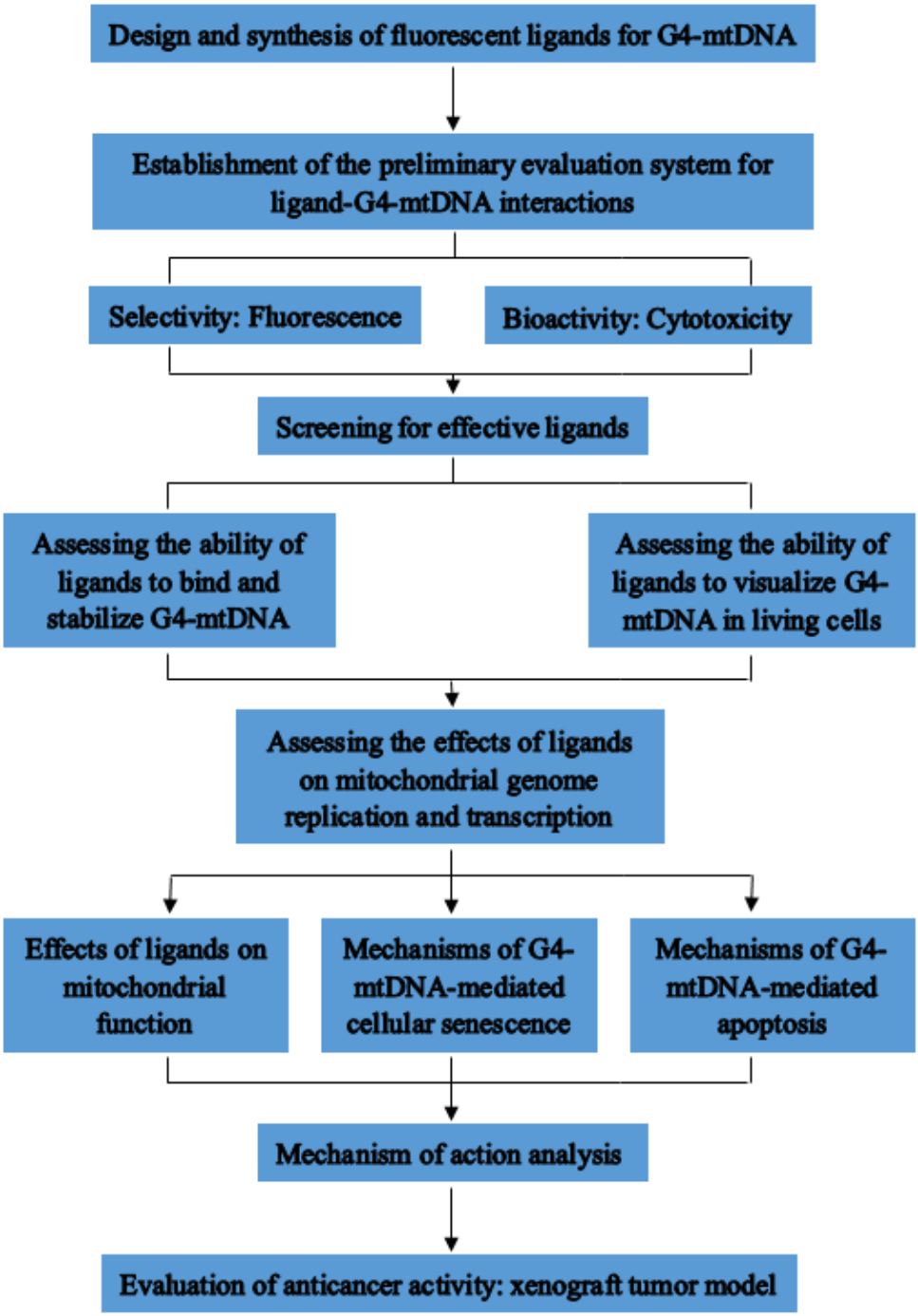

Figure 2.1. Experimental designs for this project.

2.3 References

[1] S. Paramasivan, I. Rujan, P.H. Bolton, Circular dichroism of quadruplex DNAs: applications to structure, cation effects and ligand binding, Methods 43(4) (2007) 324-31.

[2] A. De Cian, L. Guittat, M. Kaiser, B. Saccà, S. Amrane, A. Bourdoncle, P. Alberti, M.P. Teulade-Fichou, L. Lacroix, J.L. Mergny, Fluorescence-based melting assays for studying quadruplex ligands, Methods 42(2) (2007) 183-95.

[3] M. Webba da Silva, NMR methods for studying quadruplex nucleic acids, Methods 43(4) (2007) 264-77.

[4] J. Feigon, K.M. Koshlap, F.W. Smith, 1H NMR spectroscopy of DNA triplexes and quadruplexes, Methods Enzymol 261 (1995) 225-55.

Chapter 3. Discovery of small-sized and mitochondrial DNA G-quadruplex-targeting benzoindole-benzothiazole ligand for anticancer study

3.1 Synopsis

Many studies have suggested that G-rich DNA sequences may fold into G4 structures in mitochondria and play important regulatory roles, but the mechanism of action is not clear. Therefore, the development of G4-mtDNAs binding ligands for chemical biology and anticancer research is important. In this study, we investigated comprehensively the anticancer mechanism and *in vivo* antitumor efficacy targeting G4-mtDNAs with a small molecule fluorescent ligand **BYB**. A series of *in vitro* and cellular bioassays were performed to verify the selectivity of **BYB** towards G4-mtDNAs, the cellular localization of **BYB** in living cancer cells, and the cytotoxic effect of **BYB** against a panel of cancer cell lines.

3.2 The study of a small-sized benzoindole-benzothiazole ligand targeting mitochondria and G4-mtDNAs for antitumor therapy

Thiazole orange (TO) is a universal nucleic acid dye that fluorescently responds to various types of nucleic acids.[1] Its structure is very simple, made of quinoline and benzothiazole connected by methyl-single bond. Due to the poor selectivity of TO towards nucleic acid substrates, its application is thus limited. To overcome this problem, many studies have been conducted to enhance the selectivity of TO-based ligands to bind to a specific nucleic acid via structural modification in recent years.[2-7] Besides, many benzoindole derivatives were found preferably to localize in mitochondria. This may suggest that benzoindole scaffold may be a mitochondria-targeting group.[8-10] Our previous study also showed that a rigid and planar benzoindole scaffold combined with a styrene group could construct a fluorescent ligand that targets G4-mtDNAs.[11] Therefore, the benzoindole and benzothiazole coupled ligand may be able to target mitochondria selectively and interact with G4-mtDNAs in living cancer cells. The synthesis of benzindole-benzothiazole ligand, **BYB**, has been reported previously by our collaborative group and some preliminary selectivity and bioactivity evaluations with the ligand towards nucleic acids substrates *in vitro* were also performed.[12] However, the cellular targets and cellular effects induced by **BYB** in live human cancer cells are not investigated. Therefore, in this study, we investigated comprehensively the intracellular selectivity, bioactivity, and antitumor mechanism of **BYB** to elucidate its regulatory function on mitochondria and G4-mtDNAs and validate its potential as an antitumor agent. Moreover, the ligand **BYB** obtained

with 97.8% purity for this study was synthesized and purified by following the reported procedures. The characterizations of the compounds are given in Appendix, **Figure S7** for reference were found comparable to the reported data.[12]

3.3 Results and discussion

3.3.1 Study the antiproliferation effect of **BYB** against human cancer and non-cancerous cells

In our previous study, **BYB** was found to have cytotoxicity against some human cancer cells, including cervical cancer cells HeLa, glioma cells U87, and prostate cancer cells PC3. The preliminary IC_{50} estimated was about 15 μM for a 48-hour treatment.[12] To understand whether **BYB** targeting G4-mtDNAs could show cytotoxic effects against a broad-spectrum of human cancer cells, a variety of cancer cell lines including melanoma cells A375 and SK-MEL-2, cervical cancer cells HeLa, pancreatic cancer cells MIA PaCa-2, hepatocellular carcinoma cells HepG2, breast cancer cells MDA-MB-231, and colorectal cancer cells HCT116 were examined. To evaluate the selective toxicity of **BYB** against cancer and noncancerous cells, the toxicity of **BYB** was also examined with two normal cells BJ and HFF1. MTT assays were performed to evaluate the cell proliferation rate of the cells treated with **BYB** for 48 hours. The IC_{50} values **BYB** against different cell lines were summarized in **Table 3-1**. The screening results reveal that **BYB** generally shows higher antiproliferative activity against cancer cells, including A375, HeLa, MIA PaCa-2, SK-MEL-2, HepG2, MDA-MB-231, and HCT116, with IC_{50} values ranging from 5.4 to 9.7 μM approximately. In contrast, **BYB** shows relatively lower toxicity toward non-cancerous cells (BJ and HFF1, IC_{50} > 25 μM). Therefore, **BYB** may have certain degree of cytotoxic selectivity toward human cancer cells.

Table 3-1. IC_{50} of **BYB** against human cancer and nonmalignant cells. The treatment time is 48 h.

BYB	Cell line	IC_{50} (μM)
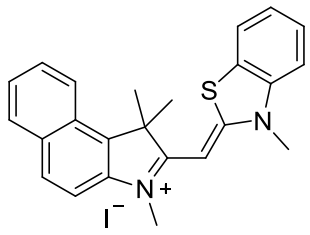	A375	5.4
	HeLa	7.6
	MIA PaCa-2	7.8
	SK-MEL-2	8.1
	HepG2	8.4
	MDA-MB-231	9.2
	HCT-116	9.7
	BJ	25.5
	HFF1	26.9

3.3.2 Study the cellular location and binding target of **BYB** in living HeLa cells

Based on the MTT results, **BYB** generally exhibits notable antiproliferative activity against cancer cells. Since we have previously established a HeLa tumor xenograft mouse model for anticancer studies and evaluation of lead compounds in our laboratory, we selected HeLa cells for further intracellular studies with **BYB**. In our previous studies, **BYB** was found to be localized in mitochondria of U87 cells, but its cellular selectivity targeting nucleus and other organelles is not well-studied. Meanwhile, the intracellular location and target of **BYB** in HeLa cells are not validated.[12] To verify its cellular localization in living HeLa cells, the cells were incubated with **BYB** and an intense fluorescence (green foci) was observed in the cells. The results suggest that the ligand may interact with specific cellular targets. We then performed live-cell imaging to colocalize **BYB** with various organelle-specific probes, including Hoechst 33342 (nucleus), Mito-Tracker Deep Red (mitochondria), Lyso-Tracker Blue (lysosome), and ER-Tracker Blue (endoplasmic reticulum). The merged images reveal that the **BYB**-imaged sites significantly overlapped with Mito-Tracker Deep Red (MTDR) (**Figure 3.1**), indicating that **BYB** primarily localizes to the mitochondria. These results suggest that **BYB** is a mitochondria-targeting ligand and does not enter the nucleus in living HeLa cells.

To further prove that the primary cellular target of **BYB** is the mitochondria rather than the nucleus, live-cell assays comparing the localization of **BYB** in HeLa cells with and without digitonin treatment were conducted. Digitonin can enhance nuclear membrane permeability. In this assay, we used Propidium Iodide (PI) staining as a reference. From **Figure 3.2 A** and **B**, PI did not penetrate the nucleus (no red staining observed) in HeLa cells without digitonin treatment, while it showed significant red foci when the cells were treated with digitonin, indicating that digitonin successfully increased the nuclear membrane permeability. Likewise, **BYB** only exhibited green foci in the nuclei of HeLa cells treated with digitonin under the same treatment conditions (**Figure 3.2 C** and **D**). These results demonstrate that **BYB** cannot penetrate the nuclear membrane of intact HeLa cells (without digitonin treatment), supporting the conclusion that **BYB** does not enter the nucleus in living cells.

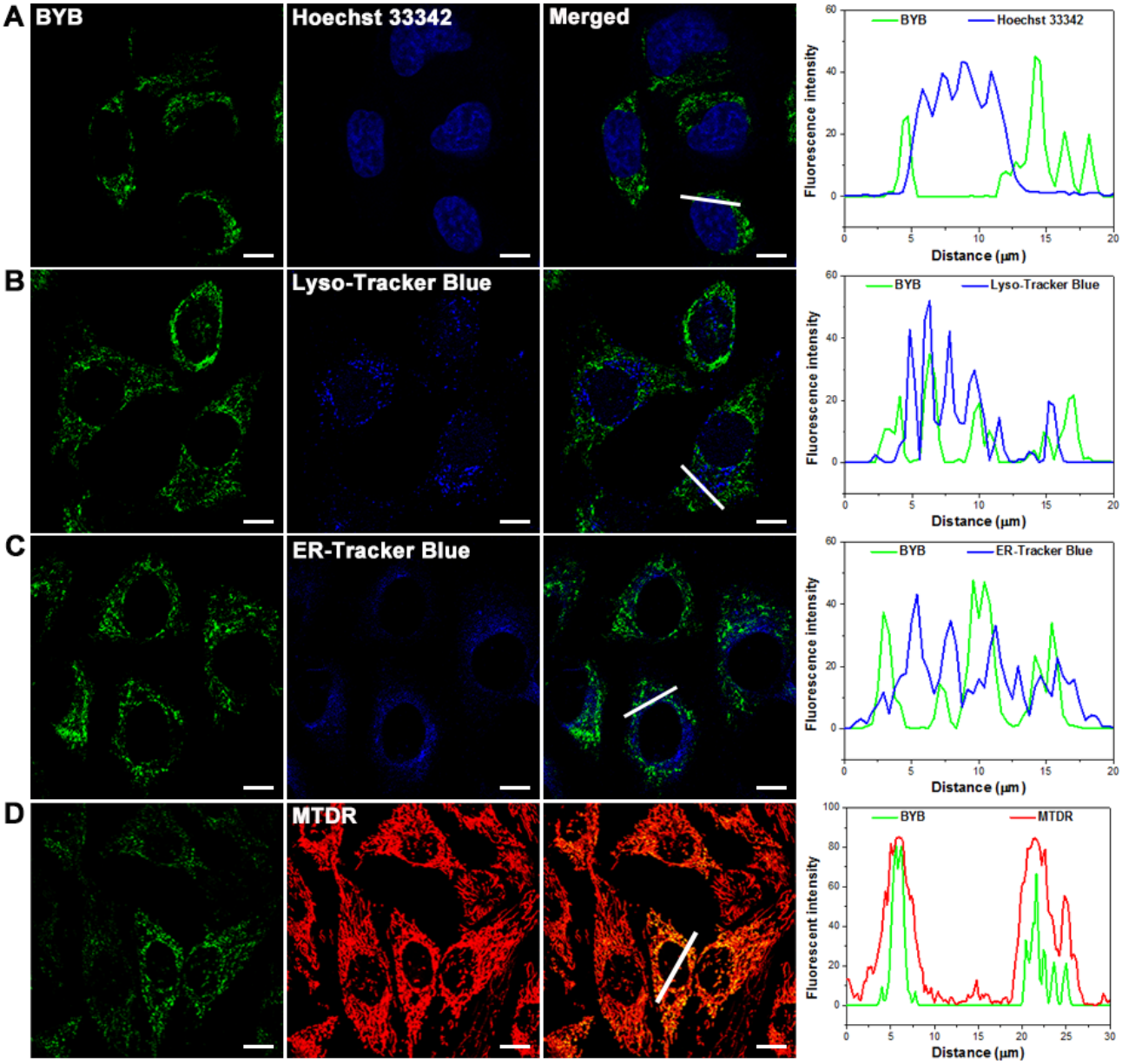

Figure 3.1. Single confocal plane images. (A) Living HeLa cells treated with 2 μM **BYB** (Green, λ_{ex}=488 nm) for 30 min and 1 μM Hoechst 33342 (Blue, λ_{ex}=405 nm) for 30 min. (B) Living HeLa cells treated with 2 μM **BYB** (Green, λ_{ex}=488 nm) for 30 min and 1 μM Lyso-Tracker Blue (Blue, λ_{ex}=405 nm) for 30 min. (C) Living HeLa cells treated with 2 μM **BYB** (Green, λ_{ex}=488 nm) for 30 min and 1 μM ER-Tracker Blue (Blue, λ_{ex}=405 nm) for 30 min. (D) Living HeLa cells treated with 2 μM **BYB** (Green, λ_{ex}=488 nm) for 30 min and 200 nM Mito-Tracker Deep Red (Red, λ_{ex}=635 nm) for 30 min. The scale bar is 10 μm.

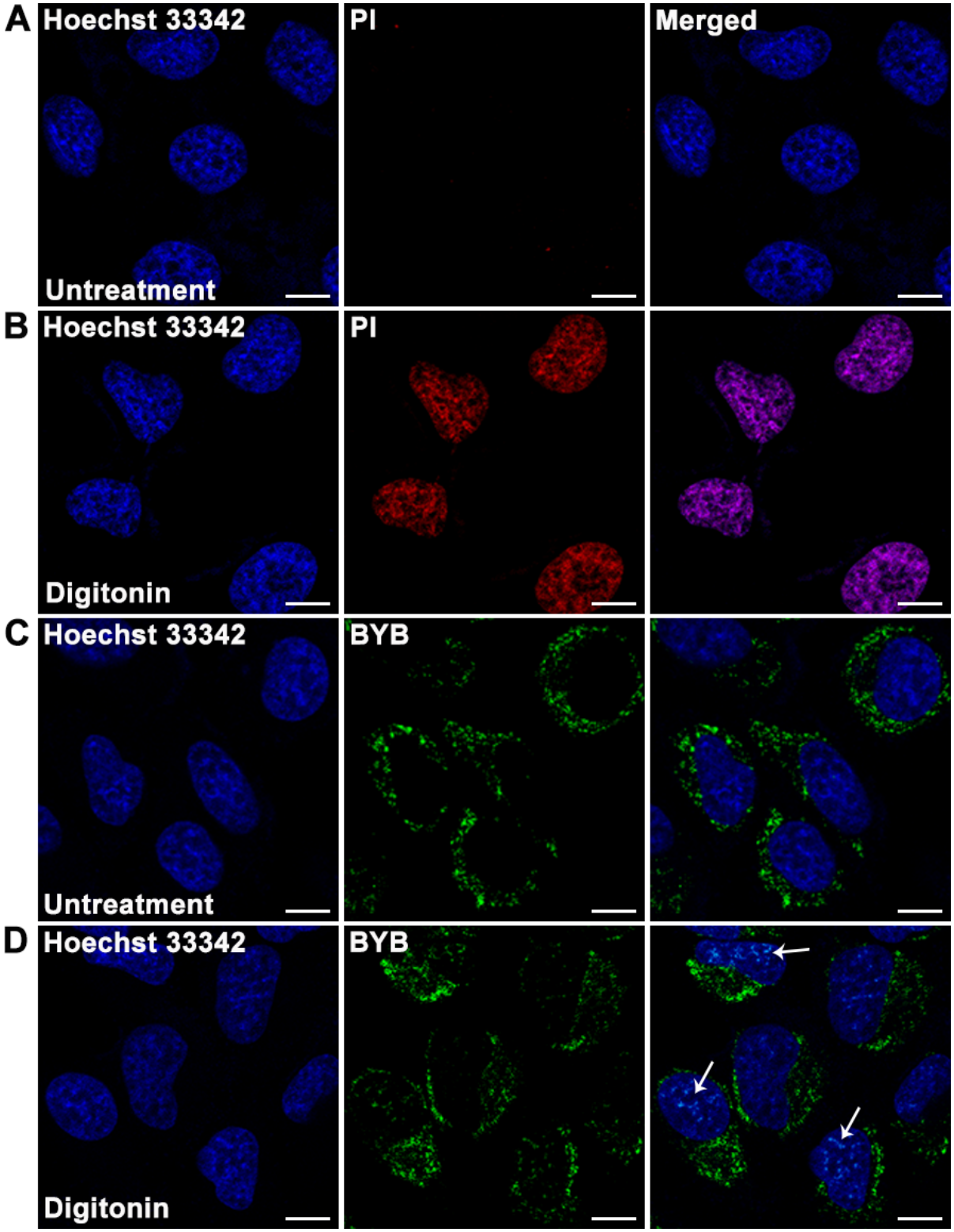

Figure 3.2. Single confocal plane images. (A) Living HeLa cells treated with 2 μg/mL PI (Red, λ_{ex}=488 nm) for 15 min and 1 μM Hoechst 33342 (Blue, λ_{ex}=405 nm) for 30 min without Digitonin (30 μg/mL) treatment. (B) Living HeLa cells treated with 2 μg/mL **PI** (Red, λ_{ex}=488 nm) for 10 min and 1 μM Hoechst 33342 (Blue, λ_{ex}=405 nm) for 30 min after Digitonin (30 μg/mL) treatment for 15 min. (C) Living HeLa cells treated with 2 μM **BYB** (Green, λ_{ex}=488 nm) for 30 min and 1 μM Hoechst 33342 (Blue, λ_{ex}=405 nm) for 30 min without Digitonin (30 μg/mL) treatment. (D) Living HeLa cells treated with 2 μM **BYB** (Green, λ_{ex}=488 nm) for 30 min and 1 μM Hoechst 33342 (Blue, λ_{ex}=405 nm) for 30 min after Digitonin (30 μg/mL) treatment for 15 min. The scale bar is 10 μm.

Next, we tried to understand the mechanism by which **BYB** is delivered into the mitochondria in HeLa cells. It is known that small molecules can enter mitochondria via mitochondrial membrane potential (MMP) and/or the mitochondrial membrane permeability transition pore (mPTP). To investigate this, we used FCCP to depolarize the MMP in HeLa cells.[13] As shown in **Figure 3.3**, FCCP-treated cells exhibited almost no green foci (**BYB**) compared to the control. Additionally, a potent mPTP inhibitor cyclosporin A (CsA) was applied to block the mPTP in HeLa cells prior to **BYB** treatment.[14] The green foci of **BYB** remained clearly visible in CsA-treated cells and were comparable to those in the control. Collectively, these live-cell imaging results suggest that the delivery of **BYB** into mitochondria is primarily facilitated by MMP.

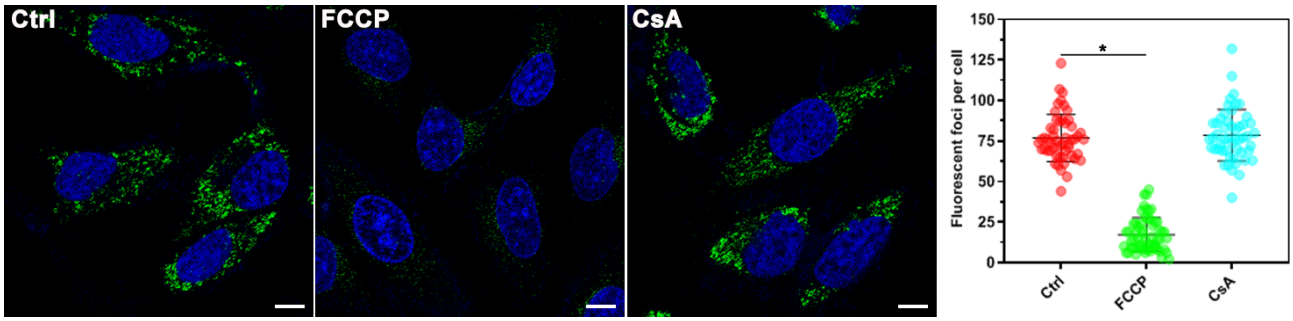

Figure 3.3. Living HeLa cells incubated with 2 μM **BYB** (Green, λ_{ex}=488 nm) for 30 min and 1 μM Hoechst 33342 (Blue, λ_{ex}=405 nm) for 30 min after treatment with 1 μM FCCP for 20 min or 1 μM CsA for 24 h. The scale bar is 10 μm. The data are presented as mean ± SEM, and statistics were determined using ANOVA, $*p < 0.05$.

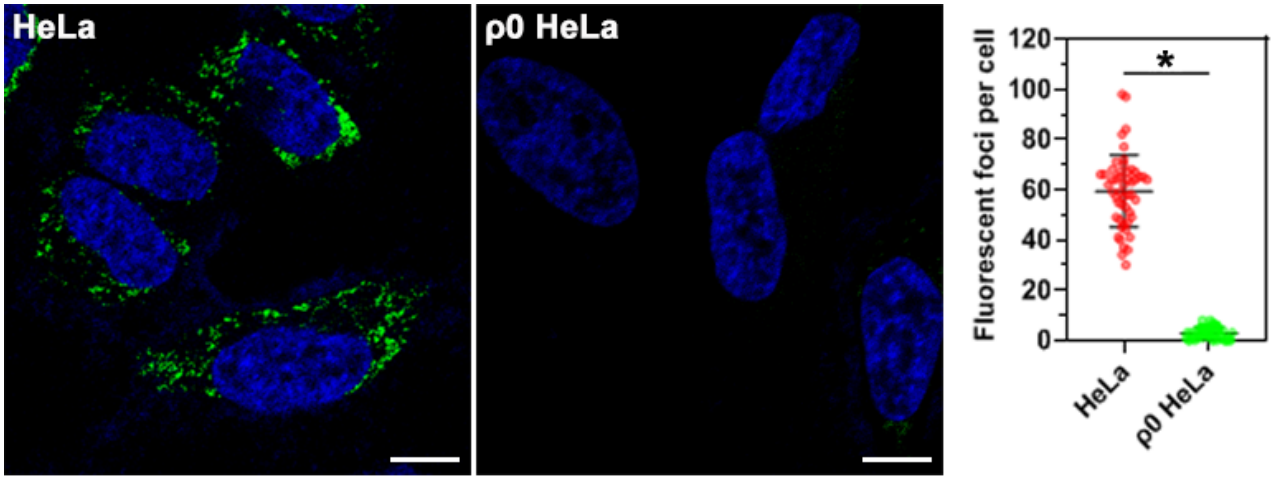

Figure 3.4. Living HeLa cells and ρ0 HeLa cells treated with 2 μM **BYB** (Green, λ_{ex}=488 nm) for 30 min and 1 μM Hoechst 33342 (Blue, λ_{ex}=405 nm) for 30 min. The scale bar is 10 μm. The data are presented as mean ± SEM, and statistics were determined using ANOVA, $*p < 0.05$.

To verify whether **BYB** binds to nucleic acids in the mitochondria, mtDNA-depleted ρ0 HeLa cells were established. Parental HeLa cells were cultured for 40 days in low dose EtBr to deplete mtDNAs and resulting mtRNAs and subsequently were investigated with **BYB**.[15] As shown in **Figure 3.4**, the green foci of **BYB** were nearly absent in the ρ0 HeLa cells due to the depletion of mtDNAs and resulting mtRNAs, suggesting that the cellular targets of **BYB** are mitochondrial DNA and/or RNA. To further confirm whether **BYB** interacts with DNA, enzymatic digestion assays were performed. **Figure 3.5** showed that the green foci of **BYB** significantly decreased after treatment with DNase I, while there was almost no change after treatment with RNase A. These findings indicate that the primary targets of **BYB** in the mitochondria of living HeLa cells are DNAs but not RNAs.

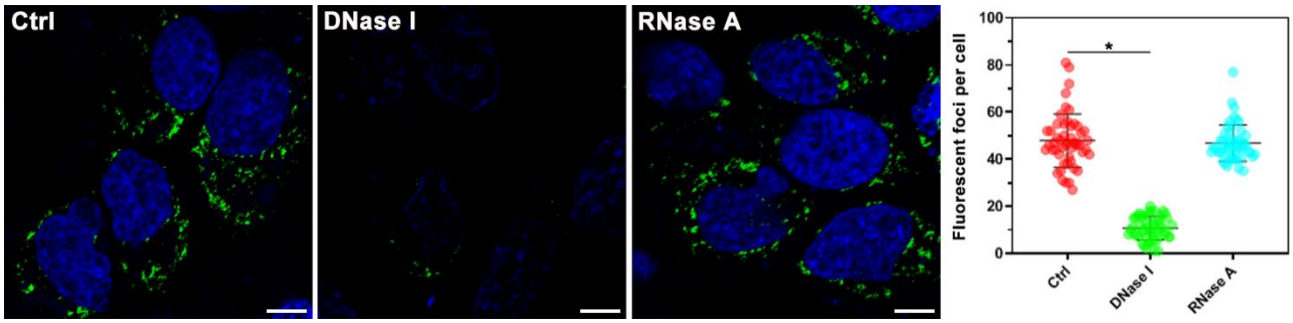

Figure 3.5. Living HeLa cells incubated with 2 μM **BYB** (Green, λ_{ex}=488 nm) for 30 min and 1 μM Hoechst 33342 (Blue, λ_{ex}=405 nm) for 30 min, then the cells were fixed and incubated with 200 units DNase I for 3 h or incubated with 200 units RNase A for 3 h. The scale bar is 10 μm. The data are presented as mean ± SEM, and statistics were determined using ANOVA, $*p < 0.05$.

3.3.3 Study the interaction property between **BYB** and G4-mtDNAs *in vitro* and *in cellulo*

Our previous study suggests that **BYB** may interact with G4-mtDNAs in solution, but the selectivity of **BYB** towards different types of nucleic acids was not well-studied.[12] Besides, we have proved that **BYB** is primarily interacted with mtDNAs and produces green foci in living cells, so we select several mtDNA and rRNA substrates, including both G4 and non-G4 structures, for interaction studies. The topology of the selected G4 sequences was determined prior to the experiments. As shown in **Figure 3.6**, a significant enhancement in fluorescence intensity when **BYB** interacted with G4-mtDNAs was observed, ranging from 25.2 to 154.4 times. However, the increase in fluorescence intensity for non-G4 substrates was much lower (only 0.4 to 5.1 times). Additionally, the fluorescence enhancement for *rRNA* (1.9 times), antisense G4-mtDNA sequences (0.2 to 0.8 times), and mutated G4-mtDNA sequences (1.2 to 2.3 times) was substantially weaker compared to that of G4-mtDNAs. These fluorescence titration results indicate that **BYB** shows significantly greater selectivity for G4-mtDNAs, resulting in much more intense fluorescence signals during interaction. To assess the

binding affinity of **BYB** with different nucleic acids, we performed isothermal titration calorimetry (ITC) assays to determine the dissociation constants (K_D) (**Figure 3.7**). The K_D values were summarized in **Table 3-2** for comparison. For the tested G4-mtDNA substrates, **BYB** exhibited a significantly stronger affinity (K_D = 1.96–5.22 μM) compared to non-G4 substrates and *rRNA*, which showed no affinity for **BYB**. Among the substrates evaluated, *Mito 6363* and *Mito 16250* demonstrated the highest affinity (K_D = 1.96–2.20 μM). Taken together, **BYB** may have higher selectivity and better interaction for G4-mtDNAs.

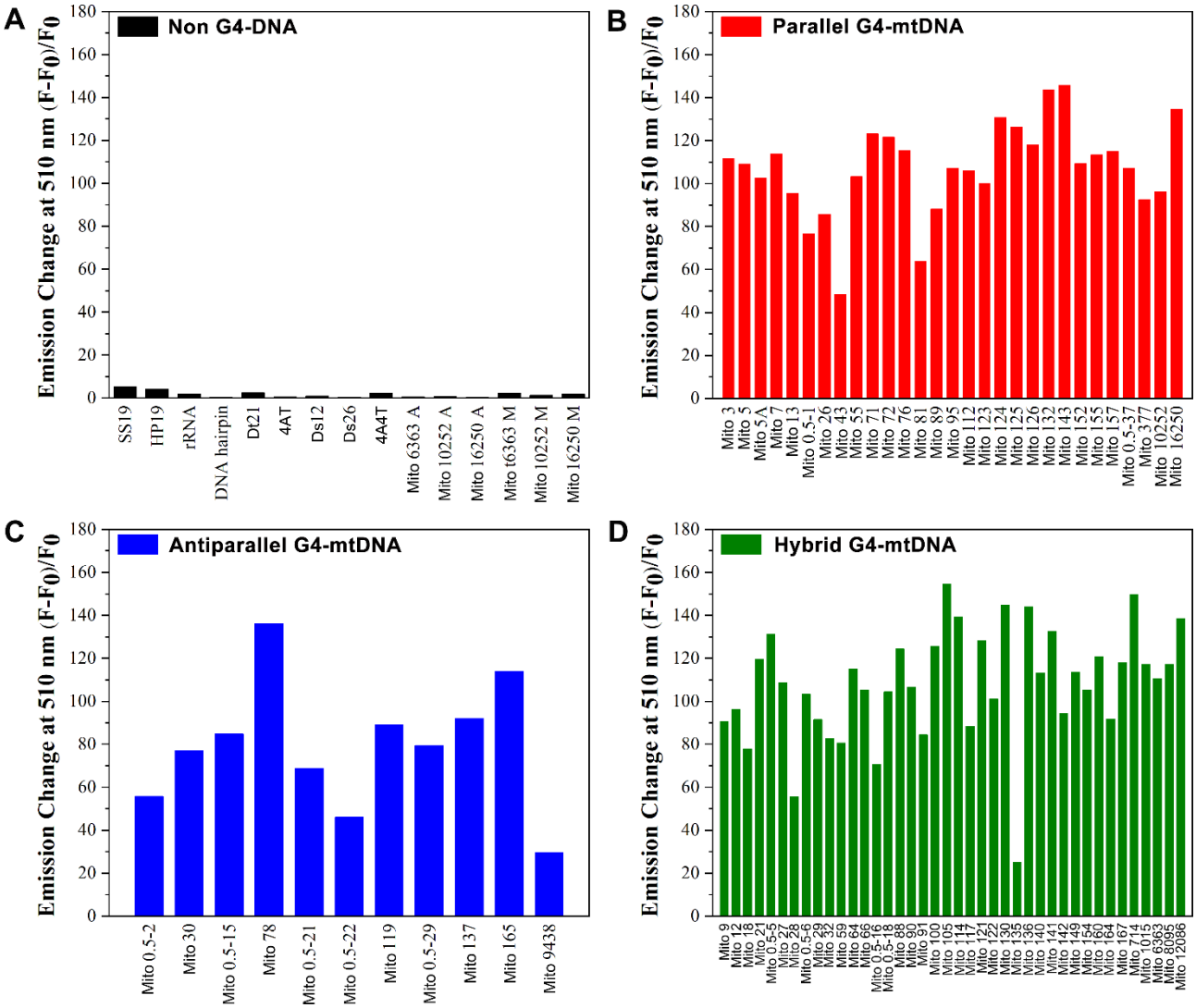

Figure 3.6. The study of the interaction of **BYB** with different G4 and non-G4 nucleic acid structures in a Tris-HCl buffer (10 mM, 100 mM KCl, pH = 7.4). (A) G4-mtDNAs with parallel topology. (B) G4-mtDNAs with antiparallel topology. (C) G4-mtDNAs with hybrid topology. (D) non-G4-DNA substrates including *rRNA*, single-stranded DNA (*SS19* and *Dt21*), double-stranded DNA (*4AT*, *Ds12*, *Ds26* and *4A4T*), hairpin DNA (*HP19* and *DNA hairpin*), antisense G4-mtDNA (*Mito 6363 A*, *Mito 10252 A* and *Mito 16250 A*) and mutated G4-DNA (*Mito 6363 M*, *Mito 10252 M* and *Mito 16250 M*). The enhanced fluorescence signals for the interaction of **BYB** with different nucleic acids in buffer were measured at 510 nm. The concentration of **BYB** used was 0.5 μM, and the concentration of nucleic acids was 2.8 μM.

Table 3-2. Dissociation constants determined by ITC for **BYB** interacted with different nucleic acids at 25 °C.

Oligonucleotides	Dissociation constant (K_D), μM
rRNA	n.d.
Dt21	n.d.
Ds26	n.d.
SS19	n.d.
HP19	n.d.
Mito 377	2.56
Mito 714	5.15
Mito 1015	5.22
Mito 6363	1.96
Mito 8095	2.30
Mito 9438	4.70
Mito 10252	4.02
Mito 12086	2.61
Mito 16250	2.20
Mito 6363 A	n.d.
Mito 10252 A	n.d.
Mito 16250 A	n.d.
Mito 6363 M	n.d.
Mito 10252 M	n.d.
Mito 16250 M	n.d.

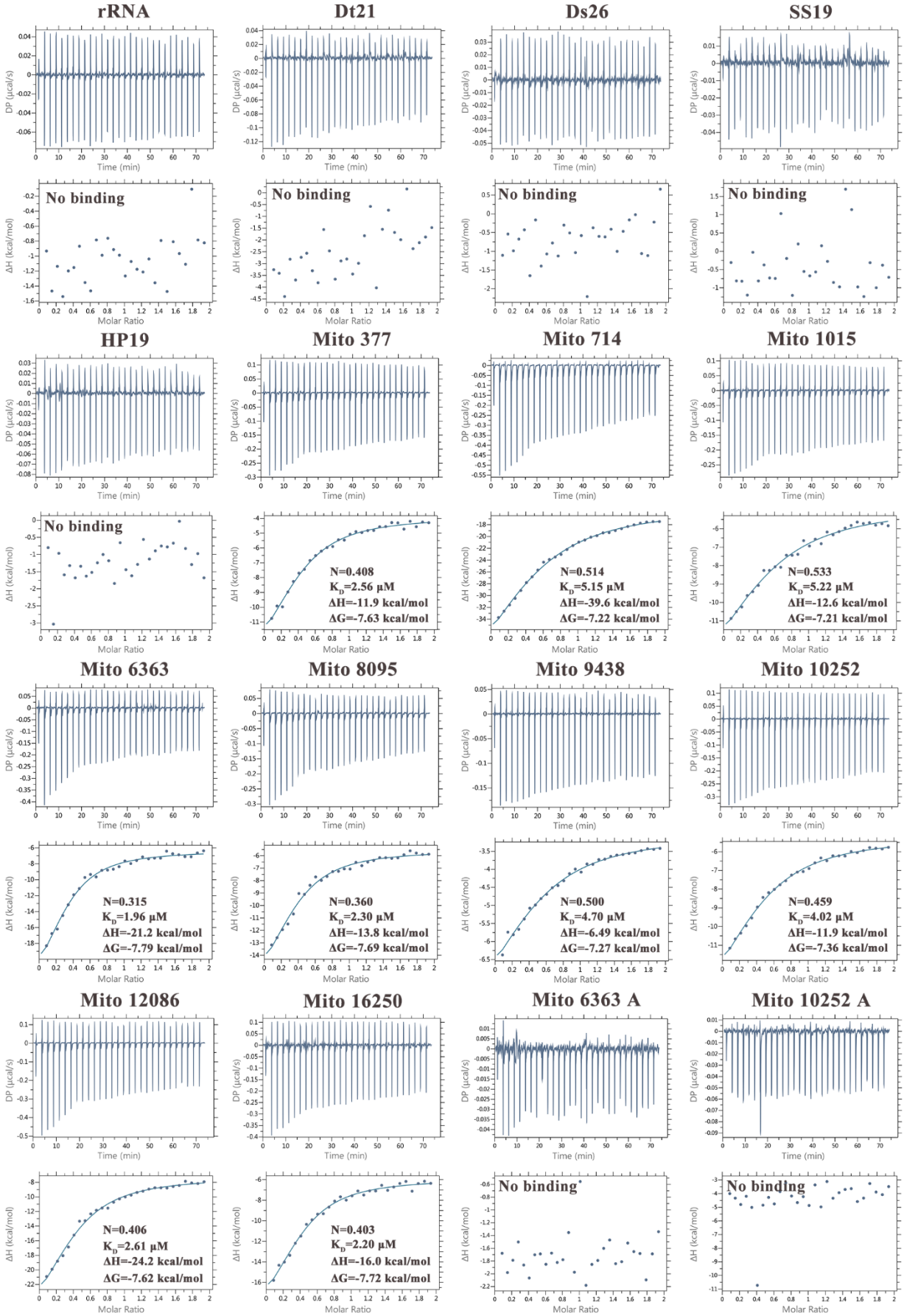
rRNA
Dt21
Ds26
SS19
DP (µcal/s)
Time (min)
ΔH (kcal/mol)
Molar Ratio
No binding
No binding
No binding
No binding
HP19
Mito 377
Mito 714
Mito 1015
No binding
N=0.408
K_D=2.56 µM
ΔH=-11.9 kcal/mol
ΔG=-7.63 kcal/mol
N=0.514
K_D=5.15 µM
ΔH=-39.6 kcal/mol
ΔG=-7.22 kcal/mol
N=0.533
K_D=5.22 µM
ΔH=-12.6 kcal/mol
ΔG=-7.21 kcal/mol
Mito 6363
Mito 8095
Mito 9438
Mito 10252
N=0.315
K_D=1.96 µM
ΔH=-21.2 kcal/mol
ΔG=-7.79 kcal/mol
N=0.360
K_D=2.30 µM
ΔH=-13.8 kcal/mol
ΔG=-7.69 kcal/mol
N=0.500
K_D=4.70 µM
ΔH=-6.49 kcal/mol
ΔG=-7.27 kcal/mol
N=0.459
K_D=4.02 µM
ΔH=-11.9 kcal/mol
ΔG=-7.36 kcal/mol
Mito 12086
Mito 16250
Mito 6363 A
Mito 10252 A
N=0.406
K_D=2.61 µM
ΔH=-24.2 kcal/mol
ΔG=-7.62 kcal/mol
N=0.403
K_D=2.20 µM
ΔH=-16.0 kcal/mol
ΔG=-7.72 kcal/mol
No binding
No binding

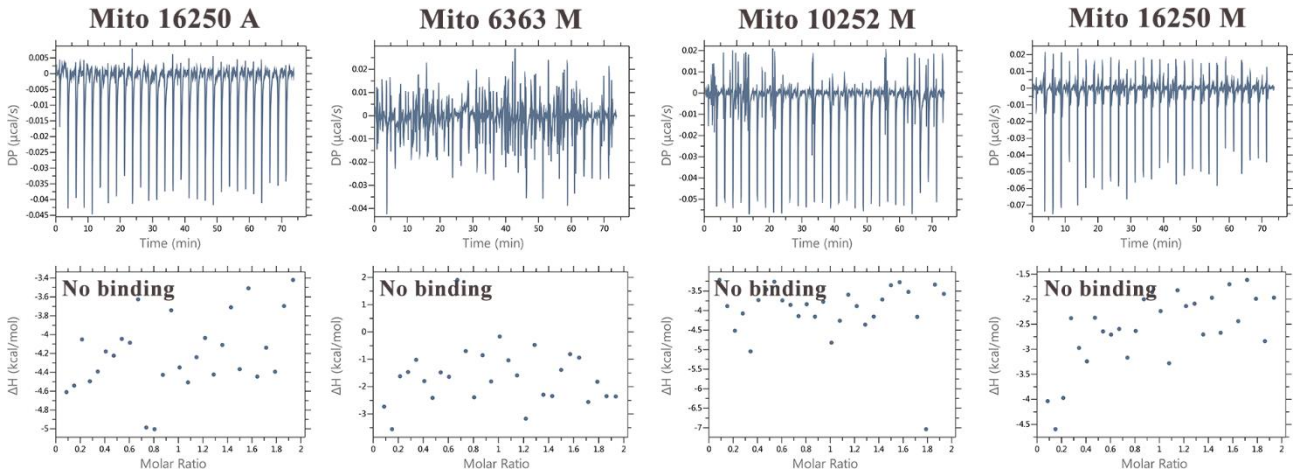

Figure 3.7. The binding affinity of **BYB** with different oligonucleotides was determined with isothermal titration calorimetry (ITC). The isothermal plot of **BYB** in the presence of *rRNA*, *Dt21*, *Ds26*, *SS19*, *HP19*, *Mito 377*, *Mito 714*, *Mito 1015*, *Mito 6363*, *Mito 8095*, *Mito 9438*, *Mito 10252*, *Mito 12086*, *Mito 16250*, *Mito 6363 A*, *Mito 10252 A*, *Mito 16250 A*, *Mito 6363 M*, *Mito 10252 M* and *Mito 16250 M* in 25 mM KH_2PO_4, 60 mM KCl buffer (pH 7.4, containing 0.4% (v/v) DMSO). The concentration of **BYB** was 100 μM and the concentration of oligonucleotides was 10 μM.

Many studies have reported that the conformation of G-quadruplexes could be changed upon interacting with small molecules. To investigate whether **BYB** could induce conformation changes of G4-mtDNAs, we also utilized circular dichroism (CD) to study the interaction between **BYB** and G4-mtDNAs. As shown in **Figure 3.8**, the addition of **BYB** to these sequences did not obviously change the CD spectra in the 240–320 nm range, which corresponds to their G4 structures, implying that the ligand does not induce a conversion between different structural forms, which is consistent with our previous studies.[12] However, our previous studies did not verify whether **BYB** induced circular dichroism (ICD). ICD is a spectroscopic phenomenon used to characterize the structural changes and dynamic properties of target biomolecules when binding molecules are introduced. Our new results shown in **Figure 3.8** revealed that **BYB** did induce marked changes in the CD spectra for several G4-mtDNA substrates, particularly *Mito 714*, *Mito 1015*, *Mito 6363*, *Mito 9438*, *Mito 12086*, and *Mito 16250*. These induced CD signals were clearly observed in the range of 400–600 nm, while no such induced CD signals were detected for non-G4 substrates and *rRNA*, suggesting that **BYB** may interact with the loop or flanking residues of the G4-structure.

Moreover, the thermal melting study using CD revealed that **BYB** increased the melting points of G4-mtDNAs by 6.6 to 16.3 °C, whereas the non-G4 substrates showed only slight increases of 0.2 to 2.5 °C (**Figure 3.9**). These thermal melting results suggest that **BYB** may stabilize G4 structures

during interaction. Taken together, these biophysical findings demonstrate that **BYB** exhibits a high selectivity for G4-mtDNAs, as evidenced by its strong binding affinity (K_D as low as 1.96 μM).

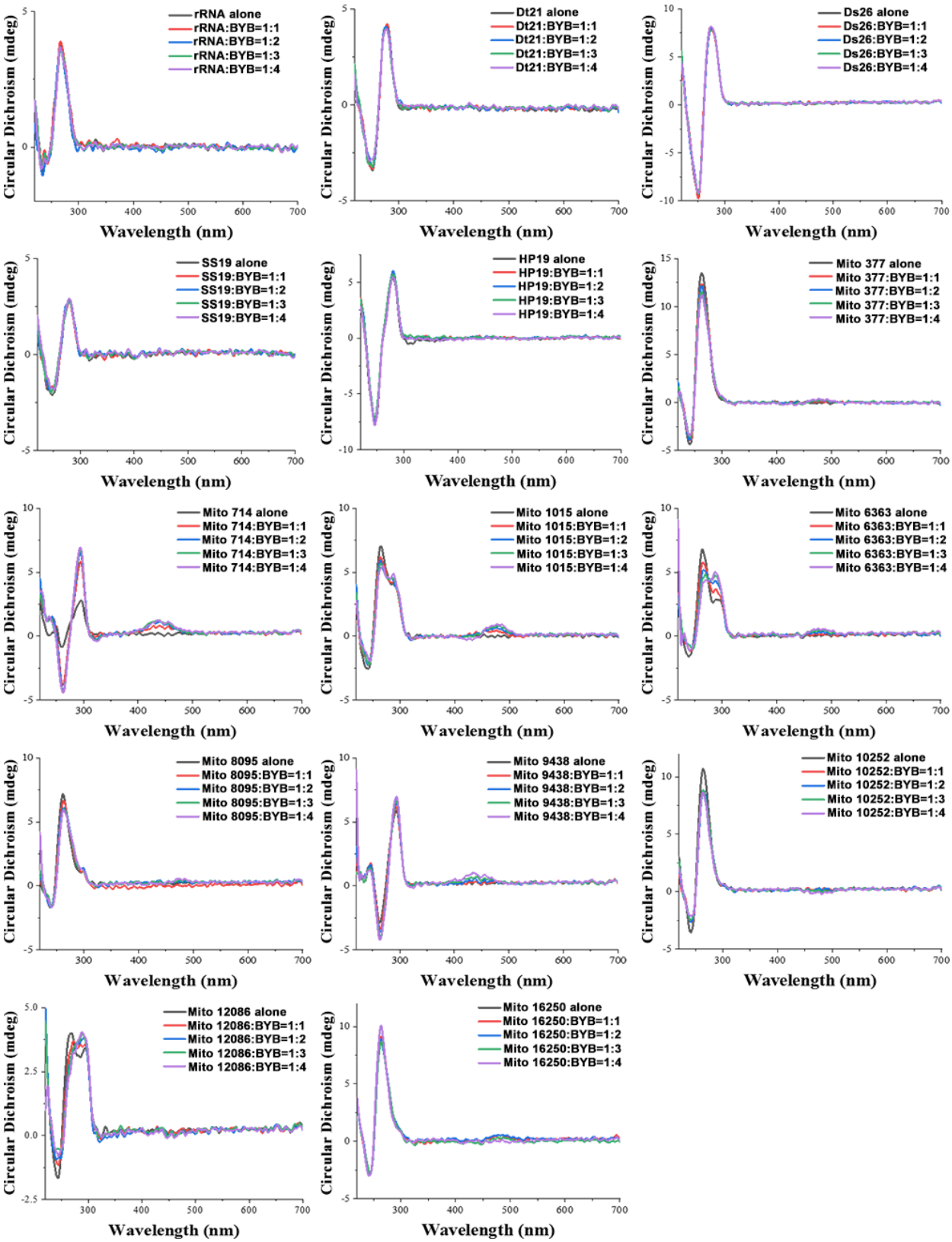

Figure 3.8. CD spectra of **BYB** with *rRNA*, *Dt21*, *Ds26*, *SS19*, *HP19*, *Mito 377*, *Mito 714*, *Mito 1015*, *Mito 6363*, *Mito 8095*, *Mito 9438*, *Mito 10252*, *Mito 12086* and *Mito 16250* in a Tris-HCl buffer (10 mM, 100 mM KCl, pH = 7.4). The concentration of the oligonucleotides used were 5 μM.

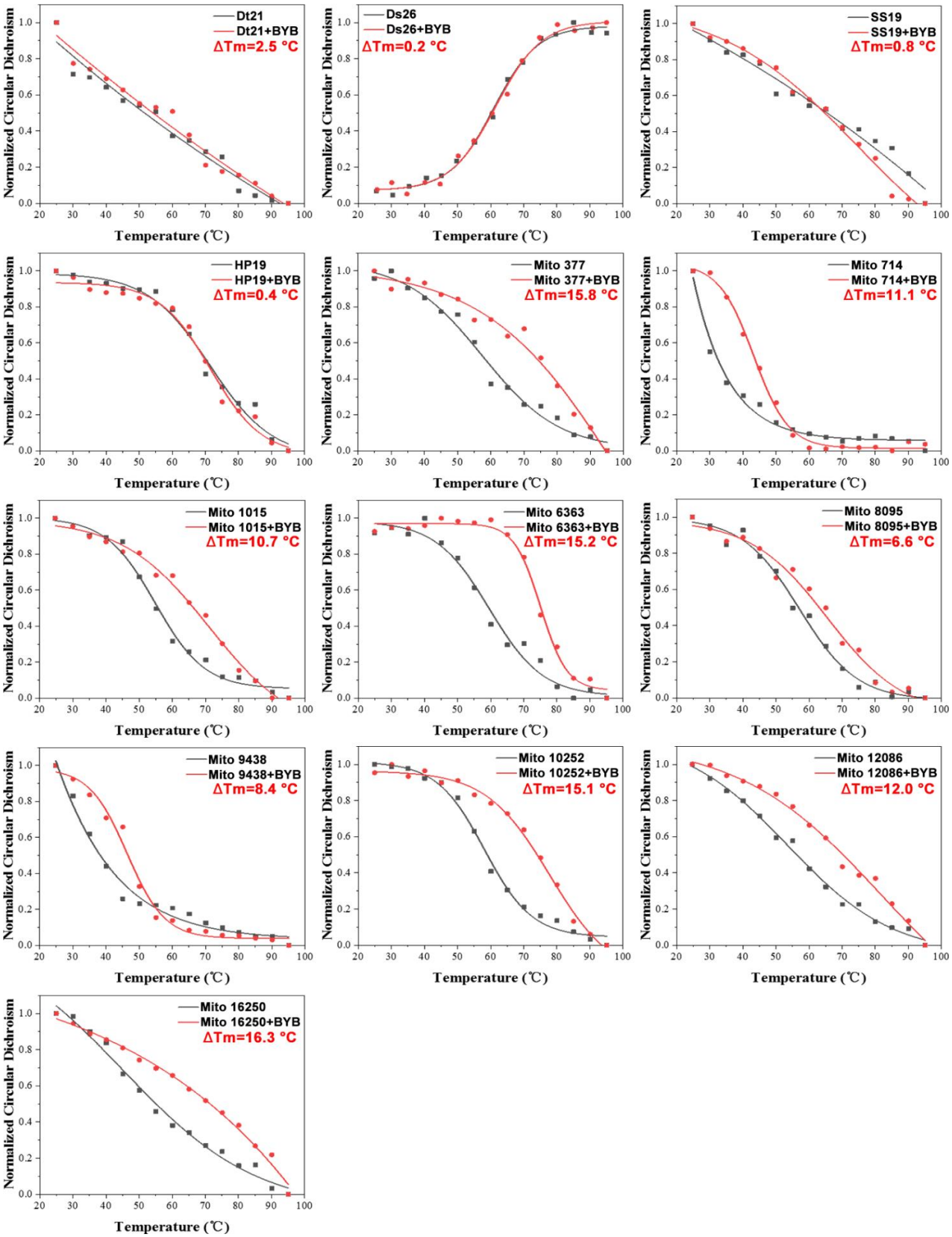

Figure 3.9. Thermal melt CD study for the interaction of G4-mtDNAs (or Non G4-mtDNAs) and **BYB**. Normalized CD signal of the *Dt21*, *Ds26*, *SS19*, *HP19*, *Mito 377*, *Mito 714*, *Mito 015*, *Mito 6363*, *Mito 8095*, *Mito 9438*, *Mito 10252*, *Mito 12086* and *Mito 16250* in a Tris-HCl buffer (10 mM, 20 mM KCl, pH = 7.4) during melting process. The concentrations of **BYB** and oligonucleotides were 10 μM and 5 μM, respectively.

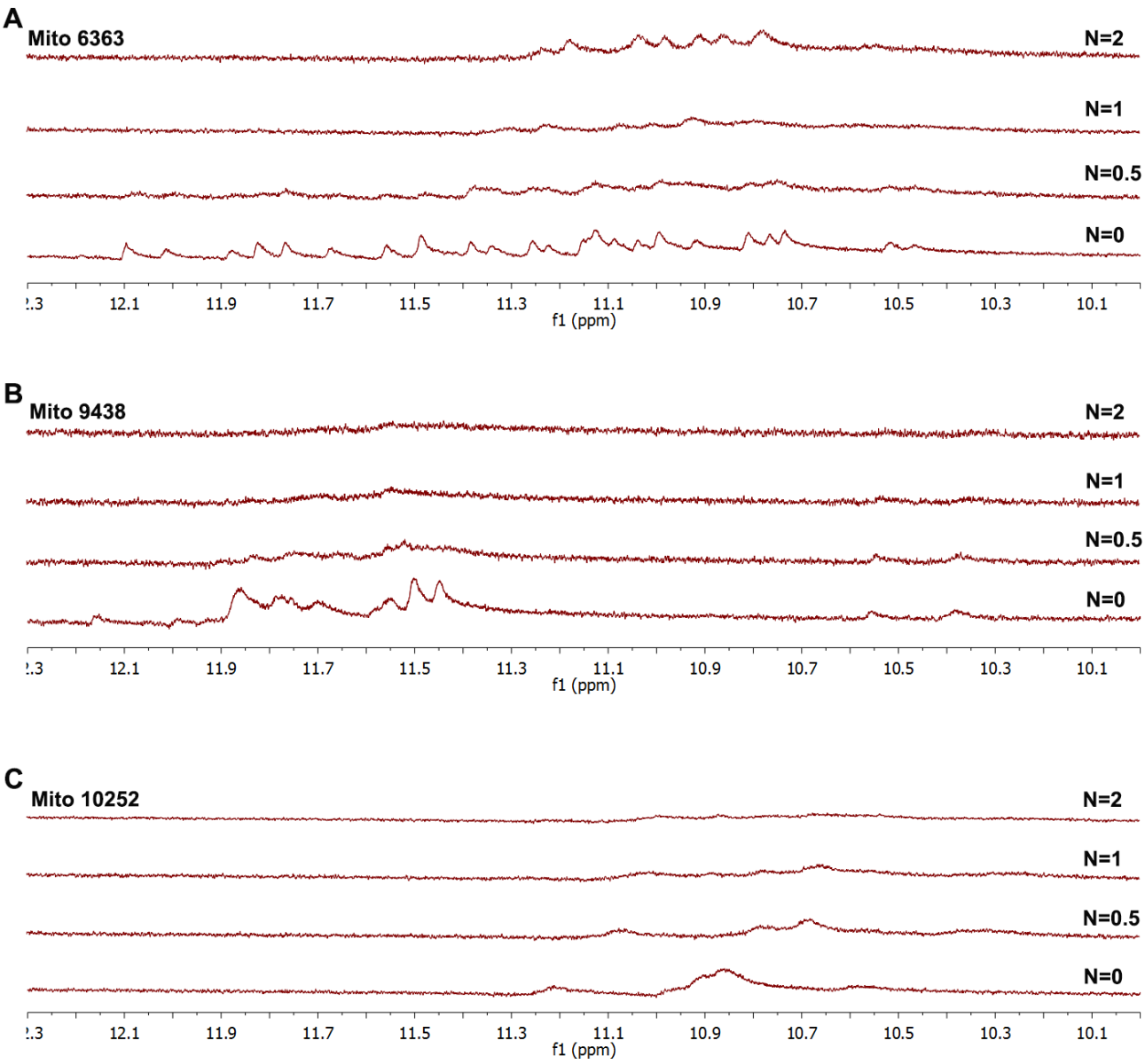

Figure 3.10. NMR was used to study the interaction between G4-mtDNAs and **BYB**. (A) Imino proton regions of ^{1}H NMR spectra of *Mito 6363* (hybrid G4-mtDNA) either alone or with **BYB** at different ratio (0.5, 1 and 2 equivalent). (B) Imino proton regions of ^{1}H NMR spectra of *Mito 9438* (antiparallel G4-mtDNA) either alone or with **BYB** at different ratio (0.5, 1 and 2 equivalent). (C) Imino proton regions of ^{1}H NMR spectra of *Mito 10252* (parallel G4-mtDNA) either alone or with **BYB** at different ratio (0.5, 1 and 2 equivalent).

The interaction between **BYB** and G4-mtDNAs selected in a buffer was also investigated using ^{1}H NMR spectroscopy. As shown in **Figure 3.10**, the imino proton signals for the oligonucleotides of *Mito 6363* (hybrid G4-mtDNA), *Mito 9438* (antiparallel G4-mtDNA), and *Mito 10252* (parallel G4-mtDNA) were detected in the 10–12 ppm region in a pH 7.4 buffer solution containing K^{+} ions, indicating the formation of G4 structures. Upon adding **BYB** to these substrates, some imino proton peaks were either shifted or disappeared. These phenomena demonstrate that **BYB** may have interactions with the G-quartet, including parallel, antiparallel and hybrid G4-mtDNA structures.

To explore whether **BYB** interacts with G4-mtDNAs in living HeLa cells, the G4-mtDNA-selective fluorescent ligand, MitoISCH,[16] was employed to do the intracellular colocalization studies with **BYB**. From **Figure 3.11 A**, **BYB** was found to colocalize well with MitoISCH, suggesting a potential binding to G4-mtDNAs within living cells. To further support that the targets of **BYB** in living HeLa cells could be G4-mtDNAs, the helicase Pif1 was over-expressed in HeLa cells. Pif1 is a known G4-DNA helicase capable of unfolding G4 structures in mitochondria.[17] As shown in **Figure 3.11 B**, the green foci of **BYB** significantly diminished in HeLa cells overexpressing RFP-tagged Pif1, while the negative control, which only overexpressed RFP, exhibited almost no changes in the green foci. On the other hand, we also over-expressed two other helicases in HeLa cells, including Twinkle (a mtDNA helicase) [18] and GRSF1 (a G4-mtRNA helicase).[19] Due to these two helicases cannot resolve G4-mtDNAs, the green foci of **BYB** remained largely unchanged. Collectively, these living cell imaging results, particularly with the use of target-specific helicases, strongly support that **BYB** may selectively target G4-mtDNAs living HeLa cells.

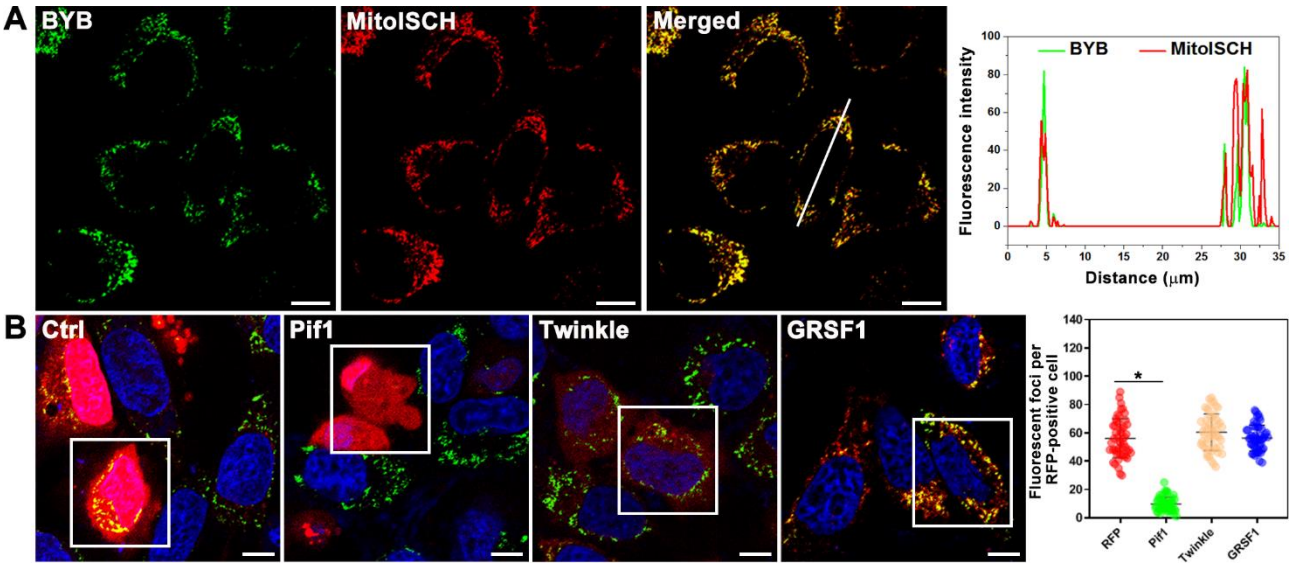

Figure 3.11. Recognition of G4-mtDNAs with **BYB** in living HeLa cells. (A) Living HeLa cells treated with 2 μM **BYB** (Green, λ_{ex}=488 nm) for 30 min and 1 μM MitoISCH (Red, λ_{ex}=561 nm) for 2 h. The scale bar is 10 μm. (B) Living HeLa cells with overexpression of RFP-tagged proteins (Red, λ_{ex}=561 nm, white box) and then incubated with 2 μM **BYB** (Green, λ_{ex}=488 nm) for 30 min. The scale bar is 10 μm. The data are presented as mean ± SEM, and statistics were determined using ANOVA, *p < 0.05.

3.4 Summary

In summary, the small-sized benzoindole-benzothiazole ligand **BYB** could specifically recognize G4-mtDNAs by a series of *in vitro* studies on the interaction of **BYB** with nucleic acids. Fluorescence titration, CD titration, and NMR titration showed that **BYB** is able to selectively bind G4-mtDNAs, whereas it had poor selectivity for other types of nucleic acids, including ssDNA, dsDNA, hairpin DNA, mutant G4-mtDNA and rRNA. ITC titration study showed that **BYB** had a high binding ability for G4-mtDNAs, with binding affinity (K_D) ranging from 1.96-5.22 μM. Moreover, CD melting studies demonstrated that **BYB** increased the melting point of G4-mtDNAs by 6.6-16.3 °C, which suggests that **BYB** can stabilize the structures of G4-mtDNA. In intracellular experiments, organelle co-localization imaging and digitonin pre-treatment assay showed that **BYB** was mainly localized to mitochondria instead of nucleus, lysosome or endoplasmic reticulum in living HeLa cells. Further enzymatic digestion assays, G4-mtDNA ligand co-localization assays, and G4-mtDNA helicases overexpression assays indicated that the primary target of **BYB** in living cells is G4-mtDNAs. In terms of cytotoxicity, **BYB** has a strong inhibitory effect on the proliferation of a variety of cancer cells including A375, HeLa, MIA PaCa-2, SK-MEL-2, HepG2, MDA-MB-231 and HCT116, in which the IC_{50} values of **BYB** were found about 5.4-9.7 μM. In contrast, **BYB** showed relatively less toxic against noncancerous cells (BJ and HFF1, $IC_{50} > 25$ μM). Taken together, **BYB** may be a G4-mtDNA-selective ligand that effectively inhibits the proliferation of a variety of human cancer cells. The anticancer mechanism was investigated, and the results were discussed in detail in Chapter 4.

3.5 References

[1] J. Nygren, N. Svanvik, M. Kubista, The interactions between the fluorescent dye thiazole orange and DNA, Biopolymers 46(1) (1998) 39-51.

[2] Y.-J. Lu, Q. Deng, J.-Q. Hou, D.-P. Hu, Z.-Y. Wang, K. Zhang, L.G. Luyt, W.-L. Wong, C.-F. Chow, Molecular Engineering of Thiazole Orange Dye: Change of Fluorescent Signaling from Universal to Specific upon Binding with Nucleic Acids in Bioassay, ACS Chemical Biology 11(4) (2016) 1019-1029.

[3] Y.-J. Lu, Q. Deng, D.-P. Hu, Z.-Y. Wang, B.-H. Huang, Z.-Y. Du, Y.-X. Fang, W.-L. Wong, K. Zhang, C.-F. Chow, A molecular fluorescent dye for specific staining and imaging of RNA in live cells: a novel ligand integration from classical thiazole orange and styryl compounds, Chemical Communications 51(83) (2015) 15241-15244.

[4] W. Long, Y.-X. Zeng, B.-X. Zheng, Y.-B. Li, Y.-K. Wang, K.-H. Chan, M.-T. She, Y.-J. Lu, C.

Cao, W.-L. Wong, Targeting hTERT Promoter G-Quadruplex DNA Structures with Small-Molecule Ligand to Downregulate hTERT Expression for Triple-Negative Breast Cancer Therapy, Journal of Medicinal Chemistry 67(15) (2024) 13363-13382.

[5] W. Long, B.-X. Zheng, Y. Li, X.-H. Huang, D.-M. Lin, C.-C. Chen, J.-Q. Hou, T.-M. Ou, W.-L. Wong, K. Zhang, Y.-J. Lu, Rational design of small-molecules to recognize G-quadruplexes of c-MYC promoter and telomere and the evaluation of their in vivo antitumor activity against breast cancer, Nucleic Acids Research 50(4) (2022) 1829-1848.

[6] W. Long, B.-X. Zheng, X.-H. Huang, M.-T. She, A.-L. Liu, K. Zhang, W.-L. Wong, Y.-J. Lu, Molecular Recognition and Imaging of Human Telomeric G-Quadruplex DNA in Live Cells: A Systematic Advancement of Thiazole Orange Scaffold To Enhance Binding Specificity and Inhibition of Gene Expression, Journal of Medicinal Chemistry 64(4) (2021) 2125-2138.

[7] W. Long, Y.-J. Lu, K. Zhang, X.-H. Huang, J.-Q. Hou, S.-Y. Cai, Y. Li, X. Du, L.G. Luyt, W.-L. Wong, C.-F. Chow, Boosting the turn-on fluorescent signaling ability of thiazole orange dyes: The effectiveness of structural modification site and its unusual interaction behavior with nucleic acids, Dyes and Pigments 159 (2018) 449-456.

[8] S.O. Raja, G. Sivaraman, S. Biswas, G. Singh, F. Kalim, P. Kandaswamy, A. Gulyani, A Tunable Palette of Molecular Rotors Allows Multicolor, Ratiometric Fluorescence Imaging and Direct Mapping of Mitochondrial Heterogeneity, ACS Applied Bio Materials 4(5) (2021) 4361-4372.

[9] X.-D. Wang, Y.-S. Liu, Z.-L. Liang, M.-H. Hu, Mitochondrial DNA-targeted triphenylamine-thiophene (TPATP)-derived ligands boost type-I/II photodynamic therapy for triple-negative breast cancer, European Journal of Medicinal Chemistry 289 (2025) 117489.

[10] Z. Wang, J. Zhou, L. Lin, M.-H. Hu, Discovery of a far-red carbazole-benzoindolium fluorescent ligand that selectively targets mitochondrial DNA and suppresses breast cancer growth, European Journal of Medicinal Chemistry 264 (2024) 116046.

[11] M.-T. She, J.-W. Yang, B.-X. Zheng, W. Long, X.-H. Huang, J.-R. Luo, Z.-X. Chen, A.-L. Liu, D.-P. Cai, W.-L. Wong, Y.-J. Lu, Design mitochondria-specific fluorescent turn-on probes targeting G-quadruplexes for live cell imaging and mitophagy monitoring study, Chemical Engineering Journal 446 (2022) 136947.

[12] B.-X. Zheng, Indole-benzothiazole derivatives as mitochondrial and c-MYC G-quadruplex ligands, Guangdong University of Technology (2021).

[13] Z.Z. Gizatullina, T.M. Gaynutdinov, H. Svoboda, D. Jerzembek, A. Knabe, S. Vielhaber, M.

Malesevic, H.-J. Heinze, G. Fischer, F. Striggow, F.N. Gellerich, Effects of cyclosporine A and its immunosuppressive or non-immunosuppressive derivatives [D-Ser]8-CsA and Cs9 on mitochondria from different brain regions, Mitochondrion 11(3) (2011) 421-429.

[14] K.-S. Park, I. Jo, Y. Pak, S.-W. Bae, H. Rhim, S.-H. Suh, S. Park, M. Zhu, I. So, K. Kim, FCCP depolarizes plasma membrane potential by activating proton and Na+ currents in bovine aortic endothelial cells, Pflügers Archiv 443(3) (2002) 344-352.

[15] M. Yu, Y. Shi, X. Wei, Y. Yang, Y. Zhou, X. Hao, N. Zhang, R. Niu, Depletion of mitochondrial DNA by ethidium bromide treatment inhibits the proliferation and tumorigenesis of T47D human breast cancer cells, Toxicol Lett 170(1) (2007) 83-93.

[16] X.-C. Chen, G.-X. Tang, W.-H. Luo, W. Shao, J. Dai, S.-T. Zeng, Z.-S. Huang, S.-B. Chen, J.-H. Tan, Monitoring and Modulating mtDNA G-Quadruplex Dynamics Reveal Its Close Relationship to Cell Glycolysis, Journal of the American Chemical Society 143(49) (2021) 20779-20791.

[17] S. Bannwarth, L. Berg-Alonso, G. Augé, K. Fragaki, J.E. Kolesar, F. Lespinasse, S. Lacas-Gervais, F. Burel-Vandenbos, E. Villa, F. Belmonte, J.-F. Michiels, J.-E. Ricci, R. Gherardi, L. Harrington, B.A. Kaufman, V. Paquis-Flucklinger, Inactivation of Pif1 helicase causes a mitochondrial myopathy in mice, Mitochondrion 30 (2016) 126-137.

[18] S.K. Bharti, J.A. Sommers, J. Zhou, D.L. Kaplan, J.N. Spelbrink, J.-L. Mergny, R.M. Brosh, DNA Sequences Proximal to Human Mitochondrial DNA Deletion Breakpoints Prevalent in Human Disease Form G-quadruplexes, a Class of DNA Structures Inefficiently Unwound by the Mitochondrial Replicative Twinkle Helicase*, Journal of Biological Chemistry 289(43) (2014) 29975-29993.

[19] Z. Pietras, M.A. Wojcik, L.S. Borowski, M. Szewczyk, T.M. Kulinski, D. Cysewski, P.P. Stepien, A. Dziembowski, R.J. Szczesny, Dedicated surveillance mechanism controls G-quadruplex forming non-coding RNAs in human mitochondria, Nature Communications 9(1) (2018) 2558.

Chapter 4. Study the anticancer mechanism of ligand BYB

4.1 Synopsis

In Chapter 3, we have revealed that the small-sized benzoindole-benzothiazole ligand, **BYB**, selectively targets G4-mtDNAs *in vitro* and *in cellulo* with high affinity. Besides, **BYB** was found to inhibit the proliferation of a panel of human cancer cells, including human cervical cancer cell HeLa. As our research group has previously established a HeLa tumor xenograft mouse model for anticancer study and lead compound evaluation in our laboratory, we thus selected HeLa cells as the model cancer cell for in-depth intracellular study with **BYB**.

4.2 Results and discussion

4.2.1 Study the effect of **BYB** in inhibiting replication and transcription of mitochondrial DNA and mitochondrial oxidative phosphorylation in HeLa cells

Having established that **BYB** targets mitochondria and exhibits high affinity and selective binding to G4-mtDNAs, we investigated its effects on mitochondrial DNA replication and transcription. As shown in **Figure 4.1 A**, HeLa cells treated with **BYB** had a significant reduction in mtDNA copy numbers, indicating that **BYB** may inhibit mtDNA replication. Next, the mRNA expression levels of 13 selected mitochondrial genes were quantified (**Figure 4.1 B**). Notably, *ND6*, located on the light strand of mitochondrial DNA, does not have G4-forming sequences. Among the 13 genes, the mRNA expression levels of nine genes including *ND1*, *ND4*, *ND4L*, *ND5*, *COX2*, *COX3*, *CYTB*, *ATP6*, and *ATP8* were found to have significant reduction in a concentration-dependent manner in cells treated with **BYB**. These genes encode subunits of the mitochondrial respiratory chain complexes, and their substantial downregulation suggests that **BYB** may suppress the expression of these complexes. As expected, Western blot analysis demonstrated that the levels of complexes I (NDUFB8), II (SDHB), III (UQCRC2), and IV (COX II) were significantly reduced in **BYB**-treated HeLa cells (**Figure 4.1 C** and **D**). Overall, these findings support the conclusion that **BYB** may inhibit both the replication and transcription of mitochondrial DNA, leading to downregulation of mitochondrial respiratory chain complexes I, II, III, and IV.

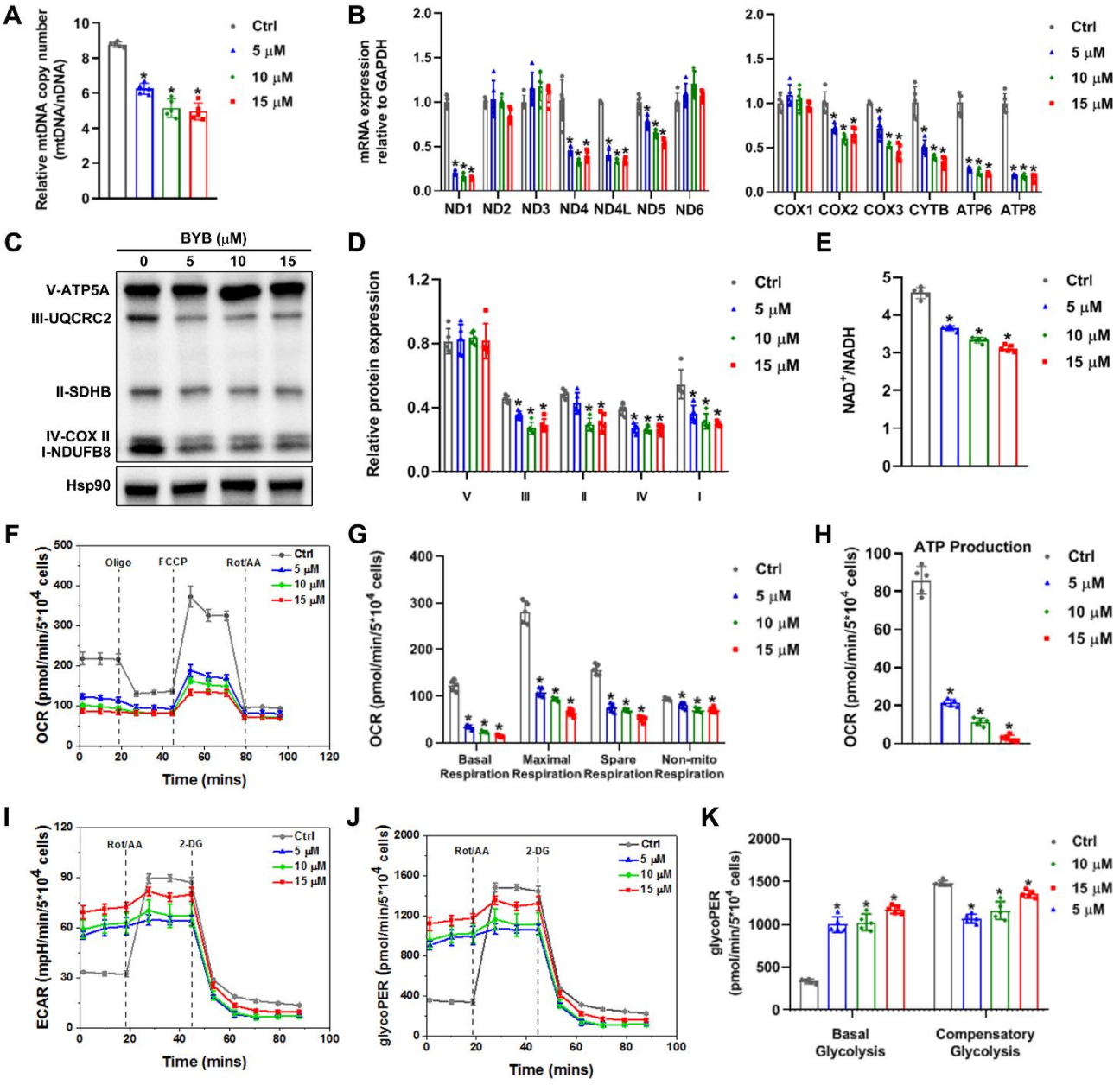

Figure 4.1. BYB may inhibit the replication and transcription of mitochondrial DNA and mitochondrial oxidative phosphorylation in HeLa cells. (A) Effects of **BYB** on mitochondrial DNA replication by q-PCR: HeLa cells were treated with **BYB** (0-15 μM) for 24 h (n=5). (B) Effect of **BYB** on mitochondrial DNA transcription by qRT-PCR: HeLa cells were treated with **BYB** (0-15 μM) for 24 h (n=5). (C-D) Western blot assays to determine the translation of complex I-V and Hsp90 in HeLa cells after treating with **BYB** (0-15 μM) for 24 h (n=5). (E) Determination of intracellular NAD^+/NADH ratio after treating with **BYB** (0-15 μM) for 24 h (n=5). (F) Kinetic profiles of OCR of HeLa cells after treated with **BYB** (0-15 μM) for 3 h (n=5). (G) Values of the basal respiration, maximal respiration, spare respiratory and non-mitochondrial respiration capacity. (H) The analysis of ATP production of **BYB**-treated cells. (I) Kinetic profiles of ECAR of HeLa cells after treatment with **BYB** (0-15 μM) for 3 h (n=5). (J) Kinetic profiles of glycoPER of HeLa cells after treatment with **BYB** (0-15 μM) for 3 h. (K) Values of the basal and compensatory glycolytic PER of the **BYB**-treated cells. The data are presented as mean ± SEM, and statistics were determined using ANOVA, $*p < 0.05$.

Mitochondria are the primary sites for ATP production, with oxidative phosphorylation being crucial to this process.[1] Given that **BYB** downregulates mitochondrial respiratory chain complexes I, II, III, and IV, it may disrupt electron transport within the mitochondrial respiratory chain. Nicotinamide adenine dinucleotide (NAD^+) and its reduced form, NADH, are essential for this chain, facilitating the transfer of electrons from NADH to oxygen, which regenerates NAD^+ for ongoing cellular respiration.[2] Consequently, the downregulation of these complexes could block this process, leading to a decrease in NAD^+ levels. As shown in **Figure 4.1 E**, the NAD^+/NADH ratio significantly decreased in **BYB**-treated HeLa cells in a concentration-dependent manner. Meanwhile, ATP production also declined markedly over the treatment period (**Figure 4.2**). These findings suggest that **BYB** may impair mitochondrial respiratory chain function, resulting in the reduction of ATP production.

To obtain more information about the influence of **BYB** on mitochondrial oxidative phosphorylation, a mito-stress test and a glycolytic rate test on HeLa cells treated with **BYB** were performed. We measured the oxygen consumption rate (OCR) and extracellular acidification rate (ECAR) of the treated cells. A significant reduction in both OCR and ATP production was observed (**Figure 4.1 F-H**). Conversely, the glycolytic rate in **BYB**-treated cells increased markedly **(Figure 4.1 I-K**). This increase may be a compensatory response to the repression of ATP production, aimed at maintaining cellular energy levels for survival. Overall, these findings provide substantial evidence that **BYB** may diminish mitochondrial oxidative phosphorylation in HeLa cells.

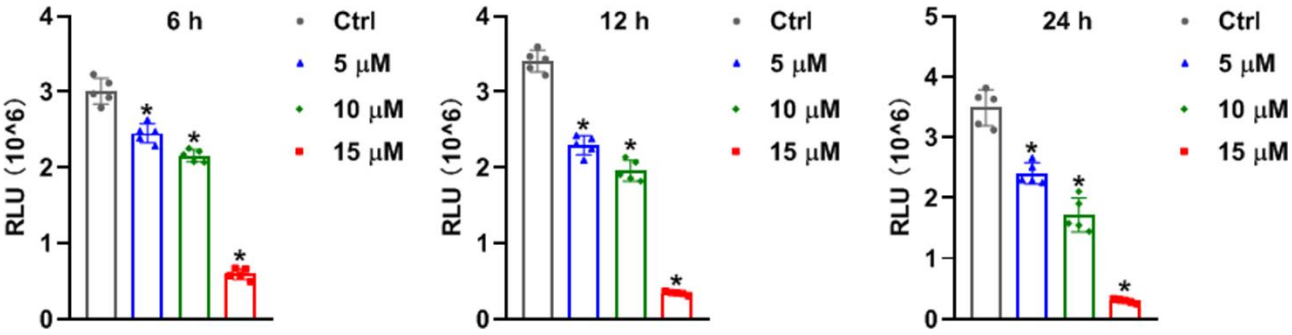

Figure 4.2. Determination of cellular ATP for HeLa cells treated with **BYB** (0-15 μM) for 0-24 h (n=5). The data are presented as mean ± SEM, and statistics were determined using ANOVA, *$p <$ 0.05.

4.2.2 Study the effect of **BYB** in inducing mitochondrial dysfunction and calcium overload

Mitochondria are crucial for maintaining cellular homeostasis, participating in several essential biological processes such as energy production, membrane potential (MMP) regulation, calcium ion balance, and reactive oxygen species (ROS) management.[3] To determine whether **BYB** induces mitochondrial dysfunction, we first studied the changes in MMP in HeLa cells treated with **BYB**. As shown in **Figure 4.3 A**, the fluorescence intensity of TMRE (tetramethylrhodamine ethyl ester), a dye used for quantitative measurement of MMP, significantly decreased in a concentration-dependent manner in the **BYB**-treated cells, indicating that **BYB** causes MMP depolarization.

We have confirmed that **BYB** downregulates the expression of complexes I, II, III, and IV, leading to decreased ATP production in HeLa cells (**Figure 4.2 C** and **D**). Previous studies have indicated that complexes I and II are essential for maintaining normal mitochondrial Ca^{2+} homeostasis.[4] Additionally, calcium ions play a critical regulatory role in oxidative phosphorylation, particularly concerning complexes I, III, and IV.[5, 6] Therefore, it is possible that **BYB** disrupts calcium ion balance within the mitochondria. To investigate this hypothesis further, we conducted additional experiments.

From **Figure 4.3 B**, ATP production in cells treated with **BYB** for 24 hours decreased in a concentration-dependent manner. In contrast, mitochondrial calcium ions gradually increased with rising **BYB** concentrations (**Figure 4.3 C**). Similar trends were observed at different time intervals in **BYB**-treated cells (**Figure 4.3 E** and **F**). Specifically, ATP levels significantly declined over time (**Figure 4.3 E**), while mitochondrial calcium ions increased in a time-dependent manner (**Figure 4.3 F**). These findings suggest that the reduction in ATP production caused by **BYB** may lead to the increase of mitochondrial calcium levels. To verify this hypothesis, we employed the DIDS sodium salt, a VDAC1 inhibitor,[7] to examine the effect of **BYB** on mitochondrial calcium ion levels. The voltage-dependent anion channel (VDAC) is an ion channel protein located in the outer mitochondrial membrane, playing a crucial role in regulating calcium ion flow into and out of the mitochondria. As shown in **Figure 4.3 D**, the mitochondrial calcium levels showed only slight changes when co-treated with **BYB** and DIDS sodium salt, compared to treatment with **BYB** alone (**Figure 4.3 C**), suggesting when mitochondrial calcium channels were closed by DIDS sodium salt, the level of mitochondrial calcium ion in **BYB**-treated HeLa cells would be significantly reduced. These results strongly indicate

that **BYB** is the major factor driving the increase of mitochondrial calcium ions in the cells.

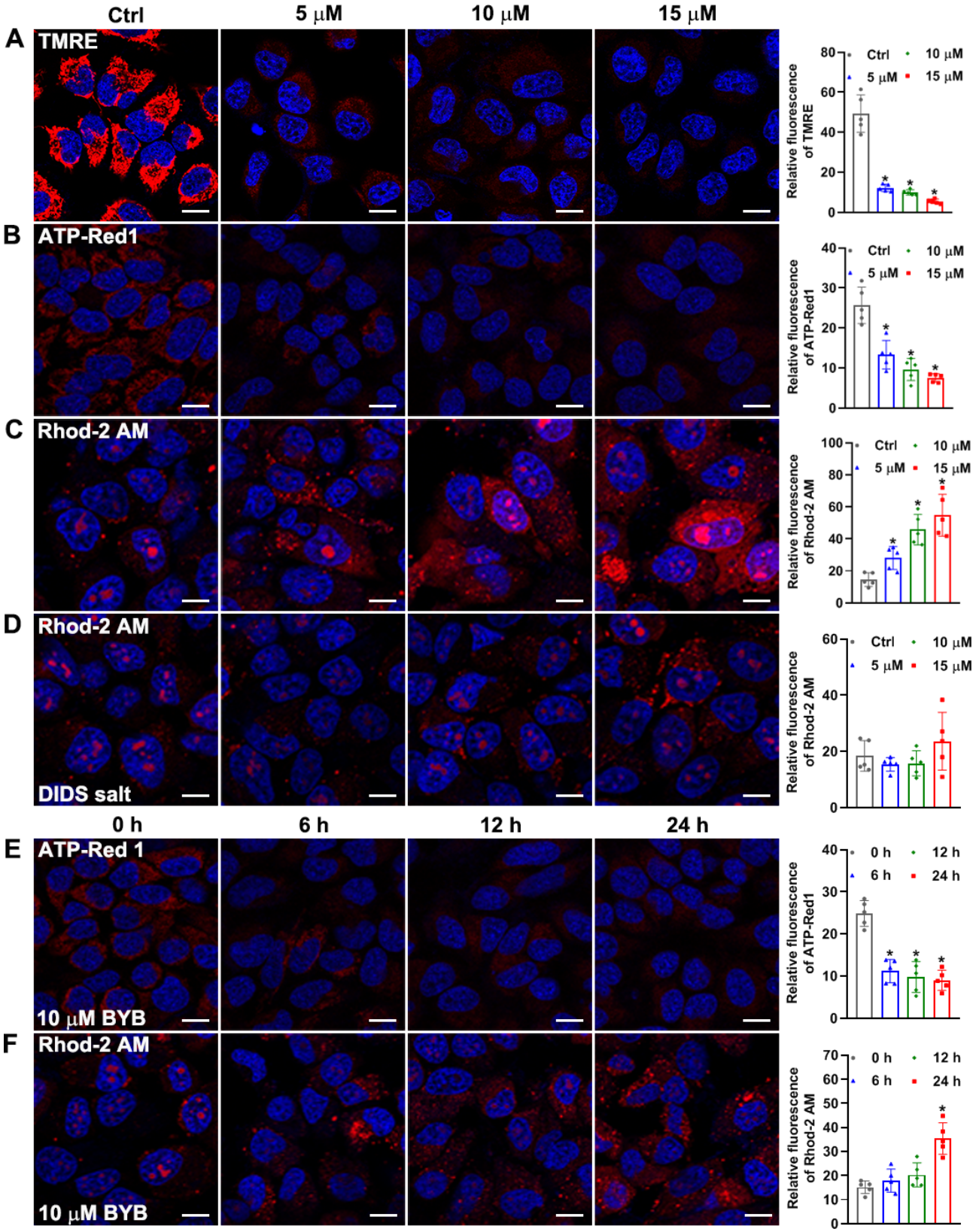

Figure 4.3. (A) The effect of **BYB** (0-15 μM) on mitochondrial membrane potential in HeLa cells. Mitochondrial membrane potential was evaluated with TMRE (Red, λ_{ex}=561 nm); incubation for 24 h (n=5). The scale bar is 10 μm. (B) ATP production in HeLa cells after **BYB** (0-15 μM) treatment for 24 h. The ATP was evaluated with ATP-Red1 (Red, λ_{ex}=561 nm) (n=5). The scale bar is 10 μm. (C) Mitochondrial calcium ion in HeLa cells after **BYB** (0-15 μM) treatment for 24 h. The

mitochondrial calcium ion was evaluated with Rhod-2 AM (Red, λ_{ex}=561 nm) (n=5). The scale bar is 10 μm. (D) Mitochondrial calcium ion in HeLa cells after **BYB** (0-15 μM) and 150 μM DIDS sodium salt co-treatment for 24 h. The mitochondrial calcium ion was evaluated with Rhod-2 AM (Red, λ_{ex}=561 nm) (n=5). The scale bar is 10 μm. (E) The effect of 10 μM **BYB** on ATP production in HeLa cells at different times (0, 6,12 and 24 h). The ATP was evaluated with ATP-Red1 (Red, λ_{ex}=561 nm) (n=5). The scale bar is 10 μm. (F) The effect of 10 μM **BYB** on mitochondrial calcium ion in HeLa cells at different times (0, 6,12 and 24 h). The mitochondrial calcium ion was evaluated with Rhod-2 AM (Red, λ_{ex}=561 nm) (n=5). The scale bar is 10 μm. The data are presented as mean ± SEM, and statistics were determined using ANOVA, $*p < 0.05$.

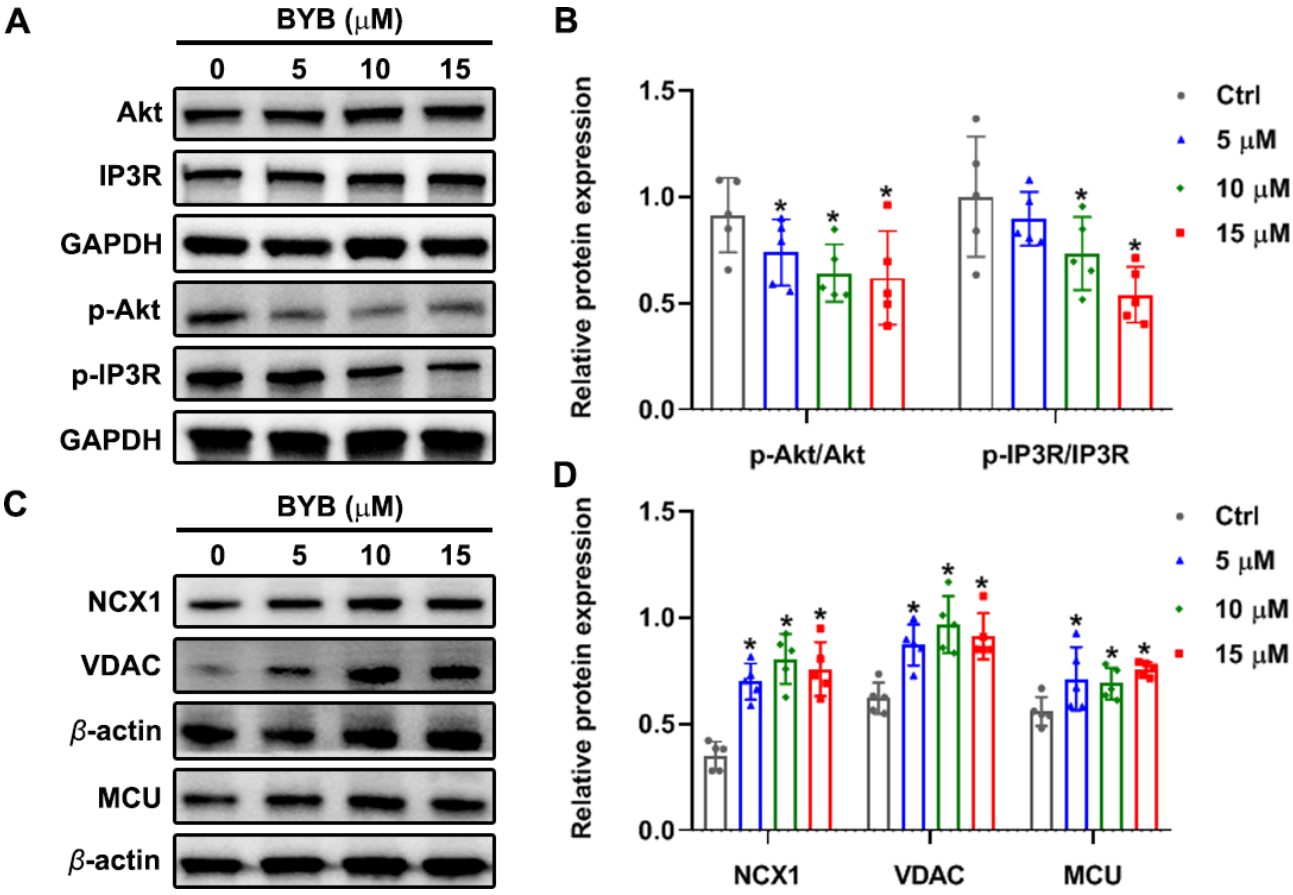

Figure 4.4. (A-B) Western blot assays to determine the translation of Akt, Phospho-Akt, IP3R, Phospho-IP3R and GAPDH in HeLa cells treated with **BYB** (0-15 μM) for 24 h (n=5). (C-D) Western blot assays to determine the translation of NCX1, VDAC, MCU and *β*-actin in HeLa cells treated with **BYB** (0-15 μM) for 24 h (n=5). The data are presented as mean ± SEM, and statistics were determined using ANOVA, $*p < 0.05$.

Calcium ions are mainly stored in the endoplasmic reticulum (ER) within cells. Inositol 1,4,5-triphosphate receptors (IP3R) are part of a family of intracellular calcium release channels located in the ER.[8] Under normal conditions, IP3R is phosphorylated to prevent the outflow of calcium ions from the ER, thereby inhibiting apoptosis.[9] Protein kinase B (PKB), also known as Akt, plays a vital role in phosphorylating IP3R to protect cells from undergoing apoptosis.[10] As shown **in**

Figures 4.4 A and **B**, the levels of phospho-Akt and phospho-IP3R were downregulated in HeLa cells treated with **BYB** for 24 hours, indicating that **BYB** may induce calcium ion efflux from the endoplasmic reticulum. Moreover, Western blot analysis revealed that the expression of mitochondrial calcium ion transport-related proteins, including VDAC, MCU, and NCX1, was upregulated in **BYB**-treated cells (**Figure 4.4 C** and **D**), suggesting that these released calcium ions may enter mitochondria through these channels. Collectively, these results suggest that **BYB** may lead to an increase in mitochondrial calcium ions, ultimately resulting in mitochondrial calcium overload in the cells.

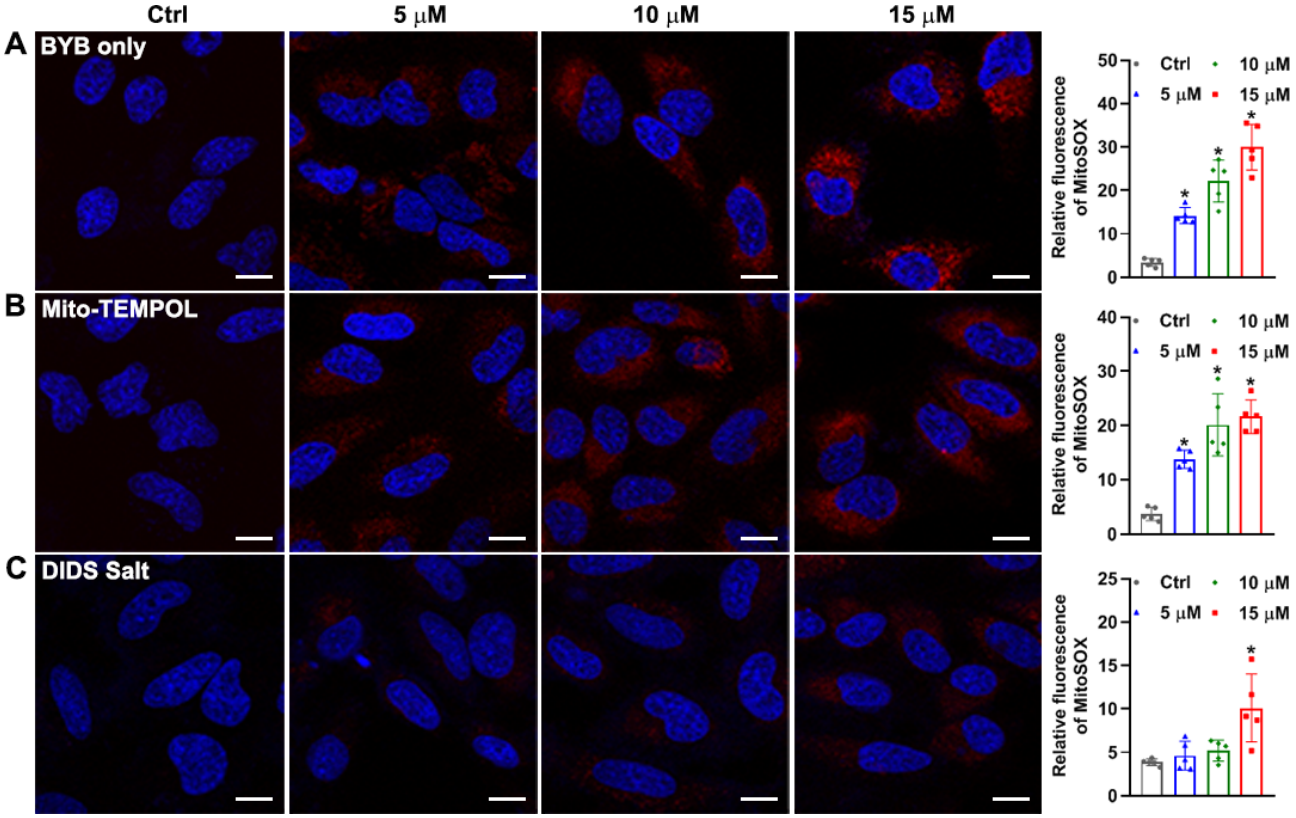

Figure 4.5. (A) Mitochondrial ROS in HeLa cells after **BYB** (0-15 μM) treatment for 24 h. The mitochondrial ROS was evaluated with MitoSOX (Red, λ_{ex}=561 nm) (n=5). The scale bar is 10 μm. (B) Mitochondrial ROS in HeLa cells after **BYB** (0-15 μM) and 10 μM Mito-TEMPOL co-treatment for 24 h. The mitochondrial ROS was evaluated with MitoSOX (Red, λ_{ex}=561 nm) (n=5). The scale bar is 10 μm. (C) Mitochondrial ROS in HeLa cells after **BYB** (0-15 μM) and 150 μM DIDS sodium salt co-treatment for 24 h. The mitochondrial ROS was evaluated with MitoSOX (Red, λ_{ex}=561 nm) (n=5). The scale bar is 10 μm. The data are presented as mean ± SEM, and statistics were determined using ANOVA, $*p < 0.05$.

Overloaded calcium ions in mitochondria may interact with the electron transport chain complexes, causing electron leakage and enhancing production of mitochondrial reactive oxygen species (mtROS). To test this hypothesis, we used the mtROS probe MitoSOX to measure mtROS levels in **BYB**-treated cells. As shown in **Figure 4.5 A**, the fluorescent signal from MitoSOX significantly

increased with higher concentrations of **BYB**, indicating that **BYB** markedly enhances mtROS production. To confirm that mtROS production was primarily due to mitochondrial calcium overload, we applied Mito-TEMPOL, a mitochondria-targeting antioxidant,[11] to remove mtROS causing by **BYB** in HeLa cells. Compared to the control (**Figure 4.5 A**, **BYB** alone), the mtROS levels showed little reduction in cells treated with both **BYB** and Mito-TEMPOL (**Figure 4.5 B**). However, Mito-TEMPOL effectively removed all mtROS in HeLa cells not treated with **BYB** (**Figure 4.5 B**, Mito-TEMPOL alone). These findings suggest that **BYB** significantly increases mtROS production in HeLa cells. It is noteworthy that the mtROS levels were substantially reduced in cells after together treatment with **BYB** and DIDS sodium salt (**Figure 4.5 C**). This reduction may be due to DIDS sodium salt blocking the mitochondrial calcium overload pathway during co-treatment, thus suppressing mtROS production. These results indicate that mitochondrial calcium overload could be a primary contributor to mtROS production in **BYB**-treated HeLa cells. In summary, we propose that **BYB** induces mitochondrial calcium overload, which may subsequently lead to increased mtROS production. Therefore, **BYB** could serve as a promising mitochondria-targeting anticancer agent by triggering mitochondrial calcium overload, promoting mtROS production, and causing mitochondrial dysfunction.

4.2.3 Study the effect of **BYB** in inducing mitophagy

We have verified that **BYB** may induce mitochondrial dysfunction and calcium overload to enhance mtROS production, we next investigated whether **BYB** could trigger mitophagy in HeLa cells. HeLa cells were first transfected with LC3 protein, a well-known marker for autophagy, labeled with RFP, and subsequently treated with **BYB**. We observed a significant increase in the red signal from RFP-LC3 in cells. The cellular localization of RFP-LC3 (red) and **BYB** (green) showed substantial colocalization (**Figure 4.6 A** and **D**), indicating that **BYB** may increase the expression of LC3 protein. Moreover, we detected autophagosomes using MDC staining. As shown in **Figure 4.6 B** and **D**, the blue signal from MDC significantly increased in **BYB**-treated cells, and this signal colocalized well with **BYB** (green) and mitochondria (red). This suggests that the mitochondria bound to **BYB** were being engulfed by autophagosomes. Because the damaged mitochondria would be delivered to lysosomes for degradation, we examined the changes in mitochondrial positioning following **BYB** treatment. In **Figure 4.6 C** and **D**, the blue foci of lysosomes were found to colocalize with **BYB** (green) and mitochondria (red), indicating that **BYB**-bound mitochondria were being transported to

lysosomes for degradation.

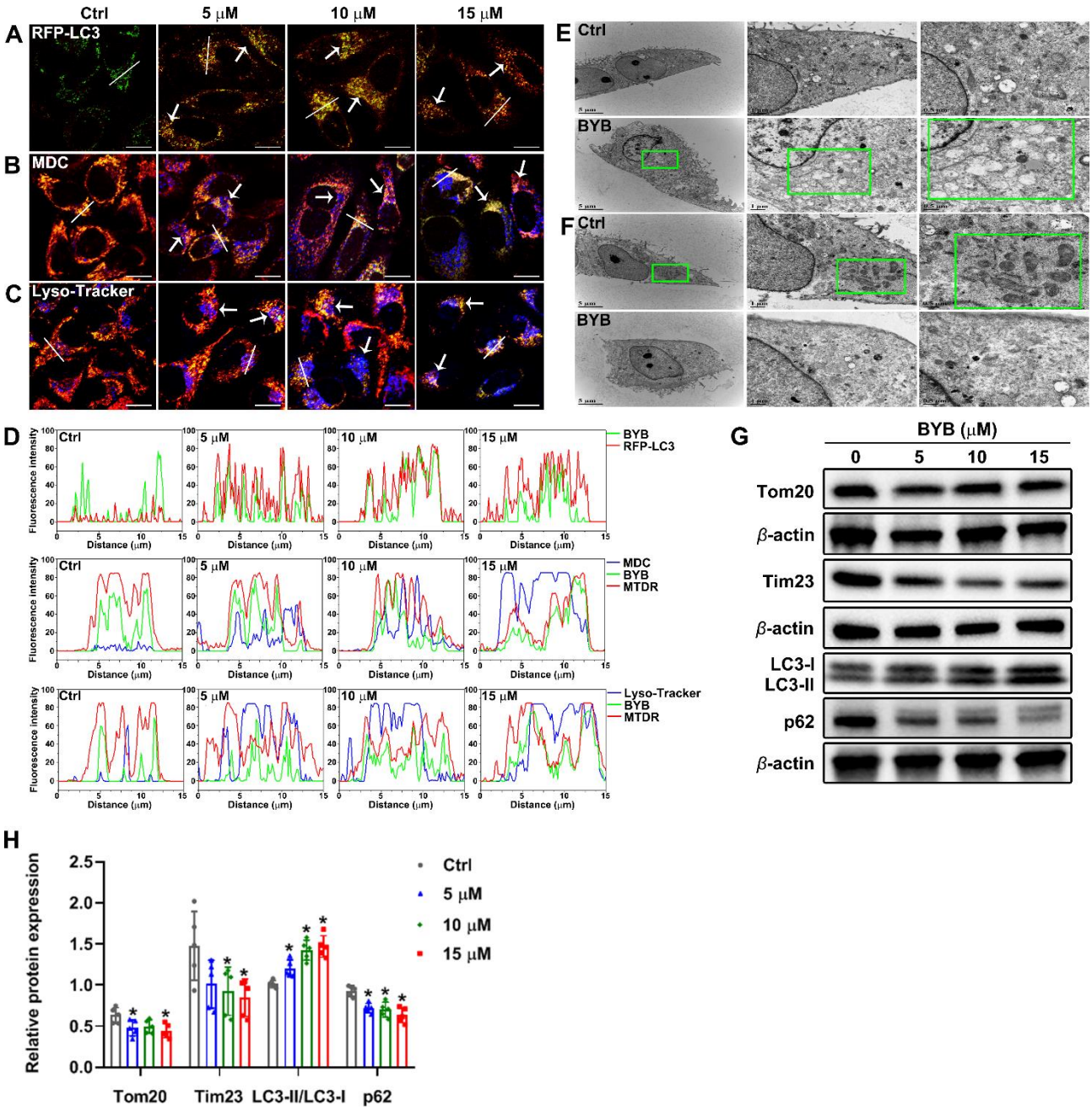

Figure 4.6. (A) HeLa cells were transfected with the autophagy sensor LC3-RFP and cultured for 24 h (Red, λ_{ex}=561 nm). The cells were then treated with **BYB** (Green, λ_{ex}=488 nm, 0-15 μM) for 24 h. The scale bar is 10 μm. (B) HeLa cells were treated with **BYB** (Green, λ_{ex}=488 nm, 0-15 μM) for 24 h, then the cells were stained with 10 μM MDC (Blue, λ_{ex}=405 nm) for 30 min and 200 nM Mito-Tracker Deep Red (Red, λ_{ex}=635 nm) for 30 min. The scale bar is 10 μm. (C) HeLa cells were treated with **BYB** (Green, λ_{ex}=488 nm, 0-15 μM) for 24 h, then the cells were stained with 1 μM Lyso-Tracker (Blue, λ_{ex}=405 nm) for 30 min and 200 nM Mito-Tracker Deep Red (Red, λ_{ex}=635 nm) for 30 min. The scale bar is 10 μm. (D) Relative fluorescence intensity profiles across the white line in Figure A-C. (E) HeLa cells were treated with or without 10 μM **BYB** for 24 h and TEM was employed to detect the autophagosomes, and the magnified view of the electron photomicrograph exhibited autophagosomes. (F) HeLa cells were treated with or without 10 μM **BYB** for 24 h and TEM was employed to detect the mitochondria, and the magnified view of the electron photomicrograph exhibited mitochondria. (G-H) Western blot assays to determine the translation of Tom20, Tim23,

LC3, p62 and *β*-actin in HeLa cells treated with **BYB** (0-15 μM) for 24 h (n=5). The data are presented as mean ± SEM, and statistics were determined using ANOVA, $*p < 0.05$.

To provide further evidence that **BYB** may induce mitophagy, we utilized transmission electron microscopy (TEM) to study changes in autophagosomes and mitochondria. As shown in the TEM images in **Figure 4.6 E**, the number of large autophagosomes (highlighted in green boxes) was significantly increased in **BYB**-treated cells. Additionally, compared to the control, there was a dramatic reduction in the presence of mitochondria in **BYB**-treated cells (**Figure 4.6 F**). Furthermore, Western blot analysis further supported these findings, revealing that the mitophagy-related protein LC3-II was upregulated, while p62 levels were downregulated. It is because the mitochondria were degraded in lysosome, the level of mitochondrial membrane proteins Tom20 and Tim23 were also downregulated (**Figure 4.6 G** and **H**). Collectively, **BYB** may induce mitochondrial dysfunction and promote mitophagy in HeLa cells.

4.2.4 Study the effect of **BYB** in inducing DNA damage

Having proved that **BYB** may lead to mitochondrial calcium overload and a significant increase in mtROS levels in HeLa cells. Excessive mtROS production can result in oxidative damage to mtDNA,[12] so we tried to investigate whether **BYB** induces mtDNA damage. Some studies have suggested that excess mtROS may lead to the generation of mtDNA fragments that can be released into the cytoplasm.[13] As shown in **Figure 4.7 A**, the amount of *MT-ND1* and *MT-ND2*, genes located in mtDNA, were found to be elevated in the cytosol, suggesting that **BYB** may initiate mtROS production, resulting in mtDNA damage and subsequent release of damaged fragments into the cytoplasm. To further confirm mtDNA damage, we assessed the level of the 8.8 kb mtDNA, which is commonly used for quantitative PCR detection of mtDNA damage. As shown in **Figure 4.7 B**, PCR amplification of the 8.8 kb mtDNA was reduced, with a decrease of 5.9-17.4% observed as **BYB** concentration increased. These findings strongly indicated that mtDNA was damaged in HeLa cells after treating **BYB**.

Apart from mtDNA damage, we also investigated potential nuclear DNA damage in **BYB**-treated HeLa cells. Comet assays revealed significant nuclear DNA damage, as evidenced by the lengthened comet tails observed in the treated cells (**Figure 4.7 C** and **D**). Besides, a markedly increased *γ*-H2A.x and p53 protein levels supported that **BYB** may induce nuclear DNA damage in HeLa cells (**Figure**

4.7 E and **F**). In addition, cell cycle analysis further indicated a concentration-dependent increase in the proportion of **BYB**-treated cells arrested in the S phase (**Figure 4.7 G**). The percentage of cells in S phase increased from approximately 29% to 44%. All these results suggested that **BYB** may induce nuclear DNA damage in HeLa cells, despite the mechanism is still unclear at present.

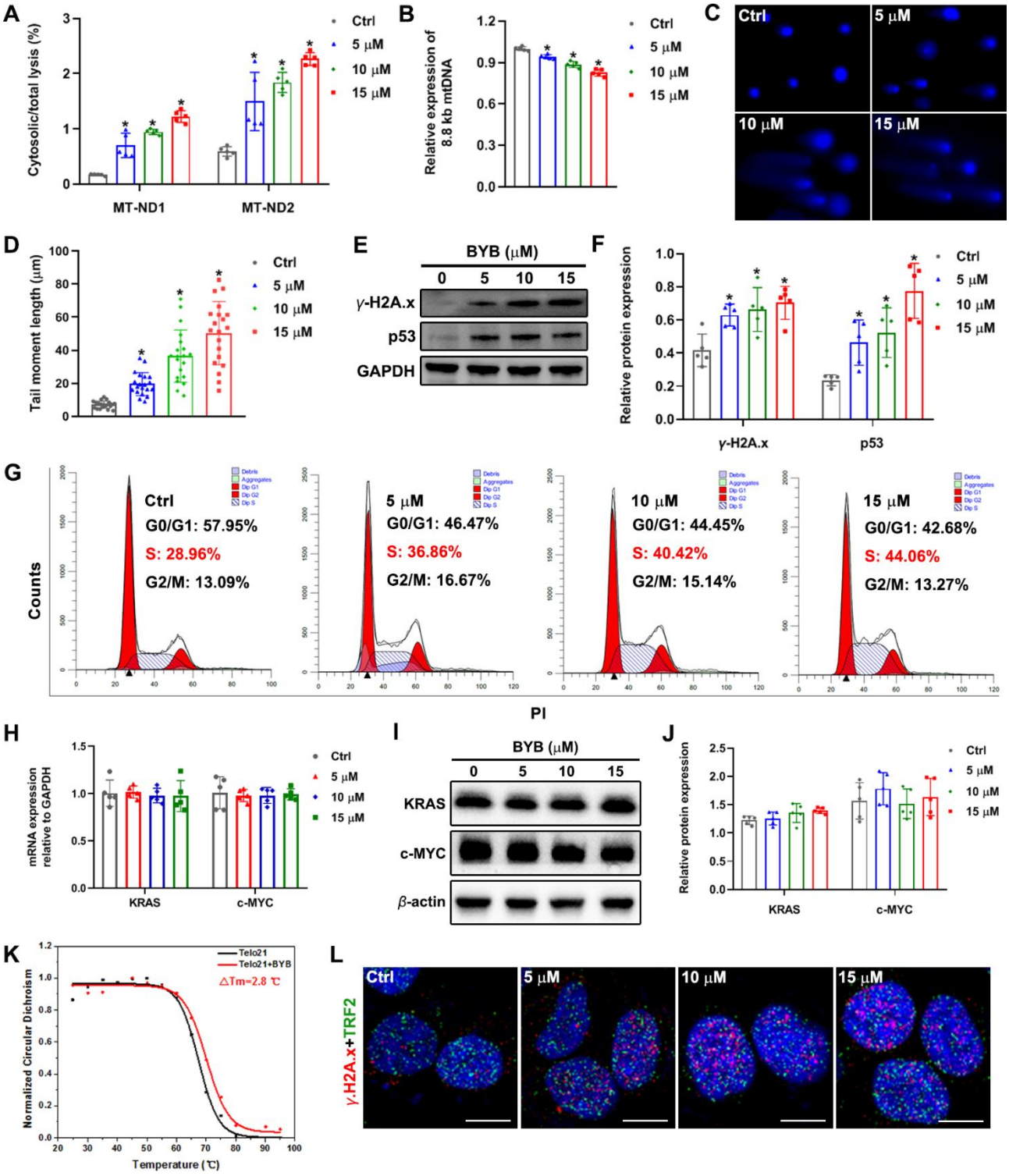

Figure 4.7. (A) q-PCR to study the release of mtDNA in HeLa cells after **BYB** (0-15 μM) treatment for 24 h. (n=5, cytosolic/total lysis, percent). (B) q-PCR to analyze the level of 8.8 kb mitochondrial DNA copy number determination after **BYB** (0-15 μM) treatment for 24 h (n=5). (C-D) Comet assay to analyze DNA damage induced by **BYB** (0-15 μM) for 24 h treatment in HeLa cells. The cell was stained by DAPI (Blue, λ_{ex}=405 nm). Approximately 20 cells were measured. (E-F) Western blot

assays to determine the translation of γ-H2A.x, p53 and GAPDH in HeLa cells treated with **BYB** (0-15 μM) for 24 h (n=5). (G) Cell cycle analysis of HeLa cells treated with **BYB** (0-15 μM) for 24 h. (H) The effect of **BYB** on the transcription of *KRAS* and *c-MYC* by qRT-PCR. HeLa cells were treated with **BYB** (0-15 μM) for 24 h (n=5). (I-J) Western blot assays to determine the translation of *KRAS*, *c-MYC* and β-actin in HeLa cells treated with **BYB** (0-15 μM) for 24 h (n=5). (K) Normalized CD signal of Telo21 in 10 mM Tris-HCl buffer (containing 20 mM KCl, pH = 7.4) during melting process. The concentrations of **BYB** and *Telo21* were 10 μM and 5 μM, respectively. (L) Confocal images of TRF2 (green, λ_{ex}=561 nm) and γ-H2A.x (red, λ_{ex}=635 nm) in HeLa cells after **BYB** (0-15 μM) treatment for 24 h, the nucleus was stained by Hoechst 33342 (blue, λ_{ex}=405 nm). The scale bar is 10 μm. The data are presented as mean ± SEM, and statistics were determined using ANOVA, $*p < 0.05$.

It is important to note that **BYB** does not penetrate the nucleus of HeLa cells, because of the absence of fluorescent signals from **BYB** in the nucleus (**Figure 3.2**). To further demonstrate that nuclear DNA damage is not primarily attributed to interactions between **BYB** and G4-DNAs found in the nucleus, we detected the mRNA and protein levels of KRAS and c-MYC in **BYB**-treated cells. Both *KRAS* and *c-MYC* are well-established genes located in the nucleus that can form G4 structures.[14] The results clearly indicated that **BYB** does not significantly influence the transcription and translation of these genes (**Figure 4.7 H-J**), providing strong support for the notion that **BYB** is mitochondria-specific, targeting G4-mtDNAs rather than nuclear G4-DNAs in living cells.

On the other hand, telomeres are rich in G4-forming sequences, and G4-specific ligands often lead to telomere DNA damage. Therefore, we investigated whether **BYB** interacts with telomeric G4-DNA. Thermal melting studies using circular dichroism (CD) revealed that **BYB** only slightly stabilized the G4 structure of telomere (*Telo21*), increasing by 2.8 °C (**Figure 4.7 K**). In addition, we conducted immunofluorescence analysis for γ-H2AX in combination with TRF2, a component of the telomere complex. The results showed that γ-H2AX and TRF2 did not significantly colocalize in **BYB**-treated cells (**Figure 4.7 L**), suggesting that **BYB** does not induce telomere DNA damage.

Some studies have revealed that mitochondrial dysfunction can lead to ferroptosis, which is closely linked to nuclear DNA damage.[15, 16] We have demonstrated that **BYB** induces mitochondrial dysfunction, calcium overload, elevated mtROS levels, and mtDNA damage. Importantly, mtDNA stress has the potential to activate the cGAS-STING pathway, which may result in autophagy-dependent ferroptotic cell death in cancer cells.[17, 18] The cGAS-STING pathway serves as an intracellular DNA sensing and stress signal transduction mechanism that detects free cytoplasmic DNA, including mitochondrial DNA, and triggers downstream inflammatory and immune

responses.[17] A recent study has shown that mtDNA depletion and oxidative DNA damage can activate the cGAS-STING pathway, initiating an immune response that may lead to ferroptosis.[18] Since that **BYB** causes mtDNA damage and that these damaged mtDNA fragments are released into the cytoplasm (**Figure 4.7 A**), it is possible that the cGAS-STING pathway may be activated. Western blot analysis revealed a significant upregulation of proteins associated with the cGAS-STING pathway, including cGAS, p-STING, p-TBK1, and p-IRF3, in **BYB**-treated HeLa cells (**Figure 4.8 A** and **B**). Collectively, these findings suggest that **BYB** may activate the cGAS-STING pathway, likely due to the mtDNA damage induced by **BYB**.

We then investigated iron overload in **BYB**-treated HeLa cells using live-cell imaging techniques. A commercially available Fe (II) fluorescent sensing probe, FerroOrange, was utilized to examine iron metabolism in cells. Our observations revealed numerous bright yellow-fluorescent spots (FerroOrange) in **BYB**-treated cells with a dose-dependent manner (**Figure 4.8 C**), suggesting that **BYB** may trigger ferroptosis in HeLa cells. Moreover, Western blot analysis indicated that **BYB** downregulates the expression of glutathione peroxidase (GPX4) in cells (**Figure 4.8 D** and **E**), further supporting the conclusion that **BYB** triggers ferroptosis. The induction of ferroptosis may elevate cellular levels of Fe (II) ions in HeLa cells. We have proved that **BYB** could increase the level of mtROS in HeLa cells, and mtROS mainly include hydrogen peroxide, so these Fe (II) ions could react with hydrogen peroxide to produce hydroxyl radicals through the Fenton reaction, which could lead to nuclear DNA damage.[16]

As we have demonstrated that **BYB** can induce mitochondrial calcium overload, increase mtROS levels, and trigger ferroptosis in HeLa cells, we hypothesize that mitochondrial calcium overload may be a primary contributor to DNA damage. To explore this, we examined the expression level of γ-H2A.x in HeLa cells using Western blot assays under two treatment conditions: co-treatment with **BYB** and DIDS sodium salt (to block calcium overload) and co-treatment with **BYB** and Mito-TEMPOL (to inhibit mtROS production). As shown in **Figure 4.8 F** and **G**, a significant reduction in γ-H2A.x expression was found only in cells co-treated with **BYB** and DIDS sodium salt. In contrast, the co-treatment of **BYB** and Mito-TEMPOL did not produce a substantial effect on γ-H2A.x levels. This suggests that mitochondrial calcium overload, which can be mitigated by DIDS sodium salt, is a najor factor in the downregulation of γ-H2A.x. On the other hand, we have also confirmed that **BYB**

induces ferroptosis, which may further enhance ROS production through the Fenton reaction, potentially leading to nuclear DNA damage. To address this, we used the antioxidant N-Acetylcysteine (NAC) to eliminate total ROS induced by **BYB** in the cells, including both mtROS and nuclear ROS. The results indicated a significant downregulation of γ-H2A.x following co-treatment with **BYB** and NAC (**Figure 4.8 H** and **I**), suggesting that ROS is a major trigger of nuclear DNA damage. Collectively, these findings implied that **BYB** may cause mitochondrial calcium overload, which likely contributes to mtROS production and ferroptosis. The resulting excess ROS may lead to damage in both mtDNA and nuclear DNA in **BYB**-treated HeLa cells through direct and/or indirect mechanisms that warrant further investigation.

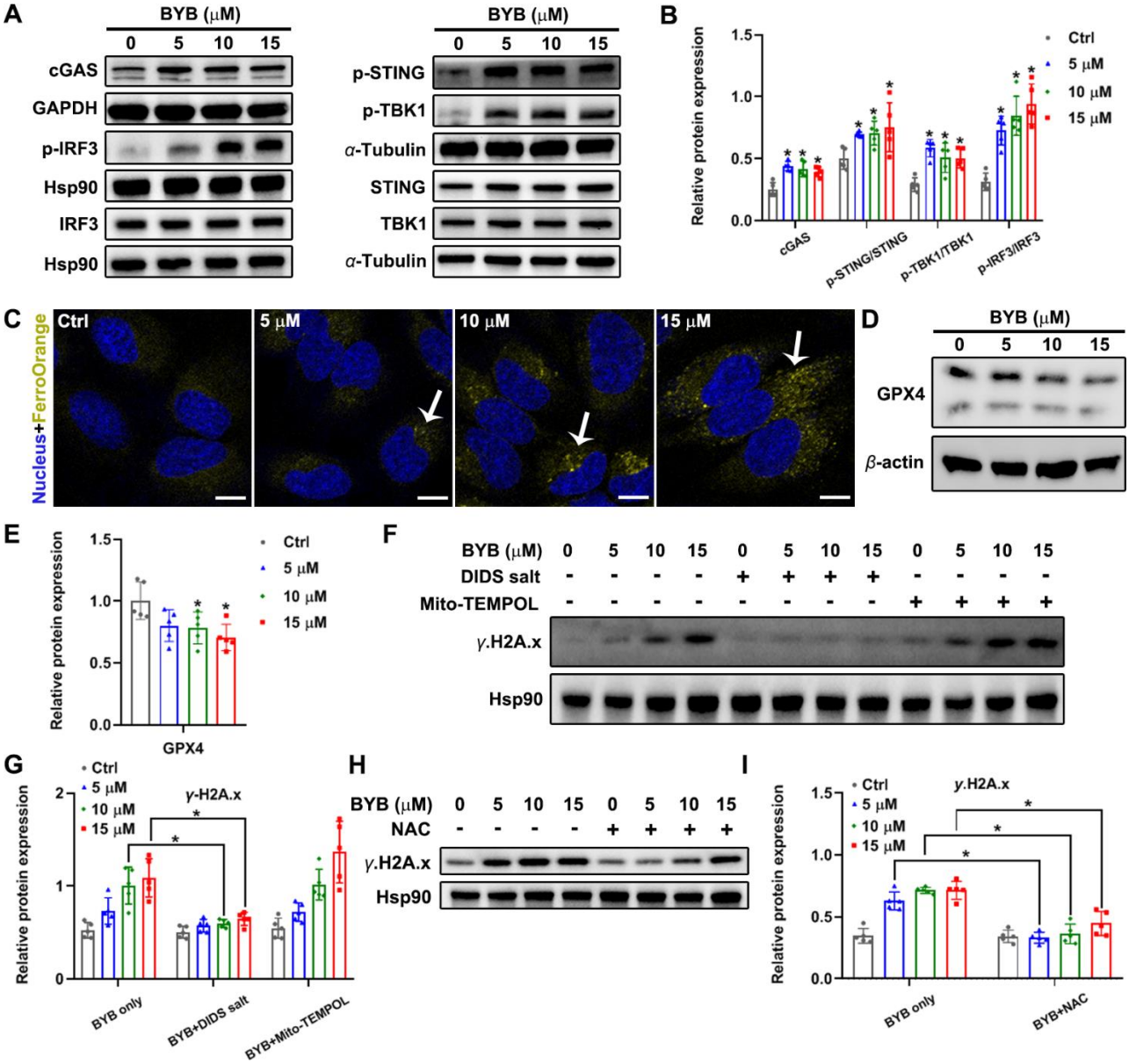

Figure 4.8. (A-B) Western blot assays to determine the translation of cGAS, STING, Phospho-STING, TBK1, Phospho-TBK1, IRF3, Phospho-IRF3 and GAPDH, α-Tubulin and Hsp90 in HeLa cells treated with **BYB** (0-15 μM) for 24 h (n=5). (C) Analysis of Fe^{2+} production in HeLa cells after **BYB** (0-15 μM) treatment for 24 h. The scale bar is 10 μm. (D-E) Western blot assays to determine

the translation of GPX4 and β-actin in HeLa cells treated with **BYB** (0-15 μM) for 24 h (n=5). (F-G) Western blot assays to determine the translation of γ-H2A.x and Hsp90 in **BYB**-treated (0-15 μM) HeLa cells with or without 150 μM DIDS sodium salt or 10 μM Mito-TEMPOL. The incubation time is 24 h (n=5). (H-I) Western blot assays to determine the translation of γ-H2A.x and Hsp90 in **BYB**-treated (0-15 μM) HeLa cells with or without 1 mM NAC. The incubation time is 24 h (n=5). The data are presented as mean ± SEM, and statistics were determined using ANOVA, $*p < 0.05$.

4.2.5 Study the effect of **BYB** in activating mitochondrial-controlled apoptosis pathway

Mitochondrial-controlled apoptosis is a regulated form of programmed cell death primarily governed by the mitochondria.[19] This pathway can be activated by various intracellular signals, including mtDNA damage, mitochondrial calcium overload, and cellular stress. Given that **BYB** may induce mitochondrial calcium overload and mtDNA damage in HeLa cells, these cellular changes could activate mitochondrial-controlled apoptosis. A critical event in this process is the release of cytochrome c from the mitochondria into the cytoplasm. Once released, cytochrome c facilitates the formation of the apoptosome, which subsequently activates pro-Caspase-9, leading to the activation of effector caspases.[20] Additionally, Smac, an endogenous inhibitor of caspases, may also be released from mitochondria into the cytoplasm during the activation of mitochondrial-controlled apoptosis.[21]

Western blot analysis indicated a significant increase in the expression levels of cytochrome c and Smac in the cytosolic fraction, while their levels in the mitochondrial fraction were markedly reduced in **BYB**-treated cells (**Figure 4.9 A-D**). These results suggest that **BYB** activates the mitochondrial-controlled apoptosis pathway in HeLa cells. Furthermore, staining HeLa cells with Annexin V-647 and 7-AAD revealed that **BYB** induced both apoptosis and necrosis, increasing from 6.6% to 78.7% in a concentration-dependent manner after 24 hours of treatment (**Figure 4.9 E**). Interestingly, necrosis constituted the majority of these effects, accounting for approximately 61%. Western blot assays also showed that in the **BYB**-treated HeLa cells, the mitochondrial-controlled apoptosis pathway related pro-apoptotic proteins including Bax, Cleaved-caspase9, Cleaved-caspase3, and Cleaved-PARP were upregulated, while the anti-apoptotic protein Bcl2 was downregulated (**Figure 4.9 F** and **G**).

Since we have demonstrated that **BYB** primarily causes mitochondrial calcium overload in HeLa cells, which may serve as a major trigger for mtROS production and mtDNA damage, we speculate that this calcium overload could be the key factor in activating the mitochondrial-controlled apoptotic

pathway. From **Figure 4.9 E**, co-treatment with **BYB** and DIDS sodium salt significantly reduced apoptosis and necrosis compared to treatment with **BYB** alone. In contrast, co-treatment with **BYB** and Mito-TEMPOL did not lead to a reduction in apoptosis or necrosis and was similar to the effects of **BYB** treatment alone. These findings suggest that the mitochondrial calcium overload induced by **BYB** is a primary contributor to the activation of the mitochondrial-controlled apoptotic pathway. Moreover, the levels of mitochondrial-controlled apoptosis-related proteins, including Cleaved-PARP, Cleaved-caspase-9, and Cleaved-caspase-3, were remarkably decreased in HeLa cells after co-treatment with **BYB** and DIDS sodium salt. However, these proteins were significantly upregulated with either **BYB** treatment alone or in conjunction with Mito-TEMPOL (**Figure 4.9 H** and **I**).

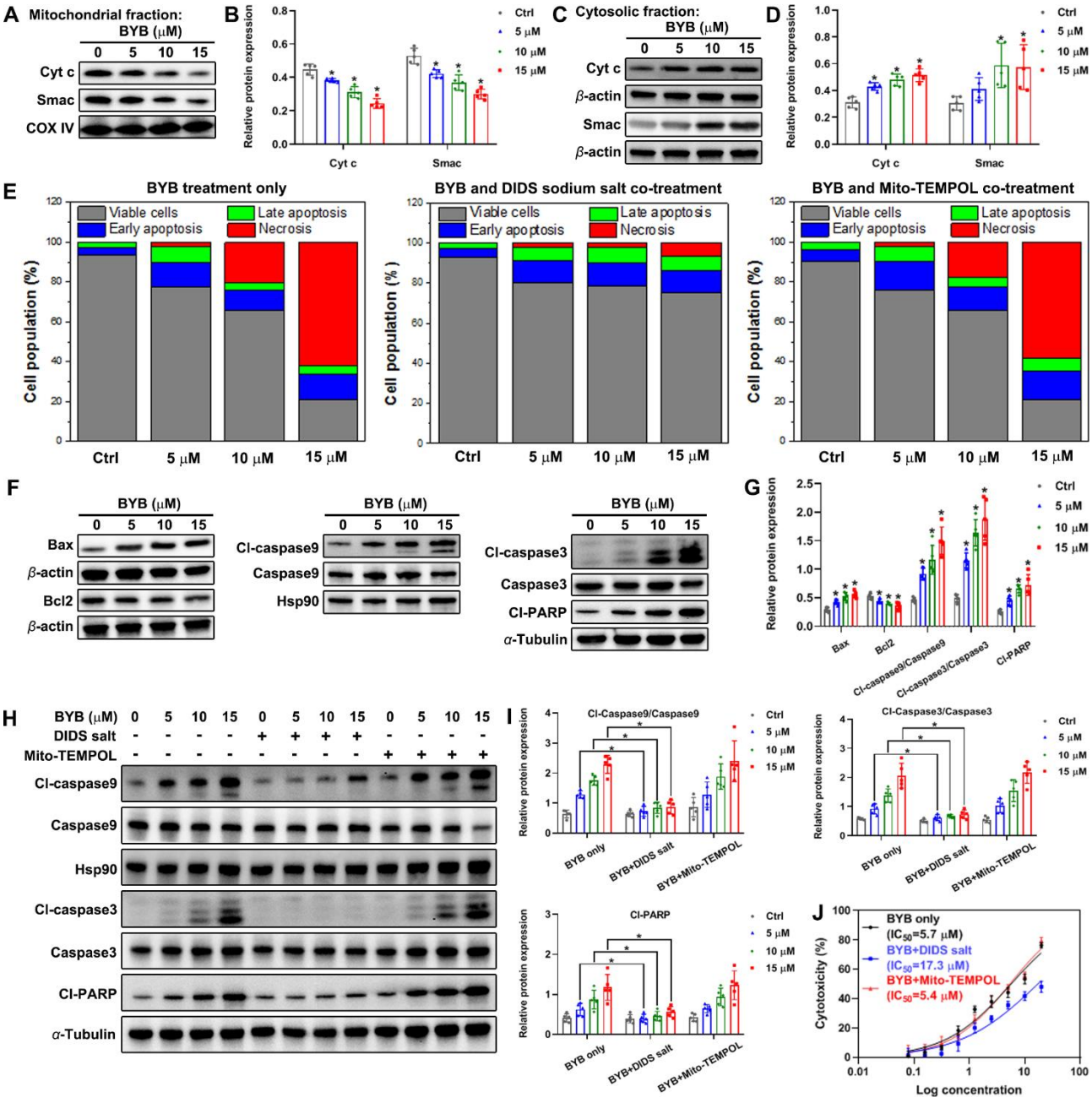

Figure 4.9. (A-B) Western blot assays to determine the translation of cytochrome c, Smac and COX IV in mitochondrial fractions of HeLa cells after **BYB** (0-15 μM) treatment for 24 h (n=5). (C-D) Western blot assays to determine the translation of cytochrome c, Smac and *β*-actin in cytosolic fractions of HeLa cells after **BYB** (0-15 μM) treatment for 24 h (n=5). (E) Cell apoptosis analysis of **BYB**-treated HeLa cells with or without 150 μM DIDS sodium salt or 10 μM Mito-TEMPOL. The concentration of **BYB** is 0-15 μM. The incubation time is 24 h. The cells were stained by Annexin V-647 and 7-AAD. (F-G) Western blot assays to determine the translation of Bax, Bcl2, Caspase9, Cleaved-caspase9, Caspase3, Cleaved-caspase3, Cleaved-PARP, *β*-actin, *α*-Tubulin and Hsp90 in HeLa cells after **BYB** (0-15 μM) treatment for 24 h (n=5). (H-I) Western blot assays to determine the translation of Caspase9, Cleaved-caspase9, Caspase3, Cleaved-caspase3, Cleaved-PARP, *α*-Tubulin and Hsp90 in **BYB**-treated HeLa cells with or without 150 μM DIDS sodium salt or 10 μM Mito-TEMPOL. The concentration of **BYB** is 0-15 μM. The incubation time is 24 h (n=5). (J) Crystal violet assay was used to study the antiproliferation activity of **BYB** with or without 150 μM DIDS sodium salt or 10 μM Mito-TEMPOL to HeLa cells after 48 h treatment (n=5). The data are presented as mean ± SEM, and statistics were determined using ANOVA, $*p < 0.05$.

Furthermore, the crystal violet assay demonstrated that co-treatment with **BYB** and DIDS sodium salt significantly reduced antiproliferative activity against HeLa cells (IC_{50} = 17.3 μM), compared to **BYB** treatment alone (IC_{50} = 5.7 μM) and the combination of **BYB** and Mito-TEMPOL (IC_{50} = 5.4 μM) (**Figure 4.9 J**), suggesting that the inhibition of mitochondrial calcium overload induced by **BYB** in the presence of DIDS sodium salt markedly diminishes the antiproliferative effects of **BYB** in HeLa cells. This result further suggest **BYB**-induced mitochondrial calcium overload is the major factor in triggering cell death in HeLa cells.

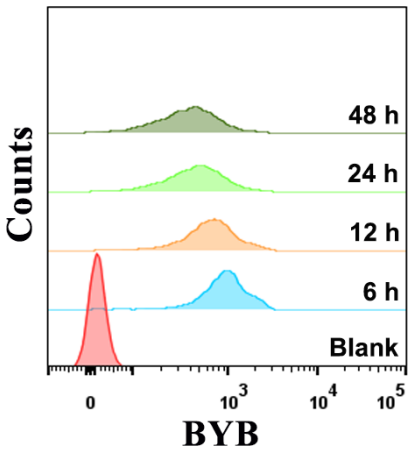

Figure 4.10. HeLa cells treated with **BYB** were analyzed by flow cytometry at different time point. The concentration of **BYB** was 2 μM.

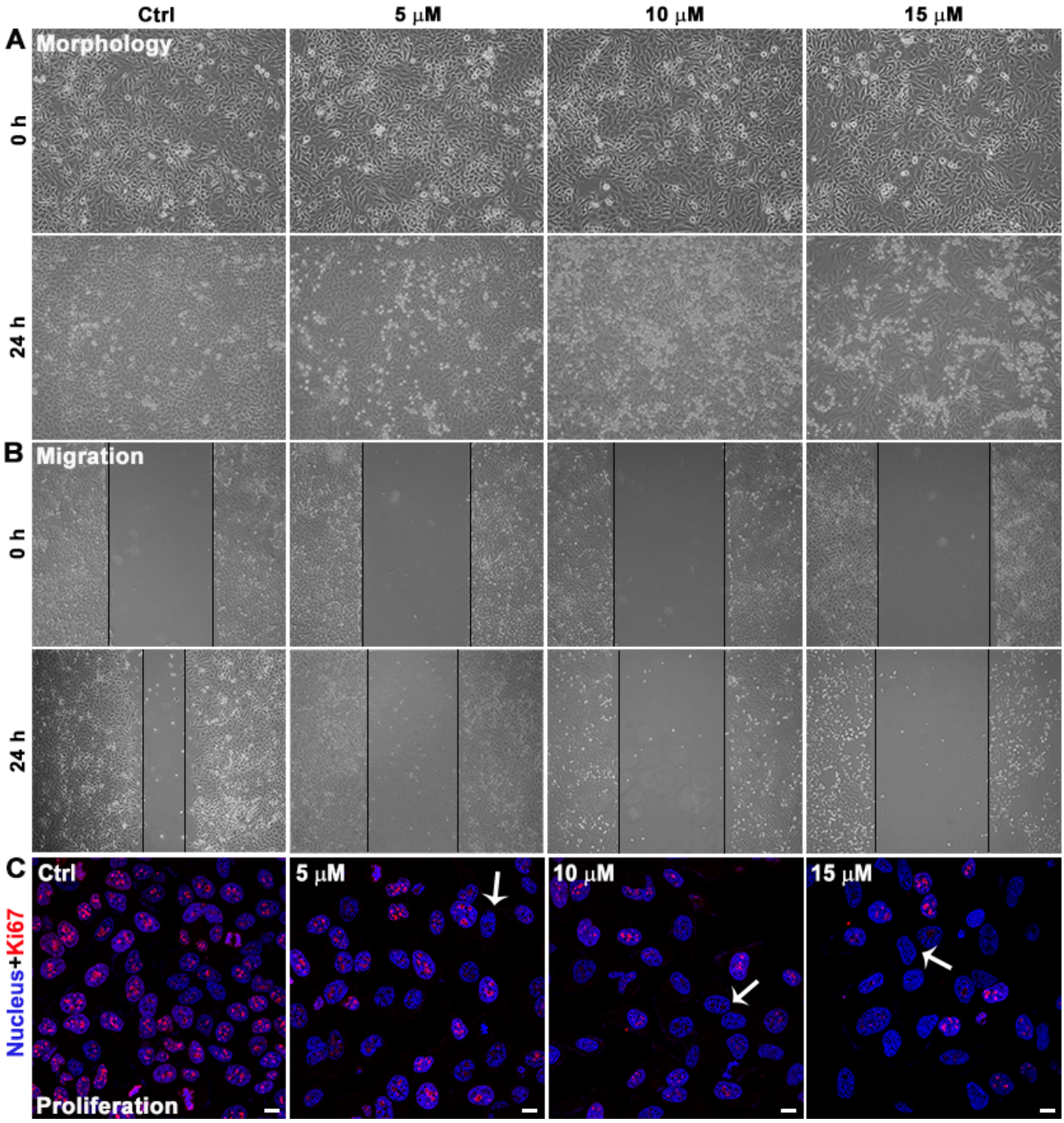

Figure 4.11. (A) The study of cell morphology of HeLa cells treated with **BYB** (0-15 μM) for 24 h. (B) The migration of HeLa cells treated with **BYB** (0-15 μM) for 24 h. (C) Immunofluorescent analysis of Ki67 (Red, λ_{ex}=635 nm) in HeLa cells after **BYB** (0-15 μM) treatment for 24 h. The cell nucleus was indicated by DAPI (Blue, λ_{ex}=405 nm). The scale bar is 10 μm.

4.2.6 Study the antitumor efficacy of **BYB** *in vitro* and *in vivo*

To further evaluate the **in vitro** antitumor activity of **BYB**, which may lead to mitochondrial calcium overload and subsequent cancer cell death, several experiments were performed. Initially, we analyzed the cell membrane permeability of **BYB** (2 μM) in HeLa cells using flow cytometry. As shown in **Figure 4.10**, **BYB** was detected in most cells after being treated for 6 hours, demonstrating its effective membrane permeability. Subsequently, we examined the effect of **BYB** on the

morphology and migration of HeLa cells. According to **Figure 4.11 A**, the morphology of HeLa cells treated with **BYB** showed significant alterations compared to the control group, with a notable increase in cell death. Additionally, **BYB** significantly inhibited cell migration, as shown in **Figure 4.11 B**. Furthermore, we observed a clear reduction in the cell proliferation marker Ki67 in **BYB**-treated HeLa cells, which was dependent on the concentration of **BYB** (**Figure 4.11 C**). These results indicate that **BYB** effectively suppresses the growth of HeLa cells.

The pharmacokinetic properties of **BYB** were investigated in Sprague–Dawley rats following a tail vein injection at a dose of 1 mg/kg. As shown in **Figure 4.12** and **Table 4-1**, **BYB** demonstrated favorable pharmacokinetic (PK) profiles, characterized by high plasma exposure ($AUC_{0-\infty}$ = 109 h*ng/mL) and a suitable half-life ($T_{1/2}$=1.93 h). Moreover, **BYB** was almost entirely metabolized within approximately 4 hours, suggesting that it can be cleared from the body within this timeframe, thereby potentially reducing *in vivo* adverse reactions and side effects associated with the ligand.

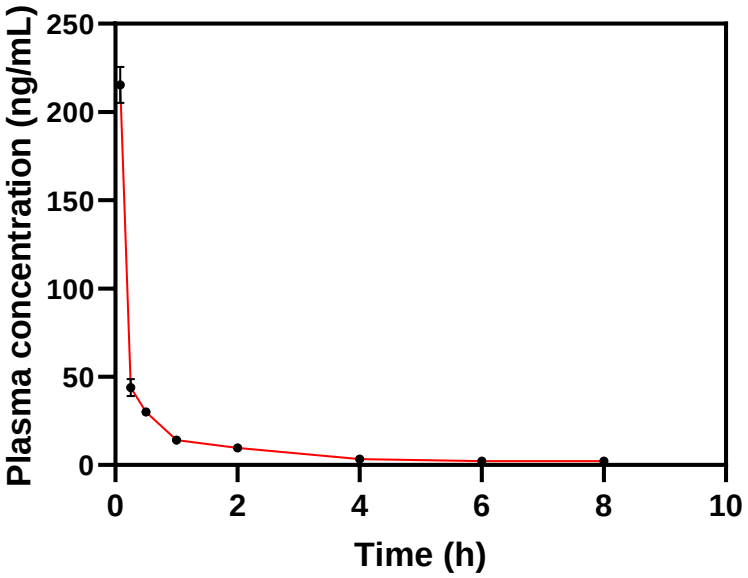

Figure 4.12. Mean blood concentration–time profiles of compound **BYB** in Sprague–Dawley rats after tail vein injection (1 mg/kg) (n = 3). The data are presented as mean ± SEM.

Table 4-1. The pharmacokinetic property of ligand **BYB** in rats.[a]

Parameter	Unit	Rat 1	Rat 2	Rat 3	Mean±SD
$T_{1/2}$[b]	h	2.58	0.99	2.23	1.93±0.84
C_0	ng/mL	501	491	442	478±31
AUC_{0-t}[c]	h*ng/mL	106	92	110	103±9
$AUC_{0-\infty}$	h*ng/mL	115	96	116	109±11
AUC Extrapolated	%	7.3	3.6	5.8	6±2
CL[d]	mL/h/kg	8726	10434	8597	9252±1025
$MRT_{0-\infty}$[e]	h	1.87	0.80	1.80	1.49±0.60
Vd[f]	mL/kg	32467	14875	27624	24989±9088

[a] The ligand dose was 1 mg/kg by tail vein injection; [b] Plasma elimination half-life; [c] Plasma exposure; [d] Clearance rate; [e] Mean residence time; [f] Apparent volume of distribution.

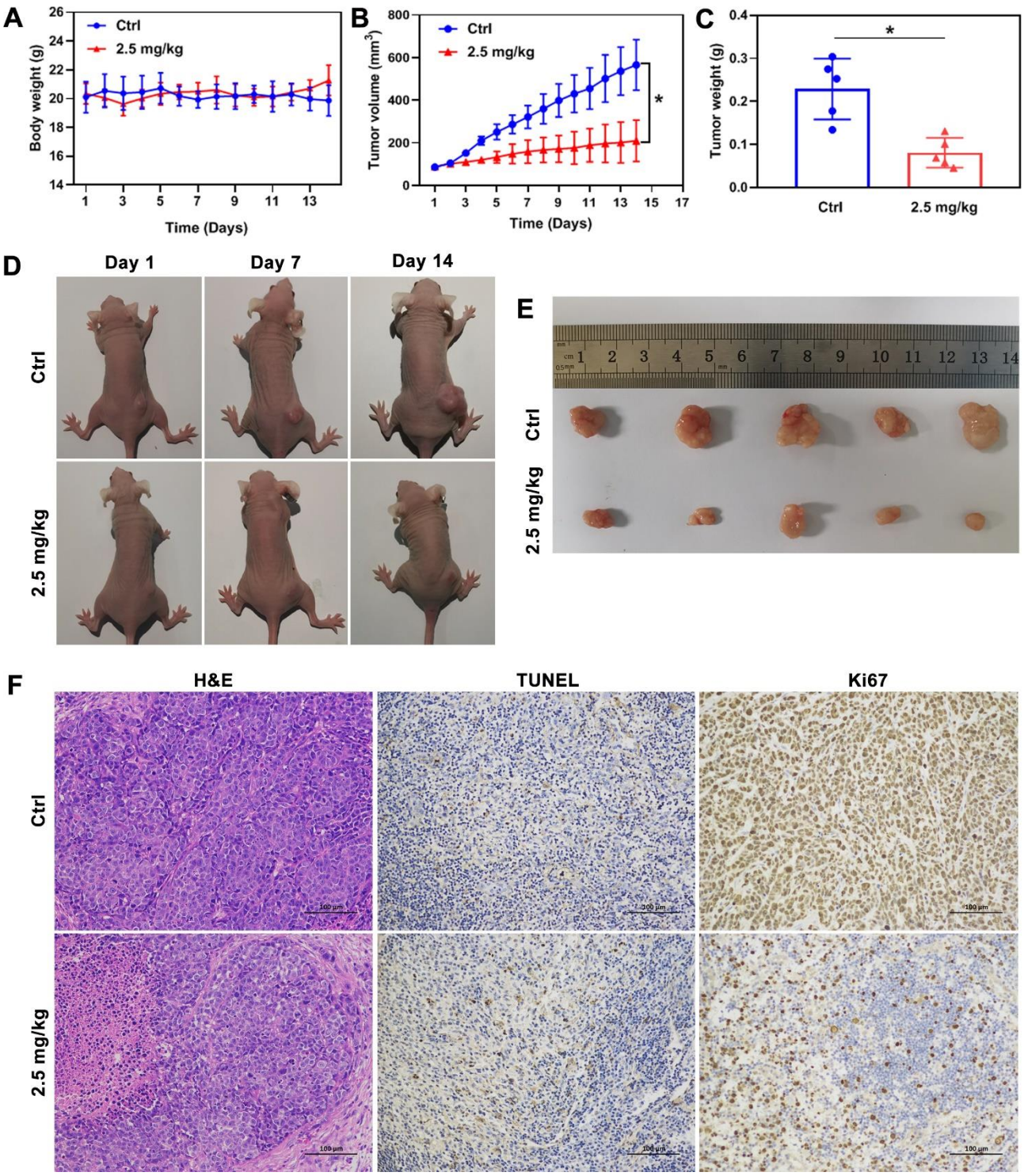

Figure 4.13. The antitumor efficacy of **BYB** in a mouse xenograft model of cervical cancer. (A) Body weight change of HeLa tumor-bearing nude mice injected with PBS (Group 1) or **BYB** (2.5 mg/kg, Group 2) in tail vein over 14 days (n = 5). (B) Time-dependent change of tumor volume after different treatments for 14 days. (C) Weight of isolated tumors in HeLa tumor-bearing nude mice after 14 days of treatment. (D) Digital photographs of different groups of HeLa tumor-bearing nude mice on day 1, day 7 and day 14. (E) Digital photographs of isolated tumors from different groups of HeLa-bearing nude mice after 14 days. The scale bar is 100 μm. (F) Representative histological images of Ki67, TUNEL and H&E antigen immunofluorescence-stained tumor tissue sections of HeLa tumor-bearing nude mice tumors from different groups after 14 days of treatment. The scale bar is 100 μm. The data are presented as mean ± SEM, and statistics were determined using ANOVA, $*p < 0.05$.

Then the *in vivo* antitumor efficacy of **BYB** using a cervical cancer (HeLa) xenograft mouse model was studied. Two groups of female Balb/c nude mice bearing HeLa tumors, with 5 mice in each group, were used: Group 1 received PBS, and Group 2 was treated with **BYB** at a dose of 2.5 mg/kg. The treatments were administered intravenously every two days. Throughout the study, there were no significant changes in body weight for either group (**Figure 4.13 A**), and all mice in both groups survived until day 14. Tumor growth in the control group was rapid (**Figure 4.13 B-E**), whereas in the **BYB**-treated group, tumor growth was significantly suppressed. Compared to the control group, the tumor volume decreased by 58.3% (**Figure 4.13 B**), and the tumor weight was reduced by 64.6% following **BYB** treatment (**Figure 4.13 C**).

To further explore the inhibitory effects of **BYB** on tumor growth, we analyzed tumor tissues from both groups of mice (Group 1 and Group 2) as shown in **Figure 4.13 F**. Compared to the control group, the H&E images revealed noticeable nuclear sequestration and fragmentation. Additionally, TUNEL staining indicated that **BYB** enhanced apoptosis in tumor cells. Ki67 staining assays further demonstrated that **BYB** effectively inhibited tumor cell proliferation. Overall, these *in vivo* findings suggest that **BYB** possesses significant antitumor activity against cervical cancer.

To assess the biocompatibility and *in vivo* toxicity of **BYB**, whole blood samples were collected for biochemical analysis when the mice were killed on day 14. The analysis included various biochemical parameters such as white blood cell count (WBC), lymphocyte count (Lymph), monocyte count (Mon), neutrophil count (Gran), red blood cell count (RBC), hemoglobin (HGB), hematocrit, mean red blood cell volume (MCV), mean red blood cell hemoglobin content (MCH), mean red blood cell hemoglobin concentration (MCHC), mean platelet volume (MPV), platelet count (PLT), and platelet volume distribution width (PDW). The findings, presented in **Figure 4.14 A**, showed no significant differences in these parameters between the **BYB**-treated mice and the control group. These results suggest that **BYB** has high in vivo biocompatibility and low toxicity. Besides, **BYB** at a dose of 2.5 mg/kg did not induce pathological changes in major organs, including the heart, liver, spleen, lung, and kidney (**Figure 4.14 B**). Consequently, **BYB** appears to be a promising anticancer agent with excellent biocompatibility and minimal toxicity.

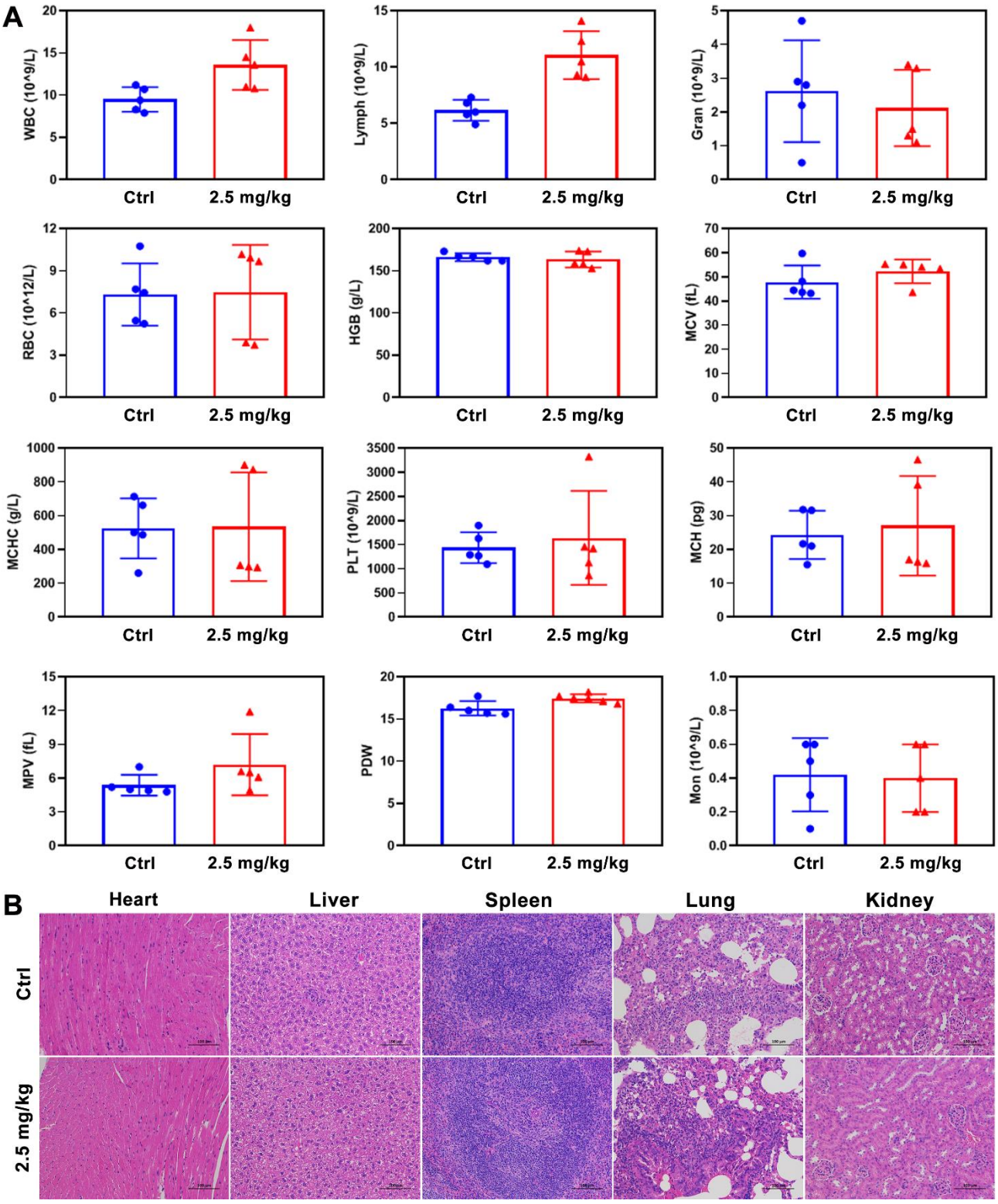

Figure 4.14. The *in vivo* effects of **BYB** on tissues and blood of nude mice. (A) Biochemical blood analysis of the ligands-treated mice 14 days post-injection under various conditions (n=5, mean ± SD). (B) H&E-stained images of the major organs (heart, liver, spleen, lung, and kidney) from different groups. The scale bar is 200 μm.

4.3 Summary

In summary, we found that the G4-mtDNA binding ligand **BYB** can significantly inhibit the mtDNA replication and then downregulate the transcription of most mitochondrial respiratory chain related genes including *ND1*, *ND4*, *ND4L*, *ND5*, *COX2*, *COX3*, *CYTB*, *ATP6* and *ATP8,* which resulted in the impeded assembly of the respiratory chain complex (I-IV) in human cervical cancer HeLa cells. Subsequently, several interesting cellular events occur in cancer cells, including leading to mitochondrial dysfunction, inhibition of ATP production, and elevated mtROS production, as well as induction of mitophagy, mitochondrial calcium overload, iron metastasis, mtDNA and nuclear DNA damage, and apoptosis. Despite the mechanisms to all these cellular events observed in **BYB**-treated HeLa cells are unclear at present, it seems that the induced mitochondrial calcium overload, ferroptosis and nuclear DNA damage may have certain interrelationship that needs to be further investigated. In addition, the *in vivo* antitumor efficacy of **BYB** in a HeLa cell xenograft tumor model was further validated. The ligand at 2.5 mg/kg was able to reduce the tumor weight by 64.6% compared to the control. In general, **BYB** exhibited high *in vivo* antitumor efficacy and low toxicity.

Based on the cell-based experimental results obtained thus far, we presumably speculate that **BYB** causes remarkable mitochondrial dysfunction and reduction of ATP production and consequently, mitochondrial calcium overload may possibly be trigger in the **BYB**-treated HeLa cells. Then, mitochondrial calcium overload may elevate mtROS production in the cells and thus, oxidative stress may cause mtDNA damage and mitophagy. The markedly induced mtDNA stress in **BYB**-treated HeLa cells may probably trigger ferroptosis to cause cell death. Moreover, the increased concentration of ferrous irons in cells may mediate Fenton reaction and contribute to the generation of ROS that causes nuclear DNA damage. A proposed anticancer mechanism is shown in **Figure 4.15.**

To the best of our knowledge, this is the first study targeting G4-mtDNAs with G4-mtDNA ligand to induce mitochondrial calcium overload and then cause cell death. Currently, the induction of mitochondrial calcium overload and ferroptosis in cancer cells has been a hot research area, to develop effective strategy to induce mitochondrial calcium overload in cancer cells may show great potential to treat multifarious cancers with high efficiency and low drug resistance induction. Therefore, this study may provide new insights into drug discovery targeting G4-mtDNA and induce mitochondrial calcium overload.

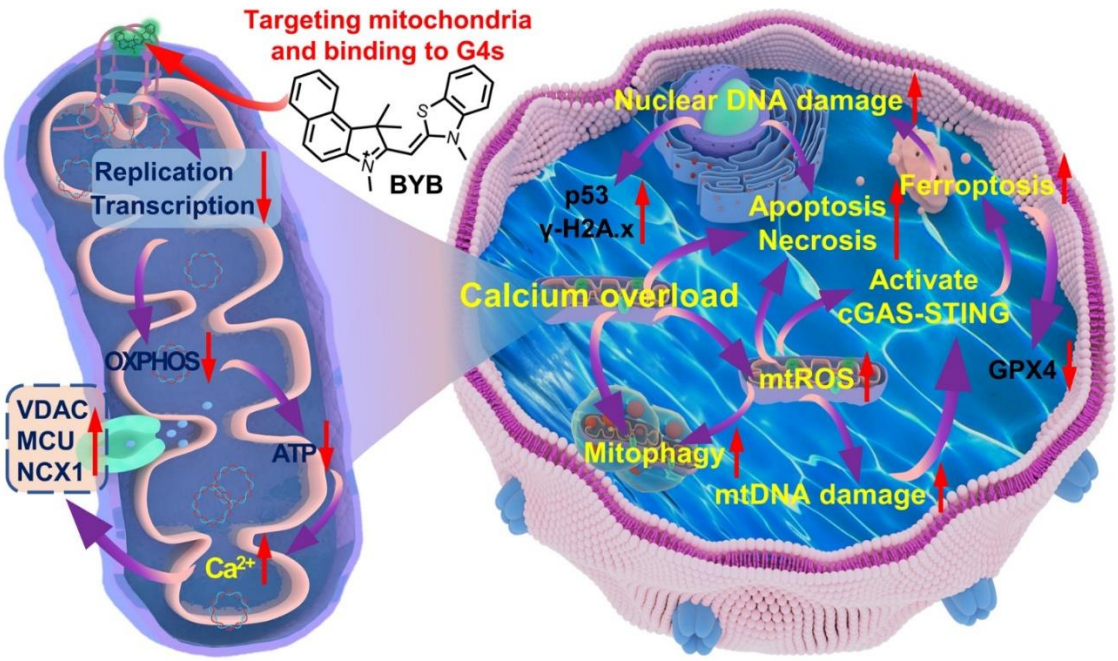

Figure 4.15. The proposed anticancer mechanism of ligand **BYB** in human HeLa cells.

4.4 References

[1] L.D. Popov, Mitochondrial biogenesis: An update, J Cell Mol Med 24(9) (2020) 4892-4899.

[2] C. Cantó, K.J. Menzies, J. Auwerx, NAD(+) Metabolism and the Control of Energy Homeostasis: A Balancing Act between Mitochondria and the Nucleus, Cell Metab 22(1) (2015) 31-53.

[3] S.J. Annesley, P.R. Fisher, Mitochondria in Health and Disease, Cells 8(7) (2019).

[4] F. Jaña, G. Bustos, J. Rivas, P. Cruz, F. Urra, C. Basualto-Alarcón, E. Sagredo, M. Ríos, A. Lovy, Z. Dong, O. Cerda, M. Madesh, C. Cárdenas, Complex I and II are required for normal mitochondrial Ca^{2+} homeostasis, Mitochondrion 49 (2019) 73-82.

[5] G.S. Williams, L. Boyman, W.J. Lederer, Mitochondrial calcium and the regulation of metabolism in the heart, J Mol Cell Cardiol 78 (2015) 35-45.

[6] B. Glancy, W.T. Willis, D.J. Chess, R.S. Balaban, Effect of calcium on the oxidative phosphorylation cascade in skeletal muscle mitochondria, Biochemistry 52(16) (2013) 2793-809.

[7] H. Chen, W. Gao, Y. Yang, S. Guo, H. Wang, W. Wang, S. Zhang, Q. Zhou, H. Xu, J. Yao, Z. Tian, B. Li, W. Cao, Z. Zhang, Y. Tian, Inhibition of VDAC1 prevents Ca^{2+}-mediated oxidative stress and apoptosis induced by 5-aminolevulinic acid mediated sonodynamic therapy in THP-1 macrophages, Apoptosis 19(12) (2014) 1712-26.

[8] D.E. Clapham, Calcium signaling, Cell 131(6) (2007) 1047-58.

[9] V. Vanderheyden, B. Devogelaere, L. Missiaen, H. De Smedt, G. Bultynck, J.B. Parys, Regulation

of inositol 1,4,5-trisphosphate-induced Ca2+ release by reversible phosphorylation and dephosphorylation, Biochim Biophys Acta 1793(6) (2009) 959-70.

[10] S. Marchi, M. Marinello, A. Bononi, M. Bonora, C. Giorgi, A. Rimessi, P. Pinton, Selective modulation of subtype III IP_3R by Akt regulates ER Ca^{2+} release and apoptosis, Cell Death Dis 3(5) (2012) e304.

[11] G.S. Supinski, L. Wang, E.A. Schroder, L.A.P. Callahan, MitoTEMPOL, a mitochondrial targeted antioxidant, prevents sepsis-induced diaphragm dysfunction, Am J Physiol Lung Cell Mol Physiol 319(2) (2020) L228-l238.

[12] Q. Li, L. Yang, K. Wang, Z. Chen, H. Liu, X. Yang, Y. Xu, Y. Chen, Z. Gong, Y. Jia, Oxidized mitochondrial DNA activates the cGAS-STING pathway in the neuronal intrinsic immune system after brain ischemia-reperfusion injury, Neurotherapeutics 21(4) (2024) e00368.

[13] W. Zhang, G. Li, R. Luo, J. Lei, Y. Song, B. Wang, L. Ma, Z. Liao, W. Ke, H. Liu, W. Hua, K. Zhao, X. Feng, X. Wu, Y. Zhang, K. Wang, C. Yang, Cytosolic escape of mitochondrial DNA triggers cGAS-STING-NLRP3 axis-dependent nucleus pulposus cell pyroptosis, Experimental & Molecular Medicine 54(2) (2022) 129-142.

[14] B.X. Zheng, J. Yu, W. Long, K.H. Chan, A.S. Leung, W.L. Wong, Structurally diverse G-quadruplexes as the noncanonical nucleic acid drug target for live cell imaging and antibacterial study, Chem Commun (Camb) 59(11) (2023) 1415-1433.

[15] R. She, D. Liu, J. Liao, G. Wang, J. Ge, Z. Mei, Mitochondrial dysfunctions induce PANoptosis and ferroptosis in cerebral ischemia/reperfusion injury: from pathology to therapeutic potential, Front Cell Neurosci 17 (2023) 1191629.

[16] D. Chen, C. Zhao, J. Zhang, C.W.J. Knol, A. Osipyan, N.a. Majerníková, T. Chen, Z. Xiao, J. Adriana, A.J. Griffith, A.S. Gamez, P.E. van der Wouden, R.P. Coppes, A.M. Dolga, H.J. Haisma, F.J. Dekker, Small Molecule MIF Modulation Enhances Ferroptosis by Impairing DNA Repair Mechanisms, Advanced Science 11(32) (2024) 2403963.

[17] K.P. Hopfner, V. Hornung, Molecular mechanisms and cellular functions of cGAS-STING signalling, Nat Rev Mol Cell Biol 21(9) (2020) 501-521.

[18] C. Li, Y. Zhang, J. Liu, R. Kang, D.J. Klionsky, D. Tang, Mitochondrial DNA stress triggers autophagy-dependent ferroptotic death, Autophagy 17(4) (2021) 948-960.

[19] L.A. Pradelli, M. Bénéteau, J.-E. Ricci, Mitochondrial control of caspase-dependent and -independent cell death, Cellular and Molecular Life Sciences 67(10) (2010) 1589-1597.

[20] X. Jiang, X. Wang, Cytochrome C-Mediated Apoptosis, Annual Review of Biochemistry 73(Volume 73, 2004) (2004) 87-106.

[21] C. Du, M. Fang, Y. Li, L. Li, X. Wang, Smac, a Mitochondrial Protein that Promotes Cytochrome c–Dependent Caspase Activation by Eliminating IAP Inhibition, Cell 102(1) (2000) 33-42.

Chapter 5. The discovery of mitochondrial DNA G-quadruplex-targeting di-cationic small-sized lipophilic ligands for anticancer study

5.1 Synopsis

G-rich DNA sequences in mitochondria may fold into G4 structures. These structures may play important regulatory roles for mitochondrial functions. To gain deeper insights into the roles of G4-mtDNAs and their interactions with G4 ligands both *in vitro* and intracellularly, we designed and synthesized a series of novel G4-mtDNA ligands for further investigation. We conducted *in vitro* and cellular bioassays to examine the selectivity of these newly developed ligands targeting G4-mtDNAs, their cellular localization in living cells, and their cytotoxic effects on a panel of human cancer cell lines.

5.2 Design of di-cationic small-sized lipophilic ligands targeting mitochondria and G4-mtDNAs

Mitochondria are special organelles, and comprehending their structural characteristics is vital for the effective design of fluorescent ligands. Central to the process of mitochondrial energy transfer is the proton pump, which plays a crucial role in generating the proton gradient necessary for ATP synthesis. As protons are transported from the mitochondrial matrix into the intermembrane space, this movement creates a positive charge within the intermembrane space while leaving the matrix negatively charged. This charge separation leads to the establishment of a substantial negative mitochondrial membrane potential (MMP, $\Delta\Psi m$), typically around −150 to -180 mV.[1-3] For this reason, most fluorescent ligands that target mitochondria contain lipophilic cations.

Triphenylphosphine (TPP^+) is the most widely used molecule for designing mitochondria-selective ligands for cancer therapy delivery.[4, 5] TPP^+-based drugs have mitochondrial membrane targeting; however, there is a lack of ligand designs based on lipophilic small-sized molecular scaffolds with multiple positive charges that target mitochondria with high mitochondrial membrane potential. In addition, it was shown that the mitochondrial membrane potential difference was higher in tumor cells compared to normal cells, with a difference of about 60 mV between them,[1, 2, 4] implying that the more negative MMP of tumor cells may have a stronger ability to drive more multi-positively charged and small-sized ligands into the mitochondria. Taking the advantage of this property, small-sized ligands with multiple positive charges may be more enriched in the mitochondria of tumor cells and less in normal cells, which may facilitate the targeting of antitumor drugs and reduce the side

effects of the drugs. Based on the membrane potential properties of mitochondria in cancer cells, we design ligands with two positive charges to improve its mitochondrial targeting ability.

Thiazole Orange (TO) is a classical nucleic acid probe that has been shown to bind G4-DNAs intracellularly, but it also has a high affinity for double-stranded DNAs.[6] Thus it is commonly utilized as a nonspecific nucleic acid dye. To reduce the affinity of TO for double-stranded DNAs and increase its selectivity towards G4s, many researchers have structurally modified TO, resulting in a series of TO derivatives that are selectively binding to G4-DNAs.[7-10] During the structural modification process, the quinolinium scaffold are often preserved, suggesting that the quinolinium scaffold may be crucial to facilitate the interaction of the ligand with G4s. In addition, it was found that the selectivity of the ligand could be effectively improved by introducing a styryl group to the quinolinium scaffold.[7-10] In our previous study, we also synthesized a series of quinolinium derivatives and confirmed that these derivatives have higher selectivity for G4-DNAs and lower affinity for double-stranded DNAs.[7-10] Therefore, in designing the G4-mtDNA ligands, we employed quinolinium as the basic molecular scaffold for structural modification.

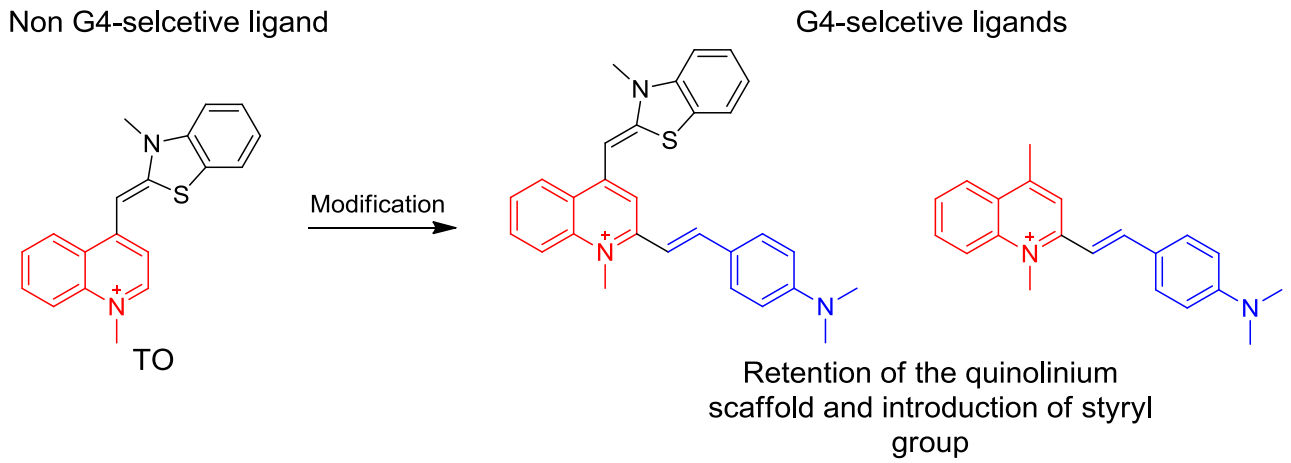

Figure 5.1. Diagram showing the molecular structure of non-G4-selective ligand TO and a strategy for structural modification of TO ligand to enhance G4 selectivity, where the quinolinium scaffold and the styryl group are shown in red and blue, respectively.

Currently, most G4 ligands reported are mono-cationic and nonspecific to mitochondria.[11, 12] Thus, the ligand also enters the nucleus and/or other organelles in living cells. Considering the unique feature of high MMP of mitochondria and the role of the quinolinium scaffold in the design of G4 ligands, we rationally designed a series of lipophilic ligands bearing two cationic quinolinium

scaffolds that were bridged with a flexible alkyl chain to enhance the cellular selectivity in targeting mitochondria. In addition, the quinolinium scaffold was further integrated with a styryl moiety to optimize the G4-selectivity of the ligand. The integration of molecular scaffolds was achieved via a rigid but rotatable ethylene bridge. The two π-conjugated scaffolds may form a coplanar structure upon interaction with targeted G4s and then the adduct can generate intensive fluorescence for real-time imaging and monitoring G4s in living cells.[13] To the best of our knowledge, there are no such small-sized, di-cationic, mitochondria-selective and G4-targeting ligands reported.

5.3 Results and discussion

5.3.1 Synthesis and characterization of di-cationic small-sized lipophilic ligands

The general synthetic procedures to the ligands are described in Chapter 7, Section 7.3.1. The synthetic routes and molecular structures of the target ligands are shown in **Figure 5.2** and **Figure 5.3**. All ligands obtained were characterized by ^{1}H NMR, ^{13}C NMR and HRMS, and the purity were determined by HPLC. The detailed characterizations for the ligands are given in the section of Appendix, **Figure S8-S17**.

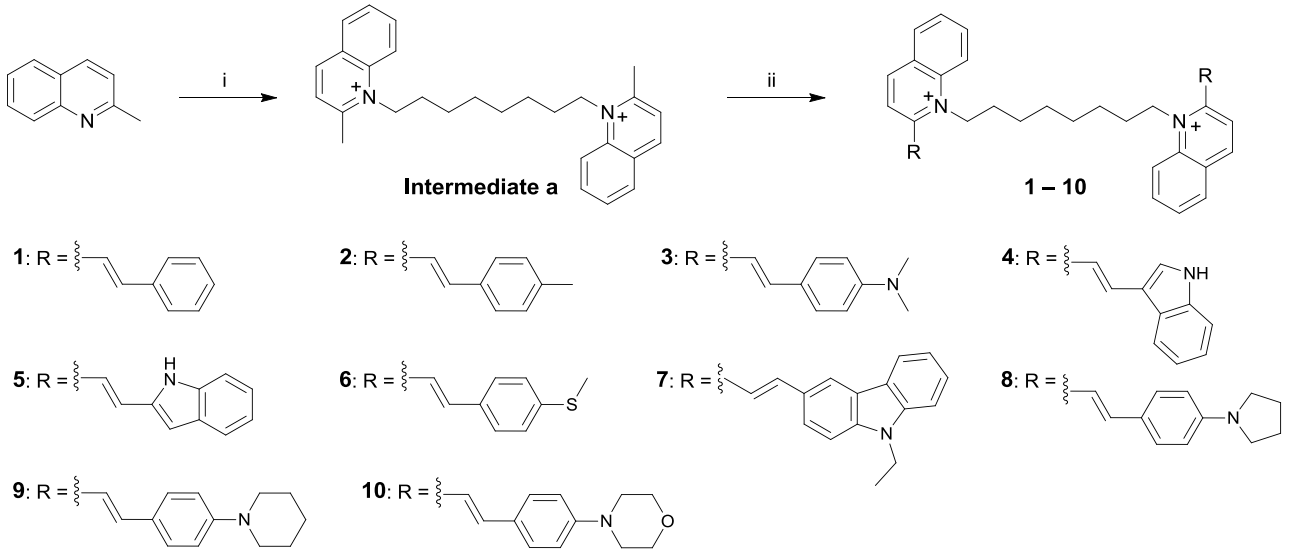

Figure 5.2. Synthetic routes to new di-cationic compounds **1–10**. Reaction conditions: (i) 1,8-diiodooctane, ethanol, 100 °C, 24 h; (ii) Selected aldehyde, ethanol, 4-methylpiperidine, 100 °C, overnight.

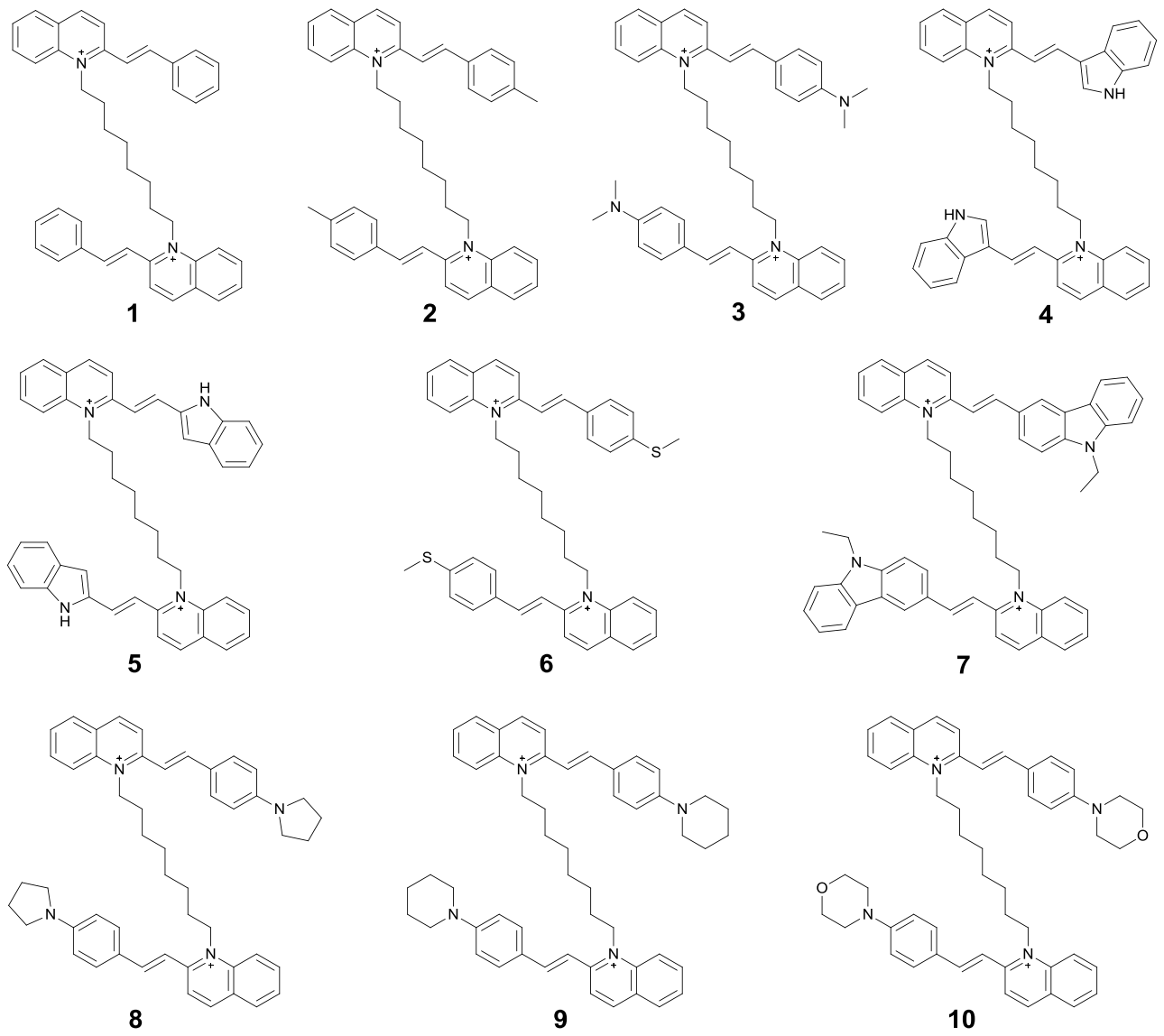

Figure 5.3. Molecular structures of the new di-cationic ligands **1–10** synthesized in the present study.

5.3.2 Screening for di-cationic ligands that target G4-mtDNAs and are toxic to cancer cells

Studies have shown that G4-mtDNAs may have an important regulatory role and are strongly associated with cancer development. The development of fluorescent ligands that can specifically target G4-mtDNAs can provide a powerful tool to study the regulatory role of G4-mtDNAs, which is one of the objectives of this study. In addition to this, another aim of this study is to investigate whether G4-mtDNAs could be the anti-tumor target. Therefore, screening for ligands that can specifically target G4-mtDNAs and show inhibitory effects on the growth or proliferation of cancer cells is fundamental to this study. For this purpose, we screened the synthesized ligands by evaluating their selectivity and binding ability towards G4-mtDNAs and toxicity against various human cancer cell lines *in vitro*.

Figure 5.4. The fluorescence intensity of ligands **1–10** in sensing with different DNAs. The concentration of the ligands was 5 μM, and the concentration of DNA was 20 μM.

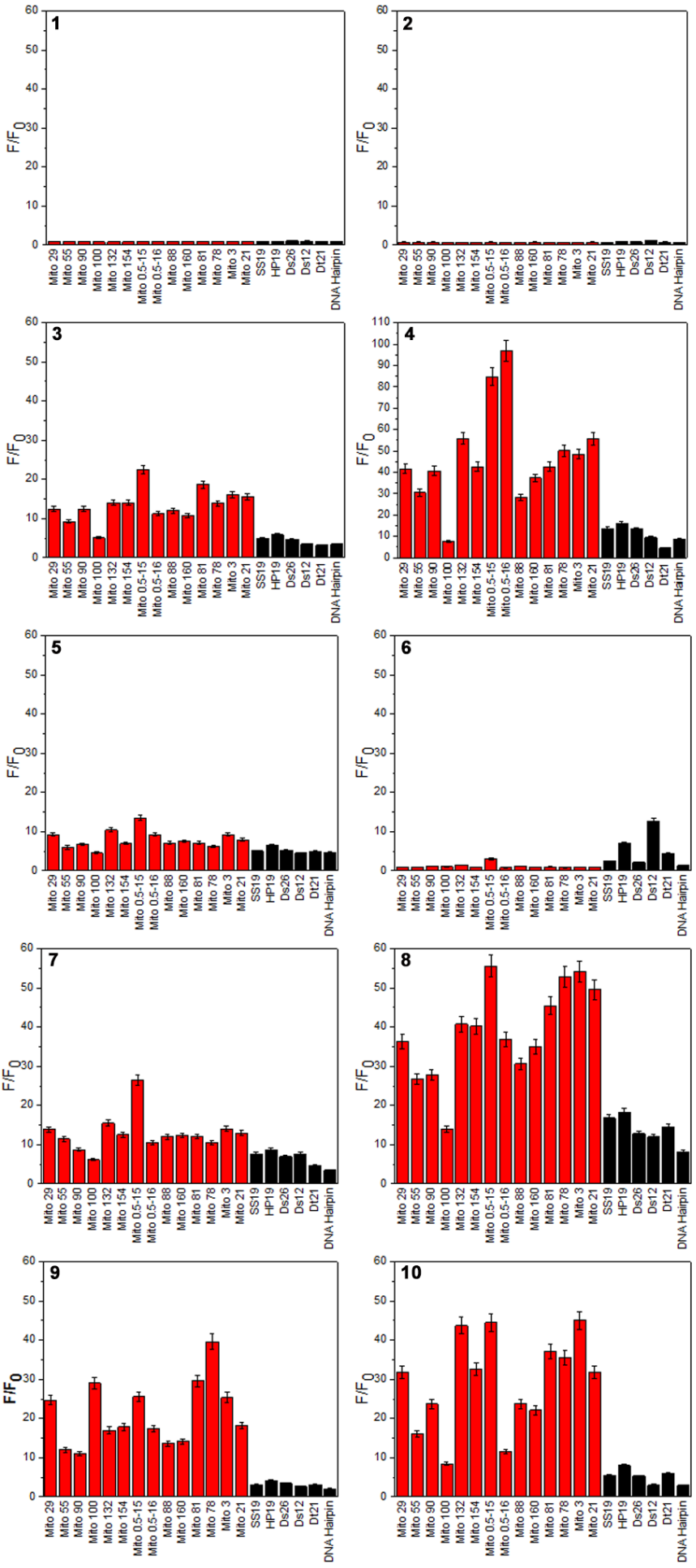

Fluorescence spectroscopy is one of the simple and direct methods to study ligand-G4 interactions. When the ligand interacts with nucleic acids, the free rotation of the ligand may be restricted, the planar rigidity of the ligand is enhanced, the π-conjugation is increased, and the electrons undergo π-π leaps, which in turn produce fluorescence.[6, 14] Therefore, the detection of fluorescence signals produced by a ligand bound to different types of nucleic acids is an effective method to determine ligand selectivity preliminary. In the present study, a number of G4-mtDNA sequences (*Mito 29*, *Mito 55*, *Mito 90*, *Mito 100*, *Mito 132*, *Mito 154*, *Mito 0.5-15*, *Mito 0.5-16*, *Mito 88*, *Mito 160*, *Mito 81*, *Mito 78*, *Mito 3* and *Mito 21*) and non-G4-DNA sequences (*SS19*, *HP19*, *Ds26*, *Ds12*, *Dt21* and *DNA Hairpin*) were selected as the model substrates to investigate the selectivity of the new di-cationic ligands **1–10**. The UV absorption spectra of these ligands were shown in Appendix, **Figure S3**.

To enable rapid screening of these new ligands against different nucleic acids, a nucleic acid concentration equivalent to 4 times that of the ligand was employed for the *in vitro* interaction study in a buffered solution. The results were summarized in **Figure 5.4**. All ligands exhibited only weak background fluorescence. However, upon interaction with G4-mtDNAs, ligands **3**, **4**, **7**, **8**, **9**, and **10** produced significantly enhanced fluorescence, typically showing F/F0 increases of 10 to 40 times. Overall, the ligands generated much stronger interaction signals with G4-mtDNAs compared to other nucleic acid substrates, indicating a higher sensitivity to G4-mtDNAs. Nevertheless, ligands **3**, **4**, **7**, and **8** showed relatively low selectivity for G4-mtDNAs, as strong fluorescent signals from interactions with non-G4-DNA substrates were also observed under the same titration conditions, with F/F0 values generally ranging from 2 to 15 folds. It is worth noting that ligand **9** displays the highest selectivity for G4-mtDNA substrates, with F/F0 values between 12 and 40 folds, and *Mito 78* achieving the peak intensity at 40 folds, while interactions with other non-G4-DNAs remained below 4 folds. These findings suggest that the integrated styryl moiety (R group) is crucial in determining the ligand's selectivity.

Next, we evaluated the affinity of the ligands binding to G4-mtDNAs using surface plasmon resonance (SPR) in a buffered solution. Four G4-mtDNAs (*Mito 78*, *Mito 55*, *Mito 29*, and *Mito 0.5-16*) along with a non-G4-DNA (*HP19*) were chosen as model substrates. The affinity results are summarized in **Table 5-1**, while the SPR sensorgrams are given in Appendix, **Figure S4**. Most ligands show significantly stronger affinity for G4-mtDNAs compared to non-G4-DNAs. For G4-mtDNA

Mito 78, the K_D values for most ligands ranged from 0.02 to 0.29 μM, whereas the K_D values for *HP19* exceeded 2 μM, indicating at least a 6-fold higher binding affinity for G4-mtDNA *Mito 78*. The binding results clearly support that these ligands show stronger affinity with G4-mtDNAs than other substrates.

Table 5-1. The affinity (K_D, μM) of ligands binding to G4-mtDNA and non-G4-DNA substrates determined with Surface Plasmon Resonance (SPR) at 25 °C.

	1	**2**	**3**	**4**	**5**	**6**	**7**	**8**	**9**	**10**
Mito 78	0.29	0.07	0.03	0.08	1.84	0.05	0.02	0.13	0.04	0.12
Mito 55	0.58	0.91	0.13	0.61	0.22	0.46	0.52	0.17	0.17	0.47
Mito 29	0.50	0.72	0.14	0.23	0.14	0.34	0.21	0.15	0.11	0.24
Mito 0.5-16	1.02	1.17	0.11	0.25	> 2	0.15	0.96	0.41	0.29	0.28
HP19	> 2	> 2	> 2	> 2	> 2	> 2	> 2	> 2	> 2	1.86

Table 5-2. The binding parameters were obtained from isothermal titration calorimetry (ITC) study for **9** interacting with nucleic acids [a].

	K_D (μM)	N (sites)	ΔH (kcal/mol)	ΔG (kcal/mol)
Mito 29	0.24	0.24	-18.0	-9.0
Mito 55	0.19	0.13	-32.4	-9.2
Mito 0.5-15	4.26	0.22	-12.8	-7.3
Mito 0.5-16	0.22	0.29	-22.3	-9.1
Mito 78	0.06	0.81	-4.3	-9.9
Mito 81	0.27	0.17	-48.3	-9.0
HP19	4.71	1.30	-41.9	-7.3
SS19	n.d.	n.d.	n.d.	n.d.
Mut 55	n.d.	n.d.	n.d.	n.d.
Mut 78	n.d.	n.d.	n.d.	n.d.

[a] The dissociation constant of **9** with oligonucleotides determined with ITC at 25 °C. n.d. denotes not determined due to the ligand-DNA binding signal is too weak for estimation.

Notably, ligand **9** showed a binding affinity to the selected G4-mtDNA substrates that was at least 6 times stronger than its affinity for the non-G4-DNA (*HP19*, K_D > 2 μM). The K_D values for ligand **9** with various G4-mtDNA substrates were as follows: *Mito 0.5-16* (K_D = 290 nM), *Mito 29* (K_D = 110 nM), *Mito 55* (K_D = 170 nM), and *Mito 78* (K_D = 40 nM), indicating that **9** is generally selective towards G4-mtDNAs. Further studies using isothermal titration calorimetry (ITC) tested more G4-

mtDNA substrates, including *Mito 29*, *Mito 55*, *Mito 0.5-15*, *Mito 0.5-16*, *Mito 78*, and *Mito 81* (**Figure 5.5** and **Table 5-2**). It was found that most K_D values for these G4-mtDNA substrates fell within the nanomolar to sub-micromolar range (K_D: 0.06-0.27 μM), significantly higher than the non-G4-DNAs (K_D > 4.7 μM). These results suggest that ligand **9** may interact with various G4-mtDNA structures with strong affinity.

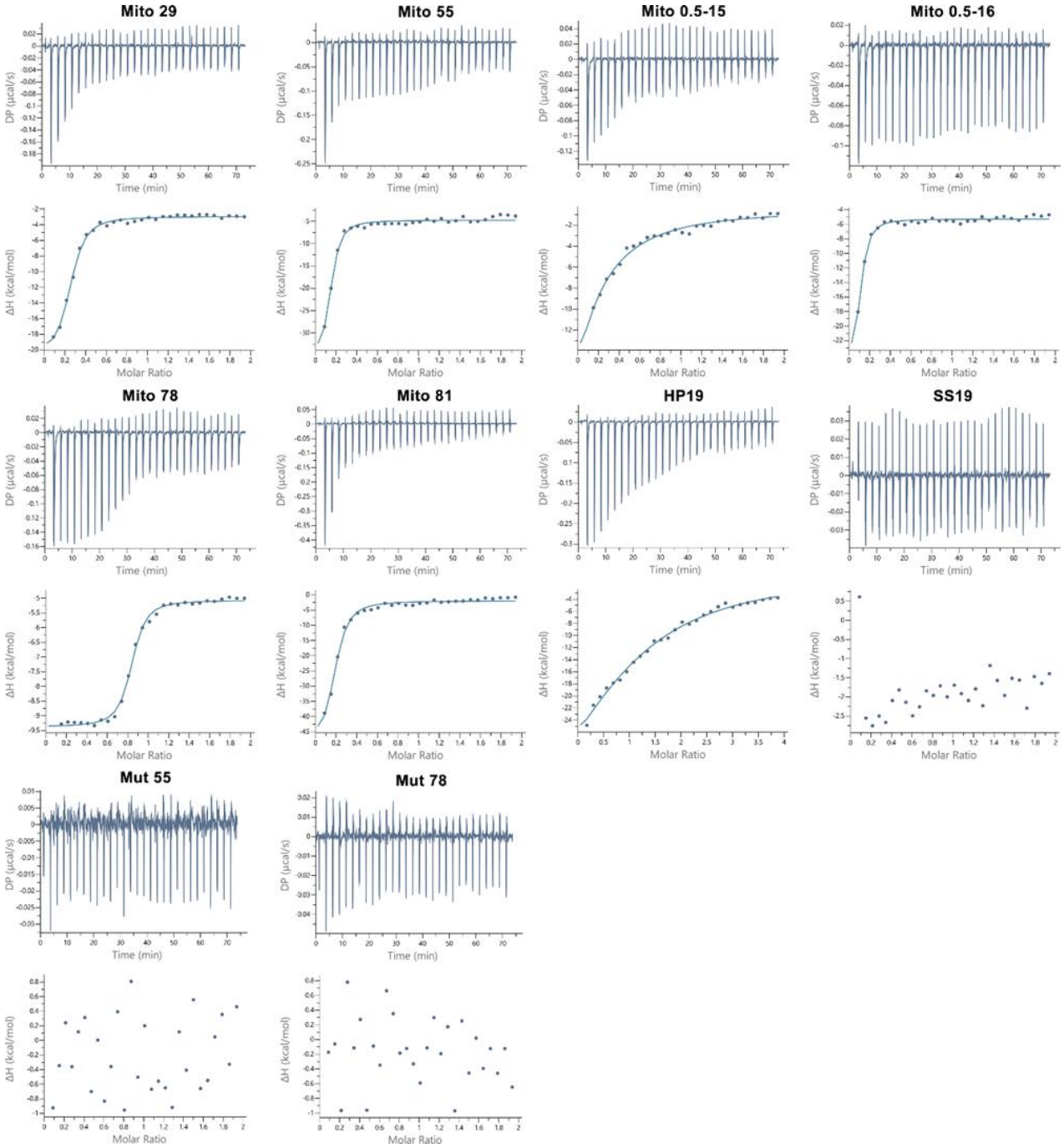

Figure 5.5. The binding of *Mito 29*, *Mito 55*, *Mito 0.5-15*, *Mito 0.5-16*, *Mito 78*, *Mito 81*, *HP19*, *SS19*, *Mut 55* and *Mut 78* to **9** was studied by isothermal titration calorimetry (ITC). The isothermal plot of **9** in the presence of different oligonucleotides in 25 mM KH_2PO_4, 100 mM KCl buffer (pH 7.4, containing 0.2% (v/v) DMSO). The concentration of **9** and oligonucleotides were 10 μM and 100 μM respectively.

Cell-based MTT assays were conducted to assess the cytotoxicity of the ligands against a variety of cancerous and non-cancerous cell lines. The results are summarized in **Table 5-3**. In general, the ligands exhibited mild toxicity towards human cancer cell lines (HCT116, HeLa, HepG2, MDA-MB-231, PANC-1, and LoVo) and non-cancerous cell lines (HFF1 and BJ), with most IC_{50} values exceeding 20 μM, and some even greater than 40 μM. However, ligand **9** showed the highest cytotoxicity against two colorectal cancer cell lines: HCT116 (IC_{50} = 3.4 μM) and LoVo (IC_{50} = 13.4 μM). In contrast, ligand **9** exhibited relatively mild cytotoxicity towards HFF1 and BJ cells (IC_{50} > 32 μM). The results indicate that colorectal cancer cells are markedly more sensitive to ligand **9**. Therefore, this ligand has potential as an anticancer agent for the treatment of human colorectal cancer (CRC), which remains a significant global challenge in clinical oncology.

Table 5-3. Half-maximal inhibitory concentration (IC_{50}, μM) of ligands against human cancer cell lines (HCT116, LoVo, HeLa, HepG2, MDA-MB-231 and PANC-1) and noncancerous cell lines (HFF1 and BJ) with incubation for 48 h.

	Cancer cells						Non-cancerous cells	
	HCT116	LoVo	HeLa	HepG2	PANC-1	MDA-MB-231	HFF1	BJ
1	> 40	> 40	> 40	> 40	> 40	> 40	28.3	> 40
2	27.4	> 40	> 40	> 40	> 40	> 40	> 40	> 40
3	17.2	15.4	29.5	> 40	> 40	> 40	22.7	> 40
4	19.8	> 40	23.3	> 40	> 40	> 40	> 40	> 40
5	8.0	> 40	34.6	37.3	> 40	> 40	> 40	> 40
6	24.7	> 40	> 40	> 40	> 40	> 40	34.8	> 40
7	8.5	> 40	32.1	25.3	> 40	> 40	> 40	> 40
8	5.4	15.0	22.1	> 40	20.5	> 40	31.1	31.4
9	3.4	13.4	23.5	> 40	24.8	34.6	32.7	> 40
10	29.2	35.4	>40	> 40	> 40	> 40	> 40	> 40

To confirm the subcellular localization of ligand **9** following its internalization in living colorectal cancer cells (HCT116), we conducted live-cell imaging using organelle-specific dyes: Hoechst 33342 (nucleus), Lyso-Tracker Blue (lysosome), ER-Tracker Blue (endoplasmic reticulum), and Mito-Tracker Deep Red (mitochondria). The confocal images shown in **Figure 5.6** indicate that ligand **9** is primarily localized in mitochondria, as indicated by a high colocalization with Mito-Tracker

(Pearson's correlation: r = 0.59). Importantly, there was no detectable colocalization signal in the nucleus or lysosome, while a weak signal was observed in the endoplasmic reticulum (Pearson's correlation: r = 0.30). These findings suggest that ligand **9** is selectively targeting mitochondria. This selectivity is likely attributed to its tailored structural features (di-cationic and small-sized), which facilitate its delivery into the mitochondria of cancer cells that exhibit high MMP.[15-17]

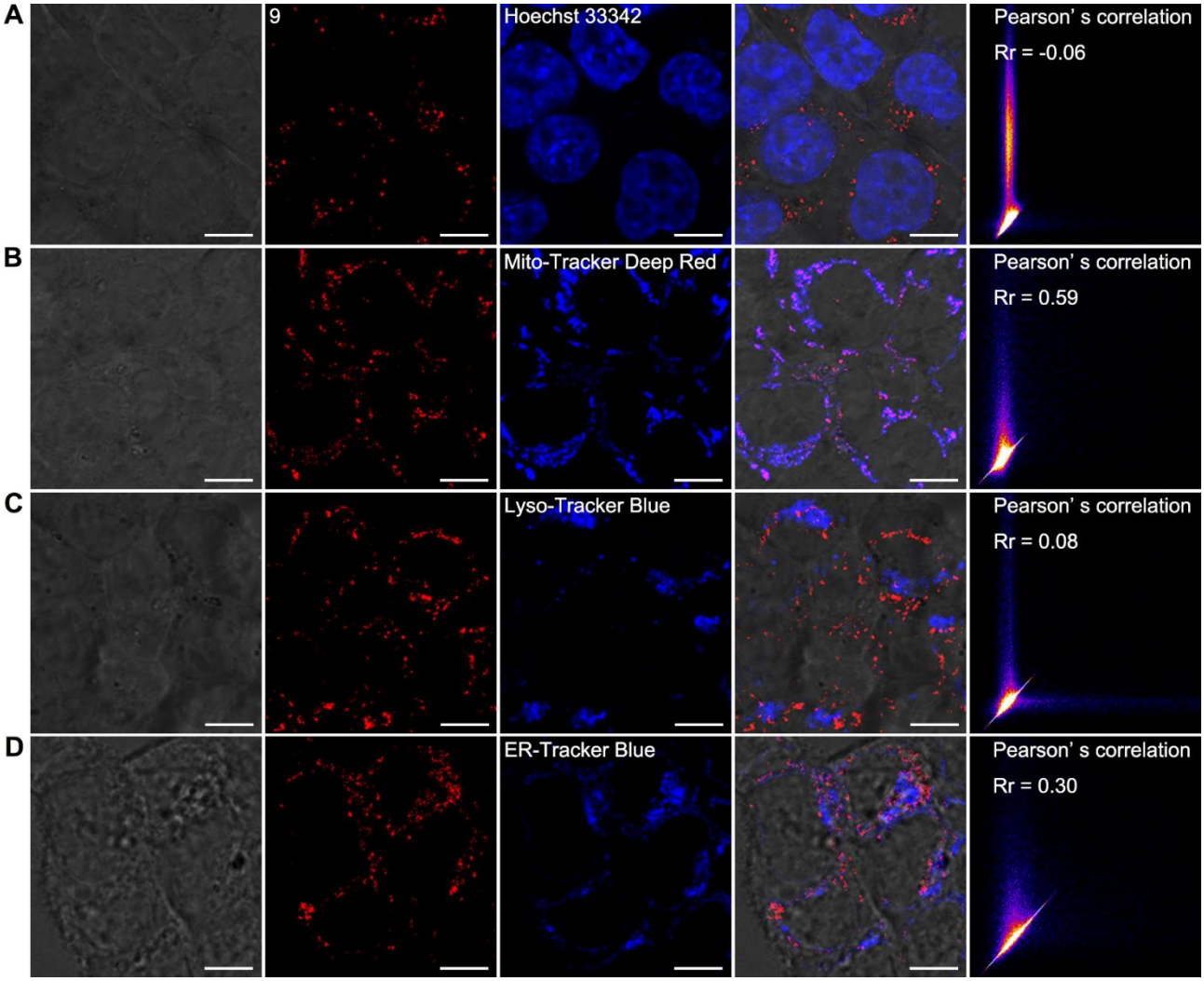

Figure 5.6. Single confocal plane images for the co-localization analysis. (A) Living HCT116 cells treated with 4 μM ligand **9** (λ_{ex}=488 nm) for 1 h and 1 μM Hoechst 33342 (λ_{ex}=405 nm) for 30 min. (B) Living HCT116 cells treated with 4 μM ligand **9** (λ_{ex}=488 nm) for 1 h and 200 nM Mito-Tracker Deep Red (λ_{ex}=635 nm blue) for 30 min. Pseudo-color (blue) was used for Mito-Tracker Deep red for the ease of visualization and comparison. (C) Living HCT116 cells treated with 4 μM ligand **9** (λ_{ex}=488 nm) for 1 h and 1 μM Lyso-Tracker Blue (λ_{ex}=405 nm) for 30 min. (D) Living HCT116 cells treated with 4 μM ligand **9** (λ_{ex}=488 nm) for 1 h and 1 μM ER-Tracker Blue (λ_{ex}=405 nm) for 30 min. The scale bar is 10 μm.

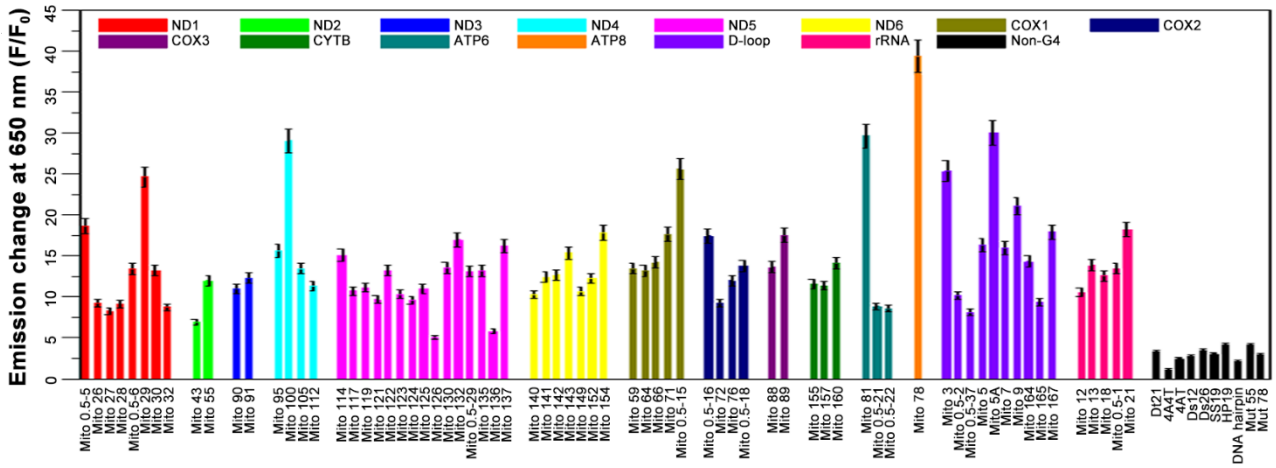

Figure 5.7. Fluorescence titration experiments. The enhanced fluorescence intensity monitored at 650 nm for the interaction of 5 μM ligand **9** with 20 μM different G4-mtDNAs and non-G4-DNAs.

5.3.3 Study the *in vitro* interactions between ligand **9** and G4-mtDNAs

Given its superior fluorescent selectivity, binding affinity, mitochondrial specificity, and bioactivity, ligand **9** was selected for further investigation. Preliminary screening experiments reveal that ligand **9** exhibits excellent selectivity targeting mitochondria and interacts with various G4-mtDNAs structures *in vitro* with strong affinities in the nanomolar to sub-micromolar range. We then explored its interactions with 71 G4-mtDNA sequences derived from 12 mitochondrial genes that encode essential proteins related to the mitochondrial respiratory chain, mitochondrial D-loop structure, and mitochondrial rRNA. These G4 structures from mitochondrial genes represent potential cellular targets for ligand **9**, and stabilizing these G4 structures with **9** may lead to mitochondrial dysfunction.

As illustrated in **Figure 5.7** and **Figure 5.8**, we observed that when ligand **9** interacted with various G4-mtDNAs, the fluorescent signal significantly increased in relation to the concentration of G4-mtDNAs used. In contrast, the fluorescence changes for non-G4-DNAs and mutant G4-DNAs (*Mut 55* and *Mut 78*) were much less obvious. The UV-Vis titration spectra also showed a clear redshift peak, indicating that ligand **9** forms adducts with these G4-mtDNAs *in situ* (**Figure 5.9**). Non-G4-DNA substrates did not exhibit such notable redshift under the same conditions. Subsequently, we performed circular dichroism (CD) measurements to investigate the interaction between ligand **9** and different G4-mtDNAs. The results revealed markedly changes in the CD spectra upon interaction. Specifically, the CD signal for *Mito 0.5-16* and *Mito 78* increased evidently at 290 nm, while the signal for *Mito 81* showed an increase at 265 nm (**Figure 5.10**). These findings suggest that ligand **9** may promote G4 formation and stabilize the resulting adducts in solution.[18] Conversely, we observed almost no changes in the CD signal in non-G4-DNAs (*HP19* and *SS19*).

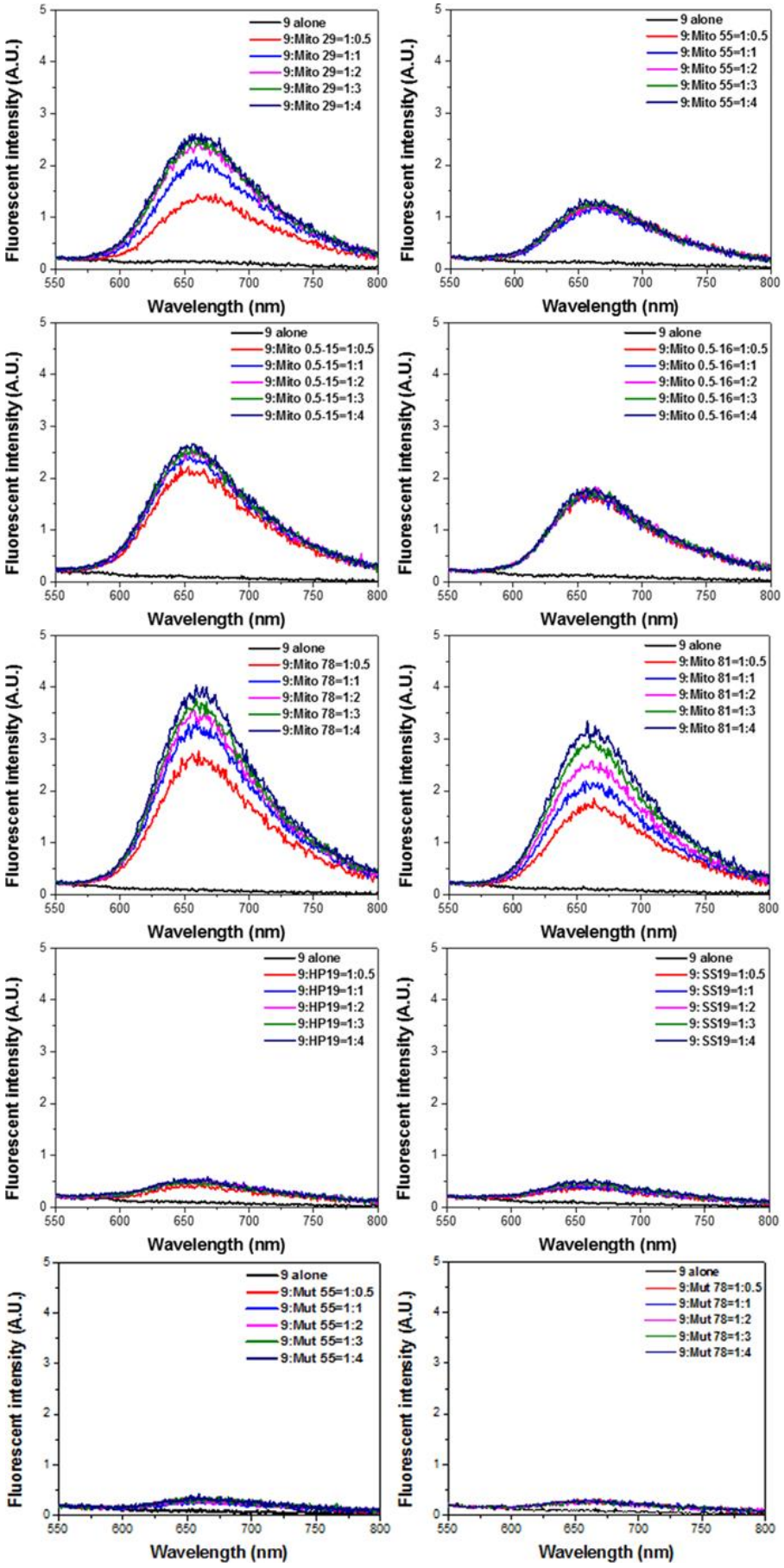

Figure 5.8. Representative fluorescence titration spectra of **9** (5 μM, λ_{ex}=490 nm) with *Mito 29*, *Mito 55*, *Mito 0.5-15*, *Mito 0.5-16*, *Mito 78*, *Mito 81*, *HP19*, *SS19*, *Mut 55* and *Mut 78* in 10 mM Tris-HCl buffer, 100 mM KCl, pH 7.4.

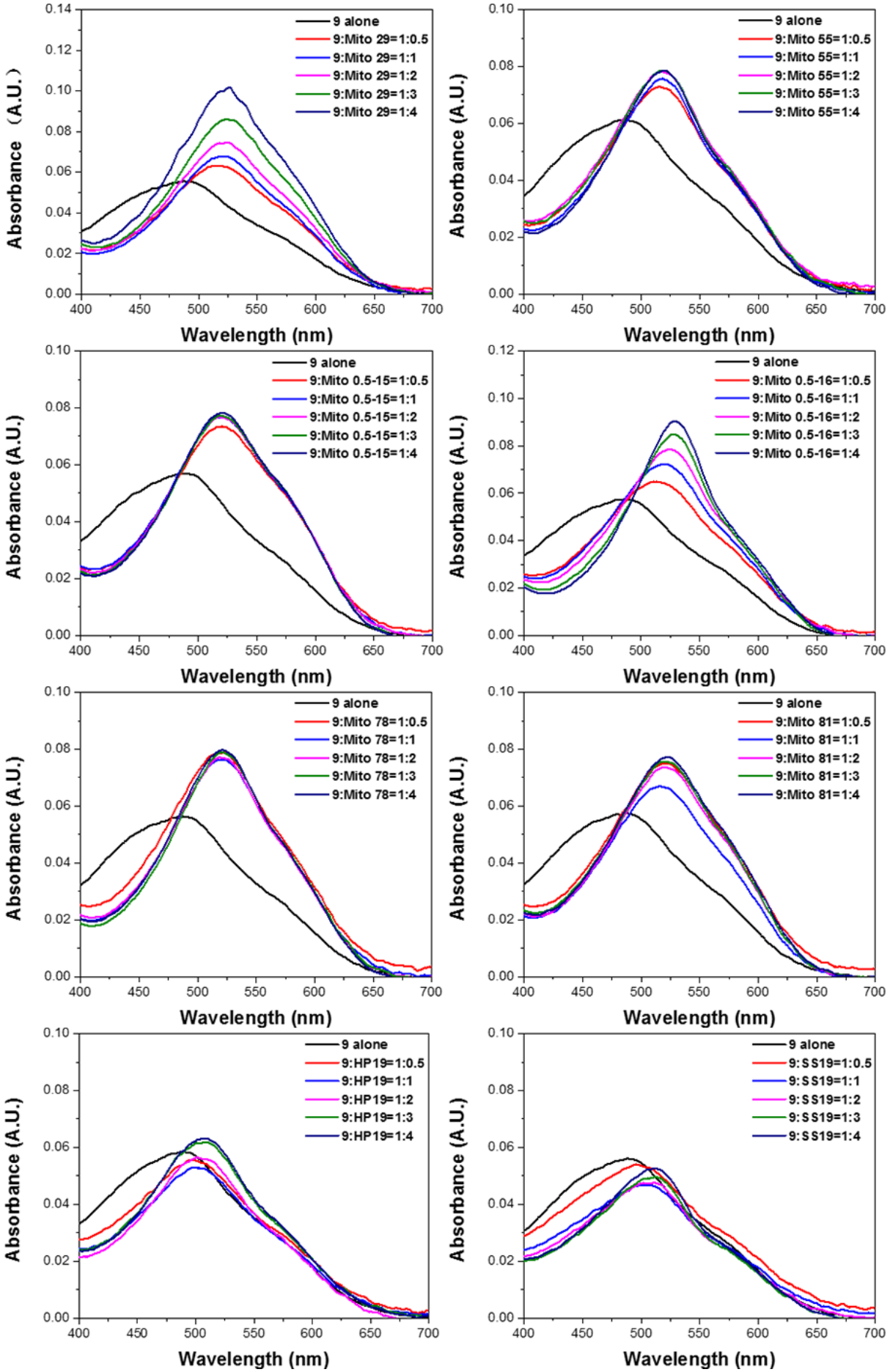

Figure 5.9. UV-vis titration spectra of 5 μM ligand **9** with *Mito 29*, *Mito 55*, *Mito 0.5-15*, *Mito 0.5-16*, *Mito 78*, *Mito 81*, *HP19* and *SS19* in 10 mM Tris-HCl buffer, 100 mM KCl, pH 7.4.

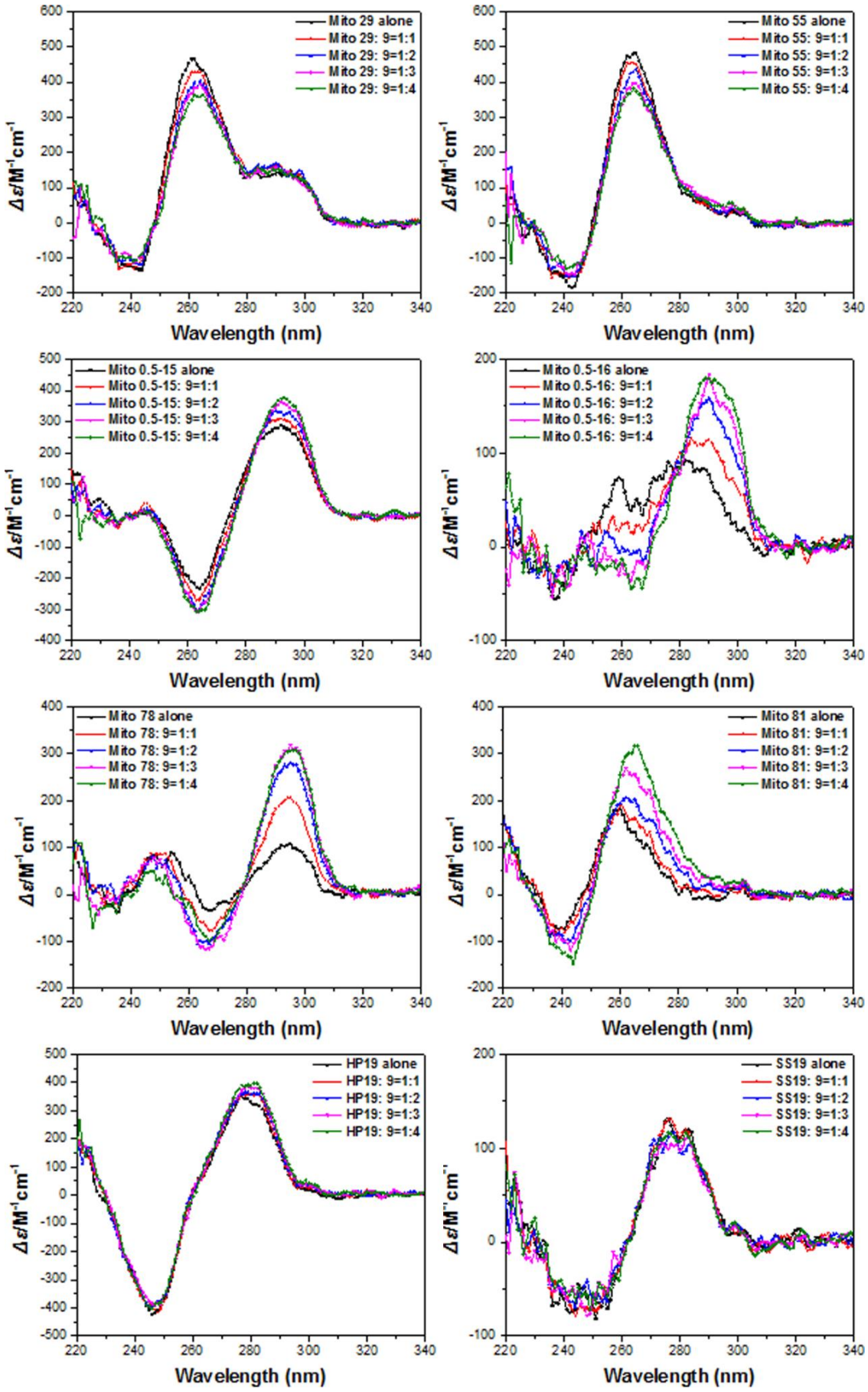

Figure 5.10. CD spectra of **9** with *Mito 29*, *Mito 55*, *Mito 0.5-15*, *Mito 0.5-16*, *Mito 78*, *Mito 81*, *HP19* and *SS19* in a Tris-HCl buffer (10 mM, pH 7.4, containing 100 mM KCl). The concentration of the oligonucleotides used was 5 μM.

To further validate the formation of G4 structures for *Mito 78* and *Mito 29* in solution, ^{1}H NMR study was performed. As shown in **Figure 5.11**, the characteristic signals of imino protons corresponding to the G4 structures of *Mito 78* and *Mito 29* appeared in the range of 10.5-12 ppm in the presence of KCl, while these signals were absent in the absence of KCl, indicating that both *Mito 78* and *Mito 29* are capable of forming G4 structures. Based on this result, ^{1}H NMR titration experiments were performed to examine the interaction between ligand **9** and the G4 structures of *Mito 78* and *Mito 29*. Upon adding 0.5 and 1 equivalent of ligand **9** to the solutions of *Mito 78* or *Mito 29*, we observed changes in the proton signals. These results suggest that the molecular interaction between **9** and the G4-structure of *Mito 78* or *Mito 29* may occur.

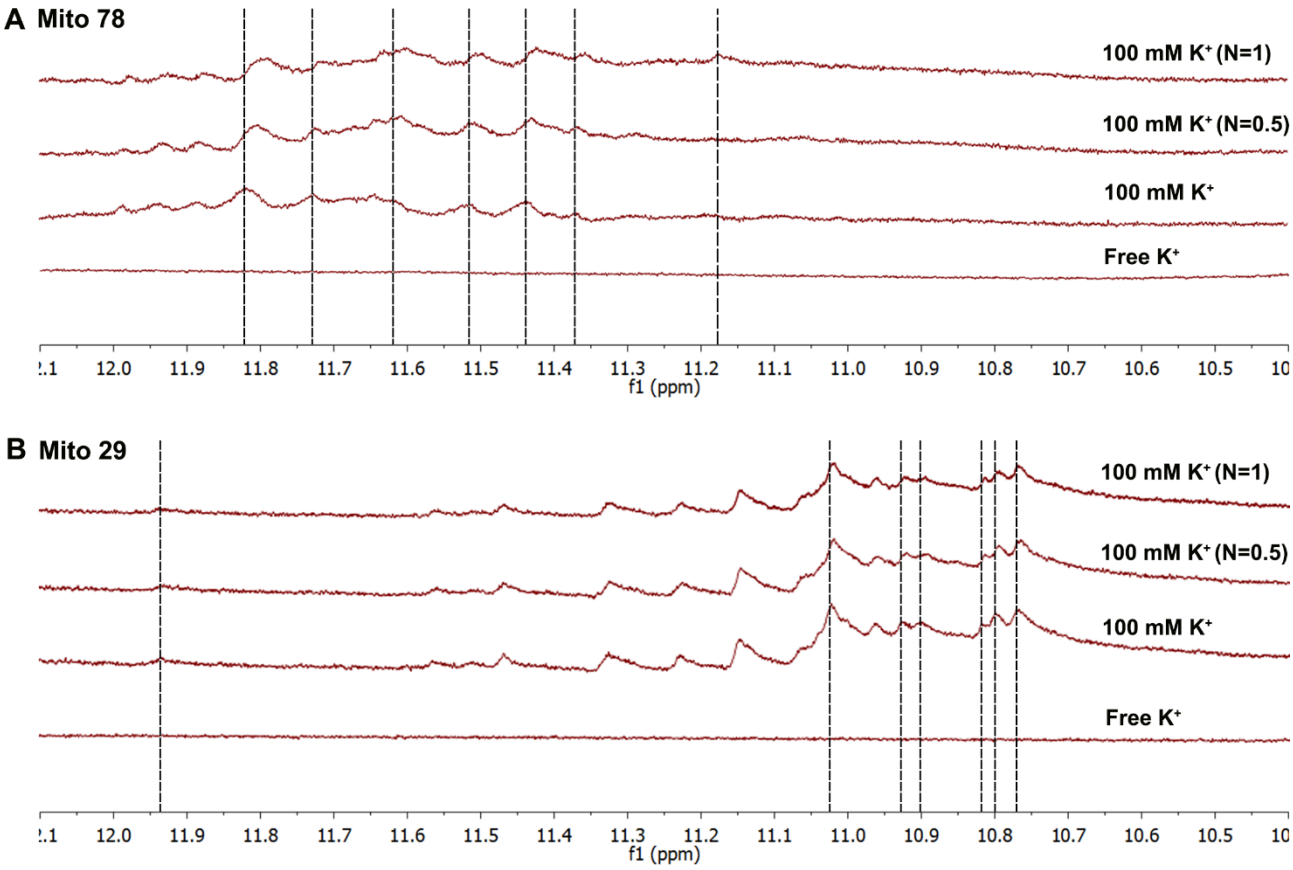

Figure 5.11. NMR study for the interaction of G4-mtDNAs and **9**. (A) Imino proton regions of ^{1}H NMR spectra of *Mito 78* either alone or with **9** at different ratio (0.5 and 1 equivalent). (B) Imino proton regions of ^{1}H NMR spectra of *Mito 29* either alone or with **9** at different ratio (0.5 and 1 equivalent). The assay was performed in 25 mM KH_2PO_4 buffer (100 mM KCl, 10% D_2O, pH 7.4) using 600 MHz Bruker spectrometers at 25 °C, and the concentration of *Mito 78* and *Mito 29* was 300 μM.

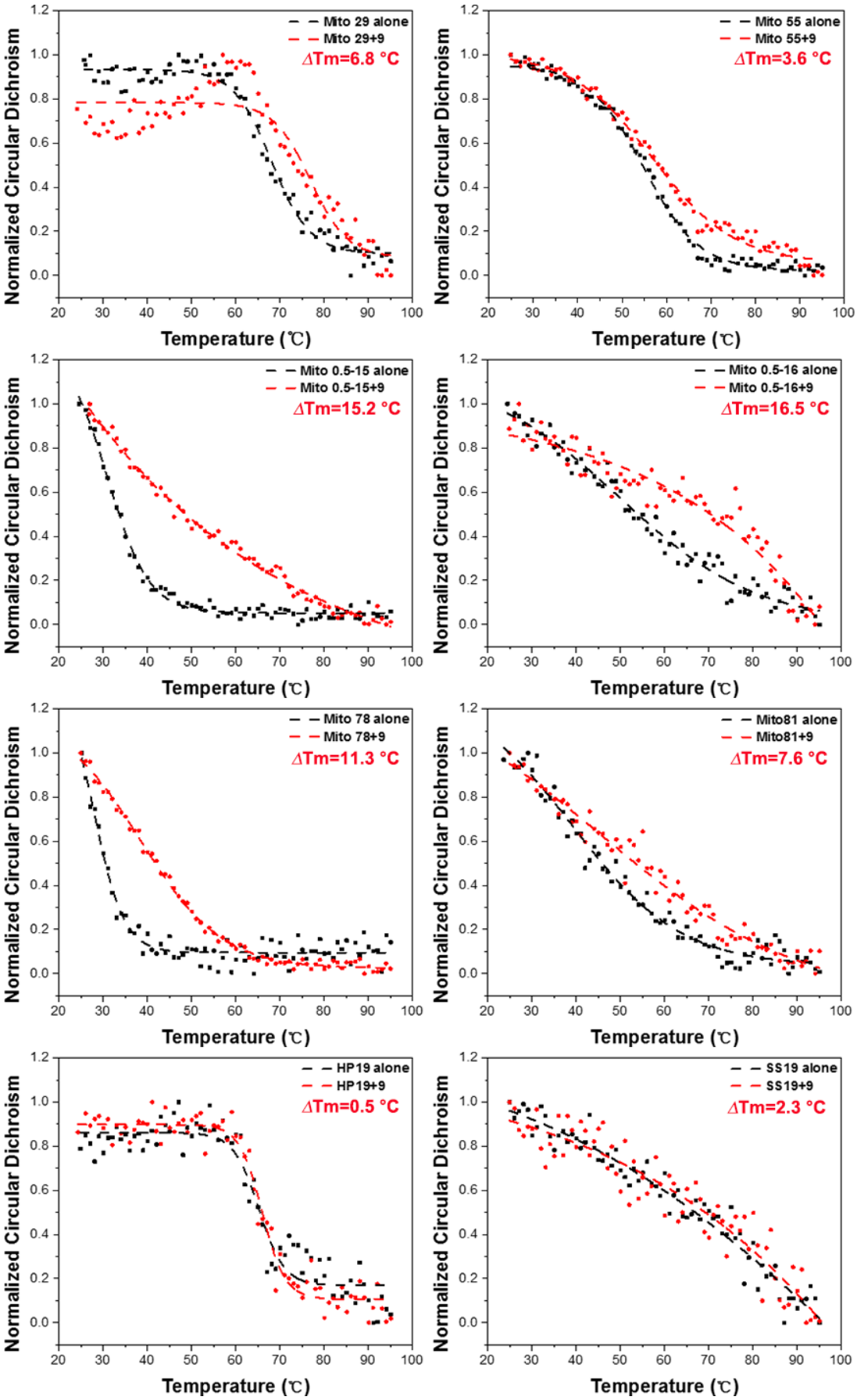

Figure 5.12. Thermal melt CD study for the interaction of G4-mtDNAs (or Non G4-mtDNAs) and **9**. Normalized CD signal of *Mito 29*, *Mito 55*, *Mito 0.5-15*, *Mito 0.5-16*, *Mito 78*, *Mito 81*, *HP19* and *SS19* during melting process. The concentrations of **9** and oligonucleotide were 5 μM and 5 μM, respectively.

To further investigate the stability of the **9**-G4-mtDNA complexes formed *in vitro*, we performed thermal melt CD assays. As shown in **Figure 5.12**, the markedly increased melting points (ΔT_m) in the range of 3.6-16.5 °C were observed. In contrast, the ΔT_m values for non-G4-DNAs were much lower, only between 0.5 and 2.3 °C. For specific complexes, such as the **9**-*Mito 78* complex (ΔT_m = 11.3 °C) and the **9**-Mito 0.5-16 complex ΔT_m = 16.5 °C), the ΔT_m values were much higher. These results support that ligand **9** interacts with G4-mtDNAs and stabilizes the complexes formed *in vitro*.

Through biophysical studies involving fluorescence and ^{1}H NMR titrations, CD measurements, thermal melt CD assays, SPR as well as ITC binding assays, we have proved that ligand **9** can potentially interact with G4-mtDNA targets. This includes the potential targets derived from 71 DNA sequences selected from 12 key mitochondrial genes, most of which showed strong affinities (K_D in sub-micromolar to nanomolar level) and form stable complexes (ΔT_m of 3.6-16.5 °C) *in vitro*. However, it remains challenging to determine which specific G4-mtDNA targets in mitochondrial genes interact with the ligand in living cells and *in vivo*. This difficulty arises because the intracellular folding of G4 structures is a transient process,[19] and its dynamics are not yet fully understood. Nevertheless, this study provides a comprehensive investigation into the biological effects and anticancer mechanisms of ligand **9** targeting mitochondria in HCT116 cells.

5.3.4 Study the intracellular interactions between ligand **9** and G4-mtDNAs

The *in vitro* results indicated that ligand **9** exhibits a strong selective binding affinity for G4-mtDNAs. We also confirmed that **9** is predominantly localized in the mitochondria, rather than the nucleus, in HCT116 cells through confocal live-cell imaging assays. Furthermore, increasing the concentration of **9** during the live-cell imaging did not alter its cellular localization (**Figure 5.13 A**). Besides, increasing the incubation time from 1 to 12 hours in living cells revealed no observable red fluorescence in the nucleus (**Figure 5.13 B**), further demonstrating that **9** is highly selective for mitochondria.

We then studied how ligand **9** was delivered into mitochondria. We previously proposed that the high negative mitochondrial membrane potential (MMP) in cancer cells could facilitate the entry of the ligand. To verify that MMP is the primary driving force for this delivery, we employed the potent mitochondrial uncoupler carbonyl cyanide 4-(trifluoromethoxy)phenylhydrazone (FCCP) to

depolarize the MMP in HCT116 cells.[20] As shown in **Figure 5.14 A**, the red foci of **9** in FCCP-treated cells decreased significantly compared to the control, indicating that MMP is indeed a critical factor. Additionally, to determine whether **9** entered mitochondria through the mitochondrial permeability transition pore (mPTP), we blocked the mPTP with cyclosporin A (CsA), a potent mPTP inhibitor,[21] prior to treating the cells with **9**. From **Figure 5.14 A**, there was no significant change in the red foci compared to the control. Taken together, these findings suggest that the delivery of **9** into mitochondria is primarily driven by MMP rather than mPTP.

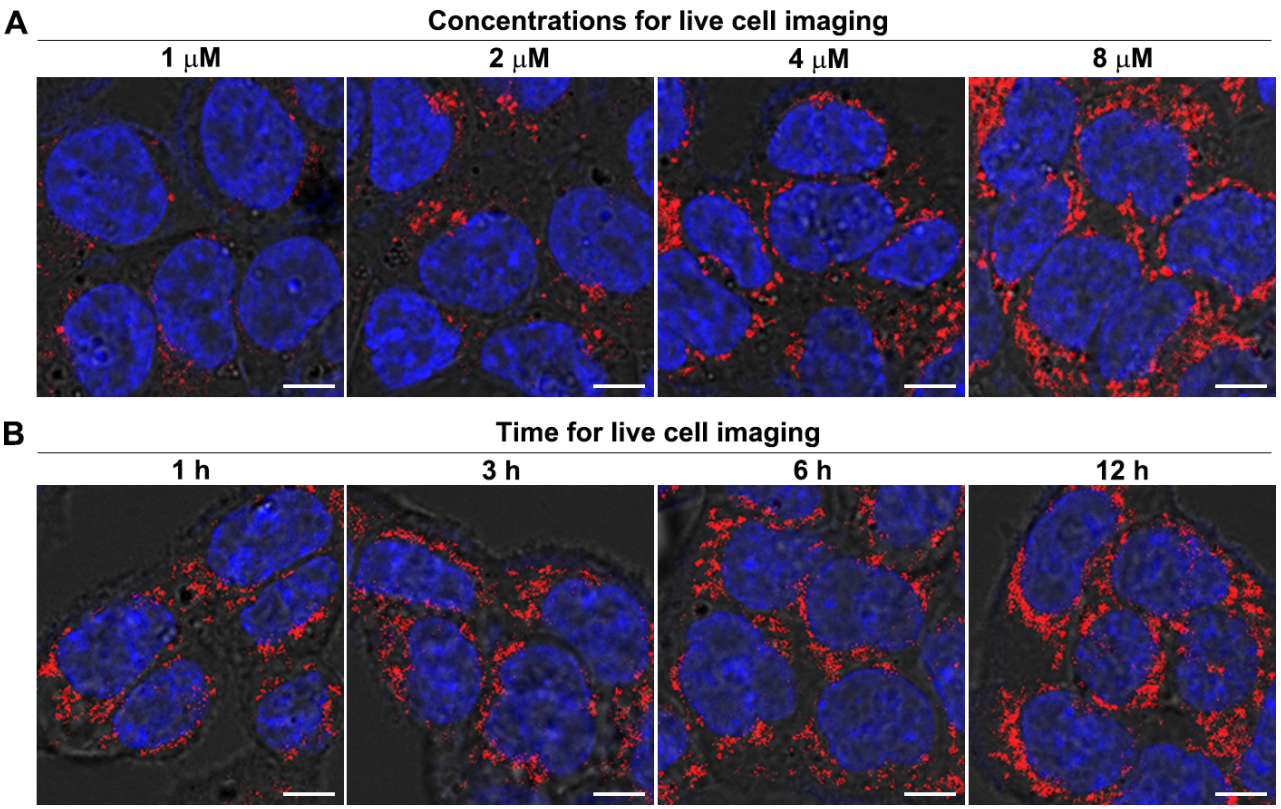

Figure 5.13. Single confocal plane images: (A) Living HCT116 cells treated with **9** at different concentrations (1, 2, 4 and 8 μM; incubation for 1 h; λ_{ex}=488 nm) and 1 μM Hoechst 33342 (incubation for 30 min; λ_{ex}=405 nm). The scale bar is 10 μm. (B) Living HCT116 cells treated with 4 μM ligand **9** (λ_{ex}=488 nm) for different time (1, 3, 6 and 12 h) and 1 μM Hoechst 33342 (λ_{ex}=405 nm) for 30 min. The scale bar is 10 μm.

To verify that the substrates in mitochondria interacting with ligand **9** are DNA rather than RNA, we performed enzymatic digestion assays. As shown in **Figure 5.14 B**, treatment with DNase I resulted in a nearly complete disappearance of the red foci, while treatment with RNase A caused no significant change in the red foci. These findings indicate that **9** binds specifically to mtDNAs in mitochondria. Moreover, to investigate whether the mtDNAs interacting with **9** is of G4 nature, MitoPDS, a known G4-mtDNAs binding ligand,[22] was utilized for intracellular competition with

9 in living cells. From **Figure 5.14 C**, following treatment with MitoPDS, the red foci representing ligand **9** decreased significantly in a concentration-dependent manner. These results suggest that **9** may compete for the same substrates as MitoPDS within the cells, and these substrates are likely G4-mtDNAs.

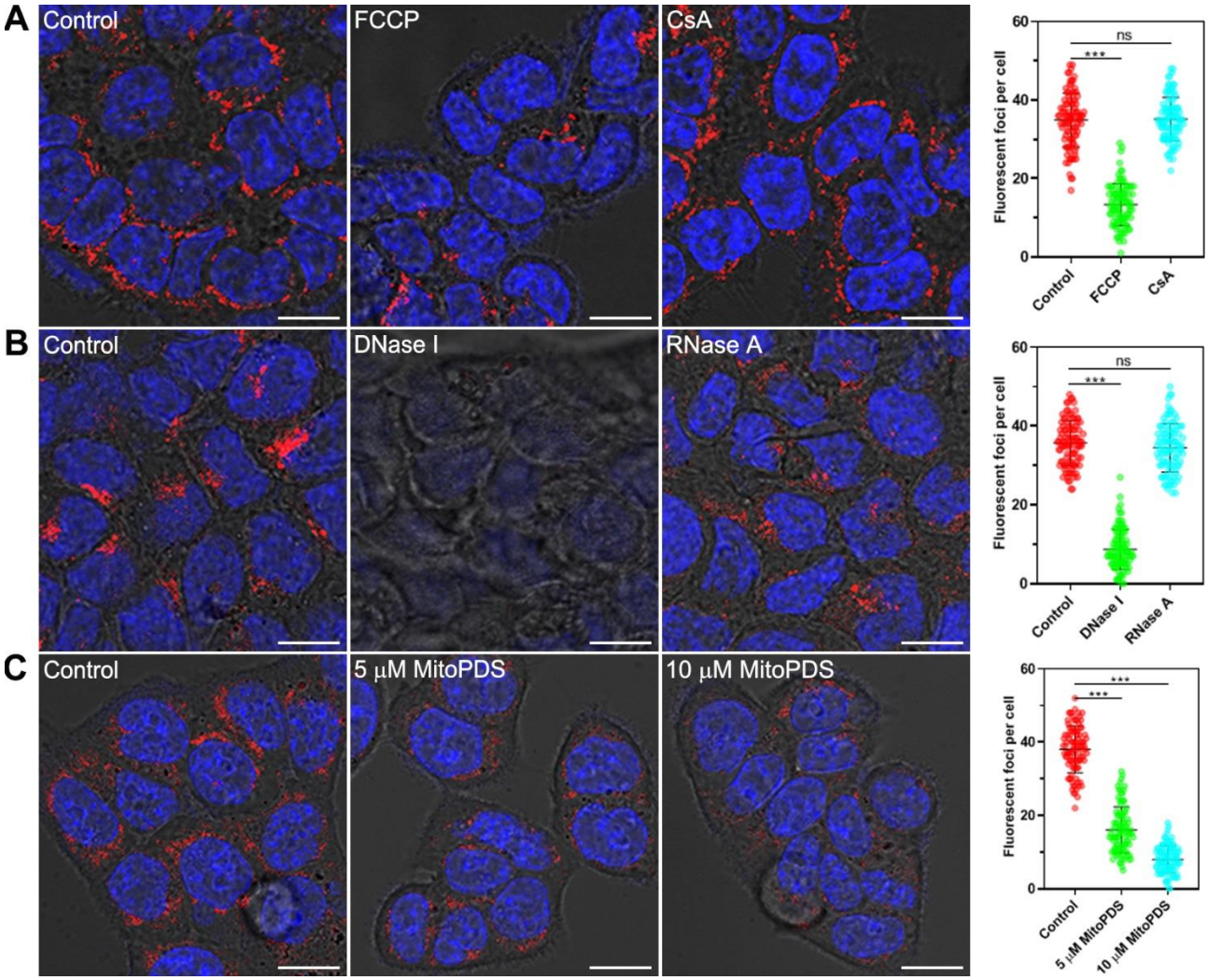

Figure 5.14. (A) Single confocal plane images: Living HCT116 cells incubated with 4 μM ligand **9** (λ_{ex}=488 nm) for 1 h and 1 μM Hoechst 33342 (λ_{ex}=405 nm) for 30 min after treatment with 1 μM FCCP for 20 min or 1 μM CsA for 24 h. (B) Single confocal plane images: Living HCT116 cells incubated with 4 μM ligand **9** (λ_{ex}=488 nm) for 1 h and 1 μM Hoechst 33342 (λ_{ex}=405 nm) for 30 min, then the cells were fixed and incubated with 200 units RNase A for 3 h or incubated with 200 units DNase I for 3 h. (C) Single confocal plane images: Living HCT116 cells incubated with 4 μM ligand **9** (λ_{ex}=488 nm) for 1 h and 1 μM Hoechst 33342 (λ_{ex}=405 nm) for 30 min, then the cells were treated with MitoPDS at different concentrations for 3 h. The scale bar is 10 μm. The data are presented as mean ± SEM, and statistics were determined using ANOVA, *$p < 0.05$, **$p < 0.01$ and ***$p < 0.001$.

Previous studies have suggested that hypoxia-induced upregulation of glycolysis can stimulate the formation of G4-mtDNAs in cancer cells.[22] HCT116 cells were treated with DMOG, a HIF-PH inhibitor known to enhance glycolysis,[23] and then incubated the cells with ligand **9**. We observed a significant increase in the number of red foci (indicating ligand **9**) in DMOG-treated cells compared to the control (**Figure 5.15 A**). On the contrary, for the treatment with HIF-1α inhibitors, 2MeOE2 [24] and KC7F2 [25] that can downregulate glycolysis, resulted in only minimal changes in the number of red foci compared with the control. Moreover, the Cy5 coupled mitochondrial DNA was transfected into HCT116 cells. As shown in **Figure 5.15 B**, ligand **9** was found good co-localization with two Cy5-G4-mtDNAs (*Mito 78*: r = 0.54 and *Mito 0.5-16*: r = 0.51), while it showed poor co-localization with Cy5-non-G4-DNAs (*SS19*: r = 0.28 and *HP19*: r = 0.18). Taken together, these intracellular results further support that ligand **9** may target G4-mtDNAs in the mitochondria of living HCT116 cells.

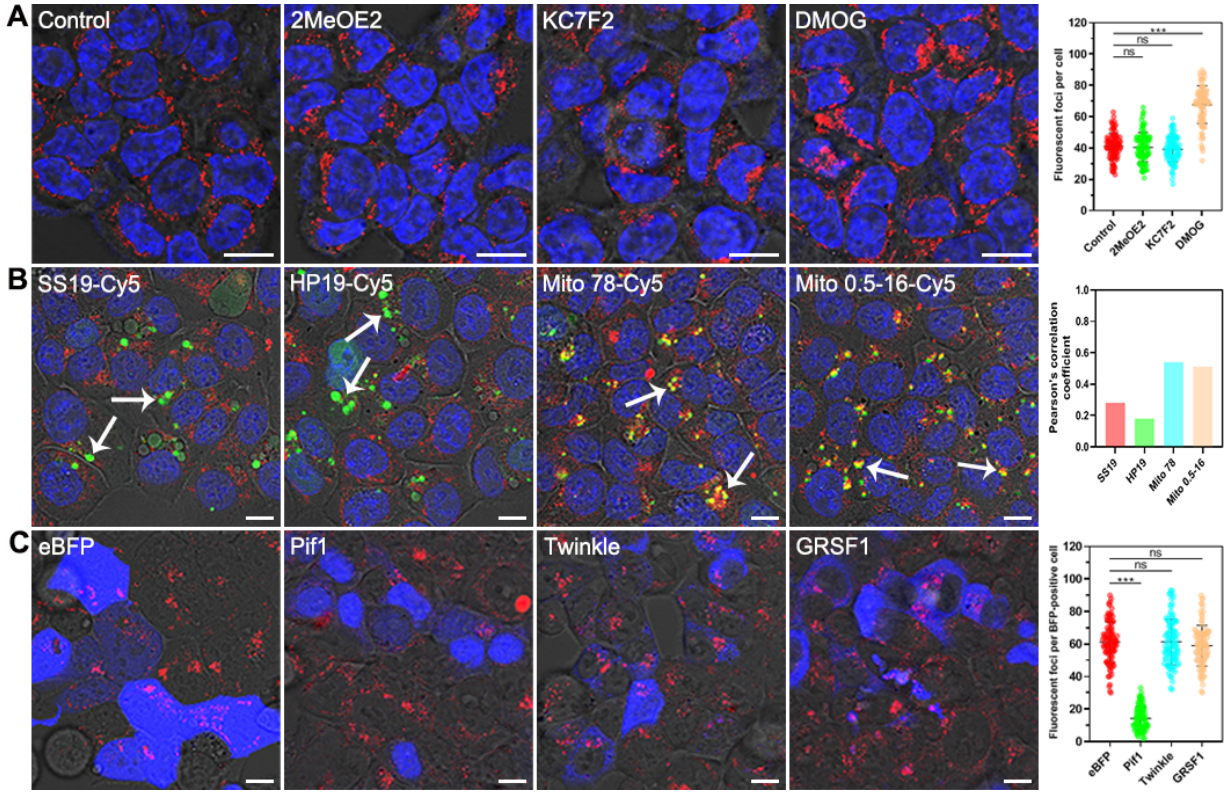

Figure 5.15. (A) Single confocal plane images: Living HCT116 cells incubated with 4 μM ligand **9** (λex=488 nm) for 1 h and 1 μM Hoechst 33342 (λ_{ex}=405 nm) for 30 min after treating 0.1 μM 2-MeOE2, 10 μM KC7F2, or 100 μM DMOG for 24 h. (B) Single confocal plane images for the co-localization analysis. Living HCT116 cells were transfected with Cy5-coupled mtDNA (λ_{ex}=635 nm) for 24 h and then incubated with 4 μM ligand **9** (λ_{ex}=488 nm) 1 h and 1 μM Hoechst 33342 (λ_{ex}=405 nm) for 30 min. For the ease of visualization and comparison, pseudo-color (green) was used for the Cy5 label. The scale bar is 10 μm. (C) Single confocal plane images: Living HCT116 cells with overexpression of eBFP-tagged proteins (λ_{ex}=405 nm) and then incubated with 4 μM ligand **9** (λex=488 nm) for 1 h. The scale bar is 10 μm. The data are presented as mean ± SEM, and statistics were determined using ANOVA, *$p < 0.05$, **$p < 0.01$ and ***$p < 0.001$.

To obtain more information about the interaction of ligand **9** with G4-mtDNA targets in living HCT116 cells, we overexpressed a G4-DNA-resolving helicase, Pif1, to unfold the G4 structures formed in mitochondria.[26] Following the overexpression of eBFP-tagged Pif1 in HCT116 cells, we found a significant decrease in the red foci of ligand **9**, whereas the negative control, which only overexpressed eBFP, showed no obvious changes in the red foci (**Figure 5.15 C**). On the other hand, two non-G4-DNA-targeting helicases were also overexpressed in HCT116 cells: Twinkle, a mitochondrial DNA helicase,[27] and GRSF1, a helicase specific to G4-mtRNA.[28] Since both Twinkle and GRSF1 are unable to unwind G4-mtDNA structures, we found that these two helicases have no significant effect on the red foci in the mitochondria of living HCT116 cells (**Figure 5.15 C**). Collectively, these intracellular results with target-specific helicases strongly support that ligand **9** may specifically target G4-mtDNAs in the mitochondria of living HCT116 cells.

5.4 Summary

In summary, we have designed and synthesized 10 new di-cationic ligands **1-10** by considering the fact that mitochondria of cancer cells have high membrane potential. We then screened the ligands in terms of their selectivity, affinity, and toxicity to cancer cells. We found that most ligands can generate significant fluorescence after interacting with G4-mtDNAs (F/F_0 = 10-40 folds), and have higher affinity toward G4-mtDNAs, the K_D down to nanomolar level. Among these ligands, ligand **9** was more selective for G4-mtDNAs (F/F_0 = 12-40 folds) and less selective for non-G4-DNAs ($F/F_0 < 4$ folds). Besides, SPR results showed that ligand **9** had a strong binding affinity for G4-mtDNAs, the K_D values are at nanomolar level (0.04-0.29 μM), while the K_D values for non-G4-mtDNAs are higher than 2 μM. In addition, **9** exhibited a low IC_{50} value, down to 3.4 μM against human colorectal cancer cell HCT116, while the IC_{50} values in human normal cell lines were higher than 32 μM. Imaging of ligand **9** in living HCT116 cells also showed that ligand **9** was primarily localized to mitochondria, not the nucleus. These findings suggest that ligand **9** may be able to target G4-mtDNAs and have biological activity in living HCT116 cells, and therefore we chose ligand **9** for deeper investigation.

Different *in vitro* experiments such as fluorescence titration, UV-visible titration, CD titration, NMR titration, ITC analysis and CD melting studies have shown that ligand **9** binds specifically to G4-mtDNAs and stabilizes the structure of G4s. Furthermore, FCCP pretreatment experiments showed that ligand **9** is dependent on the membrane potential of cancer cells to enter mitochondria, which

validates our principle of designing ligands based on the greater membrane potential difference of cancer cells. More importantly, enzymatic digestion assays, transfection of G4-mtDNAs and overexpression of G4-mtDNA helicase in living cells strongly demonstrated that ligand **9** was able to specifically target G4-mtDNAs in living HCT116 cells. Taken together, ligand **9** is a G4-mtDNA-selective ligand that effectively inhibits the proliferation of a variety of human cancer cells, especially human colorectal cancer cell HCT116. The anticancer mechanism was investigated, and the results were discussed in detail in Chapter 6.

5.5 References

[1] L.D. Zorova, V.A. Popkov, E.Y. Plotnikov, D.N. Silachev, I.B. Pevzner, S.S. Jankauskas, V.A. Babenko, S.D. Zorov, A.V. Balakireva, M. Juhaszova, Mitochondrial membrane potential, Analytical biochemistry 552 (2018) 50-59.

[2] J. Wang, J. Li, Y. Xiao, B. Fu, Z. Qin, TPP-based mitocans: A potent strategy for anticancer drug design, RSC Medicinal Chemistry 11(8) (2020) 858-875.

[3] G. Battogtokh, Y.-Y. Cho, J.Y. Lee, H.S. Lee, H.C. Kang, Mitochondrial-targeting anticancer agent conjugates and nanocarrier systems for cancer treatment, Frontiers in pharmacology 9 (2018) 922.

[4] J. Zielonka, J. Joseph, A. Sikora, M. Hardy, O. Ouari, J. Vasquez-Vivar, G. Cheng, M. Lopez, B. Kalyanaraman, Mitochondria-targeted triphenylphosphonium-based compounds: syntheses, mechanisms of action, and therapeutic and diagnostic applications, Chemical reviews 117(15) (2017) 10043-10120.

[5] C.A. Kulkarni, B.D. Fink, B.E. Gibbs, P.R. Chheda, M. Wu, W.I. Sivitz, R.J. Kerns, A novel triphenylphosphonium carrier to target mitochondria without uncoupling oxidative phosphorylation, Journal of medicinal chemistry 64(1) (2021) 662-676.

[6] J. Nygren, N. Svanvik, M. Kubista, The interactions between the fluorescent dye thiazole orange and DNA, Biopolymers 46(1) (1998) 39-51.

[7] W. Long, B.-X. Zheng, X.-H. Huang, M.-T. She, A.-L. Liu, K. Zhang, W.-L. Wong, Y.-J. Lu, Molecular Recognition and Imaging of Human Telomeric G-Quadruplex DNA in Live Cells: A Systematic Advancement of Thiazole Orange Scaffold To Enhance Binding Specificity and Inhibition of Gene Expression, Journal of Medicinal Chemistry 64(4) (2021) 2125-2138.

[8] W. Long, B.-X. Zheng, Y. Li, X.-H. Huang, D.-M. Lin, C.-C. Chen, J.-Q. Hou, T.-M. Ou, W.-L. Wong, K. Zhang, Y.-J. Lu, Rational design of small-molecules to recognize G-quadruplexes of c-

MYC promoter and telomere and the evaluation of their in vivo antitumor activity against breast cancer, Nucleic Acids Research 50(4) (2022) 1829-1848.

[9] W. Long, Y.-X. Zeng, B.-X. Zheng, Y.-B. Li, Y.-K. Wang, K.-H. Chan, M.-T. She, Y.-J. Lu, C. Cao, W.-L. Wong, Targeting hTERT Promoter G-Quadruplex DNA Structures with Small-Molecule Ligand to Downregulate hTERT Expression for Triple-Negative Breast Cancer Therapy, Journal of Medicinal Chemistry 67(15) (2024) 13363-13382.

[10] Y.-J. Lu, Q. Deng, J.-Q. Hou, D.-P. Hu, Z.-Y. Wang, K. Zhang, L.G. Luyt, W.-L. Wong, C.-F. Chow, Molecular Engineering of Thiazole Orange Dye: Change of Fluorescent Signaling from Universal to Specific upon Binding with Nucleic Acids in Bioassay, ACS Chemical Biology 11(4) (2016) 1019-1029.

[11] B.-X. Zheng, J. Yu, W. Long, K.H. Chan, A.S.-L. Leung, W.-L. Wong, Structurally diverse G-quadruplexes as the noncanonical nucleic acid drug target for live cell imaging and antibacterial study, Chemical Communications 59(11) (2023) 1415-1433.

[12] Z. Han, L. Wen, G-quadruplex in cancer energy metabolism: A potential therapeutic target, Biochimica et Biophysica Acta (BBA) - General Subjects (2025) 130810.

[13] B.-X. Zheng, W. Long, M.-T. She, Y. Wang, D. Zhao, J. Yu, A. Siu-Lun Leung, K. Hin Chan, J. Hou, Y.-J. Lu, W.-L. Wong, A Cytoplasm-Specific Fluorescent Ligand for Selective Imaging of RNA G-Quadruplexes in Live Cancer Cells, Chemistry – A European Journal 29(34) (2023) e202300705.

[14] N.I. Shank, H.H. Pham, A.S. Waggoner, B.A. Armitage, Twisted cyanines: a non-planar fluorogenic dye with superior photostability and its use in a protein-based fluoromodule, J Am Chem Soc 135(1) (2013) 242-51.

[15] Q. Cui, S. Wen, P. Huang, Targeting cancer cell mitochondria as a therapeutic approach: recent updates, Future medicinal chemistry 9(9) (2017) 929-949.

[16] L. Dong, J. Neuzil, Targeting mitochondria as an anticancer strategy, Cancer Communications 39 (2019) 1-3.

[17] S. Fulda, L. Galluzzi, G. Kroemer, Targeting mitochondria for cancer therapy, Nature reviews Drug discovery 9(6) (2010) 447-464.

[18] R. del Villar‐Guerra, J.O. Trent, J.B. Chaires, G‐quadruplex secondary structure obtained from circular dichroism spectroscopy, Angewandte Chemie International Edition 57(24) (2018) 7171-7175.

[19] Phong Lan T. Tran, M. Rieu, S. Hodeib, A. Joubert, J. Ouellet, P. Alberti, A. Bugaut, J.-F.

Allemand, J.-B. Boulé, V. Croquette, Folding and persistence times of intramolecular G-quadruplexes transiently embedded in a DNA duplex, Nucleic Acids Research 49(9) (2021) 5189-5201.
[20] K.-S. Park, I. Jo, Y. Pak, S.-W. Bae, H. Rhim, S.-H. Suh, S. Park, M. Zhu, I. So, K. Kim, FCCP depolarizes plasma membrane potential by activating proton and Na+ currents in bovine aortic endothelial cells, Pflügers Archiv 443(3) (2002) 344-352.
[21] Z.Z. Gizatullina, T.M. Gaynutdinov, H. Svoboda, D. Jerzembek, A. Knabe, S. Vielhaber, M. Malesevic, H.-J. Heinze, G. Fischer, F. Striggow, F.N. Gellerich, Effects of cyclosporine A and its immunosuppressive or non-immunosuppressive derivatives [D-Ser]8-CsA and Cs9 on mitochondria from different brain regions, Mitochondrion 11(3) (2011) 421-429.
[22] X.-C. Chen, G.-X. Tang, W.-H. Luo, W. Shao, J. Dai, S.-T. Zeng, Z.-S. Huang, S.-B. Chen, J.-H. Tan, Monitoring and Modulating mtDNA G-Quadruplex Dynamics Reveal Its Close Relationship to Cell Glycolysis, Journal of the American Chemical Society 143(49) (2021) 20779-20791.
[23] K. Schultz, V. Murthy, J.B. Tatro, D. Beasley, Prolyl hydroxylase 2 deficiency limits proliferation of vascular smooth muscle cells by hypoxia-inducible factor-1α-dependent mechanisms, American Journal of Physiology-Lung Cellular and Molecular Physiology 296(6) (2009) L921-L927.
[24] A. Aquino-Gálvez, G. González-Ávila, J. Delgado-Tello, M. Castillejos-López, C. Mendoza-Milla, J. Zúñiga, M. Checa, H.A. Maldonado-Martínez, A. Trinidad-López, J. Cisneros, L.M. Torres-Espíndola, C. Hernández-Jiménez, B. Sommer, C. Cabello-Gutiérrez, L.H. Gutiérrez-González, Effects of 2-methoxyestradiol on apoptosis and HIF-1α and HIF‑2α expression in lung cancer cells under normoxia and hypoxia, Oncol Rep 35(1) (2016) 577-583.
[25] T. Narita, S. Yin, C.F. Gelin, C.S. Moreno, M. Yepes, K. Nicolaou, E.G. Van Meir, Identification of a novel small molecule HIF-1α translation inhibitor, Clinical Cancer Research 15(19) (2009) 6128-6136.
[26] S. Bannwarth, L. Berg-Alonso, G. Augé, K. Fragaki, J.E. Kolesar, F. Lespinasse, S. Lacas-Gervais, F. Burel-Vandenbos, E. Villa, F. Belmonte, J.-F. Michiels, J.-E. Ricci, R. Gherardi, L. Harrington, B.A. Kaufman, V. Paquis-Flucklinger, Inactivation of Pif1 helicase causes a mitochondrial myopathy in mice, Mitochondrion 30 (2016) 126-137.
[27] S.K. Bharti, J.A. Sommers, J. Zhou, D.L. Kaplan, J.N. Spelbrink, J.-L. Mergny, R.M. Brosh, DNA Sequences Proximal to Human Mitochondrial DNA Deletion Breakpoints Prevalent in Human Disease Form G-quadruplexes, a Class of DNA Structures Inefficiently Unwound by the Mitochondrial Replicative Twinkle Helicase*, Journal of Biological Chemistry 289(43) (2014)

29975-29993.

[28] Z. Pietras, M.A. Wojcik, L.S. Borowski, M. Szewczyk, T.M. Kulinski, D. Cysewski, P.P. Stepien, A. Dziembowski, R.J. Szczesny, Dedicated surveillance mechanism controls G-quadruplex forming non-coding RNAs in human mitochondria, Nature communications 9(1) (2018) 2558.

Chapter 6. Study the anticancer mechanism of ligand 9

6.1 Synopsis

In Chapter 5, we have demonstrated that the di-cationic small-sized lipophilic ligand, **9**, selectively targets G4-mtDNAs *in vitro* and *in cellulo*. Besides, ligand **9** was found to be able to inhibit the proliferation of a panel of human cancer cells, especially human colorectal cancer cell HCT116. To explore the anticancer mechanism of this ligand, which targets intracellular G4-mtDNAs, we performed a series of experiments to analyze the cellular response of cancer cells to the ligand treatment. The effects of the ligand on DNA, RNA, and protein expression levels were investigated. Besides, the *in vivo* antitumor efficacy of ligand **9** against human colorectal cancer xenografts in nude mice was validated.

6.2 Results and discussion

6.2.1 Study the effects of ligand **9** on the replication, transcription and translation of mitochondrial genes in HCT116 cells

Mitochondria possess their own DNA (mtDNA). The regulation of their replication, transcription, and translation processes is vital for supporting various cellular functions. G4s may significantly influence mitochondrial transcription and replication.[1] We have revealed that ligand **9** is highly selective towards mitochondria and exhibits a strong binding affinity for G4-mtDNAs. We thus examine the impact of ligand **9** on mitochondrial DNA replication, transcription, and translation in HCT116 cells. As illustrated in **Figure 6.1**, the ligand inhibited mtDNA replication, evidenced by a notable decrease in the copy numbers of the *MT-ND1* and *MT-ND2* genes in HCT116 cells. Interestingly, this inhibitory effect was not obvious in noncancerous HFF1 cells, suggesting that G4s may play a regulatory role in the replication process in HCT116 cancer cells.

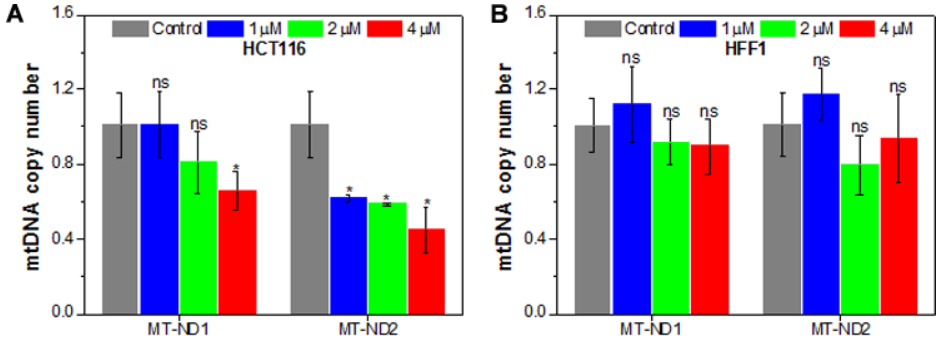

Figure 6.1. q-PCR study for the replication effects of **9**. (A) The effect of **9** (0-4 μM) on mtDNA copy number after 48 h treatment in cancer cell HCT116. (B) Effect of **9** (0-4 μM) on mtDNA copy number after 48 h treatment in normal cell HFF1. The data are presented as mean ± SEM, and statistics were determined using ANOVA, *$p < 0.05$, **$p < 0.01$ and ***$p < 0.001$.

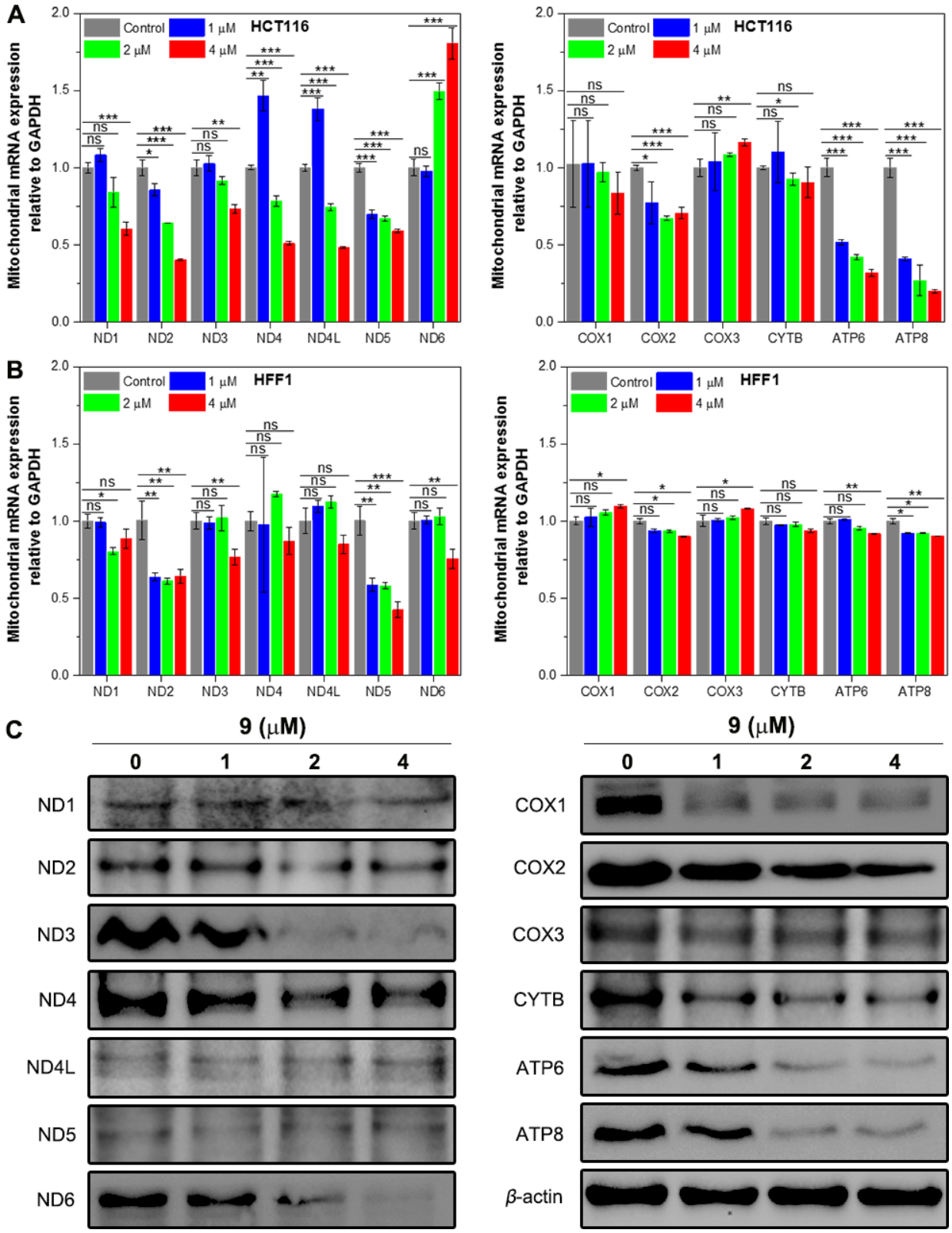

Figure 6.2. qRT-PCR study for the transcription and translation effects of **9**. (A) The influence of **9** (0-4 μM) on the transcription of the selected mitochondrial genes in HCT116 cells (cancer cell line). The incubation time was 48 h. (B) qRT-PCR study for the influence of 9 (0-4 μM) on the transcription of the selected mitochondrial genes in HFF1 cells (normal cell line). The incubation time was 48 h. The data are presented as mean ± SEM. (C) Western blot assays to determine the protein expression level of ND1, ND2, ND3, ND4, ND4L, ND5, ND6, COX1, COX2, COX3, CYTB, ATP6, ATP8 and *β*-actin in HCT116 cells treated with 9 (0-4 μM) for 48 h, and statistics were determined using ANOVA, *$p < 0.05$, **$p < 0.01$ and ***$p < 0.001$.

To assess the influence of ligand **9** on mitochondrial gene transcription, we investigated 13 key mitochondrial genes associated with oxidative phosphorylation using real-time quantitative reverse transcription PCR (qRT-PCR) in both HCT116 and HFF1 cells. The results revealed significant differences in transcriptional activity between the two cell types (**Figure 6.2 A** and **B**). In HCT116 cells, the treatment with ligand **9** led to a considerable decrease in mRNA levels for *ND1*, *ND2*, *ND3*, *ND4*, *ND4L*, *ND5*, *COX2*, *ATP6*, and *ATP8*. In contrast, the effect of ligand **9** on HFF1 cells was notably different, with only *ND2* and *ND5* showing significant reductions. Additionally, Western blotting assays indicated a marked decrease in protein levels of ND3, ND4, ND6, COX1, COX2, COX3, CYTB, ATP6, and ATP8 in HCT116 cells treated with ligand **9** (**Figure 6.2 C**). Since these 13 mitochondrial genes are subunits of the five complexes that constitute the mitochondrial respiratory chain, ligand **9** may also lead to the downregulation of these complexes. As anticipated, Western blot results demonstrated a significant reduction in the levels of complexes I, II, III, and IV in HCT116 cells treated with ligand **9** (**Figure 6.3**). Overall, ligand **9** selectively binds to G4-mtDNA targets in mitochondria with high affinity, effectively inhibiting the replication, transcription, and translation of mtDNA in HCT116 cells.

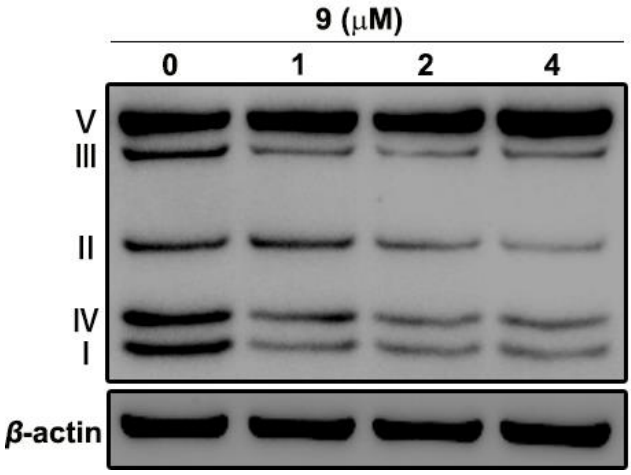

Figure 6.3. Western blot assays to determine the translation of complex I-V and *β*-actin in HCT116 cells after treating with ligand **9** (0-4 μM) for 48 h.

6.2.2 Study the effect of ligand **9** in causing mitochondrial dysfunction

To determine if ligand **9** disrupted mitochondrial functions, we investigated changes in the mitochondrial membrane potential (MMP) of HCT116 cells treated with the ligand. As shown in **Figure 6.4 A**, cells treated with ligand **9** were stained with the TMRE dye (tetramethylrhodamine ethyl ester), revealing an obvious concentration-dependent decrease in TMRE staining intensity. This reduction indicates a decline in MMP, likely due to the depolarization caused by the di-cationic nature

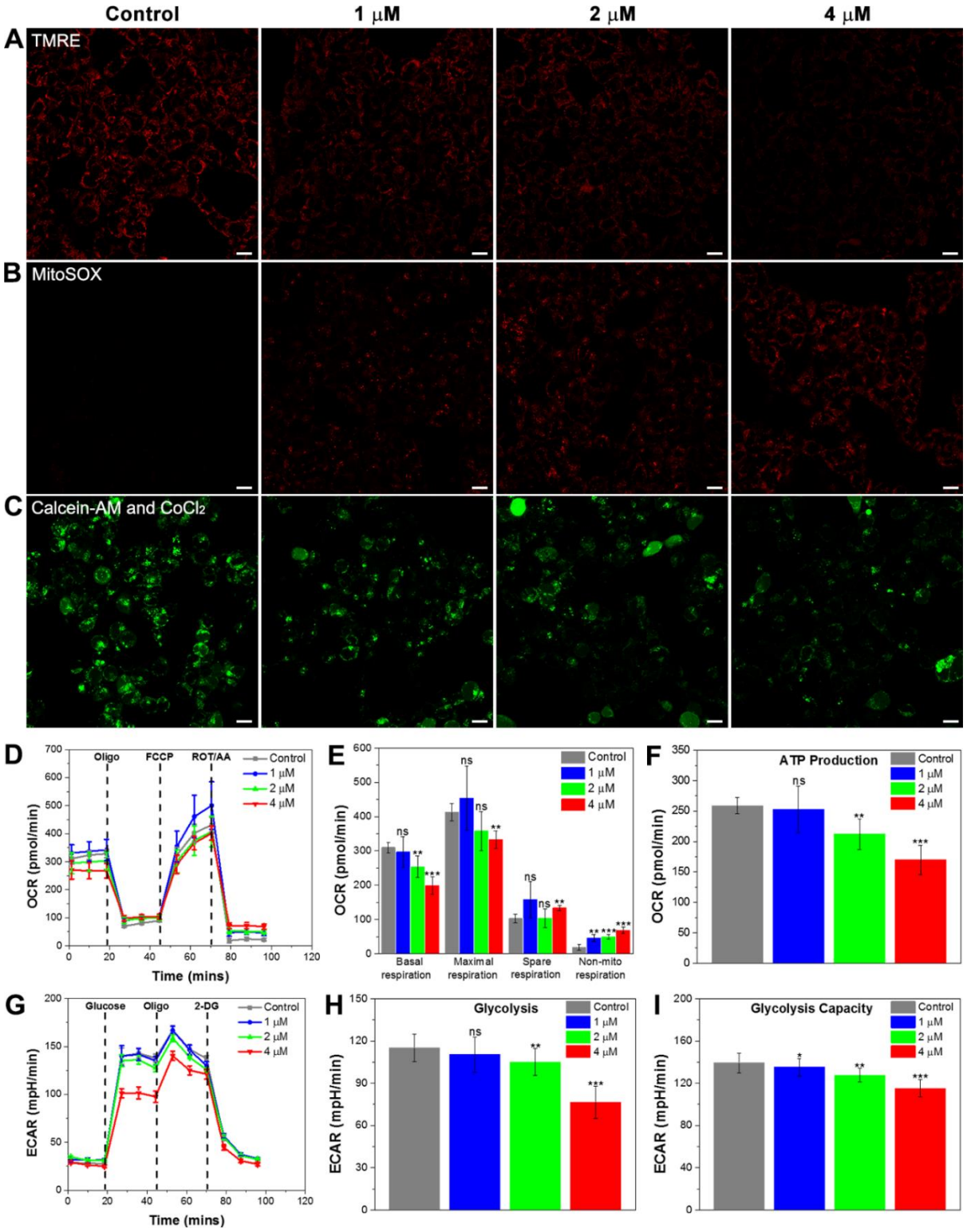

Figure 6.4. (A) Single confocal plane images: The effect of **9** (0-4 μM) on MMP in HCT116 cells. The scale bar is 10 μm. (B) Single confocal plane images: Ligand **9** (0-4 μM) induces ROS production in HCT116 cells. The scale bar is 10 μm. (C) Single confocal plane images: The effect of **9** (0-4 μM) on mPTP opening in HCT116 cells. The scale bar is 10 μm. (D) Seahorse experiment to study OCR of HCT116 cells treated with **9** (0-4 μM) for 3 h in response to electron transfer chain inhibitors (n=5). (E) Values of the basal respiration, maximal respiration, spare respiratory and non-mitochondrial respiration capacity. (F) The analysis of ATP production of **9**-treated cells. (G) Seahorse experiment to study ECAR of HCT116 cells treated with **9** (0-4 μM) for 3 h in response to glucose stimulation (n=5). (H) Changes in glycolysis. (I) Changes of glycolysis capacity. The data are presented as mean ± SEM, and statistics were determined using ANOVA, *$p < 0.05$, **$p < 0.01$ and ***$p < 0.001$.

of ligand **9**. Next, we assessed reactive oxygen species (ROS) production in HCT116 cells treated with ligand **9** using the mitochondrial ROS probe MitoSOX. As shown in **Figure 6.4 B**, ligand **9** increased ROS levels in a concentration-dependent manner. The elevated ROS levels could potentially lead to DNA damage within the cells. In summary, these results suggest that ligand **9** may downregulate the expression of the five complexes of the mitochondrial respiratory chain, leading to mitochondrial dysfunction. Furthermore, ligand **9** appears to promote the opening of the mitochondrial permeability transition pore (mPTP) in HCT116 cells in a dose-dependent manner (**Figure 6.4 C**), which may facilitate the ligand's entry into the mitochondria.

To further confirm the effect of ligand **9** on mitochondrial dysfunction in HCT116 cells, we performed both Mito-stress and glycolysis stress tests on the cells treated with the ligand. The oxygen consumption rate (OCR) and extracellular acidification rate (ECAR) in HCT116 cells were measured after 3 hours of treatment. The results indicated significant reductions in OCR, ECAR, ATP production, and glycolysis (**Figure 6.4 D-I**). These findings suggest that ligand **9** inhibits both oxidative phosphorylation and glycolysis in HCT116 cells. Subsequently, the ability of the cells in energy production may be inhibited due to the significantly reduced mitochondrial performance and eventually it may cause cellular senescence.

6.2.3 Study the effect of ligand **9** in inducing DNA damage and cellular senescence

We observed that ligand **9** significantly increased mitochondrial ROS levels in HCT116 cells. To determine whether this could lead to DNA damage, Comet assays were performed, which revealed that ligand **9** caused DNA damage, as evidenced by the lengthened comet tails in treated HCT116 cells (**Figure 6.5 A** and **Figure 6.6 C**). Additionally, the markedly increased levels of γ-H2AX protein further confirmed that ligand **9** induces DNA damage in HCT116 cells (**Figure 6.5 G**). To verify that mtROS production induced by ligand **9** is the major trigger in causing DNA damage, we employed Mito-TEMPOL, a mitochondria-targeted antioxidant, to lower mtROS levels in HCT116 cells treated with ligand **9**. As shown in **Figure 6.6 A**, the level of mtROS induced by **9** was inhibited significantly in the presence of Mito-TEMPOL. Furthermore, the Comet assay (**Figure 6.6 B**) demonstrated that the DNA damage caused by ligand **9** was also reduced in HCT116 cells treated with Mito-TEMPOL, as shown by the significant decrease in tail moment length (**Figure 6.6 C**). Moreover, in HCT116 cells treated with Mito-TEMPOL, the DNA damage marker γ-H2AX was downregulated (**Figure 6.6**

D). Therefore, the mtROS induced by ligand **9** appears to be the primary trigger of DNA damage in HCT116 cells.

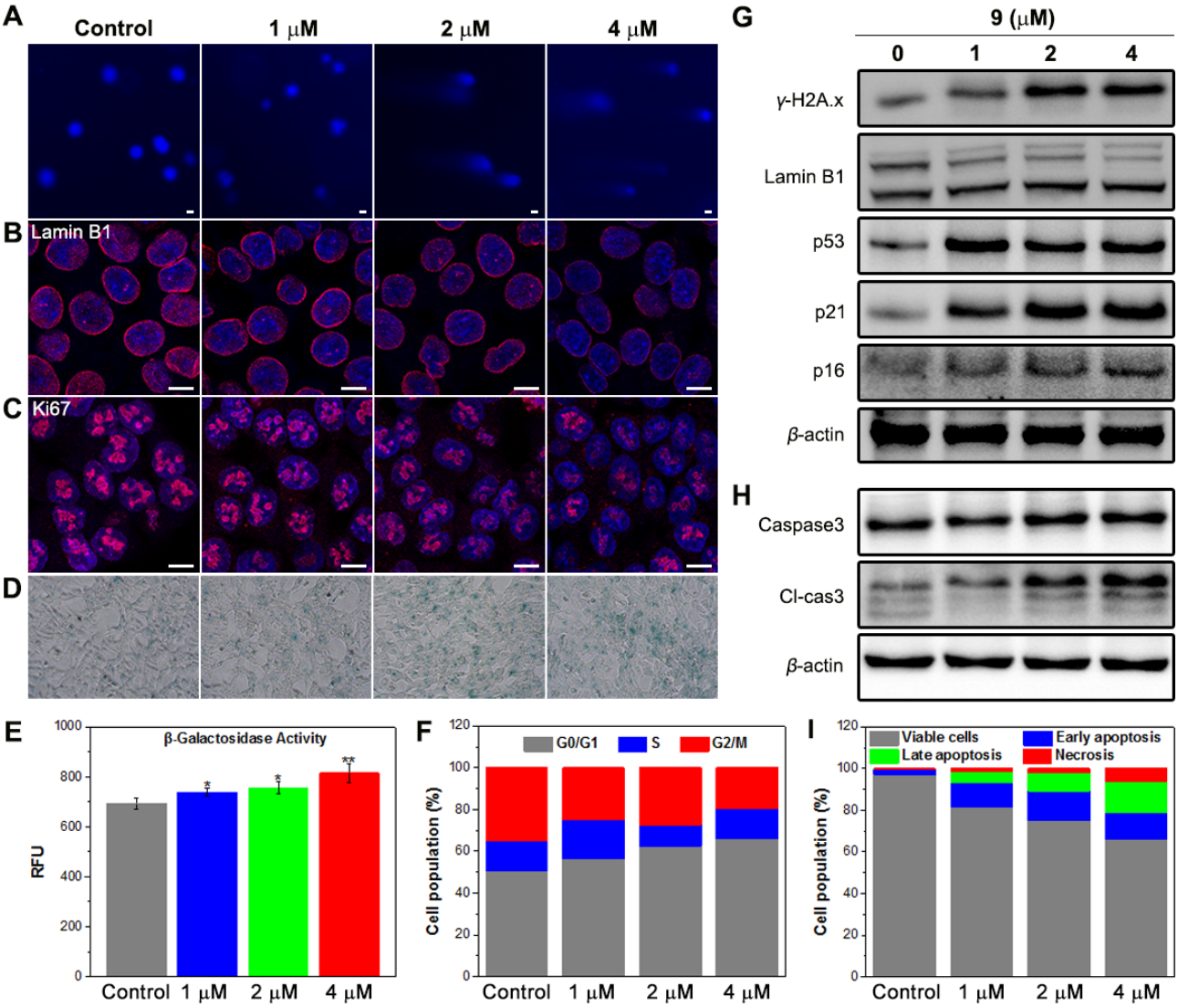

Figure 6.5. (A) Comet assay to analyze DNA damage induced by **9** (0-4 μM) for 72 h treatment in the cells. The cell was stained by DAPI (λ_{ex}=405 nm). The scale bar is 10 μm. The lengthened comet tail image indicates DNA damage. (B) Immunofluorescence analysis of Lamin B1 (λ_{ex}=635 nm) in HCT116 cells after **9** (0-4 μM) treatment for 72 h. The scale bar is 10 μm. (C) Immunofluorescence analysis of Ki67 (λ_{ex}=635 nm) in HCT116 cells after **9** (0-4 μM) treatment for 72 h. The scale bar is 10 μm. (D) SA-*β*-gal assay was used to detect the senescence of HCT116 cells after **9** (0-4 μM) treatment for 72 h. (E) *β*-galactosidase activity of HCT116 cells after **9** (0-4 μM) treatment for 72 h. The data are presented as mean ± SEM, and statistics were determined using ANOVA, *$p < 0.05$, **$p < 0.01$ and ***$p < 0.001$. (F) Cell cycle analysis of HCT116 cells treated with **9** (0-4 μM) for 72 h. (G) Western blot assays to determine the translation of Lamin B1, p53, p21, p16, *γ*-H2A.x, and *β*-actin in HCT116 cells treated with **9** (0-4 μM) for 72 h. (H) Western blot assays to determine the translation of Caspase3, Cleaved-caspase3 and *β*-actin in HCT116 cells after **9** (0-4 μM) treatment for 72 h. (I) Cell apoptosis analysis of HCT116 cells treated with **9** (0-4 μM) for 72 h. The cells were stained by Annexin V-BUV396 and 7-AAD.

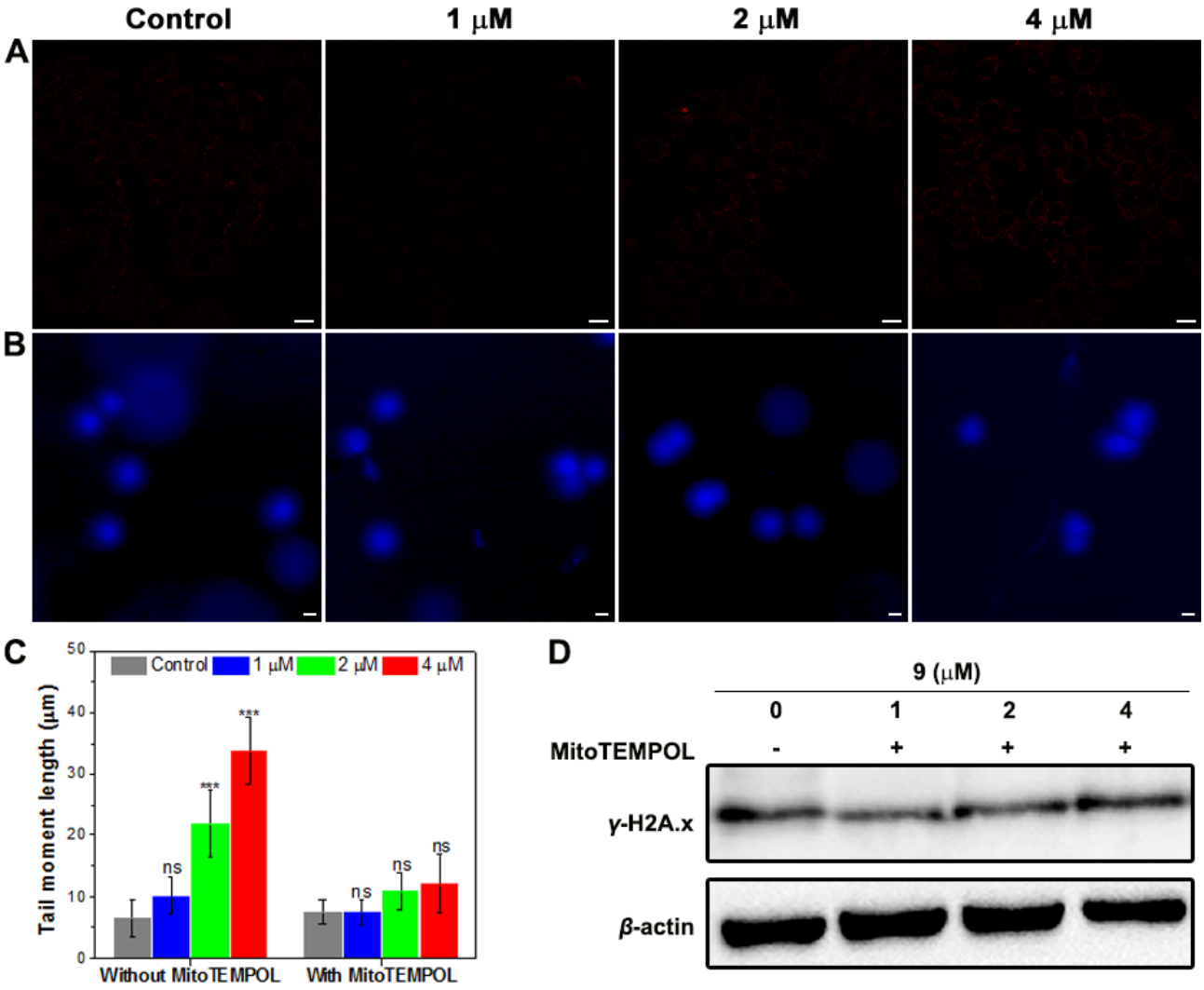

Figure 6.6. (A) Single confocal plane images: Mitochondrial ROS production in HCT116 cells was detected by MitoSOX (λ_{ex}=405 nm) after the treatment with **9** (0-4 μM) and 10 μM Mito-TEMPOL for 48 h. The cells were stained by DAPI (λ_{ex}=405 nm). The scale bar is 10 μm. (B) Comet assay to analyze DNA damage in HCT116 cells after **9** (0-4 μM) and 10 μM Mito-TEMPOL treatment for 72 h, the cells were stained by DAPI (λ_{ex}=405 nm). The scale bar is 10 μm. The lengthened comet tail image indicates DNA damage. (C) The quantification of tail moment length in Comet assay. The data are presented as mean ± SEM, and statistics were determined using ANOVA, $*p < 0.05$, $**p < 0.01$ and $***p < 0.001$. (D) Western blot assays to determine the translation of *γ*-H2A.x, and *β*-actin in HCT116 cells treated with **9** (0-4 μM) and 10 μM Mito-TEMPOL for 72 h.

Cellular senescence is a state of stable cell cycle arrest under which cells remain metabolically active, but no longer divide and do not respond to growth-promoting stimuli. Senescence can be triggered by various factors including oxidative stress, DNA damage, and mitochondrial dysfunction.[2-4] The above results suggest that ligand **9** induces mitochondrial dysfunction, elevates ROS production, and causes DNA damage in HCT116 cells. Consequently, we hypothesize that ligand **9** may also promote cellular senescence. Lamin B1, a structural component of the nuclear membrane, serves as a well-established biomarker for cellular senescence.[5] Our immunofluorescence and Western blot results

revealed a significant reduction in Lamin B1 protein levels in HCT116 cells treated with ligand **9** in a concentration-dependent manner (**Figure 6.5 B** and **G**). Also, the proliferation marker Ki67 was markedly decreased in the cells treated with ligand **9** (**Figure 6.5 C**), indicating that ligand **9** inhibited HCT116 cell growth. Furthermore, **9** was applied in SA-β-gal assays to study its effect on senescence of HCT116 cells. As shown in **Figure 6.5 D**, it is obvious that **9** is positive in the SA-β-gal staining. Besides, the β-galactosidase activity of HCT116 cells was found to increase by 6.61%-17.63% after the treatment with ligand **9** (**Figure 6.5 E**), suggesting that approximately 17.63% of the cells ultimately entered a senescent state.

Cell cycle analysis revealed that HCT116 cells treated with ligand **9** were arrested in the G0/G1 phase. The proportion of cells in the G0/G1 phase increased from 50.66% to 66.01% in a concentration-dependent manner (**Figure 6.5 F**). Additionally, the levels of cell cycle inhibitors p53, p21, and p16 were found to be upregulated in the treated cells (**Figure 6.5 G**). The apoptosis marker cleaved-caspase 3 also exhibited a significant increase in HCT116 cells treated with ligand **9** (**Figure 6.5 H**). Furthermore, staining the HCT116 cells with Annexin V-BUV396 and 7-AAD demonstrated that ligand **9** induces apoptosis in a dose-dependent manner, with the percentage of apoptotic cells rising from 2.64% to 27.4% (**Figure 6.5 I**). Collectively, these findings indicate that ligand **9** leads to significant mitochondrial dysfunction and DNA damage in HCT116 cells, ultimately resulting in cellular senescence and apoptosis.

4.2.4 RNA-sequencing analysis indicating ligand **9** targeting mitochondria in HCT116 cells

To gain further insights into the cellular targets of ligand **9** in HCT116 cells, we conducted RNA sequencing on cells treated with 4 μM of the ligand, using DMSO as a control. The heatmap provided an overview of the differentially expressed genes (**Figure 6.7 A**). We found that only about 3% of the total genes were affected by ligand **9**, with 0.8% of the genes being upregulated and 2.2% downregulated, based on a log2 fold change of > 2 or < -2 and a padj < 0.05. These findings indicate that the targets of ligand **9** in HCT116 cells are relatively specific and thus low off-target effects could be expected. Among the affected genes, 20 of them were located in the mitochondria, with 13 showing downregulation and 7 upregulation, based on a log2 fold change of > 2 or < -2 and a padj < 0.05 (**Figure 6.7 B**). Notably, of the 13 genes associated with the mitochondrial respiratory chain, the majority were downregulated. The finding is consistent with the results of qRT-PCR and Western

blotting shown in **Figure 6.2**. More importantly, many of these downregulated genes contain G-rich sequences that exhibit a strong tendency to form G4 structures, which may serve as potential targets for ligand **9**. The stabilization of these G4-mtDNA structures by ligand **9** in cells could inhibit gene expression at both transcriptional and translational levels.

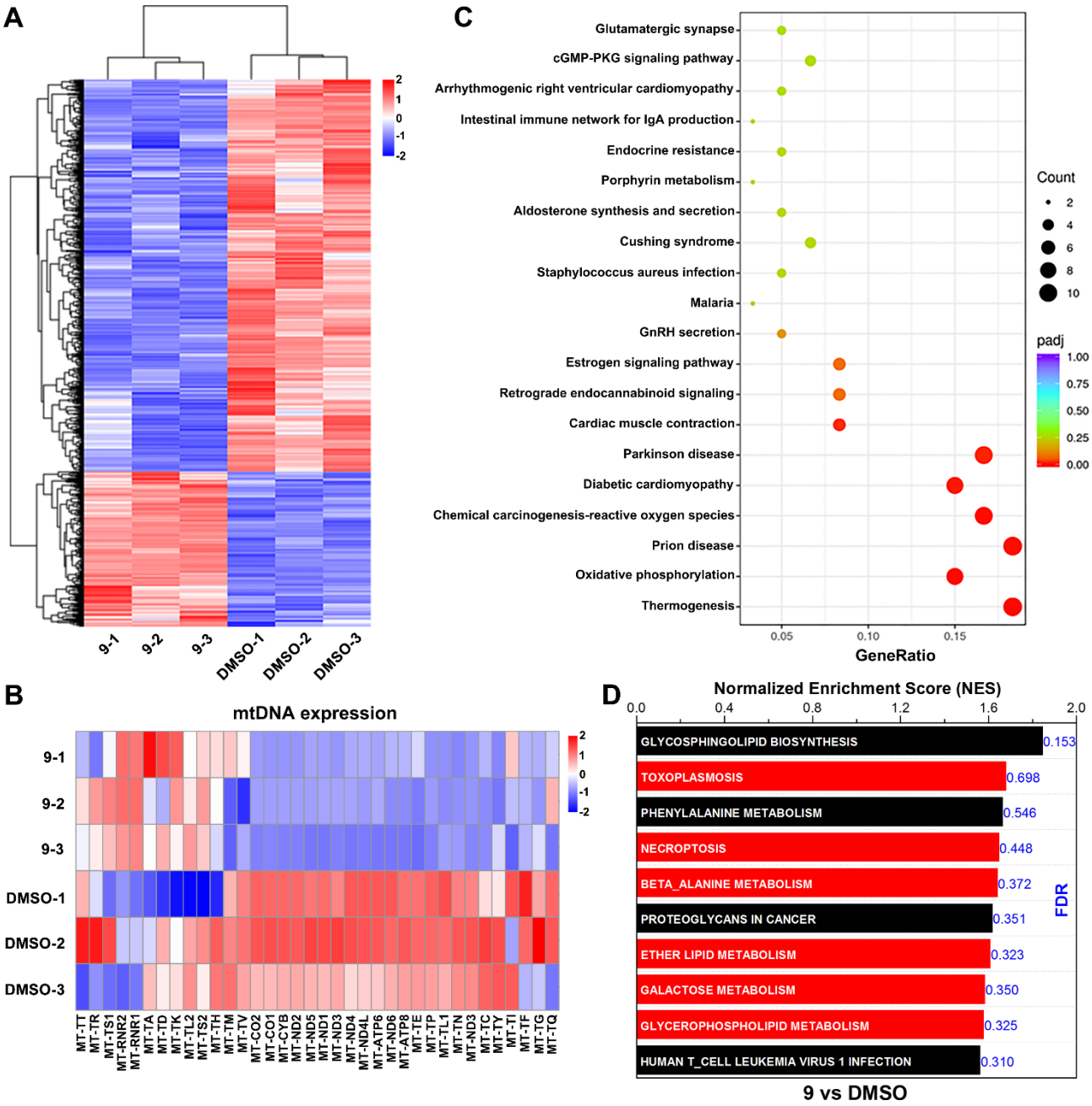

Figure 6.7. RNA-sequencing analysis. (A) Heatmap showing the expression pattern in HCT116 cells treated with 4 μM ligand **9** (vs 0.08% DMSO). Genes are clustered using hierarchical clustering. Red indicates higher expression, and blue indicates lower expression. Color bar indicates row Z score. (B) Heatmap showing the effect of 4 μM ligand **9** on mtDNA expression after 48 h treatment as determined by RNA-Seq. (C) KEGG enrichment analysis of genes change after 4 μM ligand **9** treatment. The size of bubbles represents the number of genes in each term. (D) The top 10 significantly enriched pathways in HCT116 cells treated with 4 μM ligand **9** (versus 0.08% DMSO).

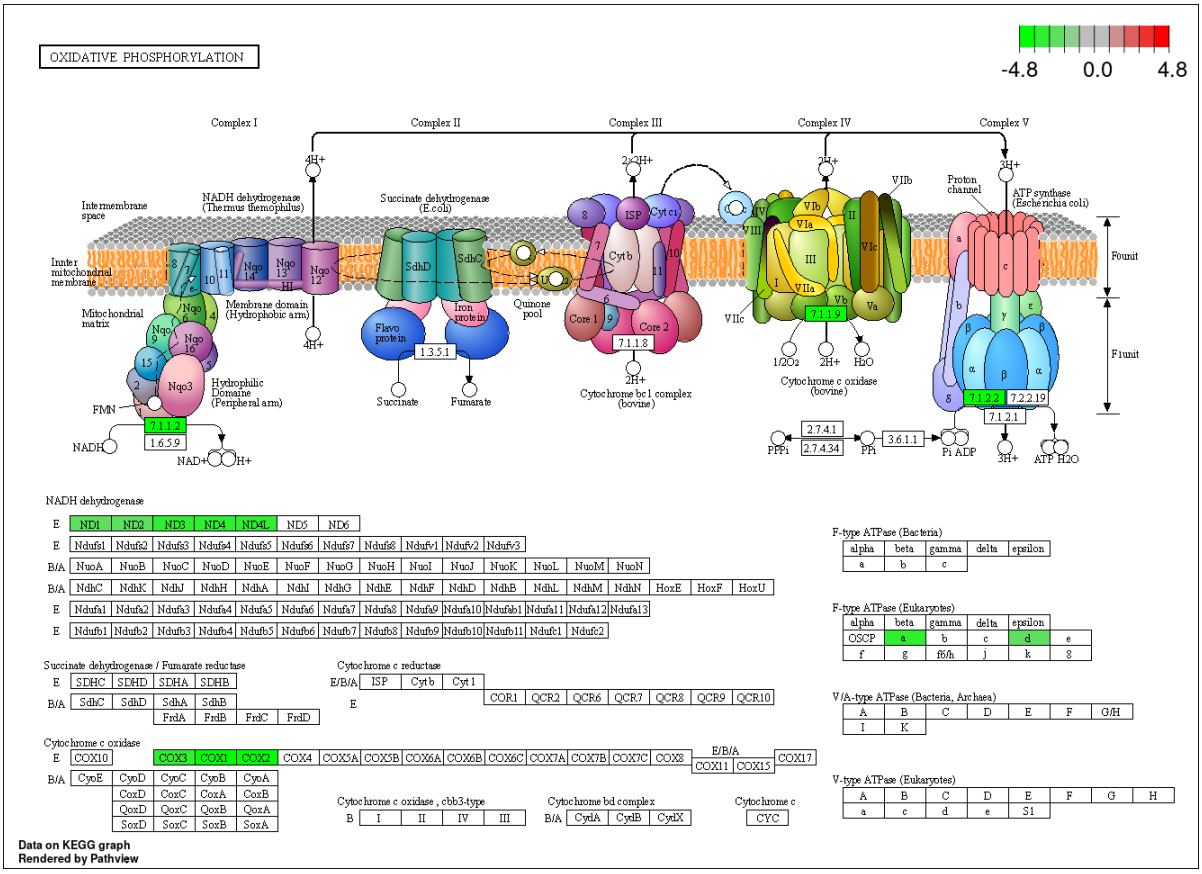

Figure 6.8. RNA-sequencing analysis. The effect of **9** at 4 μM vs 0.08 % DMSO on oxidative phosphorylation related gene expression (KEGG) in HCT116 cells after 48 h treatment.

For the enrichment and differential analysis, the Kyoto Encyclopedia of Genes and Genomes (KEGG) enrichment results are presented in **Figure 6.7 C**. Among the 20 most significantly affected KEGG pathways identified in the RNA-seq data, oxidative phosphorylation was notably influenced (**Figure 6.8**). Additionally, gene set enrichment analysis (GSEA) revealed that six mitochondria-related pathways (in red) were among the top 10 significantly enriched pathways influenced by ligand 9 (**Figure 6.7 D**). These pathways include toxoplasmosis, necroptosis, *β*-alanine metabolism, ether lipid metabolism, galactose metabolism, and glycerophospholipid metabolism, all of which are associated with mitochondrial function. The ROS produced by mitochondria are closely linked to toxoplasmosis and necroptosis.[6, 7] Since ligand **9** induces ROS production in mitochondria within HCT116 cells, these two pathways may be affected. Additionally, ether lipids play crucial roles in protecting mitochondria from oxidative stress.[8] The increased ROS levels caused by ligand **9** could thus impact ether lipid metabolism. Moreover, *β*-alanine and galactose are directly associated with oxidative phosphorylation.[9, 10] We have confirmed that ligand **9** downregulates oxidative phosphorylation in HCT116 cells, suggesting that the metabolism of *β*-alanine and galactose may also be affected in these treated cells. In addition, mitochondria are responsible for synthesizing

various phospholipids, including cardiolipin, phosphatidylglycerol, and phosphatidylethanolamine.[11] Therefore, the mitochondrial dysfunction induced by ligand **9** may influence glycerophospholipid metabolism. Collectively, the RNA-seq analysis indicates that ligand **9** specifically targets mitochondrial in HCT116 cells.

6.2.5 Study the antitumor efficacy of ligand **9** *in vitro* and *in vivo*

To further assess the *in vitro* anticancer effects of ligand **9** on colorectal cancer cells, we conducted trans-well and colony formation assays to study its impact on the morphology, migration, and colony formation of HCT116 cells. As illustrated in **Figure 6.9 A**, the morphology of HCT116 cells and HFF1 cells treated with 4 μM of ligand **9** exhibited clear differences. Obviously, ligand **9** induced significantly more cell death in HCT116 cells compared to HFF1 cells. Moreover, migration of HCT116 cells was inhibited by ligand **9**, resulting in a reduction of 40% (**Figure 6.9 B** and **C**). Additionally, the proliferation of HCT116 cells treated with ligand **9** decreased markedly in a concentration-dependent manner (**Figure 6.9 D**), with nearly complete suppression observed at 4 μM (**Figure 6.9 E**). Collectively, these findings indicate that ligand **9** demonstrates strong anticancer activity against human colorectal cancer.

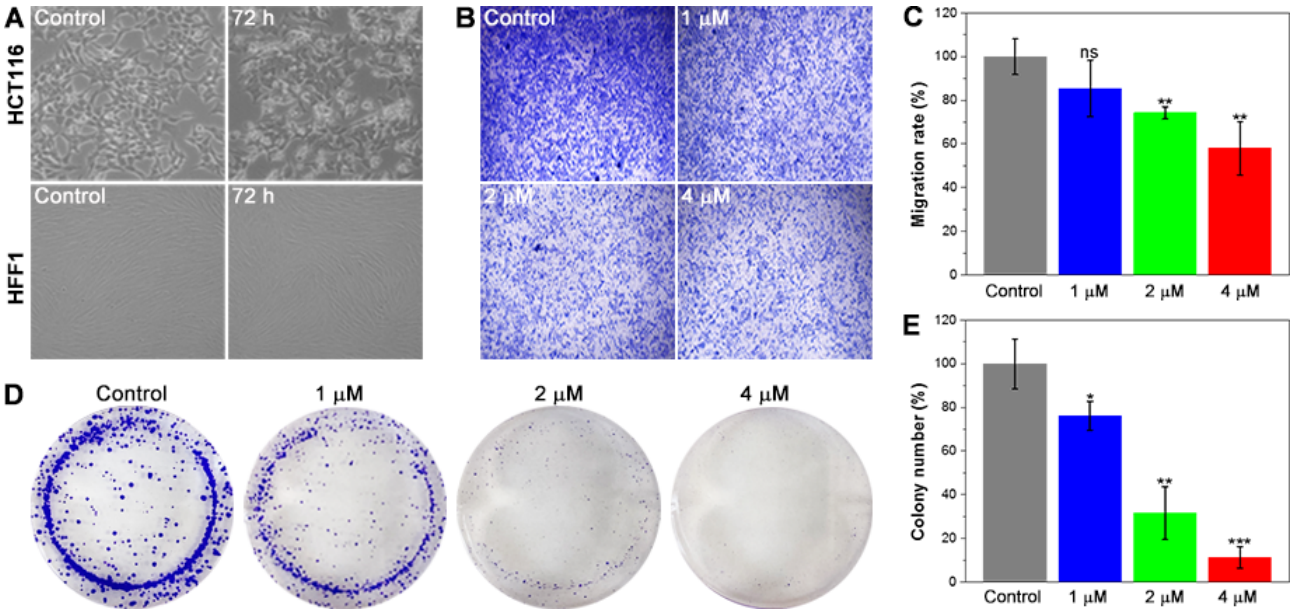

Figure 6.9. (A) The study of cell morphology for HCT116 and HFF1 cells treated with **9** (4 μM) and without **9** treatments (control). (B) The migration of HCT116 was treated with **9** for 72 h at a concentration of 0, 1, 2, 4 μM by Trans-well assay. (C) The quantification of the Trans-well assay. Data are expressed as mean ± SD. (D) The inhibition of cancer cell proliferation. HCT116 cells were treated with ligand **9** for 7 days at a concentration of 0, 1, 2, 4 μM, and their clone formation were determined. (E) The quantification of the colony-forming assay. The data are presented as mean ± SEM, and statistics were determined using ANOVA, *$p < 0.05$, **$p < 0.01$ and ***$p < 0.001$.

The pharmacokinetic (PK) properties of ligand **9** were investigated in Sprague–Dawley rats following a tail vein injection at a dose of 2.5 mg/kg. As shown in **Figure 6.10** and **Table 6-1**, ligand **9** demonstrated favorable pharmacokinetic (PK) profiles, characterized by high plasma exposure ($AUC_{0-\infty}$ = 1462 h*ng/mL) and a suitable half-life ($T_{1/2}$ = 2.55 h). Moreover, ligand **9** was almost entirely metabolized within approximately 6 hours, suggesting that it can be cleared from the body within this timeframe, thereby potentially reducing *in vivo* adverse reactions and side effects associated with the ligand.

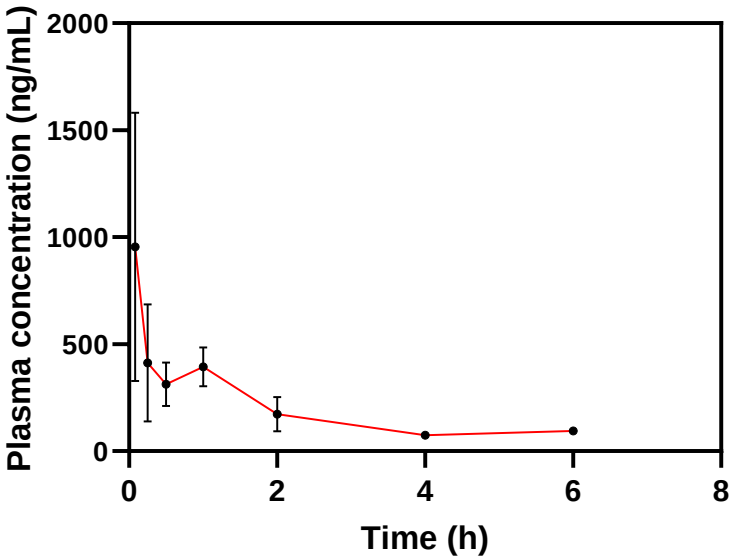

Figure 6.10. Mean blood concentration–time profiles of ligand **9** in Sprague–Dawley rats after tail vein injection (2.5 mg/kg) (n = 3). The data are presented as the means ± SD.

Table 6-1. The pharmacokinetic property of ligand **9** in rats.[a]

Parameter	Unit	Rat 1	Rat 2	Rat 3	Mean±SD
$T_{1/2}$[b]	h	2.63	2.63	2.39	2.55±0.14
C_0	ng/mL	319	2427	1711	1486±1072
AUC_{0-t}[c]	h*ng/mL	1113	2062	1212	1462±522
$AUC_{0-\infty}$	h*ng/mL	1352	2337	1448	1712±543
AUC Extrapolated	%	17.66	11.78	16.30	15.24±3.08
CL[d]	mL/h/kg	1849	1070	1727	1548±419
$MRT_{0-\infty}$[e]	h	4.11	4.94	3.83	4.30±0.58
Vd[f]	mL/kg	7608	5284	6615	6503±1166

[a] The ligand dose was 2.5 mg/kg by tail vein injection; [b] Plasma elimination half-life; [c] Plasma exposure; [d] Clearance rate; [e] Mean residence time; [f] Apparent volume of distribution.

A human HCT116 tumor xenograft mouse model was employed to evaluate the *in vivo* antitumor efficacy of ligand **9**. Two groups of male Balb/c nude mice bearing HCT116 tumors (6 mice per group) were injected intravenously every two days, with Group 1 receiving PBS and Group 2 receiving ligand **9** at a dose of 5 mg/kg. The *in vivo* results indicated that the 5 mg/kg dosage did not influence the overall growth of the mice, as there were no significant changes in body weight between the two groups (**Figure 6.11 A**). However, ligand **9** significantly inhibited tumor growth (**Figure 6.11 B-E**), with a reduction of approximately 70% in tumor weight compared to the control group. Additionally, analysis of tumor tissues from the mice revealed clear nuclear sequestration and fragmentation in H&E staining images when compared to the control group. TUNEL staining further demonstrated that ligand **9** promoted apoptosis in tumor cells. Furthermore, Ki67 staining assays indicated a marked inhibition of tumor cell proliferation in the presence of ligand **9** (**Figure 6.11 F**). Overall, these *in vivo* results suggest that ligand **9** exhibits strong anti-timor potency against human colorectal cancer.

To further evaluate the biocompatibility and *in vivo* toxicity of **9**, whole blood samples were collected for biochemical blood analysis when mice were killed on day 16. The analyzed biochemical parameters included white blood cell count, lymphocyte count, neutrophil count, red blood cell count, hemoglobin levels, mean red blood cell volume, mean red blood cell hemoglobin content, mean red blood cell hemoglobin concentration, mean platelet volume, and platelet count. The results, showed in **Figure 6.12 A**, show no significant changes in any of the biochemical parameters for the mice treated with ligand **9** compared to the control group. Importantly, H&E staining of major organs such as the heart, liver, spleen, lungs, and kidneys supported that ligand **9** likely has low or observabl toxic effects on these organs (**Figure 6.12 B**). Consequently, ligand **9** shows strong potential as a new and effective anti-colorectal cancer agent, with the capacity to target both mitochondria and G4-mtDNA structures while exhibiting low *in vivo* cytotoxicity.

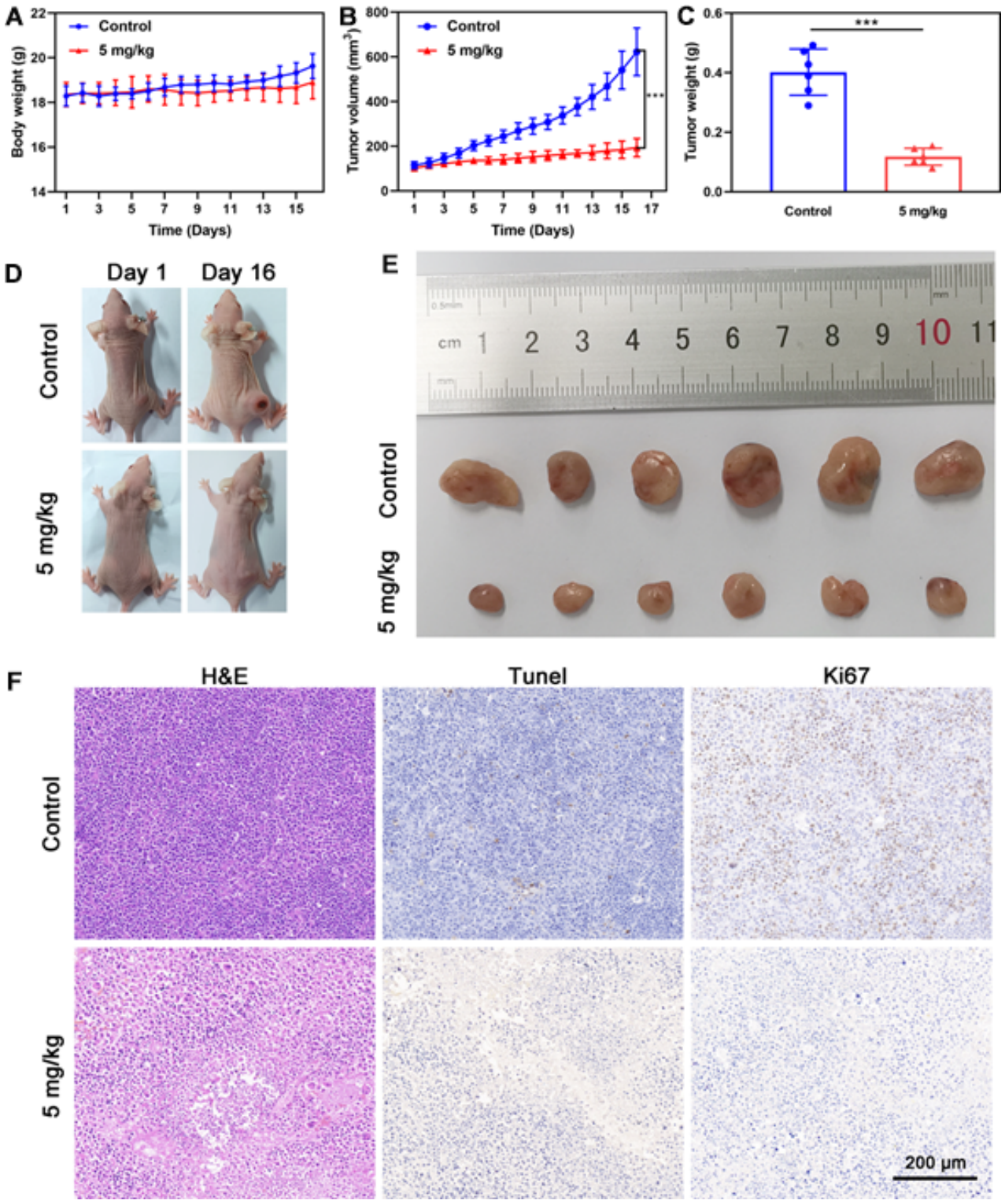

Figure 6.11. The evaluation of *in vivo* antitumor efficacy of **9**. (A) Body weight change of HCT116 tumor-bearing nude mice injected with **9** (5 mg/kg) in tail vein over 16 days (n=6). (B) Time-dependent change of tumor volume after different treatments for 16 days (n=6) (C) Weight of isolated tumors in HCT116 tumor-bearing nude mice after 16 days of treatment (n=6). (D) Digital photographs of HCT116 tumor-bearing nude mice on day 1 and day 16 of different groups. (E) Digital photographs of isolated tumors from different groups of HCT116-bearing nude mice after 16 days. (F) Representative histological images of H&E, TUNEL and Ki67 antigen immunofluorescence-stained tumor tissue sections of HCT116 tumor-bearing nude mice tumors from different groups after 16 days of treatment. The scale bar is 200 μm. The data are presented as mean ± SEM, and statistics were determined using ANOVA, *$p < 0.05$, **$p < 0.01$ and ***$p < 0.001$.

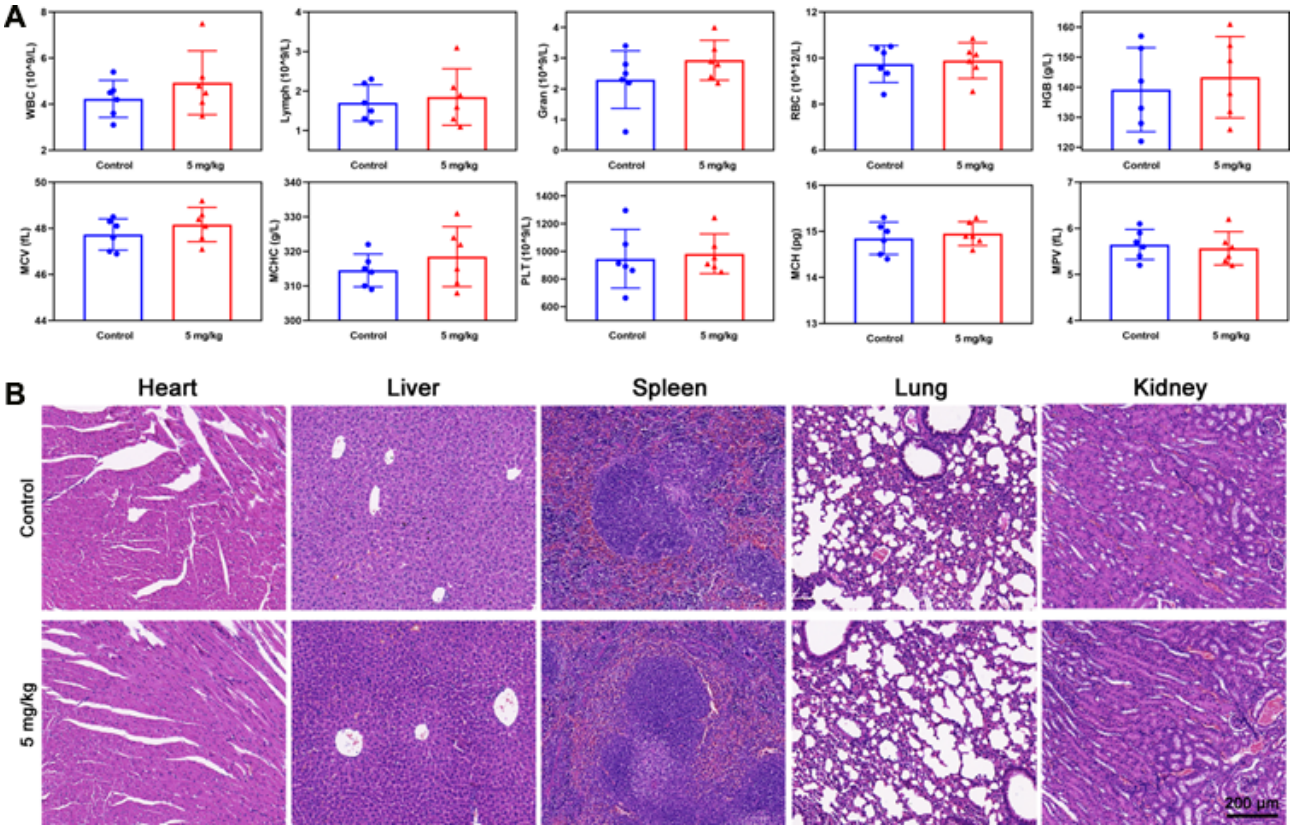

Figure 6.12. Effects on normal tissues and blood of nude mice after injection of **9**. (A) Biochemical blood analysis of the ligands-treated mice 16 days post-injection under various conditions (n = 6, mean ± SD). (B) H&E-stained images of the major organs (heart, liver, spleen, lung, and kidney) from different groups. The scale bar is 200 μm.

6.3 Summary

In conclusion, a new small-sized di-cationic ligand **9** tailored with the functionality of mitochondria-selective and G4-mtDNA-targeting was developed and demonstrated in living human colorectal cancer cells (HCT116). The results from qRT-PCR and Western blot analyses indicated that ligand **9** significantly downregulates the expression of several genes associated with the mitochondrial respiratory chain, including *ND3*, *ND4*, *ND6*, *COX1*, *COX2*, *COX3*, *CYTB*, *ATP6*, and *ATP8*. Additionally, it inhibits the expression of respiratory chain complexes I-IV. Furthermore, ligand **9** induces considerable mitochondrial dysfunction, characterized by depolarization of the mitochondrial membrane potential, increased ROS production, mPTP opening, and downregulation of both oxidative phosphorylation and glycolysis. More importantly, the ligand induced DNA damage, cellular senescence, and apoptosis in HCT116 cancer cells. In the evalution of *in vitro* antitumor efficacy of ligand **9**, results from trans-well and colony formation assays demonstrated that ligand **9** effectively inhibits both the migration and proliferation of HCT116 cells. The proposed anticancer mechanism of ligand **9** against human colorectal cancer cells HCT116 is illustrated in **Figure 6.13.**

In addition, the *in vivo* antitumor efficacy of the ligand against human colorectal cancer xenografts (HCT116) in nude mice was also validated. The ligand at 5 mg/kg was able to reduce the tumor weight by 70% compared to the control. Overall, this di-cationic ligand serves as a G4-mtDNA-targeting anticancer agent for the treatment of human colorectal cancer, exhibiting high potency and low toxicity. The mechanism of action of ligand **9** may provide valuable insights for drug discovery against human cancers.

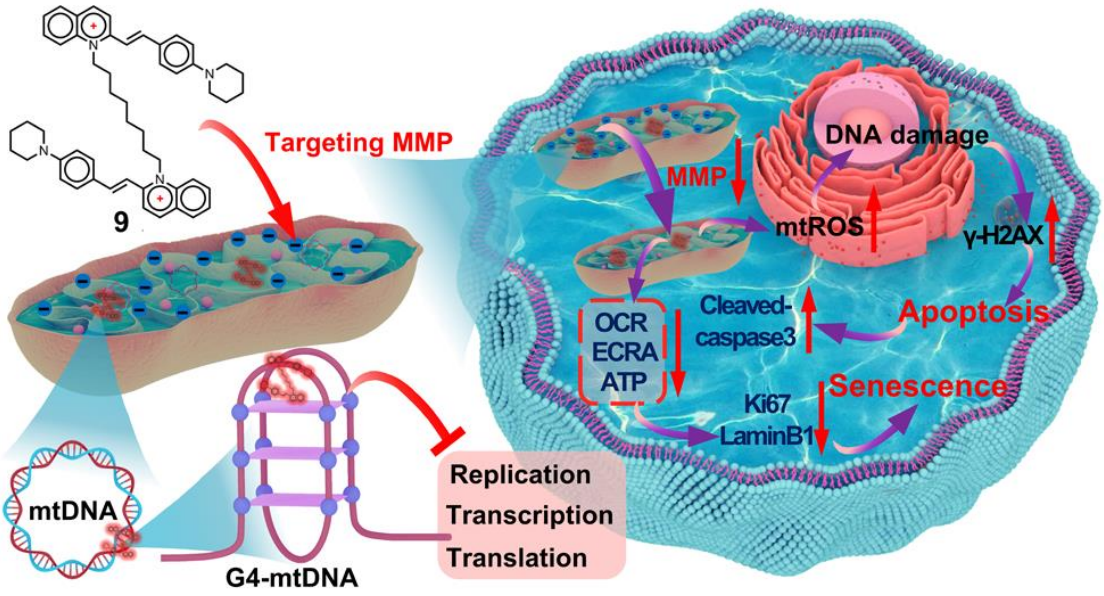

Figure 6.13. The proposed anticancer mechanism of ligand **9** in human colorectal cancer cells HCT116.

6.4 References

[1] K. Agaronyan, Y.I. Morozov, M. Anikin, D. Temiakov, Mitochondrial biology. Replication-transcription switch in human mitochondria, Science 347(6221) (2015) 548-51.

[2] F. Rodier, J. Campisi, Four faces of cellular senescence, Journal of Cell Biology 192(4) (2011) 547-556.

[3] S. He, N.E. Sharpless, Senescence in health and disease, Cell 169(6) (2017) 1000-1011.

[4] S. Miwa, S. Kashyap, E. Chini, T. von Zglinicki, Mitochondrial dysfunction in cell senescence and aging, The Journal of clinical investigation 132(13) (2022).

[5] A. Freund, R.-M. Laberge, M. Demaria, J. Campisi, Lamin B1 loss is a senescence-associated biomarker, Molecular biology of the cell 23(11) (2012) 2066-2075.

[6] K. Szewczyk-Golec, M. Pawłowska, R. Wesołowski, M. Wróblewski, C. Mila-Kierzenkowska,

Oxidative stress as a possible target in the treatment of toxoplasmosis: perspectives and ambiguities, International journal of molecular sciences 22(11) (2021) 5705.

[7] Y. Zhang, S.S. Su, S. Zhao, Z. Yang, C.-Q. Zhong, X. Chen, Q. Cai, Z.-H. Yang, D. Huang, R. Wu, RIP1 autophosphorylation is promoted by mitochondrial ROS and is essential for RIP3 recruitment into necrosome, Nature communications 8(1) (2017) 14329.

[8] Z. Chen, I.-L. Ho, M. Soeung, E.-Y. Yen, J. Liu, L. Yan, J.L. Rose, S. Srinivasan, S. Jiang, Q. Edward Chang, Ether phospholipids are required for mitochondrial reactive oxygen species homeostasis, Nature communications 14(1) (2023) 2194.

[9] L. Shi, B.P. Tu, Acetyl-CoA and the regulation of metabolism: mechanisms and consequences, Current opinion in cell biology 33 (2015) 125-131.

[10] C. Aguer, D. Gambarotta, R.J. Mailloux, C. Moffat, R. Dent, R. McPherson, M.-E. Harper, Galactose enhances oxidative metabolism and reveals mitochondrial dysfunction in human primary muscle cells, PloS one 6(12) (2011) e28536.

[11] E.M. Mejia, G.M. Hatch, Mitochondrial phospholipids: role in mitochondrial function, Journal of bioenergetics and biomembranes 48 (2016) 99-112.

Chapter 7. Experimental

7.1 Materials

All reagents and chemicals used were of AR grade and did not require further purification. Hoechst 33342, Mito-Tracker Deep Red, Mito-Tracker Green, ER-Tracker Blue, Lyso-Tracker Blue, MitoSOX Red, PI/RNase Staining Solution, DNase I and RNase A were obtained from Thermo Fisher Scientific. FCCP, Cyclosporin A, 2MeOE2, KC7F2, DMOG, MitoTEMPOL, DIDs sodium salt and NAC were purchased from TargetMol. Mitochondrial Permeability Transition Pore Assay Kit and BeyoFast SYBR Green One-Step qRT-PCR Kit were purchased from Beyotime Biotechnology. Seahorse XF Glycolysis Stress Test Kit and Seahorse XF Cell Mito Stress Test Kit were purchased from Agilent. Comet Assay Kit were purchased from Abcam. Annexin V-BUV396, Annexin V-647 and 7-AAD were purchased from BD Pharmingen. Plasmid were purchased from GenScript. All the oligonucleotides were synthesized and purified by Sangon Biotech and the sequences were listed in **Appendix Table S1-Table S6**. All the antibodies were listed in **Appendix Table S7**, which were purchased from Abcam, Cell Signaling Technology and Thermo Fisher Scientific. The cell lines used in this study were purchased from ATCC.

7.2 Experimental section of Chapter 3-4

7.2.1 Synthesis and characterization of ligand **BYB**

Synthesis of **BYB ((Z)-1,1,3-trimethyl-2-((3-methylbenzo[d]thiazol-2(3H)-ylidene)methyl)-1H-benzo[e]indol-3-ium iodide):**

Compound **BYB** was synthesized and purified according to the reported procedures,[1] and the synthetic route was shown in Appendix, **Figure S4**. Briefly, intermediate **A** (1.5 mmol) and **B** (1.5 mmol) were added to a round bottom flask and were dissolved in 6.0 mL of acetonitrile. Triethylamine (0.5 mmol) was added to the reaction mixture as a base. The mixture was refluxed at 75 °C for 12 h. The reaction was monitored with TLC until the reaction was completed. Then, the reaction was cooled to room temperature and 10.0 mL ethyl acetate was added to precipitate the solid. The crude product **BYB** obtained by filtration was then recrystallized in ethanol. **BYB** was obtained as an orange solid with 73% yield. The purified compound was characterized with ^{1}H, ^{13}C NMR, and HRMS. ^{1}H NMR (400 MHz, DMSO-d_6) δ 8.25 (d, J = 8.2 Hz, 1H), 8.18 (d, J = 7.8 Hz, 1H), 8.11 (dd, J = 15.0, 8.5 Hz, 2H), 7.97 (d, J = 8.2 Hz, 1H), 7.77 (d, J = 8.8 Hz, 1H), 7.75 – 7.70 (m, 1H), 7.66 (d, J = 7.2 Hz, 1H), 7.56 (dd, J = 12.8, 6.9 Hz, 2H), 6.21 (s, 1H), 4.07 (s, 3H), 3.72 (s, 3H), 1.92 (s, 6H). ^{13}C NMR (101

MHz, DMSO-d_6) δ 176.97, 164.85, 141.60, 141.15, 132.11, 131.83, 130.53, 130.23, 128.91, 128.19, 128.06, 126.50, 126.23, 125.93, 125.29, 123.62, 122.93, 118.68, 115.10, 112.26, 82.16, 51.59, 35.40, 25.25. HRMS m/z: calcd for $C_{24}H_{23}N_2S^+$, [M-I] $^+$ = 371.1576, found 371.1583. HPLC analysis: retention time at 6.362 min eluted with MeOH/H_2O = 50:50 v/v, purity = 97%.

7.2.2 Fluorescence spectroscopy

Fluorescence spectra were recorded with a LS-45 fluorescence spectrometer (Perkin Elmer). The slit width of the colorimetric dish is 1 mm, and the optical diameter is 10 mm. The emission of **BYB** was acquired by exciting the sample in solution at 445 nm. The emission spectra collection range of **BYB** was 470-700 nm. All oligonucleotides were pre-annealed by heating at 95 °C for 10 min in Tris-HCl buffer (10 mM, pH 7.4) with 100 mM KCl before being used for the titration experiments. The annealed oligonucleotides were then allowed cooling to room temperature and used as the stock solution for further use. In the titration, a certain aliquot of a stock solution of oligonucleotides were added into the solution containing **BYB** at the fixed concentration (0.5 μM) and the final concentration of oligonucleotides was 2.8 μM. Then, the mixture was stirred and allowed to equilibrate for at least 1 min. The emission of the mixture was measured with the fluorescence spectrometer.

7.2.3 Circular dichroism (CD) and melting point assay

CD spectra were recorded using a JASCO J-1500 Circular Dichroism Spectrometer. A quartz cuvette with a path length of 1 mm was employed to measure spectra within a wavelength range of 220 to 700 nm, utilizing a bandwidth of 1 nm, a step size of 1 nm, and a data acquisition time of 1 second per point. Initially, 400 μL of nucleic acid at a concentration of 5 μM was placed in the cuvette, and the CD spectra were collected. Subsequently, ligand **BYB** was added sequentially at concentrations of 5 μM, 10 μM, 15 μM, and 25 μM, with spectra recorded for each concentration. For melting point assays, measurements were conducted at a fixed wavelength while gradually increasing the temperature from 25 to 95 °C, with a step size of 1 nm and a time of 5 seconds per point. The experiments involved 10 μM of ligand **BYB** and 5 μM of various nucleic acids in a 10 mM Tris-HCl buffer at pH 7.4 containing 20 mM KCl. The collected data were normalized using Origin software.

7.2.4 Isothermal titration calorimetry (ITC) assay

ITC experiments were carried out in a MicroCal PEAQ-ITC (Malvern, USA) microcalorimeter. Oligonucleotides were pre-annealed in a buffer consisting of 25 mM KH_2PO_4 and 60 mM KCl (pH 7.4, containing 0.2% (v/v) DMSO) by heating to 95 °C in a water bath for 5 minutes. The solution was then cooled to 25 °C and stored at 4 °C overnight. The pre-annealed oligonucleotides (10 μM) in buffer was kept in the sample cell (400 μL) and 40 μL **BYB** (100 μM) was loaded into the syringe in the same buffer. **BYB** was mixed with the sample by stirring the syringe at 750 rpm at 25 °C. There were 30 injections with a duration of 4 s and an interval of 150 s. Under the same conditions, the ligand was injected into the cells containing only buffer solution for a blank titration. The heat generated by the interaction was determined by subtracting the blank heat from the heat of ligand nucleic acids titration. Finally, the corrected data are fitted into the built-in binding model to obtain the binding enthalpy. The binding affinity (K_d) was obtained by applying the built-in curve fitting model using One Set of Sites (MicroCal PEAQ-ITC (Malvern, USA)).

7.2.5 NMR spectroscopy

Before taking ^{1}H NMR measurements, *Mito 6363*, *Mito 9438* and *Mito 10252* were dissolved in a phosphate buffer (25 mM KH_2PO_4, 10% D_2O, 100 mM KCl, pH 7.4) at a concentration of 150 μM. The solution was heated to 95 °C, then allowed to cool to room temperature and incubated for 24 hours. During the measurement, ligand **9** was added sequentially at concentrations of 75 μM, 150 μM and 300 μM. The experiments were performed at 25 °C using a 600 MHz spectrometer.

7.2.6 Plasmid construction

cDNAs encoding Pif1, Twinkle and GRSF1 were obtained by gene synthesis from GenScript. To generate eBFP-tagged proteins, the cDNAs were cloned into the pcDNA3.1+ vector.

7.2.7 Cell culture

The cell lines including A375 (CRL-1619), HeLa (CRM-CCL-2), MIA PaCa-2 (CRM-CRL-1420), SK-MEL-2 (HTB-68), HepG2 (HB-8065), MDA-MB-231 (HTB-26), HCT-116 (CCL-247), human fibroblast BJ (CRL-2522) and HK2 (CRL-2190) were purchased from ATCC. The cell lines were cultured in different complete mediums as shown below: A375, HeLa, MDA-MB-231 and HK2 were cultured in DMEM (Gibco) supplemented with 10% fetal bovine serum (FBS, Gibco) and 1%

Penicillin-Streptomycin (P/S, Gibco). MIA PaCa-2 was cultured in DMEM (Gibco) supplemented with 10% FBS, 2.5 % horse serum (Gibco) and 1% P/S. HCT-116 were cultured in RPMI1640 (Gibco) supplemented 10% FBS and 1% P/S. SK-MEL-2, HepG2 and BJ was cultured in MEM (Gibco) supplemented with 10% FBS and 1% P/S. The cells were incubated in incubator at 37 °C with 5% CO_2. For the preparation of ρ0 HeLa cells, parental HeLa cells were cultured for 40 days in low-dose EtBr (Sigma) (50 ng/mL) supplemented with 1 mM pyruvate (Sigma) and 50 μg/mL uridine (Sigma). In all experiments needed for cell collection, the cells were trypsinized by 0.25% trypsin-EDTA (Gibco) and suspended in various buffers for further analysis.

7.2.8 MTT assay

The MTT assay was performed on cancer cell lines (A375, HeLa, MIA PaCa-2, SK-MEL-2, HepG2, MDA-MB-231 and HCT-116) as well as normal cells (BJ and HK2). The cells were seeded in 96-well plates at an approximate density of 4,000 cells per well and incubated at 37 °C with 5% CO_2. After cultured for 24 h, the cells were treated with **BYB** at different concentrations (0, 0.078, 0.156, 0.313, 0.625, 1.25, 2.5, 5, 10, 20 and 40 μM) for 48 h, respectively. Following the incubation, the medium was removed, and 100 μL of a 0.5 mg/mL MTT solution was added to each well. The plates were then incubated in the dark for 4 hours. After incubation, the MTT solution was discarded, and 100 μL of DMSO was added to each well to completely dissolve the formazan crystals. The absorbance of the treated plates was measured using a microplate reader at a wavelength of 570 nm. Finally, the cell survival rate and the half-maximal inhibitory concentration (IC_{50}) for the ligands were calculated based on the obtained absorbance values.

7.2.9 Crystal violet assay

In the assay, a crystal violet assay kit (Abcam: ab232855) was used for cytotoxicity and cell viability studies. HeLa cells were cultured on 96-well plates with a density of 4000 cells per well approximately. The culture condition was set at 37 °C and 5% CO_2. After cultured for 24 h, the cells were treated with **BYB** at different concentrations (0, 0.078, 0.156, 0.313, 0.625, 1.25, 2.5, 5, 10 and 20 μM) for 48 h, respectively. After that, the cells were processed according to the manufacturer's instruction. Finally, the samples were measured for the absorbance at 570 nm.

7.2.10 Living cell staining and imaging assay

HeLa cells were cultured in confocal dishes overnight with 5% CO_2 at 37 °C in DMEM medium supplemented with 10% FBS and 1% P/S. The digital images were recorded using a Leica TCS SPE Confocal Microscope. For the mitochondrial co-localization experiment, cells were treated with 200 nM Mito-Tracker Deep Red for 30 minutes, followed by 2 μM **BYB** for 30 min. In the endoplasmic reticulum co-localization experiment, the cells were exposed to 1 μM ER-Tracker Blue for 30 minutes and 2 μM **BYB** for 30 min, respectively. For lysosomal co-localization, cells were treated with 1 μM Lyso-Tracker Blue for 30 minutes and 2 μM **BYB** for 30 min, respectively. To increase the permeability of nuclear membrane, HeLa cells were treated with 30 μg/mL Digitonin for 15 min. Then, the cells were stained with 2 μg/mL Pyridine Iodide (PI) for 15 min or 2 μM **BYB** for 30 min and together with 1 μM Hoechst 33342 for 30 min for nuclear staining and imaging, respectively. In experiments involving cyclosporin A (CsA), cells were treated with 1 μM CsA for 24 hours to block the permeability transition pore on the inner mitochondrial membrane. Following CsA treatment, the cells were washed with DMEM and then incubated with 2 μM **BYB** for 30 min and 1 μM Hoechst 33342 for 30 min, respectively. For FCCP treatment, cells were treated with 1 μM FCCP for 30 minutes to induce depolarization. Afterward, the cells were washed with DMEM and incubated with 2 μM **BYB** for 30 min and 1 μM Hoechst 33342 for 30 min, respectively. For the preparation of HeLa cells overexpressing RFP-tagged proteins, cells were transfected with the constructed plasmids (4 μg) using Lipofectamine 3000 (Invitrogen, USA) and then incubated at 37 °C with CO_2 for 24 h, and then stained with 2 μM **BYB** for 30 min and 1 μM Hoechst 33342 for 30 min respectively. In co-localization experiments, cells were incubated with 2 μM ligand **BYB** and 1 μM ligand MitoISCH for 1 hour and 1 μM Hoechst33342 for 30 minutes, respectively. For the preparation of HeLa cells overexpressing RFP-tagged proteins, cells were transfected with the constructed plasmids (4 μg) using Lipofectamine 3000 (Invitrogen, USA) and then incubated at 37 °C with CO_2 for 24 h, and then stained with 2 μM **BYB** for 30 min and 1 μM Hoechst 33342 for 30 min, respectively.

7.2.11 Fixed cell staining and imaging assay

HeLa cells were cultured overnight in confocal dishes at 37 °C with 5% CO_2 in DMEM medium supplemented with 10% FBS and 1% P/S. Digital images were captured using a Leica TCS SPE Confocal Microscope. For the DNase I and RNase A digestion experiments, cells were incubated with 2 μM **BYB** for 30 min and 1 μM Hoechst 33342 for 30 min respectively before fixation. Following

incubation, the cells were fixed with 4% paraformaldehyde for 20 minutes and then permeabilized with 0.3% Triton X-100 in PBS for 1 hour. Finally, the cells were treated with 200 units/mL of DNase I or RNase A at 37 °C for 3 hours. In immunofluorescence experiment, the confocal dishes were washed with pre-cooled PBS and fixed in 4% paraformaldehyde/PBS for 20 min, and then it was infiltrated with 0.3% Triton-X 100/PBS for 1 h. Then, it was blocked with 1% BSA/PBS for 1 h. After blocking, the cells were incubated with different antibodies at 4 °C overnight. After overnight incubation, the cells were washed with pre-cooled PBS for 3 times and were incubated with incubated with antibody dilution buffer supplemented with Goat anti-Rabbit IgG Alexa Fluor 568, Goat anti-Mouse IgG Alexa Fluor 647 or Goat anti-Rabbit IgG Alexa Fluor 647 for another 1 h. After secondary antibody incubation, the cells were washed with pre-cooled PBS for 3 times and then stained with 1 μM Hoechst 33342 for 30 min. Finally, the cells were washed with pre-cooled TBST for 3 times.

7.2.12 Detection of mitochondrial membrane potential

HeLa cells were cultured in confocal dishes overnight. After the removal of medium, the confocal dishes were washed with pre-cooled PBS for three times. After that, cells were incubated with **BYB** (0, 5, 10 and 15 μM) for 24 h at 37 °C, then stained with 1 μM TMRE (ThermoFisher Scientific) for 30 min and 1 μM Hoechst 33342 for 30 min respectively. The digital images were recorded on Leica TCS SPE Confocal Microscope.

7.2.13 Detection of mitochondrial ATP

HeLa cells were cultured in confocal dishes overnight. After removing the medium, the confocal dishes were washed with pre-cooled PBS for three times. After that, cells were incubated with different concentrations of **BYB** (0, 5, 10 and 15 μM) or 10 μM **BYB** for different time (0, 6, 12 and 24 h) at 37 °C. Then, the cells were stained with 2 μM ATP-Red1 (MedChemExpress) for 30 min and 1 μM Hoechst 33342 for 30 min, respectively. The digital images were recorded on a Leica TCS SPE Confocal Microscope.

7.2.14 Detection of mitochondrial calcium ion (Ca^{2+})

HeLa cells were cultured in confocal dishes overnight. After the removal of medium, the confocal dishes were washed with pre-cooled PBS for three times. After that, cells were incubated with different concentration of **BYB** (0, 5, 10 and 15 μM) with or without 150 μM DIDS sodium salt

(MedChemExpress) for 24 h or 10 μM **BYB** for different time (0, 6, 12 and 24 h) at 37 °C, then stained with 1 μM Rhod-2 AM (ThermoFisher Scientific) for 30 min and 1 μM Hoechst 33342 for 30 min respectively. The digital images were recorded on Leica TCS SPE Confocal Microscope.

7.2.15 Detection of mitochondrial reactive oxygen species (ROS)

HeLa cells were cultured in confocal dishes overnight. After the removal of medium, the confocal dishes were washed with pre-cooled PBS for three times. After that, cells were incubated with different concentrations of **BYB** (0, 5, 10 and 15 μM) with or without 150 μM DIDS sodium salt or 10 μM Mito-TEMPOL (Abcam) for 24 h at 37 °C, then stained with 1 μM MitoSOX (ThermoFisher Scientific) for 30 min and 1 μM Hoechst 33342 for 30 min respectively. The digital images were recorded on Leica TCS SPE Confocal Microscope.

7.2.16 Detection of cellular iron metabolism

HeLa cells were cultured in confocal dishes overnight. After removing the medium, the confocal dishes were washed with pre-cooled PBS for three times. After that, cells were incubated with different concentration of **BYB** (0, 5, 10 and 15 μM) for 24 h at 37 °C. Then, the cells were stained with 100 nM the Fe^{2+} probe FerroOrange (Merck, SCT210) for 30 min and 1 μM Hoechst 33342 for 30 min respectively. The digital images were recorded on a Leica TCS SPE Confocal Microscope.

7.2.17 Detection of autophagosome and mitochondrion by transmission electron microscopy

HeLa cells were treated with or without 10 μM **BYB** for 24 h and then were collected and processed as reported in the previous study.[2] Samples were examined with transmission electron microscopy (HITACHI H-7650).

7.2.18 Cell apoptosis analysis

HeLa cells were plated at a density of 5 x 10^5 cells per flask in a 25-cm² culture flask (TPP). After incubating overnight, the cells were treated with various concentrations of **BYB** (0, 5, 10, and 15 μM) with or without 10 μM Mito-TEMPOL or 150 μM DIDS sodium salt for 24 h. Following treatment, the cells were collected via trypsinization using 0.25% trypsin without EDTA and then suspended in PBS. The cells were subsequently treated with Annexin V-647 and 7-AAD at room temperature and dark conditions for 30 min. Finally, the treated cells were analyzed for apoptosis using a BD

FACSymphony A3 Cell Analyzer.

7.2.19 Cell cycle analysis

In this experiment, propidium iodide (PI) was utilized to assess the cell cycle of HeLa cells. Initially, the cells were collected at a density of 5 x 10^5 cells/mL after being incubated with various concentrations of ligand **BYB** for 24 hours. The cells were then fixed in 70% ethanol in PBS at 4 °C for 2 hours. Following fixation, the cells were stained with PI. Finally, the stained cells were analyzed using a BD Accuri C6 Flow Cytometer.

7.2.20 Determination of NAD^+/NADH ratio (Plate-Based)

HeLa cells were seeded at density 2×10^6 cells/flask in a 25-cm^2 culture flask (TPP). After overnight incubation, the cells were treated with different concentrations of **BYB** (0, 5, 10 and 15 μM) for 24 h. After treatment, the cells were collected by scraping and washed with cold PBS. NAD levels were analyzed by use of the colorimetric total NAD/NADH assay (Abcam, ab65348) according to the manufacturer's instructions that allows the differentiation of NAD^+ and NADH. The assay reagent consisted of a mixture of NAD^+-reducing and NADH-oxidizing enzyme causing an amplification of the NAD signal. As NAD^+ but not NADH is heat labile at already 60 °C, total NAD is detected in the unheated sample and NADH is detected in the heated sample. The difference between total NAD and NADH represented the NAD^+ amount. All experiments were repeated five times.

7.2.21 Determination of ATP concentration (Plate-Based)

HeLa cells were seeded at a density of 5000 cells/well in a 96-well white clear bottom plate. After overnight incubation, the cells were treated with different concentrations of **BYB** (0, 5, 10 and 15 μM) for 0-24 h. ATP concentration was measured by Luminescent ATP Detection Assay Kit (ab113849, Abcam). Briefly, 1 vial of lyophilized substrate was reconstituted in 5 mL of substrate buffer before use. The reconstituted substrate and the detergent were equilibrated to room temperature. Once equilibrated, 50 μL of detergent was added to the wells and placed on a shaker for 5 min at 700 rpm for cell lysis and ATP stabilization. Next, 50 μL of substrate was added and the plate was agitated for a further 5 min at 700 rpm. The plate was dark-adapted for at least 10 min before luminescence was read. ATP levels were calculated from the standard curve that was run alongside the samples. All experiments were repeated five times.

7.2.22 Oxygen consumption rate measurement by Mito Stress Test

On day 1, HeLa cells were seeded at a density of 5 x 10^4 cells per well in DMEM in a 24-well Agilent Seahorse XF cell culture microplate (Agilent Technologies) and incubated overnight. Reference wells A1, B4, C3, and D6 were filled with medium only. The sensor cartridge on the calibration plate (Agilent Technologies) was calibrated using 1 mL of Agilent Seahorse XF Calibrant. This calibration plate was then placed in a non-CO_2 incubator at 37 °C overnight. On Day 2, the DMEM medium was removed from the microplate, and the cells were treated with various concentrations of ligand **BYB** (0, 5, 10 and 15 μM) for 3 hours. Following treatment, 500 μL of assay medium (DMEM assay medium provided by Agilent Technologies, supplemented with 1 mM pyruvate, 2 mM glutamine, and 10 mM D-glucose, pH 7.4 at 37 °C) was added to each well. The microplate with cells was then incubated in a non-CO_2 incubator at 37 °C for 1 hour. Meanwhile, the sensor cartridges on the calibration plate prepared on Day 1 were loaded with different ligands in assay medium: port A received 56 μL of 10 μM oligomycin; port B received 62 μL of 10 μM FCCP; and port C contained 69 μL of a mix of 10 μM rotenone and 5 μM antimycin A. The loaded sensor cartridge on the calibration plate was placed in an XF24 analyzer (Agilent Technologies) for 30 minutes. After incubation, the calibration plate was replaced with the microplate containing the cells. The Seahorse Wave software was used to conduct the Mito Stress Test, and the results were normalized to cell number.

7.2.23 Proton efflux rate measurement by Glycolytic Rate Test

On day 1, HeLa cells in DMEM were seeded at density 5×10^4 cells/well in a 24-well Agilent Seahorse XF cell culture microplate (Agilent Technologies) for 24 h (the microplate was used at day 2). The wells of A1, B4, C3 and D6 were filled with medium only as the reference wells. The sensor cartridge on the calibration plate (Agilent Technologies) was calibrated with 1 mL of Agilent Seahorse XF Calibrant (Agilent Technologies). The calibration plate was placed into a non-CO_2 37 °C incubator overnight. At day 2, DMEM was removed from the microplate prepared at day 1, the cells were treated with **BYB** (0, 5, 10 and 15 μM) for 3 h, then assay medium (DEME assay medium provided by Agilent Technology supplemented with 1 mM pyruvate, 2 mM glutamine and 10 mM D-glucose, pH 7.4 at 37 °C) were used to wash the cells three times. Finally, 500 μL of assay medium were added to each well. The microplates with cells were placed into a non-CO_2 incubator at 37 °C for 1 h. Besides, the sensor cartridges on the calibration plate prepared at day 1 were loaded with different

compounds in assay medium (port A: 56 μL of μM rotenone and 25 μM antimycin A; port B: 62 μL of 1 M 2-DG). The loaded sensor cartridge on the calibration plate was placed in a XF24 analyzer (Agilent Technologies) for 30 min. After incubation, the calibration plate was replaced with the microplate containing the cells. The Seahorse Wave software was used to conduct the Glycolytic Rate Test, and the results were normalized to cell number.

7.2.24 DNA isolation and mtDNA copy number analysis

HeLa cells were seeded at density 1×10^6 cells/flask in a 25-cm^2 culture flask (TPP). After overnight incubation, the cells were treated with different concentrations of **BYB** (0, 5, 10 and 15 μM) for 24 h. Following treatment, the cells were trypsinized and DNA was extracted using the PureLink Genomic DNA Mini Kit (ThermoFisher Scientific). The isolated DNA was used to assess mtDNA copy number by RT-PCR using the Human Mitochondrial DNA Copy Number Assay Kit (MCN1) from Detroit R&D. Each reaction mixture (20 μL) contained forward primer 1 μL, reverse primer 1 μL, sample contain genomic DNA 8 μL (2 ng/μL), and rtPCR reaction mix 10 μL. The reaction mixtures were incubated in a thermocycler under the following cycling conditions: denature at 95 °C for 10 min, followed by 40 cycles at 95 °C for 15 s and 60 °C for 60 s. All experiments were repeated three times. The data were normalized and analyzed using the ΔΔCt method.

7.2.25 RNA isolation and qRT-PCR

HeLa cells were seeded at density 1×10^6 cells/flask in a 25-cm^2 culture flask (TPP). After overnight incubation, the cells were treated with different concentrations of **BYB** (0, 5, 10 and 15 μM) for 24 h. Following treatment, the cells were trypsinized, and RNA was extracted using the RNase Mini Kit (Qiagen). The RNA samples were prepared according to the manufacturer's instructions provided with the BeyoFast SYBR Green One-Step qRT-PCR Kit (Beyotime Biotechnology). Each reaction mixture (20 μL) included 10 μL of 2 x One Step SYBR Green Mix, 1 μL of One Step SYBR Green Enzyme Mix, 0.4 μL of 50 x ROX Reference Dye, 1 μL of Gene Specific Primer Forward (0.3 μM), 1 μL of Gene Specific Primer Reverse (0.3 μM), 50 ng of total RNA, and RNase-free ddH_2O to reach a final volume of 20 μL. The reaction mixtures were then incubated in a thermocycler under the following conditions: reverse transcription at 50 °C for 30 minutes, denaturation at 95 °C for 2 minutes, followed by 40 cycles of 95 °C for 15 seconds and 60 °C for 30 seconds. The data were normalized to housekeeping gene GAPDH and analyzed using the ΔΔCt method.

7.2.26 DNA isolation and mtDNA damage analysis

HeLa cells were seeded at density 1×10^6 cells/flask in a 25-cm^2 culture flask (TPP). After overnight incubation, the cells were treated with different concentrations of **BYB** (0, 5, 10 and 15 μM) for 24 h. Following treatment, the cells were trypsinized and DNA was extracted using the PureLink Genomic DNA Mini Kit (ThermoFisher Scientific). Mitochondrial DNA (mtDNA) damage was quantified using the Human DNA Damage Analysis Kit Real-Time PCR DNA Quantification following QPCR (Detroit R&D, DD2H) according to the manufacturer's instructions. A higher product obtained represents less mtDNA damage. The kit quantifies damaged 8.8 kb mtDNA sequences by measurement of the replicated DNA with real-time PCR following QPCR analysis. For QPCR: Each reaction mixture (20 μL) contained 2x QPCR concentrated buffer 10 μL, 5x enhancer 4 μL, QPCR primer mix 5 μL (2 μM each primer, forward/reverse), and sample contain genomic DNA 1 μL (50 ng/μL). The reaction mixtures were incubated in a thermocycler under the following cycling conditions: denature at 98 °C for 30 s, followed by 30 cycles at 98 °C for 10 s, 68 °C for 10 s and 72 °C for 4 min and finally keep in 72 °C for 10 min. For Real-Time PCR: Each reaction mixture (20 μL) contained SYBR green mix 10 μL, nuclease-free H_2O 8.1 μL, real-time primer mix 0.9 μL (5 μM each primer, forward/reverse), and DNA sample 1 μL (PCR-products from above QPCR). The reaction mixtures were incubated in a thermocycler under the following cycling conditions: denature at 50 °C for 2 min and 95 °C for 10 min, followed by 40 cycles at 95 °C for 15 s and 60 °C for 60 s. All experiments were repeated three times. The standard curve was generated by plotting standard Ct values vs. standard concentration, and mtDNA level in sample was calculated from the standard curve.

7.2.27 DNA isolation and measurement of cytosolic mitochondrial DNA

HeLa cells were seeded at density 1×10^6 cells/flask in a 25-cm^2 culture flask (TPP). After overnight incubation, the cells were treated with different concentrations of **BYB** (0, 5, 10 and 15 μM) for 24 h. Mitochondrial DNA in the cytosolic fraction was detected by cell compartment fractionation followed by qPCR. Briefly, cells were lysed by mild detergent (0.1% NP-40) and incubated on ice for 15 minutes. Lysates were centrifuged at 13,000 rpm for 15 min at 4 °C. PureLink™ Genomic DNA Mini Kit (ThermoFisher Scientific) was used to purify cytosolic mitochondrial DNA from supernatant cytosolic fraction according to manufacturer's instructions. The qPCR was performed using PowerUp™ SYBR™ Green Master Mix for qPCR (ThermoFisher Scientific). All experiments were repeated three times. The data were normalized to housekeeping gene GAPDH and analyzed

using the ΔΔCt method.

7.2.28 Mitochondria isolation

HeLa cells were seeded at density 2×10^7 cells/dish in a 15 cm culture dish. After overnight incubation, the cells were treated with different concentrations of **BYB** (0, 5, 10 and 15 μM) for 24 h. After treatment, the cells were trypsinized and collected. Mitochondria Isolation Kit for Cultured cells (ThermoFisher Scientific) was used to isolated cytosol fraction and mitochondria according to manufacturer's instructions. For mitochondria lysis, the isolated mitochondria were lysed with 2% CHAPS in Tris-buffered saline (TBS containing 25 mM Tris, 0.15 M NaCl, pH 7.2). The cytosol protein and mitochondrial protein concentrations were quantified by BCA kit and analyzed by Western Blot.

7.2.29 Western blot assay

HeLa cells in the logarithmic growth phase were inoculated in 10 cm culture dishes and treated with **BYB** at different concentrations (0, 5, 10 and 15 μM) for 24 h. The cells were collected and incubated on ice for 20 min in the RIPA buffer (containing protease inhibitors and phosphatase inhibitors), followed by centrifugation at 4 °C at 12,000 × g for 10 minutes. The total protein concentration was quantified by BCA kit. The same amount of protein (20 μg) was loaded onto a 10-12% SDS-PAGE gel for separation, and the proteins were subsequently transferred to a PVDF membrane. After blocking with 5% skim milk, the membranes were incubated with primary antibodies overnight at 4 °C. The membranes were washed three times with TBST buffer for 0.5 h, then incubated with Anti-mouse IgG, HRP-linked Antibody or Anti-rabbit IgG, HRP-linked Antibody at room temperature for 2 h. Following this incubation, the membranes were thoroughly washed and subjected to chemiluminescence detection using Immobilon Western Chemiluminescent HRP substrate (Merck Millipore).

7.2.30 Comet assay for DNA damage detection

The DNA damage in HeLa cells was detected by Comet assay kit (Abcam, ab238544). After overnight incubation, the cells were treated with different concentrations of **BYB** (0, 5, 10 and 15 μM) for 24 h. After treatment, the cells were collected by trypsinization with 0.25% trypsin with EDTA and suspended in ice-cold PBS at 1×10^5 cells/mL. The sample was prepared according to the

manufacturer's instruction. Briefly, cells were mixed with comet agarose at 37 °C and pipetted the agarose/cell mixture onto the top of the base layer of comet agarose. The slide was transferred to 4 °C in the dark for 15 minutes for gelation. The slide was then transferred to a container with pre-chilled lysis buffer for 30 minutes at 4 °C in the dark. After lysis buffer treatment, the slide was treated with alkaline solution for 30 minutes at 4 °C in the dark. The treated slide was then transferred to a horizontal electrophoresis chamber for electrophoresis under alkaline electrophoresis solution (300 mM NaOH and 1 mM EDTA, pH > 13), with 30 V for 30 minutes. The slide was washed twice with cold water and immersed in cold 70 % ethanol for 5 minutes. The slide was then allowed to air dry and was stained with 1 μM DAPI for 10 minutes. The slide was subjected to Ti2-E Live-cell fluorescence imaging system (Nikon) with 405 nm excitation LED for imaging. Comet assay was quantified by the tail moment length. The tail moment length was measured from the center of the head to the center of the tail.

7.2.31 Cell uptake analysis

HeLa cells were cultured in 6-well plates with **BYB** (2 μM) for 6, 12, 24 and 48 h respectively. After treatment, the cells were hydrolyzed with trypsin and centrifuged at 1200 rpm for 3 min. Then, the cells were washed with PBS and centrifuged at 1200 rpm for 3 min. Finally, the cells were analyzed by flow cytometry (BD Accuri C6 Flow Cytometer).

7.2.32 Wound-healing experiment

HeLa cells were seeded in 6-well plates (5×10^5 cells/well) and cultured until the cells grew to 100 % confluence. A wound was created for each well with a 200-μL pipette tip, and the cells were washed with PBS three times. Serum-free DMEM medium containing **BYB** (0-15 μM) was added to the well and cultured at 37 °C and 5% CO_2. Images were taken at 24 h.

7.2.33 Pharmacokinetic studies in rat

The experiments performed in the present study were in compliance with the Animal Management Rules of the Ministry of Health of the People's Republic of China, and also were in compliance with the institutional ethics committee regulations and guidelines on animal welfare. The approved ASESC (Animal Subjects Ethics Sub-Committee) Case Number is 21-22/45-ABCT-R-GRF. Five-week-old female Sprague–Dawley rats were purchased from Guangdong Medical Laboratory Animal Center

(China) and housed in a specific pathogen-free (SPF) environment with a 12 h light/dark cycle. The rats can free access to food and water. After 1-week adaptation period, **BYB** was injected into Sprague–Dawley rats (female, weighing 200 ± 20 g) via tail vein (1 mg/kg). At the end of the study, the rats were killed by cervical dislocation. Their blood samples (0.3 mL) were collected from the orbital sinus at 5 min, 15 min, 30 min, 1 h, 2 h, 4 h, 6h, 8 h, 12 h, and 24 h post-injection, respectively. Analyte quantification was performed by a LC/MS/MS Quantum Access mass spectrometer (AB 4000). Compound detection was performed with a mass spectrometer in electrospray positive ionization mode. The pharmacokinetic parameters were calculated using WinNonlin software version 6.3 based on noncompartmental analysis (Pharsight Corporation, Mountain View, USA).

7.2.34 *In vivo* antitumor activity in the human cervical cancer (HeLa) xenograft model

All animal experiments performed in the present study were in compliance with the Animal Management Rules of the Ministry of Health of the People's Republic of China, and also were in compliance with the institutional ethics committee regulations and guidelines on animal welfare. The approved ASESC (Animal Subjects Ethics Sub-Committee) Case Number is 21-22/45-ABCT-R-GRF. The experiments were performed with 2% isoflurane to minimize suffering. Five-week-old female Balb/c nude mice were purchased from Guangdong medical laboratory animal center (China) and housed in a specific pathogen-free (SPF) environment with a 12 h light/dark cycle and free access to food and water. All animal care and procedures were approved by the university ethics committee for use in laboratory animals. After 1-week adaptation period, the mice were injected subcutaneously with HeLa cell suspension (5×10^6 cells/mouse) to establish a xenograft model. When the subcutaneous tumor diameter was 100 mm^3, the nude mice were randomly divided into two groups (5 mice per group): tail vein injection of PBS (control group) and **BYB** (treatment group). The ligand dose in the treatment group was 2.5 mg/kg, and was injected into the mice every two days. The mice were killed by cervical dislocation on the 14^{th} day after intravenous injection of the ligand. Samples of blood were collected, centrifuged and separated into cell and serum fractions for routine blood data. Major organs and tumor tissues were taken from each group for hematoxylin and eosin (H&E) staining, TUNEL staining, and Ki67 staining.

7.2.35 Statistical test

Data are presented as the means ± SEM (standard error of the mean) of at least five independent experiments (not replicates) *in vivo* and *in vitro*, which were statistically analyzed using GraphPad Prism 8.0. The number of included data per group was mentioned in the figure legends. For comparisons between two groups, Student's t-test was utilized. For analyses involving multiple groups, one-way analysis of variance (ANOVA) with Dunnett's correction was employed. A *P*-value of less than 0.05 was considered statistically significant. The sample size needed for statistical analysis was determined to be at least five samples in each group.

7.3 Experimental section of Chapter 5-6

7.3.1 Synthesis and characterization of ligands **1-10**

High-resolution mass spectra (HRMS) were acquired using an Agilent 1260-6230TOF mass spectrometer. Proton (^{1}H) and carbon (^{13}C) NMR spectra were recorded at 400 and 100 MHz, respectively, in DMSO-d_6 with a Bruker BioSpin GmbH spectrometer, using TMS as a reference. The purity of the ligands was analyzed using high-performance liquid chromatography (HPLC) on a SHIMADZU LC-16 system equipped with a Diamonsil C18 column (250 mm × 4.6 mm, 5 μm) at room temperature, employing a mobile phase of MeOH/H_2O (50:50, v/v) for elution. All synthesized ligands intended for assays were confirmed to have a purity of ≥ 95%.

General procedures for synthesizing ligands **1−10**. The synthetic route for ligands **1–10** is showed in **Chapter 5 Figure 5.2**. Intermediate **a** was synthesized by reacting 2-methylquinoline (2.004 g, 14.0 mmol) with 1,8-diiodooctane (2.488 g, 6.8 mmol) in 20 mL of ethanol at 100 °C for 24 hours. The crude product was recrystallized from acetone, yielding a brown-green solid at 73%. Ligands **1–10** were produced by reacting intermediate **a** (0.2 g, 0.15 mmol) with various aldehydes: benzaldehyde (0.042 g, 0.4 mmol), p-methylbenzaldehyde (0.048 g, 0.4 mmol), 4-(dimethylamino)benzaldehyde (0.059 g, 0.4 mmol), indole-3-carboxaldehyde (0.058 g, 0.4 mmol), 1H-indole-2-carbaldehyde (0.058 g, 0.4 mmol), 4-(methylthio)benzaldehyde (0.061 g, 0.4 mmol), N-ethylcarbazole-3-carboxaldehyde (0.089 g, 0.4 mmol), 4-(1-pyrrolidino)benzaldehyde (0.070 g, 0.4 mmol), 4-(piperidin-1-yl)benzaldehyde (0.076 g, 0.4 mmol), or 4-morpholinobenzaldehyde (0.076 g, 0.4 mmol), along with 4-methylpiperidine (30 μL) in 3 mL of ethanol. The mixture was refluxed overnight at 100 °C. The crude products were purified via flash silica gel column chromatography using a MeOH/DCM solvent

system (1:20, v/v). The resulting pure ligands were characterized by ^{1}H NMR, ^{13}C NMR, and HRMS, with HPLC analysis confirming their purity to be $\geqslant$ 95%.

(E)-1,1'-(octane-1,8-diyl)bis(2-((E)-styryl)quinolin-1-ium) iodide (1):

Brown solid with 65% yield. ^{1}H NMR (400 MHz, DMSO-d_6) δ 9.14 (d, J = 8.9 Hz, 2H), 8.61 (d, J = 9.0 Hz, 2H), 8.55 (d, J = 9.1 Hz, 2H), 8.41 (d, J = 7.1 Hz, 2H), 8.25 – 8.17 (m, 4H), 7.99 (t, J = 7.6 Hz, 2H), 7.97 – 7.91 (m, 4H), 7.88 (d, J = 15.9 Hz, 2H), 7.49 (d, J = 7.3 Hz, 6H), 5.19 – 5.06 (m, 4H), 1.86 (m, 4H), 1.51 (m, 4H), 1.35 (m, 4H). ^{13}C NMR (100 MHz, DMSO-d_6) δ 156.06, 147.77, 145.26, 138.71, 135.79, 135.26, 131.84, 130.98, 129.61, 128.84, 122.09, 119.62, 119.32, 51.16, 29.02, 26.11. HRMS m/z: calcd for $C_{42}H_{42}N_2^{2+}$, $[M]^{2+}$ = 287.3976, found 287.1637. HPLC analysis: retention time at 5.141 min eluted with MeOH/H_2O = 50:50 (v/v), purity = 99.1%.

(E)-1,1'-(octane-1,8-diyl)bis(2-((E)-4-methylstyryl)quinolin-1-ium) iodide (2):

Brown solid with 68% yield. ^{1}H NMR (400 MHz, DMSO-d_6) δ 9.10 (d, J = 8.9 Hz, 2H), 8.57 (d, J = 8.7 Hz, 2H), 8.52 (d, J = 9.0 Hz, 2H), 8.39 (d, J = 8.1 Hz, 2H), 8.15 (d, J = 15.7 Hz, 4H), 7.98 (d, J = 7.1 Hz, 2H), 7.80 (t, J = 11.0 Hz, 6H), 7.24 (d, J = 7.9 Hz, 4H), 5.06 (m, 4H), 2.24 (s, 6H), 1.77 (m, 4H), 1.52 (m, 4H), 1.36 (m, 4H). ^{13}C NMR (100 MHz, DMSO-d_6) δ 156.07, 147.98, 144.98, 142.24, 138.67, 135.68, 132.61, 130.96, 130.18, 129.61, 128.69, 121.90, 119.52, 118.12, 50.88, 28.96, 28.68, 25.92, 21.55. HRMS m/z: calcd for $C_{44}H_{46}N_2^{2+}$,$[M]^{2+}$ = 301.4242, found 301.1835. HPLC analysis: retention time at 5.141 min eluted with MeOH/H_2O = 50:50 (v/v), purity = 99.1%.

(E)-1,1'-(octane-1,8-diyl)bis(2-((E)-4-(dimethylamino)styryl)quinolin-1-ium) iodide (3):

Dark green solid with 61% yield. ^{1}H NMR (400 MHz, DMSO-d_6) δ 8.77 (d, J = 9.1 Hz, 2H), 8.42 (d, J = 9.2 Hz, 2H), 8.37 (d, J = 8.8 Hz, 2H), 8.25 (d, J = 7.0 Hz, 2H), 8.14 (d, J = 15.1 Hz, 2H), 8.07 (t, J = 7.8 Hz, 2H), 7.85 (t, J = 7.6 Hz, 2H), 7.72 (d, J = 8.9 Hz, 4H), 7.33 (d, J = 15.5 Hz, 2H), 6.64 (d, J = 9.0 Hz, 4H), 4.90 (m, 4H), 2.88 (s, 12H), 1.84 (m, 4H), 1.61 (m, 4H), 1.46 (m, 4H). ^{13}C NMR (100 MHz, DMSO-d_6) δ 155.80, 153.05, 149.76, 142.56, 138.62, 134.84, 132.32, 130.58, 128.55, 127.57, 122.67, 120.76, 118.92, 112.15, 111.23, 49.85, 28.47, 25.76. HRMS m/z: calcd for $C_{46}H_{52}N_4^{2+}$, $[M]^{2+}$ = 330.4654, found 330.2107. HPLC analysis: retention time at 5.124 min eluted with MeOH/H_2O = 50:50 (v/v), purity = 98.5%.

(E)-1,1'-(octane-1,8-diyl)bis(2-((E)-2-(1H-indol-3-yl)vinyl)quinolin-1-ium) iodide (4):

Orange solid with 71% yield. ^{1}H NMR (400 MHz, DMSO-d_6) δ 12.29 (s, 2H), 8.82 (d, J = 9.2 Hz, 2H), 8.62 (d, J = 15.3 Hz, 2H), 8.56 (d, J = 9.3 Hz, 2H), 8.38 (d, J = 9.0 Hz, 2H), 8.32 (s, 2H), 8.26 (d, J = 7.0 Hz, 2H), 8.07 (dd, J = 7.8, 3.5 Hz, 4H), 7.84 (t, J = 7.5 Hz, 2H), 7.49 – 7.45 (m, 2H), 7.40 (d, J = 15.4 Hz, 2H), 7.23 – 7.18 (m, 4H), 4.97 – 4.87 (m, 4H), 1.89 (m, 4H), 1.63 (m, 4H), 1.48 (m, 4H). ^{13}C NMR (100 MHz, DMSO-d_6) δ 185.43, 156.26, 143.95, 142.52, 138.93, 138.65, 138.12, 137.51, 135.64, 134.81, 130.62, 128.45, 127.41, 125.41, 123.92, 122.58, 122.35, 121.28, 120.44, 118.75, 118.62 – 118.53, 114.97, 113.47, 112.89, 111.08, 50.17, 29.08, 28.43, 26.35. HRMS m/z: calcd for $C_{46}H_{44}N_4^{2+}$, $[M]^{2+}$ = 326.4336, found 326.1794. HPLC analysis: retention time at 5.121 min eluted with MeOH/H_2O = 50:50 (v/v), purity = 98.1%.

(E)-1,1'-(octane-1,8-diyl)bis(2-((E)-2-(1H-indol-2-yl)vinyl)quinolin-1-ium) iodide (5):

Orange solid with 66% yield. ^{1}H NMR (400 MHz, DMSO-d_6) δ 11.90 (s, 2H), 8.97 (d, J = 9.0 Hz, 2H), 8.51 (d, J = 9.1 Hz, 2H), 8.40 (d, J = 9.1 Hz, 2H), 8.33 (d, J = 7.1 Hz, 2H), 8.23 (d, J = 15.6 Hz, 2H), 8.13 (t, J = 7.4 Hz, 2H), 7.92 (t, J = 7.5 Hz, 2H), 7.64 (d, J = 15.7 Hz, 2H), 7.53 (d, J = 8.0 Hz, 2H), 7.38 (d, J = 8.2 Hz, 2H), 7.13 (t, J = 7.6 Hz, 2H), 7.09 (s, 2H), 6.93 (t, J = 7.4 Hz, 2H), 4.93 (m, 4H), 1.74 (m, 4H), 1.56 (m, 4H), 1.40 (m, 4H). ^{13}C NMR (100 MHz, DMSO-d_6) δ 155.36, 144.13, 139.37, 138.63, 137.79, 135.41, 130.87, 129.23, 128.34, 125.82, 122.18, 121.13, 120.71, 119.23, 115.91, 112.53, 112.03, 50.55, 28.70, 25.94. HRMS m/z: calcd for $C_{46}H_{44}N_4^{2+}$, $[M]^{2+}$ = 326.4336, found 326.1795. HPLC analysis: retention time at 5.141 min eluted with MeOH/H_2O = 50:50 (v/v), purity = 97.6%.

(E)-1,1'-(octane-1,8-diyl)bis(2-((E)-4-(methylthio)styryl)quinolin-1-ium) iodide (6):

Yellow solid with 74% yield. ^{1}H NMR (400 MHz, DMSO-d_6) δ 9.08 (d, J = 9.0 Hz, 2H), 8.56 (d, J = 9.1 Hz, 2H), 8.52 (d, J = 9.1 Hz, 2H), 8.38 (d, J = 7.3 Hz, 2H), 8.17 (dd, J = 15.3, 7.6 Hz, 4H), 7.96 (t, J = 7.6 Hz, 2H), 7.86 (d, J = 8.4 Hz, 4H), 7.77 (d, J = 15.7 Hz, 2H), 7.31 (d, J = 8.4 Hz, 4H), 5.12 – 5.02 (m, 4H), 2.46 (s, 6H), 1.81 (m, 4H), 1.54 (m, 4H), 1.37 (m, 4H). ^{13}C NMR (100 MHz, DMSO-d_6) δ 155.9, 147.59, 144.78, 144.08, 138.70, 135.64, 131.53, 130.94, 130.06, 129.52, 128.64, 125.91, 121.76, 119.49, 117.73, 50.83, 28.98, 28.72, 25.98, 14.49. HRMS m/z: calcd for $C_{44}H_{46}N_2S_2^{2+}$, $[M]^{2+}$ = 333.4892, found 333.1565. HPLC analysis: retention time at 5.142 min eluted with MeOH/H_2O = 50:50 (v/v), purity = 98.2%.

(E)-1,1'-(octane-1,8-diyl)bis(2-((E)-2-(9-ethyl-9H-carbazol-3-yl)vinyl)quinolin-1-ium) iodide (7):

Red solid with 69% yield. ^{1}H NMR (400 MHz, DMSO-*d*$_6$) δ 8.65 (s, 2H), 8.60 (d, *J* = 9.0 Hz, 2H), 8.25 (d, *J* = 9.1 Hz, 2H), 8.21 (d, *J* = 9.1 Hz, 2H), 8.14 (d, *J* = 7.4 Hz, 2H), 8.08 (dd, *J* = 11.6, 3.8 Hz, 4H), 8.00 (t, *J* = 7.5 Hz, 2H), 7.95 (d, *J* = 7.7 Hz, 2H), 7.84 (t, *J* = 7.5 Hz, 2H), 7.59 (t, *J* = 11.5 Hz, 4H), 7.42 (d, *J* = 8.2 Hz, 2H), 7.34 (t, *J* = 7.8 Hz, 2H), 7.14 (t, *J* = 7.4 Hz, 2H), 4.85 (m, 4H), 4.26 (q, *J* = 6.9 Hz, 4H), 1.64 (m, 8H), 1.55 (m, 4H), 1.18 (t, *J* = 7.1 Hz, 6H). ^{13}C NMR (100 MHz, DMSO-*d*$_6$) δ 155.37, 149.56, 143.46, 141.76, 140.28, 138.18, 135.05, 130.60, 128.85, 128.53, 127.73, 126.95, 126.28, 123.05, 122.26, 120.85, 120.09, 118.81, 114.66, 110.14, 50.04, 37.61, 28.21, 27.92, 25.42, 14.11. HRMS m/z: calcd for $C_{58}H_{56}N_4^{2+}$, $[M]^{2+}$ = 404.2247, found 404.2261. HPLC analysis: retention time at 5.142 min eluted with MeOH/H_2O = 50:50 (v/v), purity = 96.6%.

(E)-1,1'-(octane-1,8-diyl)bis(2-((E)-4-(pyrrolidin-1-yl)styryl)quinolin-1-ium) iodide (8):

Black solid with 70% yield. ^{1}H NMR (400 MHz, DMSO-*d*$_6$) δ 8.71 (d, *J* = 9.2 Hz, 2H), 8.36 (dd, *J* = 9.1, 4.6 Hz, 4H), 8.23 (d, *J* = 7.1 Hz, 2H), 8.11 (d, *J* = 15.2 Hz, 2H), 8.05 (t, *J* = 7.5 Hz, 2H), 7.83 (t, *J* = 7.5 Hz, 2H), 7.68 (d, *J* = 8.7 Hz, 4H), 7.24 (d, *J* = 15.3 Hz, 2H), 6.42 (d, *J* = 8.8 Hz, 4H), 4.85 (m, 4H), 3.09 (m, 8H), 1.88 (m, 8H), 1.85 – 1.75 (m, 4H), 1.64 (m, 4H), 1.50 (m, 4H). ^{13}C NMR (100 MHz, DMSO-*d*$_6$) δ 155.67, 150.58, 149.99, 142.18, 138.60, 134.74, 132.57, 130.51, 128.37, 127.42, 122.40, 120.68, 118.82, 112.46, 110.47, 47.72, 28.30, 25.66, 25.21. HRMS m/z: calcd for $C_{50}H_{56}N_4^{2+}$, $[M]^{2+}$ = 356.5026, found 356.2266. HPLC analysis: retention time at 5.143 min eluted with MeOH/H_2O = 50:50 (v/v), purity = 98.6%.

(E)-1,1'-(octane-1,8-diyl)bis(2-((E)-4-(piperidin-1-yl)styryl)quinolin-1-ium) iodide (9):

Black solid with 71% yield. ^{1}H NMR (400 MHz, DMSO-*d*$_6$) δ 8.84 (d, *J* = 9.1 Hz, 2H), 8.47 (d, *J* = 9.3 Hz, 2H), 8.40 (d, *J* = 9.0 Hz, 2H), 8.28 (d, *J* = 7.5 Hz, 2H), 8.16 (d, *J* = 15.4 Hz, 2H), 8.09 (t, *J* = 7.9 Hz, 2H), 7.87 (t, *J* = 7.5 Hz, 2H), 7.74 (d, *J* = 8.8 Hz, 4H), 7.41 (d, *J* = 15.4 Hz, 2H), 6.90 (d, *J* = 8.8 Hz, 4H), 4.95 (m, 4H), 3.27 (m, 8H), 1.80 (m, 4H), 1.56 (m, 8H), 1.49 (m, 8H), 1.43 (m, 4H). ^{13}C NMR (100 MHz, DMSO-*d*$_6$) δ 155.96, 153.47, 149.27, 142.97, 138.67, 135.00, 132.31, 130.69, 128.71, 127.76, 123.76, 120.98, 119.04, 114.09, 112.31, 49.97, 48.03, 28.61, 25.92, 25.37, 24.35. HRMS m/z: calcd for $C_{52}H_{60}N_4^{2+}$, $[M]^{2+}$ = 370.7409, found 370.2424. HPLC analysis: retention time at 5.144 min eluted with MeOH/H_2O = 50:50 (v/v), purity = 97.8%.

(E)-1,1'-(octane-1,8-diyl)bis(2-((E)-4-morpholinostyryl)quinolin-1-ium) iodide (10):

Black solid with 77% yield. ^{1}H NMR (400 MHz, DMSO-d_6) δ 8.91 (d, J = 9.0 Hz, 2H), 8.51 (d, J = 9.2 Hz, 2H), 8.44 (d, J = 9.0 Hz, 2H), 8.31 (d, J = 7.8 Hz, 2H), 8.19 (d, J = 15.4 Hz, 2H), 8.11 (t, J = 7.8 Hz, 2H), 7.90 (t, J = 7.5 Hz, 2H), 7.79 (d, J = 8.6 Hz, 4H), 7.51 (d, J = 15.5 Hz, 2H), 6.94 (d, J = 8.6 Hz, 4H), 4.99 (m, 4H), 3.68 (t, 8H), 3.20 (t, 8H), 1.81 (m, 4H), 1.57 (m, 4H), 1.41 (m, 4H). ^{13}C NMR (100 MHz, DMSO-d_6) δ 156.03, 153.64, 148.99, 143.46, 138.67, 135.15, 131.90, 130.77, 128.94, 127.96, 125.07, 121.15, 119.18, 114.21, 113.52, 66.21, 50.20, 47.06, 28.69, 25.94. HRMS m/z: calcd for $C_{50}H_{56}N_4O_2^{2+}$, $[M]^{2+}$ = 372.5021, found 372.2215. HPLC analysis: retention time at 5.124 min eluted with MeOH/H_2O = 50:50 (v/v), purity = 95.9%.

7.3.2 Fluorescence spectroscopy

Fluorescence spectra were recorded using a LS-45 fluorescence spectrometer. The colorimetric dish had a slit width of 1 mm and an optical diameter of 10 mm. Emission spectra for the ligands were obtained by exciting the samples, with the collection range set at 550-800 nm. All oligonucleotides were pre-annealed by heating at 95 °C for 10 minutes, followed by gradual cooling to room temperature in a Tris-HCl buffer (10 mM, pH 7.4) containing 100 mM KCl. Small aliquots of the oligonucleotide stock solution were then added to the ligand solution, which was maintained at a fixed concentration of 5 μM. In the titration experiments, the final concentration of oligonucleotides was adjusted from 0 to 20 μM. After each addition, the mixture was stirred and allowed to equilibrate for at least 1 minute.

7.3.3 UV-visible spectroscopy

UV-Vis spectra were recorded using a Lambda 25 Spectrophotometer (Perkin Elmer). The colorimetric dish had a slit width of 1 mm and an optical diameter of 10 mm. The absorption spectra of the ligands were collected over a range of 300-700 nm. All oligonucleotides were pre-annealed by heating at 95 °C for 10 minutes, followed by gradual cooling to room temperature in a Tris-HCl buffer (10 mM, pH 7.4) containing 100 mM KCl. Small aliquots of the oligonucleotide stock solution were added to the ligand solution, which was maintained at a fixed concentration of 5 μM. In the titration studies, the final concentrations of oligonucleotides were adjusted sequentially to 2.5 μM, 5 μM, 10 μM, 15 μM, and 20 μM. After each addition, the mixture was stirred and allowed to equilibrate for

at least 1 minute. The UV spectra of the ligands were collected first, followed by the spectra of the nucleic acids at each concentration.

7.3.4 Circular dichroism (CD) and melting point assay

CD spectra were recorded using a JASCO J-1500 Circular Dichroism Spectrometer. A quartz cuvette with a path length of 1 mm was employed to measure spectra within a wavelength range of 220 to 700 nm, utilizing a bandwidth of 1 nm, a step size of 1 nm, and a data acquisition time of 1 second per point. Initially, 400 μL of nucleic acid at a concentration of 5 μM was placed in the cuvette, and the CD spectra were collected. Subsequently, ligand **9** was added sequentially at concentrations of 5 μM, 10 μM, 15 μM, and 20 μM, with spectra recorded for each concentration. For melting point assays, measurements were conducted at a fixed wavelength while gradually increasing the temperature from 25 to 95 °C, with a step size of 1 nm and a time of 5 seconds per point. The experiments involved 5 μM of ligand **9** and 5 μM of various nucleic acids in a 10 mM Tris-HCl buffer at pH 7.4 containing 20 mM KCl. The collected data were normalized using Origin software.

7.3.5 NMR spectroscopy

Before taking ^{1}H NMR measurements, *Mito 78* and *Mito 29* were dissolved in a phosphate buffer (25 mM KH_2PO_4, 10% D_2O, 100 mM KCl, pH 7.4) at a concentration of 300 μM. The solution was heated to 95 °C, then allowed to cool to room temperature and incubated for 24 hours. During the measurement, ligand **9** was added sequentially at concentrations of 150 μM and 300 μM. The experiments were performed at 25 °C using a 600 MHz spectrometer.

7.3.6 Isothermal titration calorimetry (ITC) assay

ITC experiments were performed using a MicroCal PEAQ-ITC microcalorimeter (Malvern, USA). Oligonucleotides were pre-annealed in a buffer consisting of 25 mM KH_2PO_4 and 60 mM KCl (pH 7.4, containing 0.2% (v/v) DMSO) by heating to 95 °C in a water bath for 5 minutes. The solution was then cooled to 25 °C and stored at 4 °C overnight. For the experiment, ligand **9** (10 μM) was placed in the sample cell, while 40 μL of pre-annealed oligonucleotides (100 μM) was loaded into the syringe, both in the same buffer. Ligand **9** was mixed with the oligonucleotides by stirring the syringe at 750 rpm at 25 °C. A total of 29 injections were made, each lasting 4 seconds with an interval of 150 seconds. Finally, the collected data were fitted to the built-in binding model to determine the

binding enthalpy.

7.3.7 Surface plasmon resonance (SPR) assay

In this assay, a Sierra SPR-32 Pro (Bruker) was used to do the immobilization of biotinylated DNA and the kinetics assay. In brief, biotinylated DNA sequences were prepared in a running buffer consisting of 10 mM Tris-HCl, 100 mM KCl, and 0.05% Tween 20 (pH 7.4). Biotinylated DNA at a concentration of 800 nM was immobilized onto a biotin capture sensor chip (Bruker Daltonics) using streptavidin chemistry, achieving a response unit (RU) reading of 800-1000. Subsequently, various concentrations of ligands were injected at a flow rate of 30 μL/min for a contact time of 200 seconds, followed by 250 seconds of dissociation at 25 °C, utilizing the multi-injection cycle kinetics (MICK) mode. The chip was regenerated by injecting 2 M KCl between consecutive cycles. Data analysis was performed using Sierra Analyzer R3 software, applying a kinetics model for fitting the data.

7.3.8 Plasmid construction

cDNAs for Pif1, Twinkle, and GRSF1 were synthesized by GenScript. To produce eBFP-tagged proteins, the cDNAs were cloned into the pcDNA3.1+ vector.

7.3.9 Cell culture

The human cancer cell lines used in this study included MDA-MB-231 (HTB-26), HeLa (CRM-CCL-2), HepG2 (HB-8065), LoVo (CCL-229), HCT116 (CCL-247), PANC-1 (CRL-1469), as well as human fibroblasts HFF-1 (SCRC-1041) and BJ (CRL-2522), all sourced from ATCC. The cell lines were maintained in different complete media as follows: MDA-MB-231, HeLa, PANC-1, and HFF-1 were cultured in DMEM (Gibco) supplemented with 10% fetal bovine serum (FBS) (Gibco) and 1% penicillin-streptomycin (P/S) (Gibco). LoVo and HCT116 were grown in RPMI 1640 (Gibco) with 10% FBS and 1% P/S. PANC-1 and BJ were cultured in MEM (Gibco) with 10% FBS and 1% P/S. The cells were incubated at 37 °C in a 5% CO_2 atmosphere. For cell collection in all experiments, the cells were trypsinized using 0.25% trypsin-EDTA (Gibco) and resuspended in various buffers for subsequent analysis.

7.3.10 MTT assay

The MTT assay was performed on cancer cell lines (MDA-MB-231, HeLa, HepG2, LoVo, HCT116,

and PANC-1) as well as normal cells (HFF1 and BJ). The cells were seeded in 96-well plates at an approximate density of 4,000 cells per well and incubated at 37 °C with 5% CO_2. After 24 hours of culture, the cells were treated with various concentrations of ligands (0, 0.625, 1.25, 2.5, 5, 10, 20, 30, and 40 μM) for 48 hours. Following the incubation, the medium was removed, and 100 μL of a 0.5 mg/mL MTT solution was added to each well. The plates were then incubated in the dark for 4 hours. After incubation, the MTT solution was discarded, and 100 μL of DMSO was added to each well to completely dissolve the formazan crystals. The absorbance of the treated plates was measured using a microplate reader at a wavelength of 570 nm. Finally, the cell survival rate and the half-maximal inhibitory concentration (IC_{50}) for the ligands were calculated based on the obtained absorbance values.

7.3.11 Living cell staining and imaging assay

HCT116 cells were cultured overnight in confocal dishes at 37 °C with 5% CO_2 in RPMI 1640 medium supplemented with 10% FBS and 1% P/S. Digital images were captured using a Leica TCS SPE Confocal Microscope. For the mitochondrial co-localization experiment, cells were treated with 200 nM Mito-Tracker Deep Red for 30 minutes, followed by 4 μM ligand **9** for 1 hour. In the endoplasmic reticulum co-localization experiment, the cells were exposed to 1 μM ER-Tracker Blue for 30 minutes and 4 μM ligand **9** for 1 hour. For lysosomal co-localization, cells were treated with 1 μM Lyso-Tracker Blue for 30 minutes and then with 4 μM ligand **9** for 1 hour. In experiments involving cyclosporin A (CsA), cells were treated with 1 μM CsA for 24 hours to block the permeability transition pore on the inner mitochondrial membrane. Following CsA treatment, the cells were washed with RPMI1640 and then incubated with 4 μM ligand **9** for 1 hour and 1 μM Hoechst33342 for 30 minutes. For FCCP treatment, cells were exposed to 1 μM FCCP for 30 minutes to induce depolarization. Afterward, the cells were washed with RPMI1640 and incubated with 4 μM ligand **9** for 1 hour and 1 μM Hoechst33342 for 30 minutes. In competition experiments, cells were initially incubated with 4 μM ligand **9** for 1 hour and 1 μM Hoechst33342 for 30 minutes, followed by the addition of either 5 μM or 10 μM MitoPDS for 3 hours. For Cy5-labeled DNA treatments, oligonucleotides (4 μg) were transfected using Lipofectamine 3000 Transfection Reagent (Invitrogen) for 24 hours before staining, and then the cells were incubated with 4 μM ligand **9** for 1 hour and 1 μM Hoechst33342 for 30 minutes. For HCT116 cells overexpressing eBFP-tagged proteins, cells were transfected with constructed plasmids (4 μg) using Lipofectamine 3000, incubated at 37 °C for

24 hours, and then treated with 4 μM ligand **9** for 1 hour and 1 μM Hoechst33342 for 30 minutes. In HIF-1α inhibitor treatments, cells were exposed to 0.1 μM 2-MeOE2 or 10 μM KC7F2 for 24 hours before imaging. For HIF-PH inhibitor treatment, cells were treated with 100 μM for 24 hours prior to imaging, followed by incubation with 4 μM ligand **9** for 1 hour and 1 μM Hoechst33342 for 30 minutes. To evaluate mitochondrial membrane potential (MMP), cells were treated with various concentrations of ligand **9** for 48 hours. After treatment, the cells were washed with RPMI1640 and then incubated with 1 μM TMRE for 30 minutes. For mitochondrial reactive oxygen species (ROS) detection, cells were treated with different concentrations of ligand **9**, with or without 10 μM MitoTEMPOL for 48 hours. Following this, the cells were washed and treated with 1 μM MitoSOX for 30 minutes. Finally, for mitochondrial permeability transition pore (mPTP) opening detection, cells were treated with various concentrations of ligand **9** for 48 hours, washed with RPMI1640, and then treated with calcein-AM and $CoCl_2$.

7.3.12 Fixed cell staining assay

HCT116 cells were cultured overnight in confocal dishes at 37 °C with 5% CO_2 in RPMI1640 medium supplemented with 10% FBS and 1% P/S. Digital images were captured using a Leica TCS SPE Confocal Microscope. For the DNase I and RNase A digestion experiments, cells were incubated with 4 μM ligand **9** for 1 hour and 1 μM Hoechst33342 for 30 minutes before fixation. Following incubation, the cells were fixed with 4% paraformaldehyde for 20 minutes and then permeabilized with 0.3% Triton X-100 in PBS for 1 hour. Finally, the cells were treated with 200 units/mL of DNase I or RNase A at 37 °C for 3 hours. In the Lamin B1 immunofluorescence experiment, cells were treated with various concentrations of ligand **9** for 72 hours. After treatment, the medium was removed, and the cells were fixed in 4% paraformaldehyde in PBS at room temperature for 20 minutes. The cells were then permeabilized with 0.3% Triton X-100 in PBS for 1 hour and blocked with 1% BSA in PBS for 1 hour. After blocking, the cells were incubated overnight at 4 °C with Lamin B1 antibody. Following incubation, the cells were washed three times with pre-cooled PBS and then incubated for 1 hour with Goat anti-Rabbit IgG Alexa Fluor 647. After secondary antibody incubation, the cells were washed three times with pre-cooled TBST and treated with 1 μM Hoechst33342 for 30 minutes. For the Ki67 immunofluorescence experiment, cells were similarly treated with different concentrations of ligand **9** for 72 hours. After treatment, the cells were fixed with 4% paraformaldehyde in PBS for 20 minutes at room temperature and permeabilized with 0.3%

Triton X-100 in PBS for 1 hour. The cells were then blocked with 1% BSA in PBS for 1 hour before being incubated overnight at 4 °C with Ki67 antibody. After washing three times with pre-cooled PBS, the cells were incubated with Goat anti-Rabbit IgG Alexa Fluor 647 for 1 hour. Post-secondary antibody incubation, the cells were washed three times with pre-cooled TBST and treated with 1 μM Hoechst33342 for 30 minutes.

7.3.13 Cell Cycle Analysis

In this experiment, propidium iodide (PI) was utilized to assess the cell cycle of HCT116 cells. Initially, the cells were collected at a density of 5 x 10^5 cells/mL after being incubated with various concentrations of ligand **9** for 72 hours. The cells were then fixed in 70% ethanol in PBS at 4 °C for 2 hours. Following fixation, the cells were stained with PI. Finally, the stained cells were analyzed using a BD Accuri C6 Flow Cytometer.

7.3.14 Cell apoptosis analysis

HCT116 cells were plated at a density of 1 x 10^5 cells per flask in a 25-cm² culture flask (TPP). After incubating overnight, the cells were treated with various concentrations of ligand **9** for 72 hours. Following treatment, the cells were collected via trypsinization using 0.25% trypsin with EDTA and then suspended in PBS. The cells were subsequently treated with Annexin V-BUV395 and 7-AAD (BD Pharmingen) following the manufacturer's guidelines. Finally, the treated cells were analyzed for apoptosis using a BD FACSymphony A3 Cell Analyzer.

7.3.15 Comet assay for DNA damage detection

DNA damage in HCT116 cells was assessed using the Comet Assay Kit (Abcam, ab238544). The cells were treated with various concentrations of ligand **9**, with or without 10 μμM MitoTEMPOL, for 72 hours. Following treatment, the cells were collected via trypsinization with 0.25% trypsin containing EDTA and suspended in ice-cold PBS at a concentration of 1 x 10^5 cells/mL. The sample preparation was carried out according to the manufacturer's instructions. In brief, cells were mixed with comet agarose at 37 °C, and the agarose/cell mixture was pipetted onto the base layer of comet agarose. The slide was then placed at 4 °C in the dark for 15 minutes to allow gelation. After gelation, the slide was treated with pre-chilled lysis buffer for 30 minutes at 4 °C in the dark. Following lysis, the slide was exposed to an alkaline solution for 30 minutes at 4 °C in the dark. Next, the slide was

transferred to a horizontal electrophoresis chamber for electrophoresis in alkaline electrophoresis solution (300 mM NaOH and 1 mM EDTA, pH > 13) at 30 V for 30 minutes. After electrophoresis, the slide was washed twice with cold water and then immersed in cold 70% ethanol for 5 minutes. The slide was allowed to air dry before being treated with 1 μM DAPI for 10 minutes. Imaging was performed using the Ti2-E Live-cell fluorescence imaging system (Nikon) with a 405 nm excitation LED. The tail moment length was measured from the center of the head to the center of the tail.

7.3.16 *β*-Galactosidase (SA-*β*-gal) staining of cell senescence

HCT116 cells were seeded in a 6-well plate and treated with various concentrations of ligand **9** for 72 hours. After treatment, the medium was discarded, and the cells were washed three times with PBS. Next, *β*-galactosidase staining fixative was added, and the cells were fixed at room temperature for 15 minutes. The fixative was then removed, and the cells were washed three times with PBS for 3 minutes each. Subsequently, the working solution for *β*-galactosidase staining was added, and the cells were incubated at 37 °C overnight. Finally, the results were observed and documented using an inverted fluorescence microscope (Olympus IX71).

7.3.17 Detection of *β*-Galactosidase activity

In this assay, the Senescence *β*-Galactosidase Activity Assay Kit (Fluorescence, Plate-Based, CST) was utilized to measure *β*-Galactosidase activity. HCT116 cells were cultured in a 6-well plate and treated with various concentrations of ligand **9** for 72 hours. Afterward, the medium was removed, and the cells were washed once with cold PBS. The cells were then processed according to the manufacturer's instructions. Finally, the samples were analyzed at an excitation wavelength of 360 nm and an emission wavelength of 465 nm.

7.3.18 RNA isolation and qRT-PCR

HCT116 or HFF1 cells were cultured at a density of 1 x 10^5 cells per flask in a 25-cm² culture flask (TPP). After incubating overnight, the cells were treated with various concentrations of ligand **9** for 48 hours. Following treatment, the cells were trypsinized, and RNA was extracted using the RNase Mini Kit (Qiagen). The RNA samples were prepared according to the manufacturer's instructions provided with the BeyoFast SYBR Green One-Step qRT-PCR Kit (Beyotime Biotechnology). Each reaction mixture (20 μL) included 10 μL of 2 x One Step SYBR Green Mix, 1 μL of One Step SYBR

Green Enzyme Mix, 0.4 μL of 50 x ROX Reference Dye, 1 μL of Gene Specific Primer Forward (0.3 μM), 1 μL of Gene Specific Primer Reverse (0.3 μM), 50 ng of total RNA, and RNase-free ddH_2O to reach a final volume of 20 μL. The reaction mixtures were then incubated in a thermocycler under the following conditions: reverse transcription at 50 °C for 30 minutes, denaturation at 95 °C for 2 minutes, followed by 40 cycles of 95 °C for 15 seconds and 60 °C for 30 seconds. The data were normalized to housekeeping gene GAPDH and analyzed using the ΔΔCt method.

7.3.19 DNA isolation and q-PCR

HCT116 or HFF1 cells were plated at a density of 1 x 10^5 cells per flask in a 25-cm² culture flask (TPP). After an overnight incubation, the cells were treated with various concentrations of ligand **9** for 48 hours. Following treatment, the cells were trypsinized and DNA was extracted using the PureLink Genomic DNA Mini Kit (ThermoFisher Scientific). The DNA samples were prepared according to the manufacturer's instructions provided with the PowerUp SYBR Green Master Mix for qPCR (ThermoFisher Scientific). Each reaction mixture (20 μL) consisted of 10 μL of 2 x SYBR Green Master Mix, 1 μL of Gene Specific Primer Forward (0.3 μM), 1 μL of Gene Specific Primer Reverse (0.3 μM), 50 ng of total DNA, and RNase-free ddH_2O to bring the total volume to 20 μL. The reaction mixtures were incubated in a thermocycler under the following conditions: UDG activation at 50 °C for 2 minutes, activation of Dual-Lock DNA polymerase at 95 °C for 2 minutes, followed by 40 cycles of 95 °C for 15 seconds and 60 °C for 1 minute. The data were normalized to housekeeping gene GAPDH and analyzed using the ΔΔCt method.

7.3.20 Western blotting

HCT116 cells were plated at a density of 80 x 10^4 cells per flask in a 25-cm² culture flask (TPP). After incubating overnight, the cells were treated with various concentrations of ligand **9** for either 48 or 72 hours. The cells were then collected and incubated on ice for 20 minutes in RIPA buffer (which included protease and phosphatase inhibitors), followed by centrifugation at 4 °C at 12,000 × g for 10 minutes. The total protein concentration was determined using a BCA kit. A consistent amount of protein (30 μg) was loaded onto a 12% SDS-PAGE gel for separation, and the proteins were subsequently transferred to a PVDF membrane. After blocking with 5% skim milk, the membranes were incubated with primary antibodies overnight at 4 °C. The membranes were washed three times with TBST buffer for 30 minutes, then incubated with either Anti-mouse IgG, HRP-linked

Antibody or Anti-rabbit IgG, HRP-linked Antibody at room temperature for 2 hours. Following this incubation, the membranes were thoroughly washed and subjected to chemiluminescence detection using Immobilon Western Chemiluminescent HRP substrate (Merck Millipore).

7.3.21 Seahorse experiment

For the Mito Stress Test, on Day 1, HCT116 cells were seeded at a density of 5 x 10^4 cells per well in RPMI1640 in a 24-well Agilent Seahorse XF cell culture microplate (Agilent Technologies) and incubated overnight. Reference wells A1, B4, C3, and D6 were filled with medium only. The sensor cartridge on the calibration plate (Agilent Technologies) was calibrated using 1 mL of Agilent Seahorse XF Calibrant. This calibration plate was then placed in a non-CO_2 incubator at 37 °C overnight. On Day 2, the RPMI1640 medium was removed from the microplate, and the cells were treated with various concentrations of ligand **9** for 3 hours. Following treatment, 500 μL of assay medium (RPMI1640 assay medium provided by Agilent Technologies, supplemented with 1 mM pyruvate, 2 mM glutamine, and 10 mM D-glucose, pH 7.4 at 37 °C) was added to each well. The microplate with cells was then incubated in a non-CO_2 incubator at 37 °C for 1 hour. Meanwhile, the sensor cartridges on the calibration plate prepared on Day 1 were loaded with different ligands in assay medium: port A received 56 μL of 10 μM oligomycin; port B received 62 μL of 10 μM FCCP; and port C contained 69 μL of a mix of 10 μM rotenone and 5 μM antimycin A. The loaded sensor cartridge on the calibration plate was placed in an XF24 analyzer (Agilent Technologies) for 30 minutes. After incubation, the calibration plate was replaced with the microplate containing the cells. The Seahorse Wave software was used to conduct the Mito Stress Test, and the results were normalized to cell number.

For the Glycolysis Stress Test, HCT116 cells were seeded at a density of 5 x 10^4 cells per well in RPMI1640 in a 24-well Agilent Seahorse XF cell culture microplate (Agilent Technologies) and incubated overnight. Reference wells A1, B4, C3, and D6 were filled with medium only. The sensor cartridge on the calibration plate (Agilent Technologies) was calibrated with 1 mL of Agilent Seahorse XF Calibrant, which was placed in a non-CO_2 incubator at 37 °C overnight. On Day 2, the RPMI1640 medium was removed from the microplate, and the cells were treated with various concentrations of ligand **9** for 3 hours. Following treatment, 500 μL of assay medium (RPMI1640 assay medium provided by Agilent Technologies, supplemented with 2 mM glutamine, pH 7.4 at 37 °C) was added

to each well. The microplate with cells was then incubated in a non-CO_2 incubator at 37 °C for 1 hour. Meanwhile, the sensor cartridges on the calibration plate prepared on Day 1 were loaded with different ligands in assay medium: port A received 56 μL of 100 mM glucose; port B received 62 μL of 10 μM oligomycin; and port C contained 69 μL of 500 mM 2-DG. The loaded sensor cartridge on the calibration plate was placed in an XF24 analyzer (Agilent Technologies) for 30 minutes. After incubation, the calibration plate was replaced with the microplate containing the cells. The Seahorse Wave software was used to perform the Glycolysis Stress Test, and the results were normalized to cell number.

7.3.22 RNA-sequencing (RNA-seq)

HCT116 cells were plated at a density of 1 x 10^5 cells per flask in a 25-cm² culture flask (TPP). After overnight incubation, the cells were treated with 4 μM ligand **9** for 48 hours. Following treatment, the cells were trypsinized, and RNA was extracted using the RNase Mini Kit (Qiagen). The RNA samples were prepared according to the manufacturer's instructions and subsequently sent to Novogene for RNA sequencing and data analysis. The raw transcriptome data have been deposited in the NCBI Sequence Read Archive (SRA) database (BioProject: PRJNA1067376). The quantity and quality of the RNA samples were evaluated using a Qubit 4.0 fluorometer (ThermoFisher Scientific) and an Agilent 2100 Bioanalyzer (Agilent), respectively. cDNA libraries were constructed from the RNA samples using the Illumina TruSeq Stranded Total RNA Prep kit (with Ribo-Zero Plus) and an indexing kit (Illumina). The prepared cDNA libraries were assessed for quantity and quality using the same Qubit and Bioanalyzer methods. The cDNA libraries from both experimental and control groups were pooled, and sequencing was performed on the Illumina NextSeq 2000 system using the 150 bp paired-end dual-indexed method. Sequencing quality for both experimental and control samples was evaluated using FastQC. Low-quality reads and adapter sequences were trimmed with Fastp. The trimmed reads were then aligned to the human reference genome (GRCh38/hg38) using the STAR package (R programming). The STAR output (reads per gene) was analyzed for differential expression with DESeq2 (R programming), defining differentially expressed genes as those with a fold-change >1 or <−1 and a p-value <0.05. A heat map of expression patterns was generated using R (pheatmap), and a volcano plot was created with R (ggplot2). Additionally, Kyoto Encyclopedia of Genes and Genomes (KEGG) analysis was conducted using clusterProfiler (R programming). Gene Set Enrichment Analysis (GSEA) was performed with GSEA software version

4.1.0 (Broad Institute), utilizing hallmark gene sets (H collection) and canonical pathways gene sets (CP in C2 collection) from the Molecular Signatures Database (MSigDB 7.2).

7.3.23 Colony formation assay

500 HCT116 cells were plated in RPMI1640 and incubated with various concentrations of ligand **9** for 7 days in 6-well plates. Following incubation, the samples were stained with crystal violet for 30 minutes. The plates were then allowed to dry, and images were captured before counting the colony numbers using ImageJ.

7.3.24 Trans-well assay

The trans-well migration assay was conducted using Trans-well chambers. A total of 1 x 10^5 HCT116 cells were plated in the upper chamber of a 24-well plate in 200 μL of serum-free RPMI1640 medium. The lower chamber was filled with 600 μL of RPMI1640 medium supplemented with 20% FBS. The chambers were incubated with various concentrations of ligand **9** at 37 °C for 72 hours. After incubation, cells on the upper surface of the membrane were gently removed with a cotton swab. The migrated cells on the lower surface of the membrane were stained with crystal violet and subsequently observed under a microscope.

7.3.25 Pharmacokinetic studies in rat

In this study, the experiments adhered to the Animal Management Rules established by the Ministry of Health of the People's Republic of China, as well as the regulations and guidelines set forth by the institutional ethics committee concerning animal welfare. The approved case number from the Animal Subjects Ethics Sub-Committee (ASESC) is 21-22/45-ABCT-R-GRF. Five-week-old male Sprague-Dawley rats were obtained from the Guangdong Medical Laboratory Animal Center (China) and housed in a specific pathogen-free (SPF) environment with a 12-hour light/dark cycle, allowing free access to food and water. After a one-week adaptation period, ligand **9** was administered to the Sprague-Dawley rats (females weighing 200 ± 20 g) via tail vein injection at a dose of 2.5 mg/kg. Blood samples (0.3 mL) were collected from the orbital sinus at 5, 15, 30 minutes, and at 1, 2, 4, 6, 8, 12, and 24 hours post-injection. At the end of the study, the rats were killed by cervical dislocation. Analyte quantification was performed using an LC/MS/MS Quantum Access mass spectrometer (AB 4000), with compound detection carried out in electrospray positive ionization mode.

Pharmacokinetic parameters were calculated using WinNonlin software version 6.3, based on noncompartmental analysis (Pharsight Corporation, Mountain View, USA).

7.3.26 *In vivo* antitumor activity in the human colorectal cancer (HCT116) xenograft model

In this study, the experiments adhered to the Animal Management Rules established by the Ministry of Health of the People's Republic of China, as well as the regulations and guidelines set forth by the institutional ethics committee concerning animal welfare. The approved case number from the Animal Subjects Ethics Sub-Committee (ASESC) is 21-22/45-ABCT-R-GRF. To minimize suffering, the procedures were performed under 2% isoflurane anesthesia. Five-week-old male Balb/c were obtained from the Guangdong Medical Laboratory Animal Center (China) and housed in a specific pathogen-free (SPF) environment with a 12-hour light/dark cycle, allowing free access to food and water. For the establishment of a xenograft model, a suspension of HCT116 cells (5×10^6 cells) was injected subcutaneously after a one-week adaptation period. Once the subcutaneous tumor reached a diameter of 100 mm^3, the nude mice were divided into two groups (six mice per group): one group received a tail vein injection of PBS (control group) and the other group received ligand **9** (treatment group). The ligand was administered at a dose of 5 mg/kg every two days. The mice were killed by cervical dislocation on the 16th day after intravenous injection of the ligand. Blood samples were collected, centrifuged, and separated into cell and serum fractions for routine blood analysis. Major organs and tumor tissues were harvested from each group for hematoxylin and eosin (H&E) staining, TUNEL staining, and Ki67 staining.

7.3.27 Statistical test

Data are presented as means ± SEM (standard error of the mean) from at least three independent experiments (not replicates) conducted both *in vivo* and *in vitro*. Statistical analyses were performed using GraphPad Prism 8.0. For comparisons between two groups, Student's t-test was applied. For multiple group comparisons, one-way analysis of variance (ANOVA) with Dunnett's correction was utilized. A p-value of < 0.05 was deemed statistically significant; ‘ns’ indicates not significant. The criterion for statistical significance was defined as follows: ns: $p > 0.05$, *$p < 0.05$, **$p < 0.01$, and ***$p < 0.001$.

7.4 References

[1] B.-X. Zheng, Indole-benzothiazole derivatives as mitochondrial and c-MYC G-quadruplex ligands, Guangdong University of Technology (2021).

[2] C. Vianello, V. Cocetta, D. Catanzaro, G.W. Dorn, 2nd, A. De Milito, F. Rizzolio, V. Canzonieri, E. Cecchin, R. Roncato, G. Toffoli, V. Quagliariello, A. Di Mauro, S. Losito, N. Maurea, C. Scaffa, G. Sales, L. Scorrano, M. Giacomello, M. Montopoli, Cisplatin resistance can be curtailed by blunting Bnip3-mediated mitochondrial autophagy, Cell Death Dis 13(4) (2022) 398.

Chapter 8. Conclusion

In the present study, we verified that a small-sized ligand **BYB** was a G4-mtDNAs targeting ligand *in vitro* and *in cellular*. And the anticancer mechanism against G4-mtDNAs in human cervical cancer cells HeLa was investigated. On the other hand, we designed and synthesized a series of di-cationic small-sized lipophilic ligands for G4-mtDNAs and screened them from their selectivity, affinity, intracellular location, and cytotoxicity. Based on the results of the screening, ligand **9** was further used to study the antitumor mechanism against G4-mtDNAs in human colorectal cancer cells HCT116. In this chapter, we will summarize the main findings of this study.

8.1 Summary of the major findings

In Chapter 3, we investigated the binding selectivity, interaction property and cellular target of a small-sized benzoindole-benzothiazole ligand **BYB** targeting G4-mtDNAs. A series of *in vitro* and intracellular experiments were performed to study the interaction between **BYB** and G4-mtDNAs. *In vitro* studies including fluorescence titration, CD titration, and NMR titration showed that **BYB** can selectively interact with G4-mtDNAs, while the selectivity of **BYB** toward non-G4-mtDNAs was found to be poor. The affinity obtained by ITC titration revealed that **BYB** had a high binding capacity for G4-mtDNAs, with binding affinity (K_D) ranging from 1.96-5.22 μM. Moreover, CD melting studies showed that **BYB** can increase the melting point of G4-mtDNAs by 6.6-16.3 °C, suggesting that **BYB** can stabilize the structure of G4-mtDNAs. In living cell imaging, organelle co-localization analysis, enzymatic digestion assays, G4-mtDNAs ligand co-localization assays, and G4-mtDNAs helicases overexpression assays indicated that the primary target of **BYB** in living HeLa cells is G4-mtDNA. Finally, **BYB** exhibited a significant inhibitory effect on the proliferation of a variety of cancer cells including A375, HeLa, MIA PaCa-2, SK-MEL-2, HepG2, MDA-MB-231 and HCT116, in which the IC_{50} values of **BYB** were found about 5.4-9.7 μM, while the cytotoxicity against noncancerous cells was relatively low (BJ and HFF1, $IC_{50} > 25$ μM). Therefore, **BYB** appears to be a G4-mtDNA-selective ligand that effectively suppresses the proliferation of various human cancer cells.

In Chapter 4, we investigated the anticancer mechanism of **BYB** against human cervical cancer cell HeLa. qPCR and qRT-PCR showed that the mtDNA replication and transcription could be significantly inhibited by **BYB**, including *ND1*, *ND4*, *ND4L*, *ND5*, *COX2*, *COX3*, *CYTB*, *ATP6* and

ATP8, resulting in the impeded assembly of the respiratory chain complex (I-IV). Due to the obstruction in the assembly of the mitochondrial respiratory chain complex, electron transport was disrupted, leading to a downregulation of oxidative phosphorylation. On the other hand, the assembly of mitochondrial respiratory chain complex was blocked, resulting in mitochondrial calcium overload. Calcium overload then triggered a series of cellular events, including leading to mitochondrial dysfunction, inhibition of ATP production, and elevated mtROS production, as well as induction of mitophagy, iron metastasis, mtDNA and nuclear DNA damage, and apoptosis. Specifically, mitochondrial calcium overload induced overproduction of mtROS, which in turn caused damage to mtDNA. At the same time excess mtROS induced ferroptosis, and stronger ROS were produced through the Fenton reaction and enter the nucleus, causing DNA damage in the nucleus. Although the mechanisms involved remain to be further investigated, the present study demonstrated that there is a link between G4-mtDNA, calcium ions, ROS, ferroptosis, and nuclear DNA damage. To the best of our knowledge, this is the first study targeting G4-mtDNAs with G4-mtDNA ligand to induce mitochondrial calcium overload and then cause nuclear DNA damage and cell death. Finally, the *in vivo* antitumor efficacy of **BYB** in a HeLa cell xenograft tumor model was further validated. Administering the ligand at a dose of 2.5 mg/kg resulted in a 64.6% reduction in tumor weight compared to the control group. Overall, **BYB** demonstrated significant antitumor activity *in vivo*.

In Chapter 5, we designed and synthesized a series of di-cationic small-sized lipophilic ligands **1-10** since mitochondria of cancer cells have a high membrane potential. Among the ligands, **9** was found to have higher selectivity for G4-mtDNAs than non-G4-mtDNAs. In addition, **9** exhibited a low IC_{50} value, down to 3.4 μM against human colorectal cancer cell HCT116, while the IC_{50} values in human normal cell lines were higher than 32 μM. The binding studies including fluorescence titration, UV-visible titration, CD titration and NMR titration suggested that ligand **9** may bind specifically to G4-mtDNAs and can stabilize the structure of G4s. Moreover, the binding affinity ranged from 0.06 to 0.27 μM toward different G4-mtDNAs was obtained by ITC titration. Confocal cell imaging studies including organelle co-localization analysis, enzymatic digestion assays, transfection of G4-mtDNAs and overexpression of G4-mtDNA helicase in living cells demonstrated that **9** can specifically target G4-mtDNAs in living HCT116 cells. Therefore, **9** was identified as a G4-mtDNA-selective ligand that effectively inhibits the proliferation of human colorectal cancer cell HCT116.

In Chapter 6, the anticancer mechanism of **9** targeting G4-mtDNAs in human colorectal cancer cell HCT116 was investigated. The results from qRT-PCR and Western blot analyses indicated that ligand **9** significantly inhibited the transcription and translation of several genes associated with the mitochondrial respiratory chain, including *ND3*, *ND4*, *ND6*, *COX1*, *COX2*, *COX3*, *CYTB*, *ATP6*, and *ATP8*, resulting the downregulation of respiratory chain complexes I-IV. Moreover, ligand **9** caused mitochondrial dysfunction including depolarization of the mitochondrial membrane potential, enhanced ROS production, mPTP opening and downregulation of both oxidative phosphorylation and glycolysis. Excess ROS induced DNA damage and eventually leaded to cell senescence and apoptosis. In assessing the *in vitro* antitumor activity of ligand **9**, trans-well and colony formation assays revealed that it significantly inhibits the migration and proliferation of HCT116 cells. The *in vivo* efficacy of the ligand was also confirmed using human colorectal cancer xenografts (HCT116) in nude mice. At a dosage of 5 mg/kg, the ligand achieved a 70% reduction in tumor weight compared to the control group. Overall, this di-cationic ligand acts as a potent and low-toxicity anticancer agent by targeting G4-mtDNAs for the treatment of human colorectal cancer.

8.2 Contributions of the research

G-quadruplexes play crucial regulatory roles and have been recognized as promising anticancer target. However, unlike nuclear DNA and RNA G-quadruplexes, mitochondrial DNA G-quadruplexes are not well understood, primarily due to the absence of specific ligands. In this study, we aimed to discover new small molecule ligands targeting G4-mtDNAs and study their regulatory roles. Moreover, we tried to evaluate the potential of G4-mtDNA as a new antitumor target. We believe our findings can contribute valuable insights to research in this field.

Firstly, we proposed for the first time utilizing the higher membrane potential of mitochondria in cancer cells as a feature to design small molecule ligands targeting G4-mtDNAs. Carrying multiple positive charges by small molecules may facilitate their entry into mitochondria and can reduce the off-target phenomenon of small molecules. This study can thus serve as a reference for designing specific ligands aimed at G4-mtDNAs.

Secondly, we have shown for the first time that targeting G4-mtDNAs with small molecule ligands can induce mitochondrial calcium overload. This overload triggers ferroptosis and nuclear DNA

damage, ultimately leading to apoptosis in cancer cells. Many existing cancer treatments struggle with drug resistance, but some studies suggest that inducing calcium overload with drugs can be more effective against various drug-resistant cancer cells. Thus, inducing calcium overload presents a promising strategy for combating drug-resistant cancers, offering a novel mechanism for designing antitumor drugs that focus on G4 structures.

Finally, we established mouse xenograft models for human colorectal and cervical cancer to evaluate the *in vivo* antitumor efficiency of small molecules targeting G4-mtDNAs. The results demonstrated that these molecules effectively inhibited tumor growth, indicating that G4-mtDNA could be a promising antitumor target. Consequently, this study may provide new therapeutic options for cancer treatment.

Appendix

List of Contents

Figure S16. ^{1}H NMR (DMSO-d_6), ^{13}C NMR (DMSO-d_6), HRMS and HPLC analysis of ligand **9**

Figure S17. ^{1}H NMR (DMSO-d_6), ^{13}C NMR (DMSO-d_6), HRMS and HPLC analysis of ligand **10**

1. List of Supporting Table

Table S1. Sequences of oligonucleotides used in the present study.[1, 2]

Abbreviation	Sequence (5′→3′)	Structure
Dt21	TTTTTTTTTTTTTTTTTTTT	Single-stranded
SS19	CAGTATCTGTCTTTGATTC	Single-stranded
4AT	ATATATATATAT	Duplex
4A4T	AAAATTTT	Duplex
Ds12	GCGCAATTGCGC	Duplex
Ds26	CAATCGGATCGAATTCGATCCGATTG	Duplex
DNA hairpin	CGCGCGCGTTTTCGCGCGCG	Hairpin
HP19	CAGTATCTGTCTTTGATTCTTTTTTGAATCAAAGACAGATACTG	Hairpin
Telo21	GGGTTAGGGTTAGGGTTAGGG	Mixed
Mito 3	CGGGGGGAGGGGGGGTTTGGTGGA	Parallel
Mito 5	TGGGAGTGGGAGGGGAAAATAATGTGTTAGTTGGGGGGTG	Parallel
Mito 5A	GAGATTAGTAGTATGGGAGTGGGAGGGG	Parallel
Mito 7	GGTGTGTGTGTGCTGGGTAGGATGGGCGGGGGTTGTATTGATGAGATTAG	Parallel
Mito 13	GGTGAGTTTTAGCTTTATTGGGGAGGGGGT	Parallel
Mito 0.5-1	GGGTAAATGGTTTGGCTAAGGTTGTCTGGTAGTAAGGTGGGGTGGGTTTGGGGCTAGG	Parallel
Mito 26	AGAGGGTGATGGTAGATGTGGCGGG	Parallel
Mito 43	TGGTAGAGTAGATGATGGGTTGGG	Parallel
Mito 55	AGGGCGATGAGTGTGGGGAGGAATGGGGTGGGT	Parallel
Mito 71	CGAATGTGTGGTAGGGTGGGGGGCA	Parallel
Mito 72	AGGATGCGTAGGGATGGGAGGGCGATGAGGACTAGGATGA	Parallel
Mito 76	TGGGCTCTAGAGGGGGTAGAGGGGGTGCTATAGGGTAAATACGGGC	Parallel
Mito 81	TTGGAGGTGGGGATCAATAGAGGGGGA	Parallel

Mito 89	TAGGAGTGGGACTTCTAGGGGATTTAGCGGGGTGATGCCTGTTGGGGGC	Parallel
Mito 95	AGGAGGGGGGTTGTTAGGGGGTCGGAGGAAAAGGTTGGGGA	Parallel
Mito 112	GGGGTTGAGGGATAGGAGGAGAATGGGGG	Parallel
Mito 123	TGGCTGAGGGGAGTCAGGGGTGGAGACCTAATTGGG	Parallel
Mito 124	GGGGGGTGGAAGCGGATGAGTAAGAAG	Parallel
Mito 125	TGGGCTATTTTCTGCTAGGGGGTGGAAG	Parallel
Mito 126	GGGAGGTTGAAGTGAGAGGTATGGT	Parallel
Mito 132	GGTAGAGGGGGATTGTTGTTTGGAAGGGGGATGCGGGGG	Parallel
Mito 143	GTGGGGTGAAAGAGTATGATGGGGTGGTGG	Parallel
Mito 152	GAATTTTGGGGGAGGTTATATGGG	Parallel
Mito 155	GGGGGTTAATTTTGCGTATTGGGG	Parallel
Mito 157	GCGGAGATGTTGGATGGGGTGGGGAGGTCGATGAATGAGTGG	Parallel
Mito 0.5-37	GGAGGATGGTGGCCAAGGG	Parallel
Mito 377	GGGGGGGGGGGGTTTGATGTGGGTTGGG	Parallel
Mito 10252	GGGTGGGAGTAGTTCCCTGCTAAGGGAGGG	Parallel
Mito 16250	GAAGCGGGGGAGGGGGGGTTTGGTGGAAAT	Parallel
Mito 0.5-2	GGTTAGGCTGGTGTTAGGG	Antiparallel
Mito 30	CGGCAAGGTCGAAGGGGGTTCGGTTGGT	Antiparallel
Mito 0.5-15	GGATTTTGGCGTAGGTTTGGTCTAGGG	Antiparallel
Mito 78	ATGGGTTTGGTGAGGGAGGTAGGTGGT	Antiparallel
Mito 0.5-21	GGGGATGGCCATGGCTAGG	Antiparallel
Mito 0.5-22	GGTTAGGCGTACGGCCAGGGCTATTGG	Antiparallel
Mito 119	GGCCTAGTAGTGGGGTGAGGCTTGG	Antiparallel
Mito 0.5-29	GGTTAGGTAGTTGAGGTCTAGGG	Antiparallel
Mito 137	GGAGTAGGGTTAGGATGAGTGGGAAGAAG	Antiparallel
Mito 165	GGGTGAGGGGTGGCTTTGGAGTTG	Antiparallel
Mito 9438	GGCGTAGGTTTGGTCTAGGG	Antiparallel
Mito 9	TGGGGGGTGTCTTTGGGGTTTGGTTGGTTCGGGGTATGGGG	Mixed
Mito 12	TGGGGGTGTGGCTAGGCTAAGCG	Mixed
Mito 18	AGGTGGGGTGGGTTTTGGGGCTAGGT	Mixed

Mito 21	GGGGATTTAGAGGGTTCTGTGGG	Mixed
Mito 0.5-5	GGGTGATGGTAGATGTGGCGGGTTTTAGGGGCTCTTTGG	Mixed
Mito 27	AGGTCGGGGCGGTGATGTAGAGGGTGAT GGT	Mixed
Mito 28	GCGATGGTGAGAGCTAAGGTCGGGG	Mixed
Mito 0.5-6	GGAGGCCTAGGTTGAGGTTGACCAGGGGGTTGGGTATGGGGAGGGGGG	Mixed
Mito 29	AGGGGGTTGGGTATGGGGAGGGGGGT	Mixed
Mito 32	CGGCTATGAAGAATAGGGCGAAGGGG	Mixed
Mito 59	CGGTCGGCGAACATCAGTGGGGGTGAGGT	Mixed
Mito 64	AGGGGCGTTTGGTATTGGGTTATGGCAGGGGGT	Mixed
Mito 66	GGCGGGGTCGAAGAAGGTGGTGTTGAGG	Mixed
Mito 0.5-16	GGAGGCCATGGGGTTGG	Mixed
Mito 0.5-18	GGATGCGTAGGGATGGGAGGGCGATGAGGACTAGGATGATGGCGGGCAGG	Mixed
Mito 88	AGTTGGGGGGTAGGGGCTAGGCTGGAGTGGTAAAAGGC	Mixed
Mito 90	TGGAGAAAGGGACGCGGGCGGGGGATATAGGGT	Mixed
Mito 91	AGGGCTCATGGTAGGGGTAAAAGGAGGGCA	Mixed
Mito 100	AGTGCGATGAGTAGGGGAAGGGAGC	Mixed
Mito 105	AGGGGTAGGCTATGTGTTTTGTCAGGGGGTTG	Mixed
Mito 114	AGGGTTAACGAGGGTGGTAAGGATGGGGGGAATTAGGGAAGTCAGGGTTAGGGT	Mixed
Mito 117	AGGGAGAGCTGGGTTGTTTGGGTTGTGG	Mixed
Mito 121	GGGGTGGAGACCTAATTGGGCTG	Mixed
Mito 122	TGGCTGAGGGGAGTCAGGGGTGGAGACCTAATTGGG	Mixed
Mito 130	TGGCGTTTAATGGGGTTTAGTAGGGTGGGG	Mixed
Mito 135	AGGTCTAGGAGGAGTAGGGGCAGGTTTTGGCTCG	Mixed
Mito 136	TGGGTTGAGGTGATGATGGAGGTGGAG	Mixed
Mito 140	GGTGCGGGGGCTTTGTATGATTATGGGCG	Mixed
Mito 141	GGGAGGATCCTATTGGTGCGGGGG	Mixed
Mito 142	GGAGAGGGGTCAGGGTTGATTCGGGAGG	Mixed
Mito 149	GAGGCATGGGGGTCAGGGGTTGAGGTCTTGGTGAGTG	Mixed

Mito 154	GAGTGTGGGTTTAGTAATGGGGGTTTGTGGGG	Mixed
Mito 160	GGGCTTGATGTGGGGAGGGGTGTTTAAGGGGTTGGCTAGGGTATAATTGTCTGGG	Mixed
Mito 164	GGGGAGGGGGTTTTGATGTGGGTTGGG	Mixed
Mito 167	GGGGAACGTGTGGGCTATTTAGG	Mixed
Mito 714	GGGAGATAGTTGGTATTAGGATTAGG	Mixed
Mito 1015	GGGCTTGATGTGGGGAGGGGTGTTTAAGGG	Mixed
Mito 6363	AGGGACGCGGGCGGGGGATATAGGGT	Mixed
Mito 8095	CCCTCCATCCACC	Mixed
Mito 12086	GGGCCAGGGGATTAATTAGTACGGGAAGGG	Mixed
rRNA	16S- and 23S-Ribosomal from *E. coli*	Duplex

Table S2. Primers of qRT-PCR assay used in the present study.

Abbreviation	Sequence (5′→3′)
ND1-F	GGCTATATACAACTACGCAAAGGC
ND1-R	GGTAGATGTGGCGGGTTTTAGG
ND2-F	ATCATAGCAGGCAGTTGAGG
ND2-R	GGGTGGGTTTTGTATGTTCA
ND3-F	AAAATCCACCCCTTACGAGT
ND3-R	TATTGGCTAAGAGGGAGTGG
ND4-F	CCCTCGTAGTAACAGCCATTCTC
ND4-R	CGACTGTGAGTGCGTTCGTAGT
ND4L-F	CCCTCGTAGTAACAGCCATTCTC
ND4L-R	CGACTGTGAGTGCGTTCGTAGT
ND5-F	TAGGTCTCCACCCCTGACTC
ND5-R	TAGATAGGGCTCAGGCGTTT
ND6-F	CCCGAGCAATCTCAATTACA
ND6-R	CCGTGCGAGAATAATGATGT
CYTB-F	CCCATTCCGATAAAATCACC
CYTB-R	CTACAAGGACAGGCCCATTT
COX1-F	GCCTGACTGGCATTGTATTA

COX1-R	GGTTCGATTCCTTCCTTTTT
COX2-F	CCTGTATGCCCTTTTCCTAA
COX2-R	TTTGCTCCACAGATTTCAGA
COX3-F	GATGAGCAGCTTTTCCAGACGAC
COX3-R	AACTGGACACCGAACAGCAGCT
ATP6-F	TAGCCATACACAACACTAAAGGACGA
ATP6-R	GGGCATTTTTAATCTTAGAGCGAAA
ATP8-F	TACTACCGTATGGCCCACCA
ATP8-R	GGGGCAATGAATGAAGCGAA
KRAS-F	CAGTAGACACAAAACAGGCTCAG
KRAS-R	TGTCGGATCTCCCTCACCAATG
c-MYC-F	TGGTGCTCCATGAGGAGACA
c-MYC-R	GTGGCACCTCTTGAGGACCT
GAPDH-F	GGGAAACTGTGGCGTGAT
GAPDH-R	TCGGCCACATTGTGAACTTT

Table S3. Primers of PCR assay used in the present study.

Abbreviation	Sequence (5′→3′)
ND1-F	CTCTTCGTCTGATCCGTCCT
ND1-R	TGAGGTTGCGGTCTGTTAGT
ND2-F	GTAGACAGTCCCACCCTCAC
ND2-R	TTGATCCCGTTTCGTGCAAG
GAPDH-F	TGACATCAAGAAGGTGGTGAAGC
GAPDH-R	AAGGTGGAAGAGTGGGAGTTGCTG

Table S4. 5’-terminal biotinylated mtDNA sequences used in the SPR analysis.

Abbreviation	Sequence (5′→3′)
Mito 0.5-16	GGAGGCCATGGGGTTGG
Mito 29	AGGGGGTTGGGTATGGGGAGGGGGGT
Mito 55	AGGGCGATGAGTGTGGGGAGGAATGGGGTGGGT

Mito 78	ATGGGTTTGGTGAGGGAGGTAGGTGGT
HP19	CAGTATCTGTCTTTGATTCTTTTTTGAATCAAAGACAGATACTG

Table S5. 5'-terminal Cy5 coupled mtDNA sequences used in the present study.

Abbreviation	Sequence (5′→3′)
Mito 0.5-16	GGAGGCCATGGGGTTGG
Mito 78	ATGGGTTTGGTGAGGGAGGTAGGTGGT
SS19	CAGTATCTGTCTTTGATTC
HP19	CAGTATCTGTCTTTGATTCTTTTTTGAATCAAAGACAGATACTG

Table S6. Antisense and mutated sequences used in the present study.

Abbreviation	Sequence (5′→3′)	Variation
Mito 6363 A	ACCCTATATCCCCCGCCCGCGTCCCT	Antisense
Mito 10252 A	CCCTCCCTTAGCAGGGTTCTACTCCCACCC	Antisense
Mito 16250 A	ATTTCCACCAAACCCCCCCTCCCCCGCTTC	Antisense
Mito 55 M	AGAGCGATGAGTGTGAAGAGGAATGAAGTGAGT	Mutation
Mito 78 M	ATGACTTTAGTGAGACATGTAAGTAGT	Mutation
Mito 6363 M	AGTGACGCGTGCGTTGTATATAGTGT	Mutation
Mito 10252 M	GTGTGTGAGTAGTTCCCTGCTAAGTGAGTG	Mutation
Mito 16250 M	GAAGCGTGTGAGTTGTTGTTTGTTGTAAAT	Mutation

Table S7. The antibodies used in the present study.

Antibody	Company (Catalog#)	Species	Dilution
MT-ND1	Abcam (ab181848)	Rabbit	1000
MT-ND2	Abcam (ab219821)	Mouse	1000
MT-ND3	CST (82933)	Rabbit	1000
MT-ND4	ThermoFisher (PA5-114379)	Rabbit	1000
MT-ND4L	ThermoFisher (PA5-103953)	Rabbit	1000
MT-ND5	Abcam (ab230509)	Rabbit	1000

MT-ND6	ThermoFisher (PA5-109993)	Rabbit	1000
MT-COX1	CST (55159)	Rabbit	1000
MT-COX2	CST (50003)	Rabbit	1000
MT-COX3	ThermoFisher (459300)	Mouse	1000
Cytochrome b	CST (54618)	Rabbit	1000
ATP6	CST (70262)	Rabbit	1000
ATP8	CST (96857)	Rabbit	1000
Lamin B1	CST (13435)	Rabbit	1000
p16	CST (92803)	Rabbit	1000
p21	CST (2947)	Rabbit	1000
Akt	CST (9272)	Rabbit	1000
Phospho-Akt	CST (4060)	Rabbit	1000
IP3R	CST (8568)	Rabbit	1000
Phospho-IP3R	CST (8548)	Rabbit	1000
NCX1	CST (79350)	Rabbit	1000
MCU	CST (14997)	Rabbit	1000
VDAC	CST (4661)	Rabbit	1000
Tom20	Abcam (ab186735)	Rabbit	1000
Tim23	Abcam (ab230253)	Rabbit	1000
LC3	CST (3868)	Rabbit	1000
P62	CST (23214)	Rabbit	1000
Total OXPHOS Human WB	Abcam (ab110411)	Mouse	1000
γ -H2A.x	CST (9718)	Rabbit	1000
p53	CST (2527)	Rabbit	1000
Smac	Abcam (ab32023)	Rabbit	1000
Cytochrome C	Abcam (ab133504)	Rabbit	1000
COX IV	CST (4850)	Rabbit	1000
Bax	Abcam (ab32503)	Rabbit	1000
Bcl2	Abcam (ab238042)	Rabbit	1000
Caspase9	Abcam (ab32068)	Rabbit	2000
Cleaved-caspase9	CST (7237)	Rabbit	1000

Caspase3	Abcam (ab32351)	Rabbit	5000
Cleaved-caspase3	Abcam (ab32042)	Rabbit	1000
Cleaved-PARP	CST (9541)	Rabbit	1000
KRAS	Abcam (ab275876)	Rabbit	1000
c-MYC	CST (5605)	Rabbit	1000
cGAS	CST (15102)	Rabbit	1000
STING	CST (13647)	Rabbit	1000
Phospho-STING	CST (50907)	Rabbit	1000
TBK1	CST (3504)	Rabbit	1000
Phospho-TBK1	CST (5483)	Rabbit	1000
IRF3	CST (11904)	Rabbit	1000
Phospho-IRF3	CST (29047)	Rabbit	1000
GPX4	CST (59735)	Rabbit	1000
β-actin	Abcam (ab8226)	Mouse	5000
GAPDH	CST (5174)	Rabbit	1000
α-Tubulin	CST (3873)	Mouse	1000
Hsp90	CST (4877)	Rabbit	1000
Ki67	Abcam (ab16667)	Rabbit	500
TRF2	ThermoFisher (PA5-116476)	Rabbit	200
γ -H2A.x	ThermoFisher (MA1-2022)	Mouse	400
Anti-Rabbit IgG, HRP-linked antibody	CST (7074)	Rabbit	5000
Anti-Mouse IgG, HRP-linked antibody	CST (7076)	Mouse	5000
Goat anti-Rabbit IgG Alexa Fluor 568	ThermoFisher (A-11011)	Goat	500
Goat anti-Mouse IgG Alexa Fluor 647	ThermoFisher (A-21235)	Goat	500
Goat anti-Rabbit IgG Alexa Fluor 647	ThermoFisher (A-21244)	Goat	500

2. List of Supplementary Figures

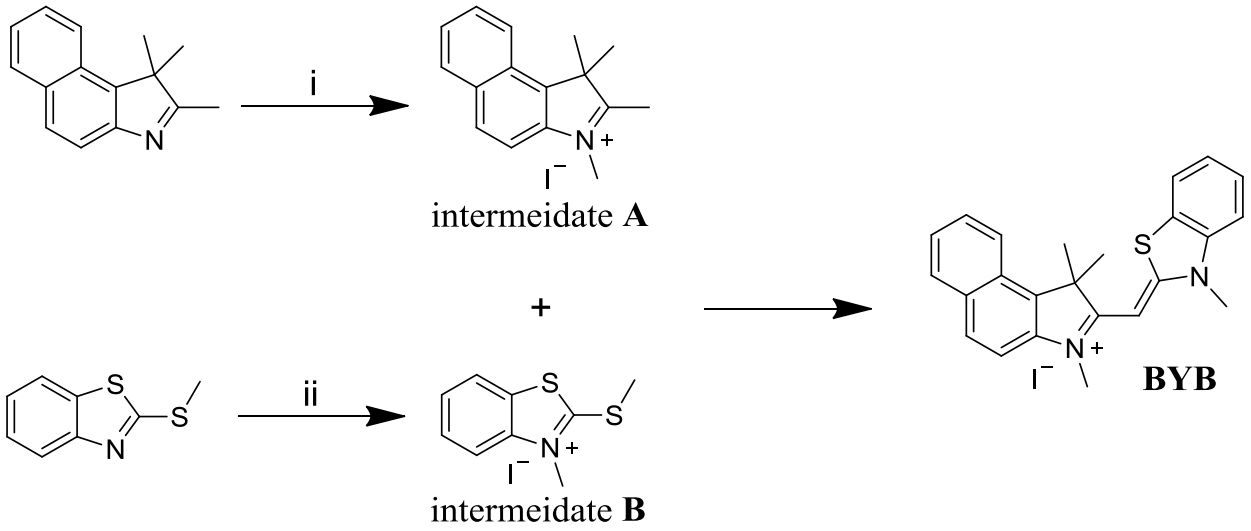

Figure S1. The synthetic route to ligand **BYB**.[3] Reagents and conditions: (i) iodomethane, acetonitrile, 80 °C, overnight; (ii) iodomethane, acetonitrile, 80 °C, overnight; (iii) acetonitrile, triethylamine, 75 °C, 12 h.

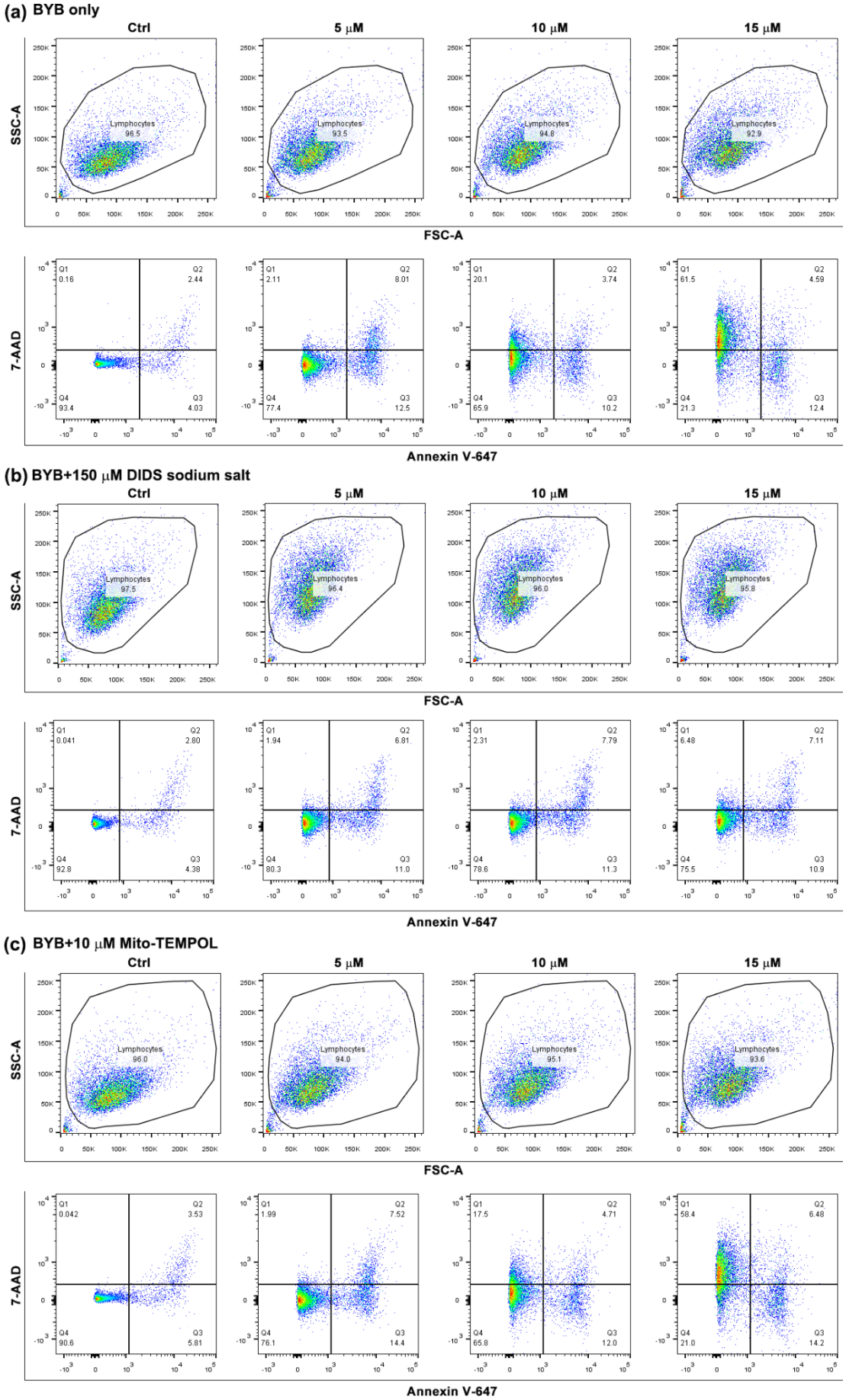

Figure S2. Cell apoptosis analysis of HeLa cells treated with **BYB** (0-15 μM) with or without 150 μM DIDS sodium salt or 10 μM Mito-TEMPOL for 24 h. The cells were stained by Annexin V-647 and 7-AAD.

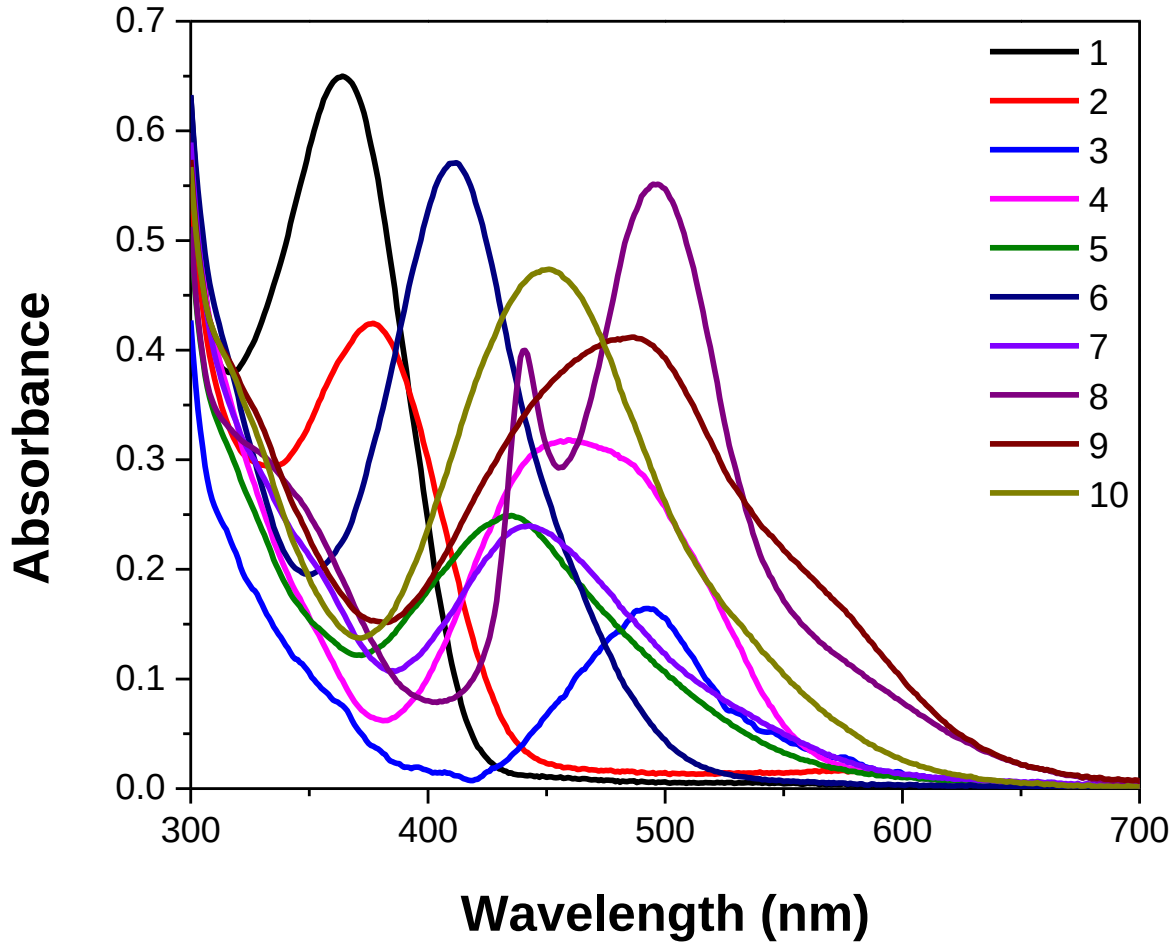

Figure S3. Absorption spectra of 50 μM of ligands **1**–**10** in Tris-HCl buffer (10 mM, pH 7.4), containing 100 mM KCl.

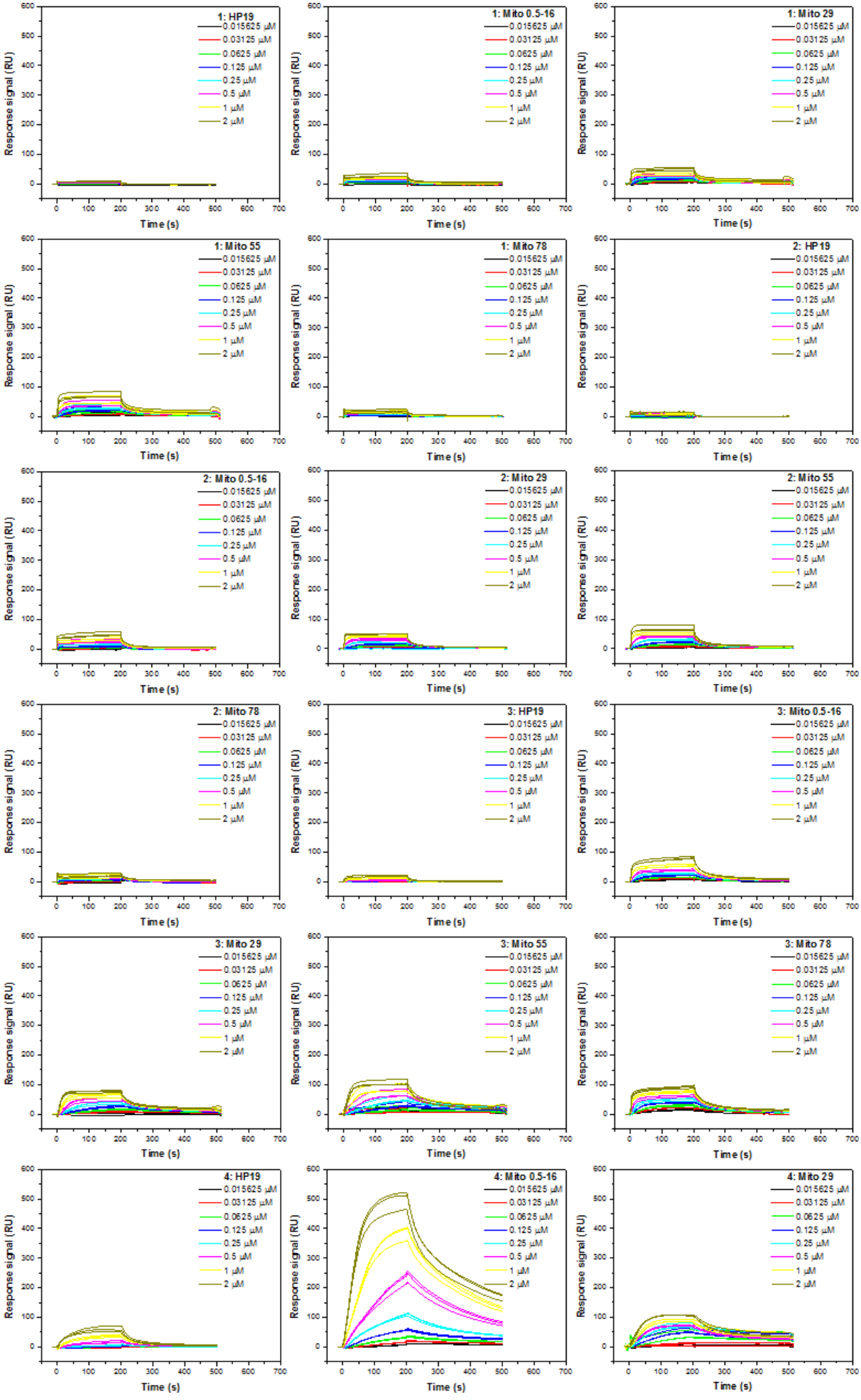
1: HP19
1: Mito 0.5-16
1: Mito 29
1: Mito 55
1: Mito 78
2: HP19
2: Mito 0.5-16
2: Mito 29
2: Mito 55
2: Mito 78
3: HP19
3: Mito 0.5-16
3: Mito 29
3: Mito 55
3: Mito 78
4: HP19
4: Mito 0.5-16
4: Mito 29
0.015625 µM
0.03125 µM
0.0625 µM
0.125 µM
0.25 µM
0.5 µM
1 µM
2 µM
Response signal (RU)
Time (s)

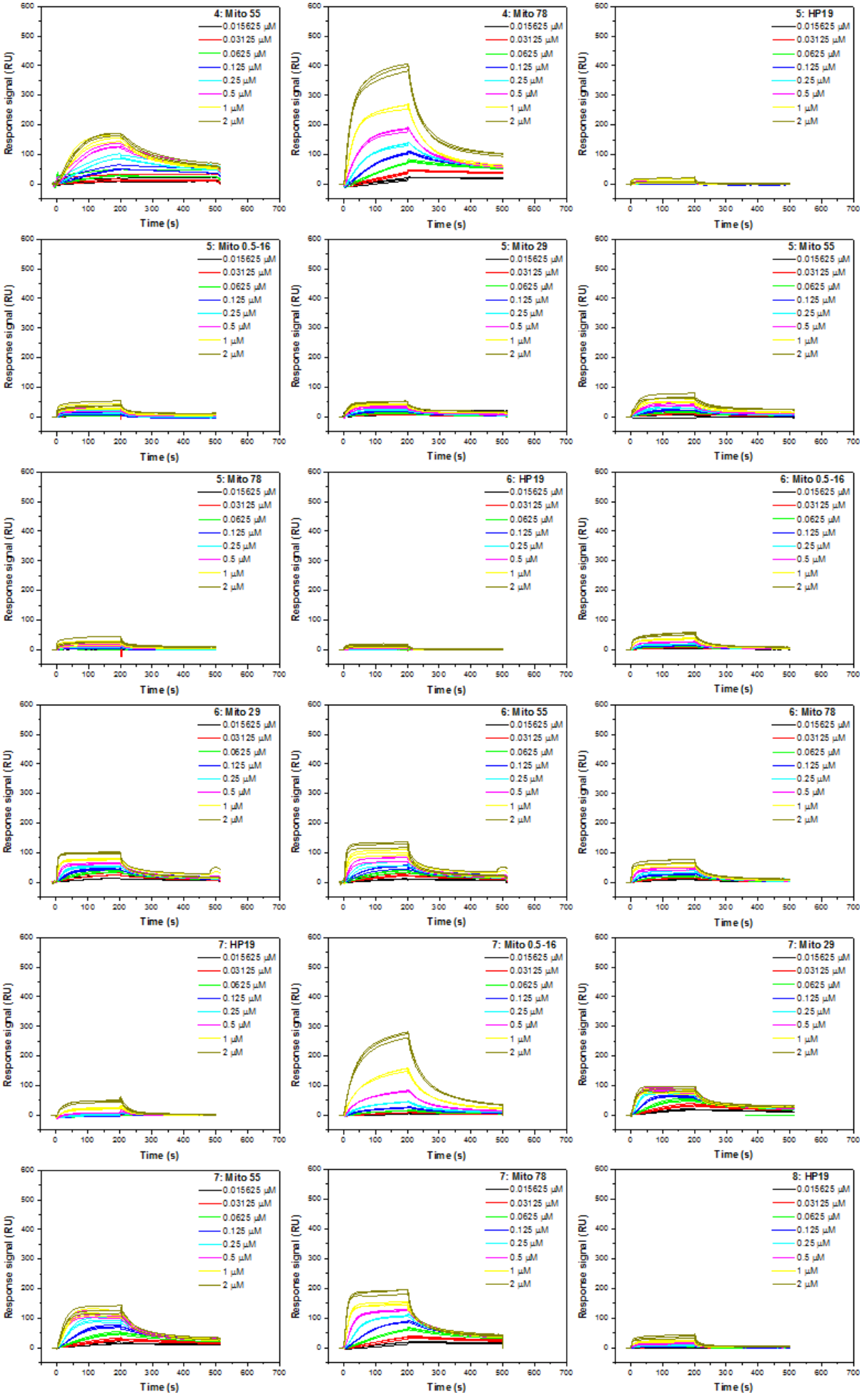
4: Mito 55
4: Mito 78
5: HP19
5: Mito 0.5-16
5: Mito 29
5: Mito 55
5: Mito 78
6: HP19
6: Mito 0.5-16
6: Mito 29
6: Mito 55
6: Mito 78
7: HP19
7: Mito 0.5-16
7: Mito 29
7: Mito 55
7: Mito 78
8: HP19
0.015625 µM
0.03125 µM
0.0625 µM
0.125 µM
0.25 µM
0.5 µM
1 µM
2 µM
Response signal (RU)
Time (s)

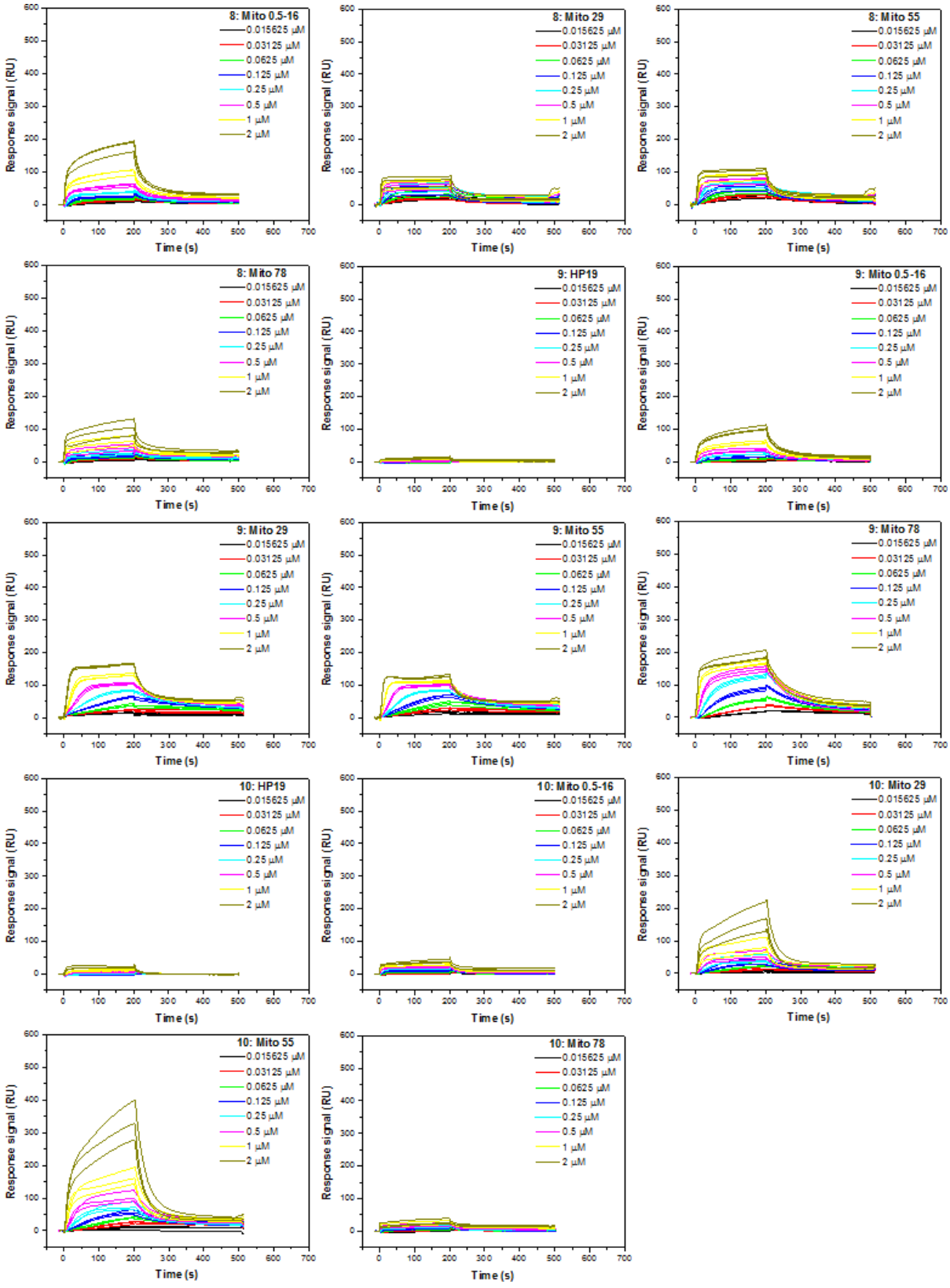

Figure S4. SPR sensorgrams for binding of ligands **1**–**10** to *HP19*, *Mito 0.5-16*, *Mito 29*, *Mito 55* and *Mito 78* in 10 mM Tris-HCl buffer, 100 mM KCl, pH 7.4.

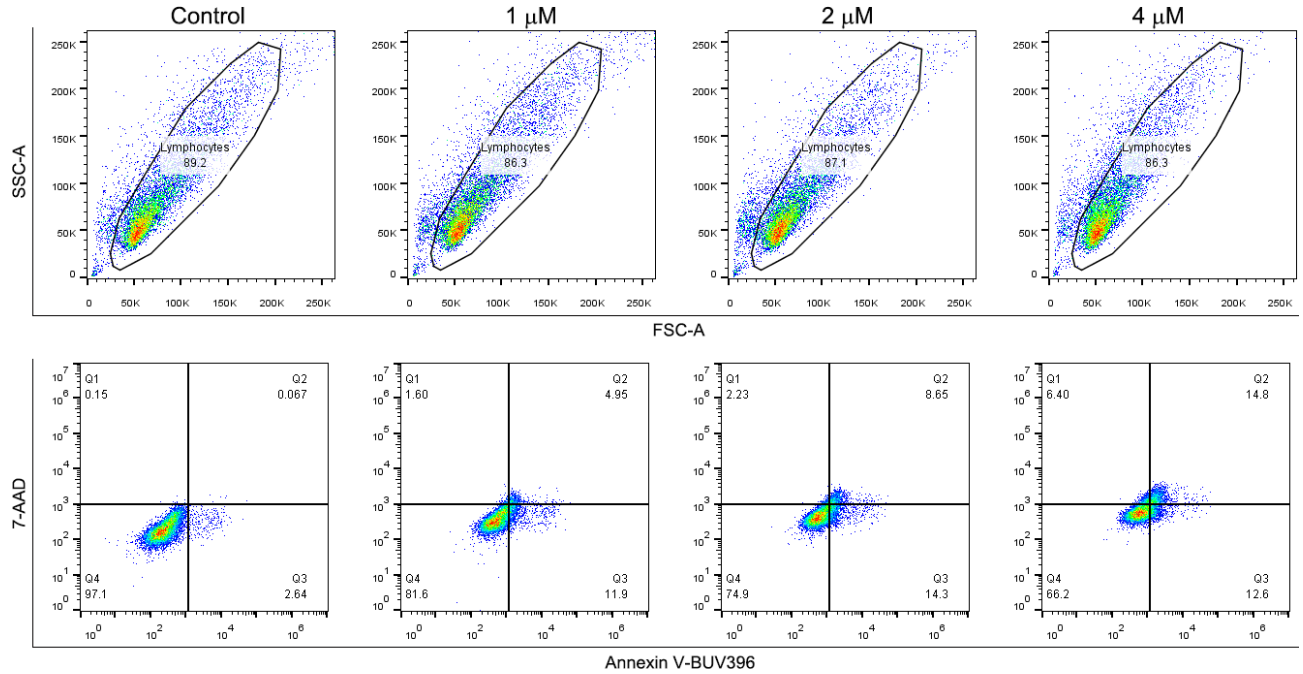

Figure S5. Cell apoptosis analysis of HCT116 cells treated with **9** (0-4 μM) for 72 h. The cells were stained by Annexin V-BUV396 and 7-AAD.

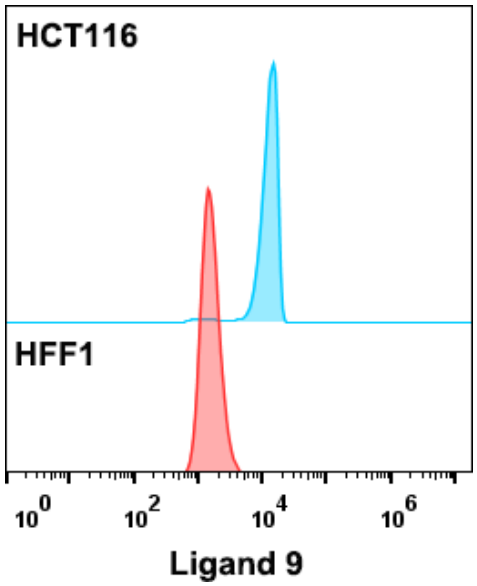

Figure S6. HCT116 and HFF1 cells treated with ligand **9** were analyzed by flow. The concentration of ligand **9** was 4 μM, and the incubation time was 1 hour.

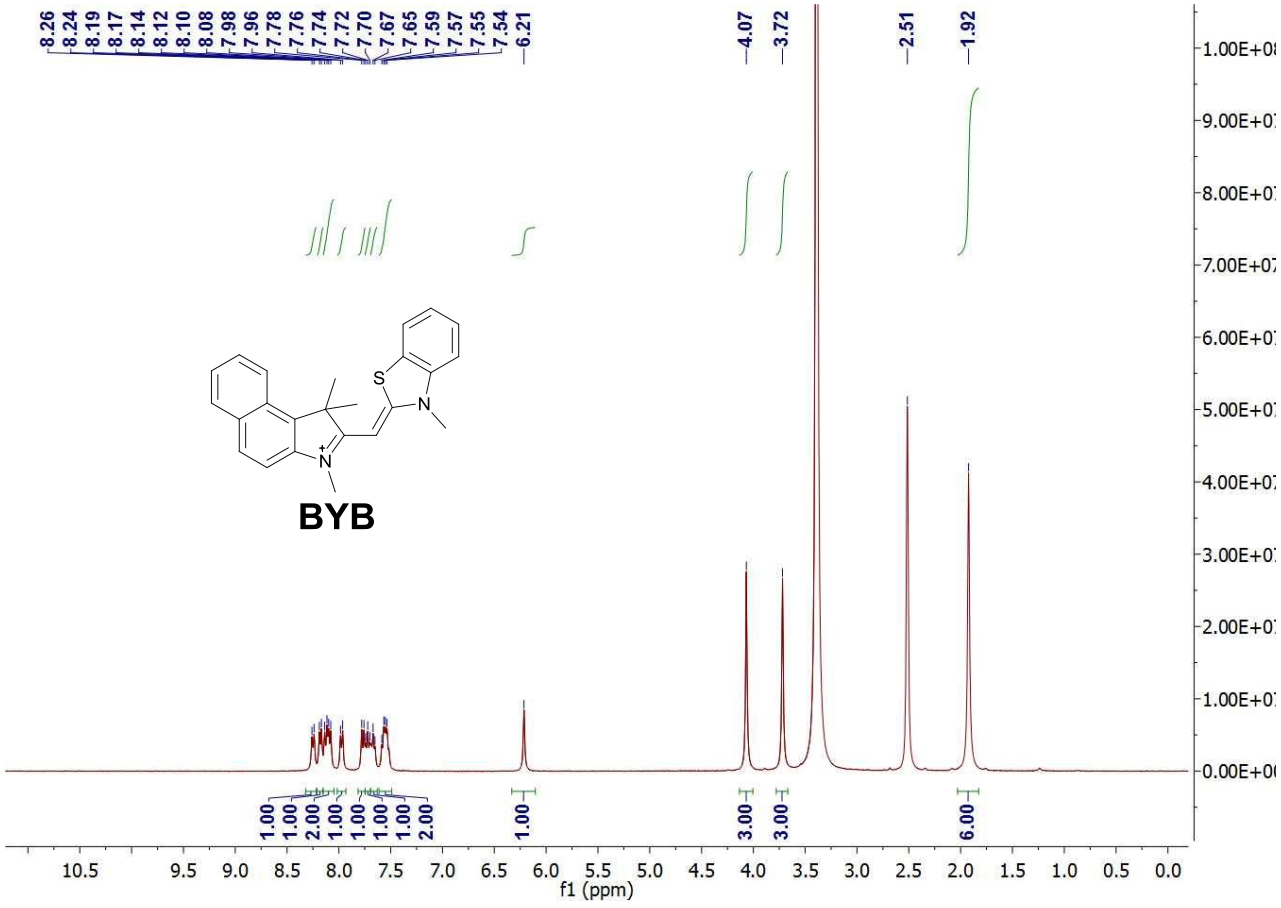
8.26
8.24
8.19
8.17
8.14
8.12
8.10
8.08
7.98
7.96
7.78
7.76
7.74
7.72
7.70
7.67
7.65
7.59
7.57
7.55
7.54
6.21
4.07
3.72
2.51
1.92
S
N
N
+
BYB
1.00
1.00
2.00
1.00
1.00
1.00
1.00
2.00
1.00
3.00
3.00
6.00
f1 (ppm)

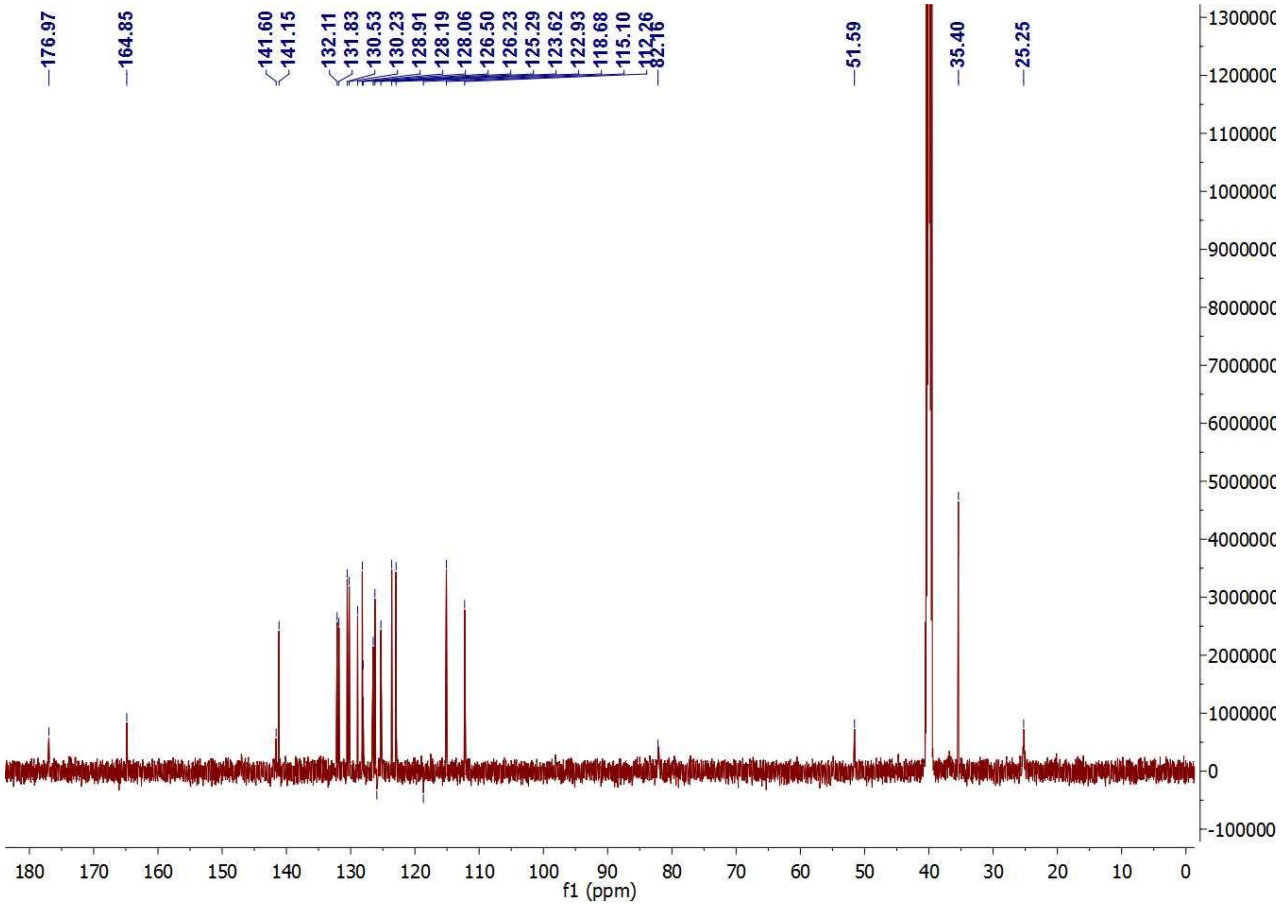
176.97
164.85
141.60
141.15
132.11
131.83
130.53
130.23
128.91
128.19
128.06
126.50
126.23
125.29
123.62
122.93
118.68
115.10
112.26
82.16
51.59
35.40
25.25
f1 (ppm)

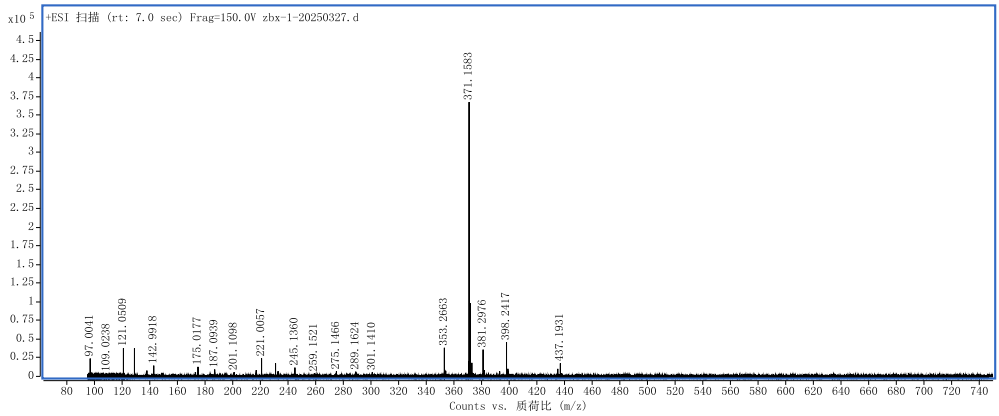

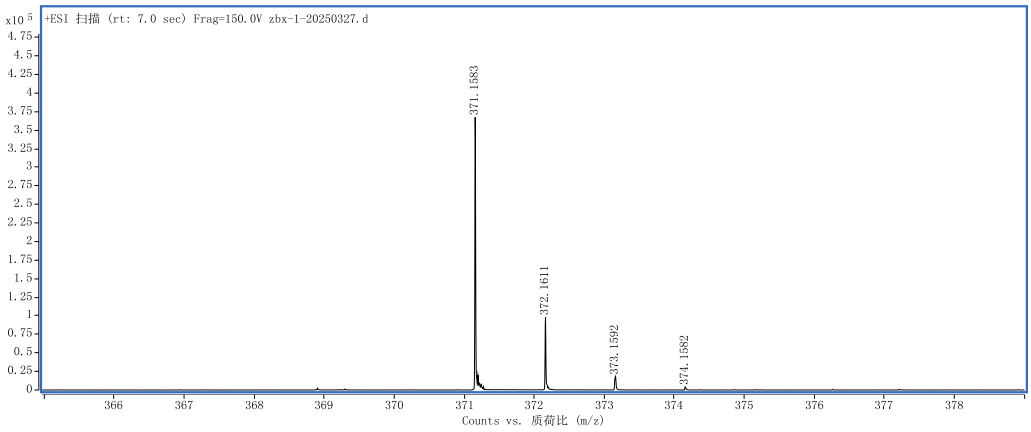

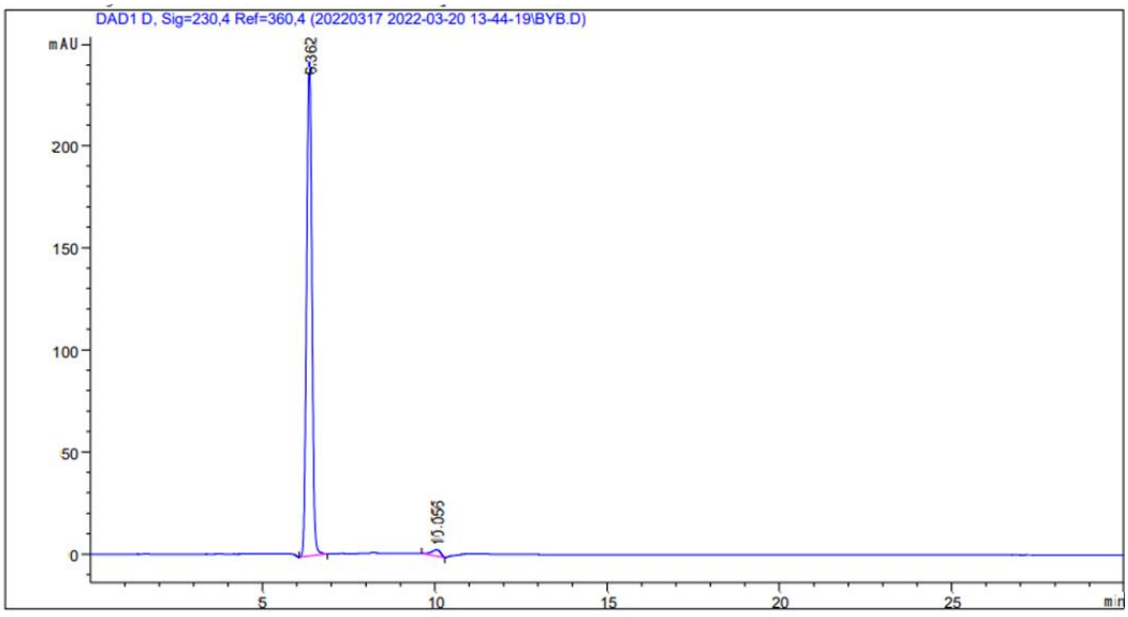

Peak #	RetTime [min]	Type	Width [min]	Area [mAU*s]	Height [mAU]	Area %
1	6.362	BB	0.1679	2577.71802	242.74210	97.8819
2	10.056	BB	0.2920	55.77921	3.04057	2.1181
Totals :				2633.49723	245.78266	

Figure S7. ^{1}H NMR (DMSO-d_6), ^{13}C NMR (DMSO-d_6), HRMS and HPLC of compound **BYB**.

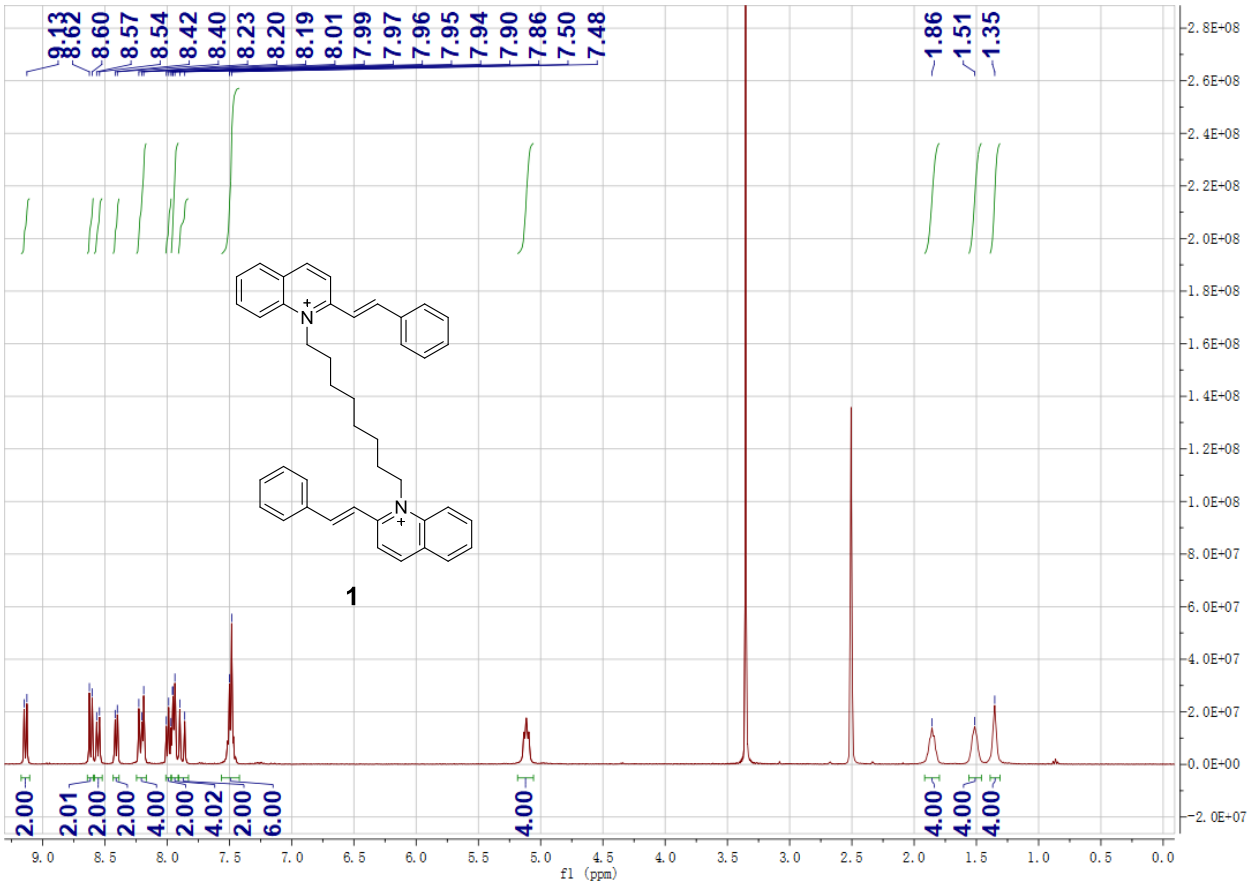
9.13
8.62
8.60
8.57
8.54
8.42
8.40
8.23
8.20
8.19
8.01
7.99
7.97
7.96
7.95
7.94
7.90
7.86
7.50
7.48
1.86
1.51
1.35
2.00
2.01
2.00
2.00
4.00
2.00
4.02
2.00
6.00
4.00
4.00
4.00
4.00
f1 (ppm)

1

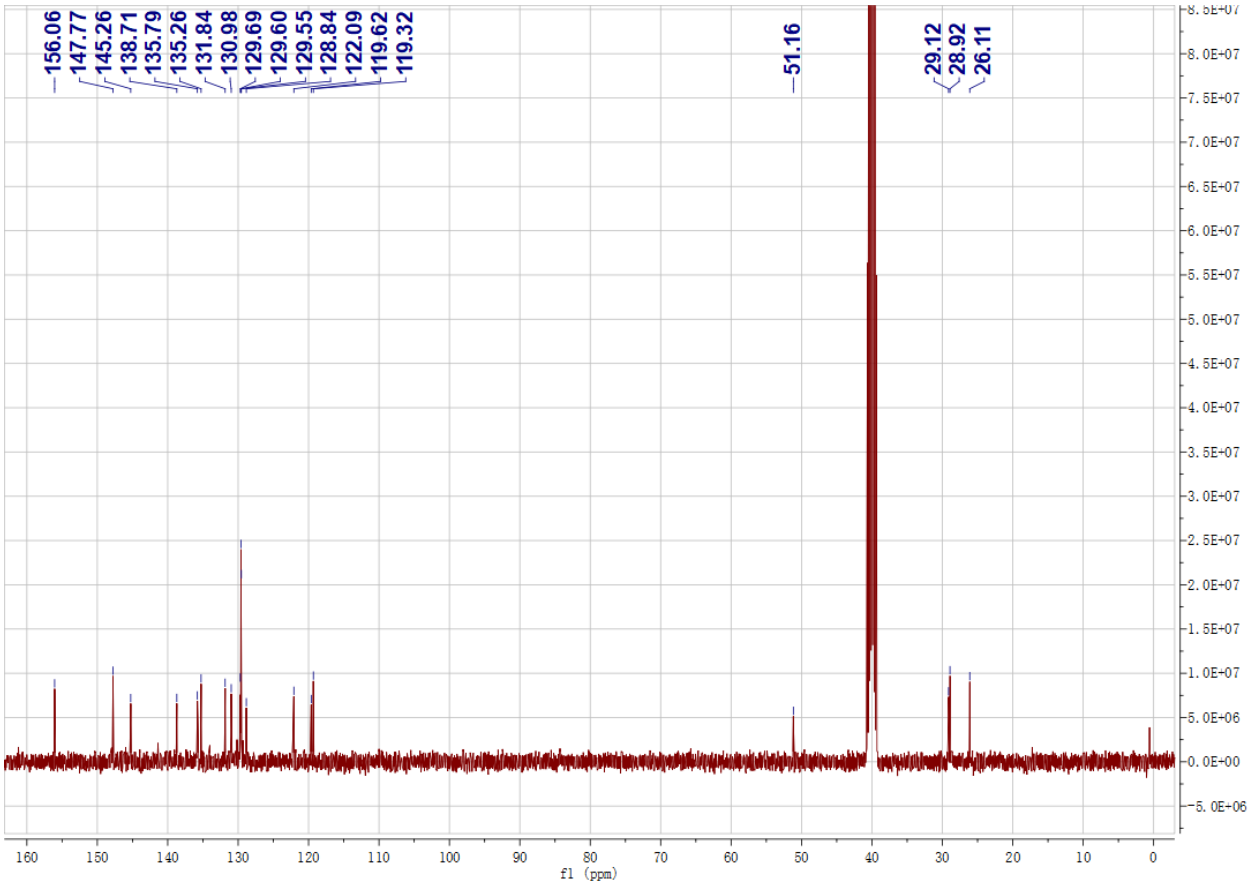
156.06
147.77
145.26
138.71
135.79
135.26
131.84
130.98
129.69
129.60
129.55
128.84
122.09
119.62
119.32
51.16
29.12
28.92
26.11
f1 (ppm)

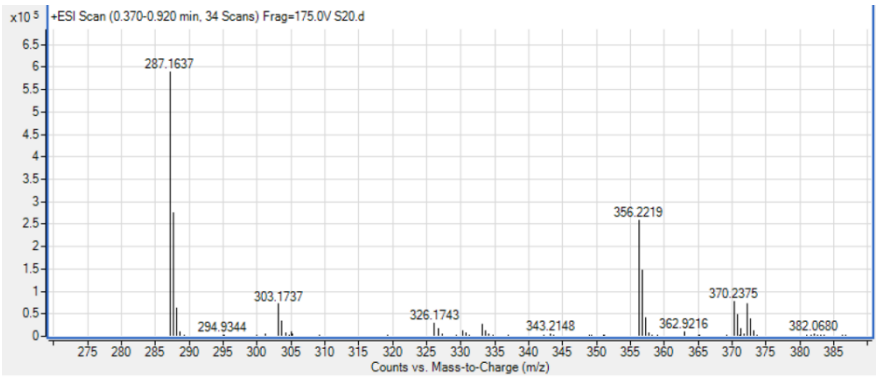

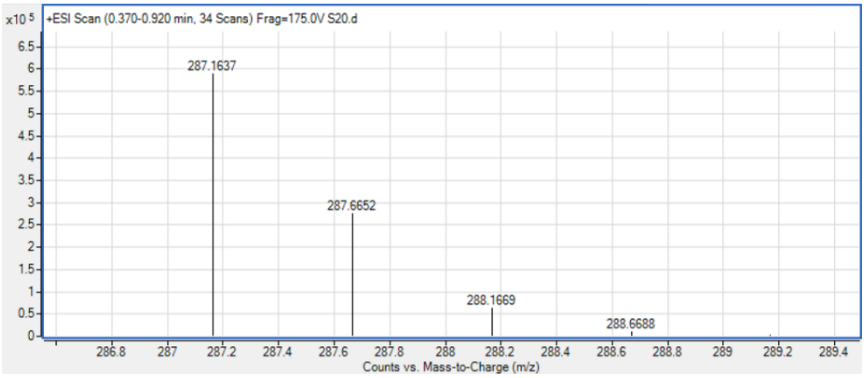

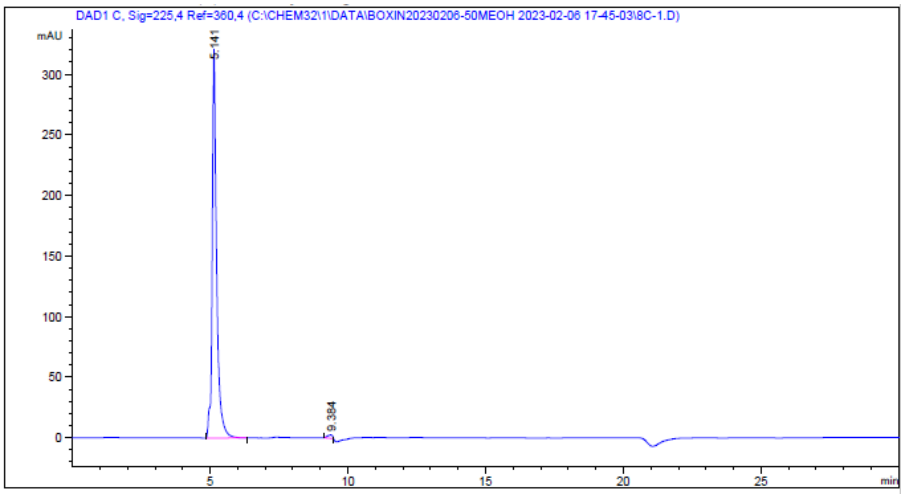


```
=====================================================================
                    Area Percent Report
=====================================================================

Sorted By             :      Signal
Multiplier            :      1.0000
Dilution              :      1.0000
Do not use Multiplier & Dilution Factor with ISTDs


Signal 1: DAD1 C, Sig=225,4 Ref=360,4

Peak RetTime Type  Width     Area      Height     Area
  #   [min]       [min]   [mAU*s]     [mAU]       %
----|-------|----|-------|----------|----------|--------|
   1   5.141 BB    0.1613 3622.51709  321.82642  99.0963
   2   9.384 MM R  0.2034   33.03581    2.70647   0.9037

Totals :                  3655.55290  324.53289
```

Figure S8. ^{1}H NMR (DMSO-d_6), ^{13}C NMR (DMSO-d_6), HRMS and HPLC analysis of ligand **1**.

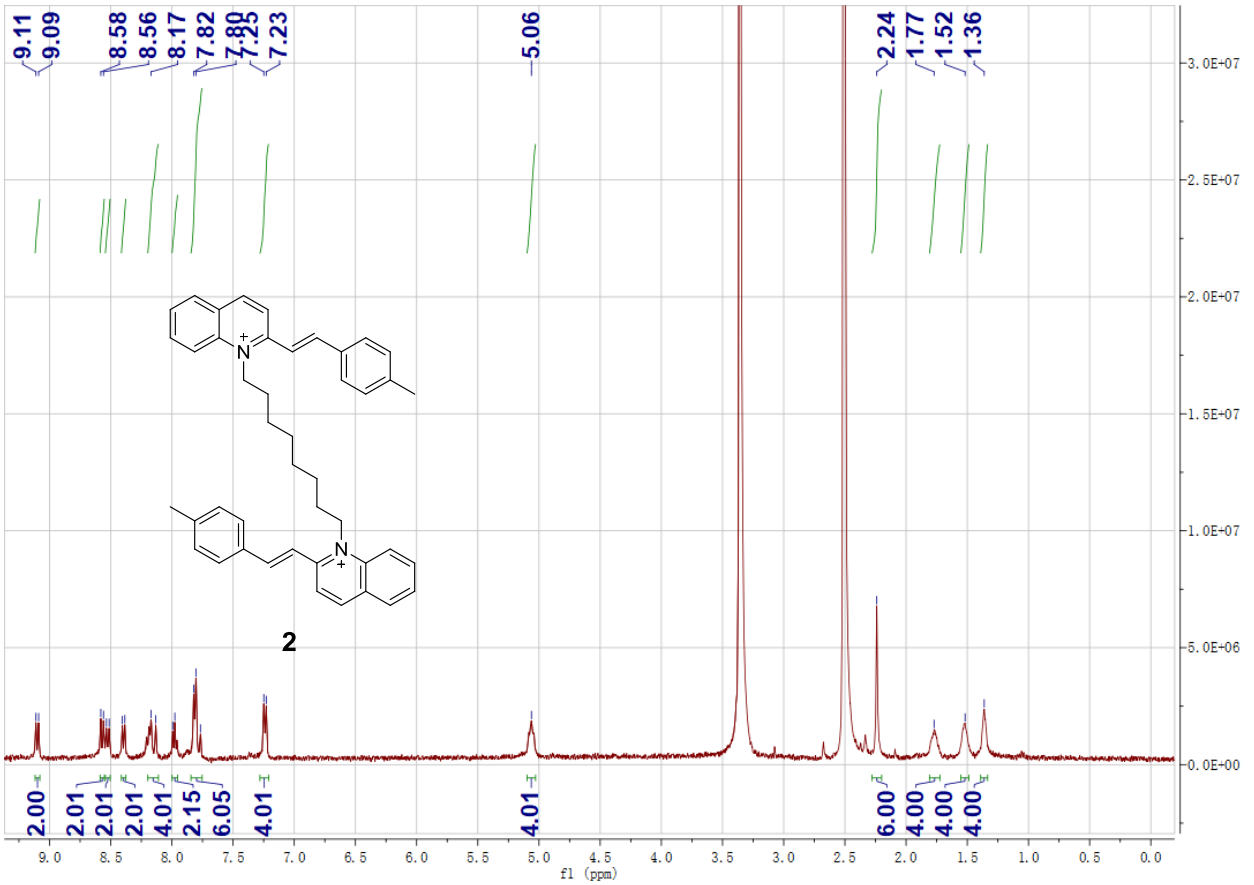
9.11
9.09
8.58
8.56
8.17
7.82
7.80
7.25
7.23
5.06
2.24
1.77
1.52
1.36
2
2.00
2.01
2.01
2.01
4.01
2.15
6.05
4.01
4.01
6.00
4.00
4.00
4.00
f1 (ppm)

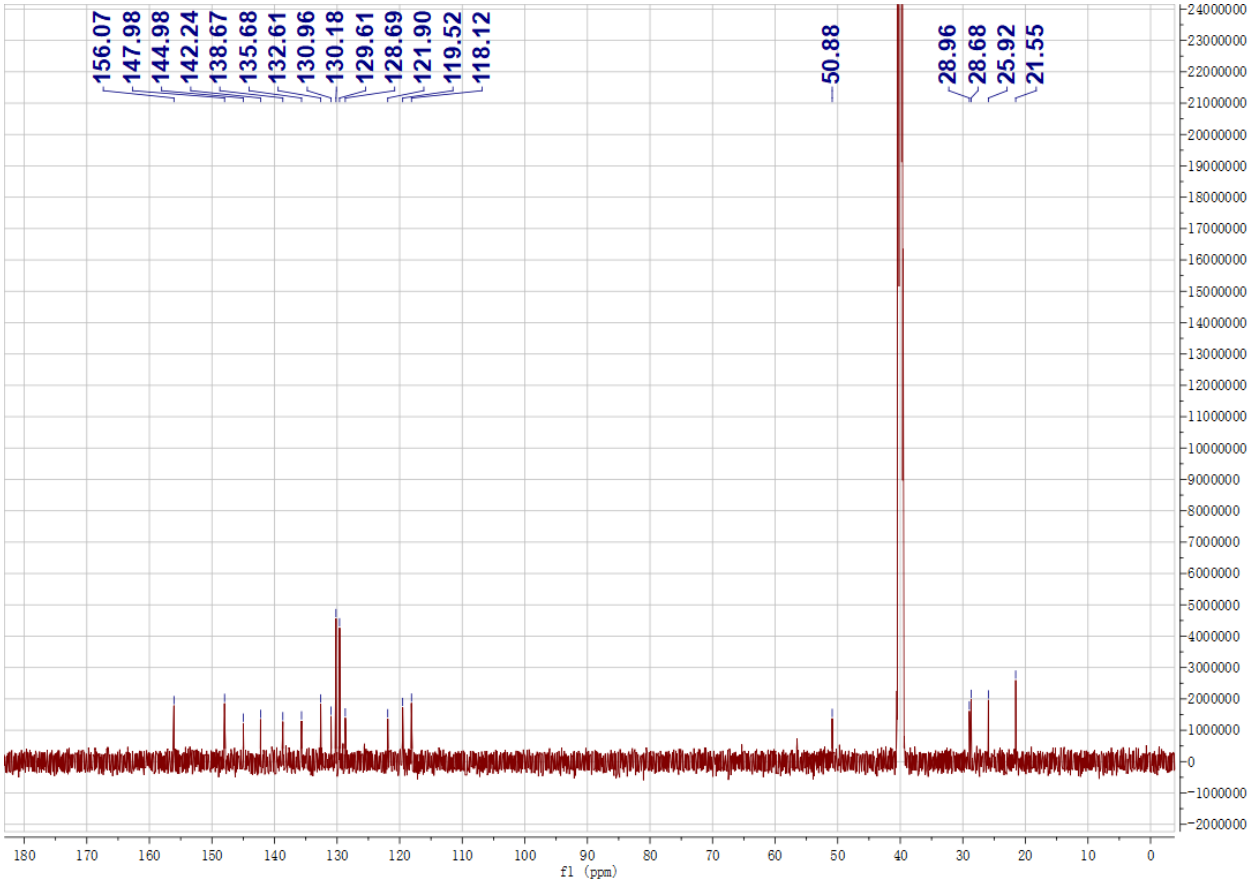
156.07
147.98
144.98
142.24
138.67
135.68
132.61
130.96
130.18
129.61
128.69
121.90
119.52
118.12
50.88
28.96
28.68
25.92
21.55
f1 (ppm)

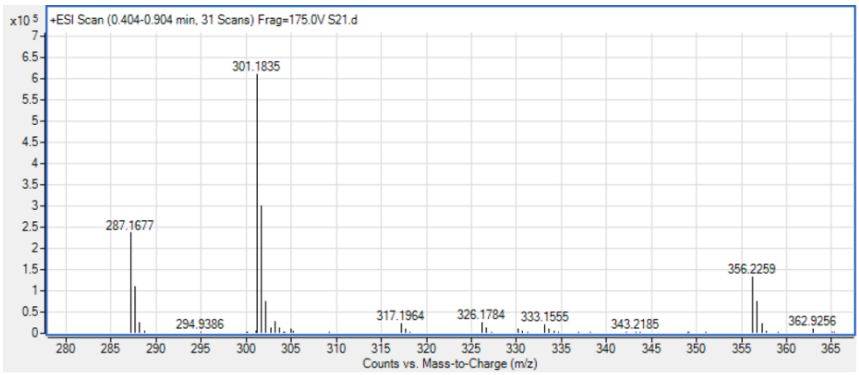

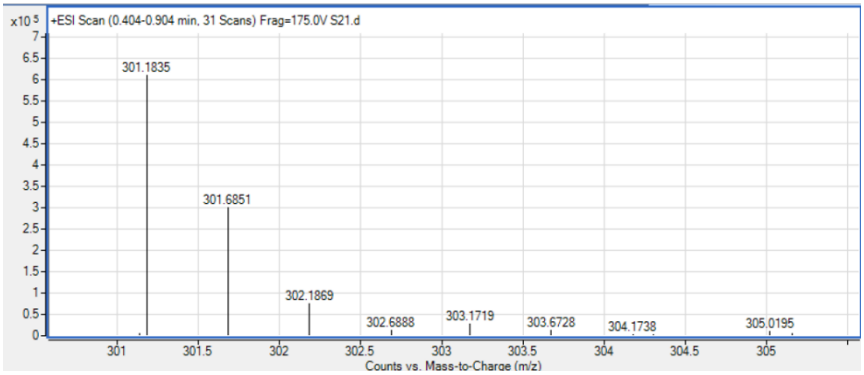

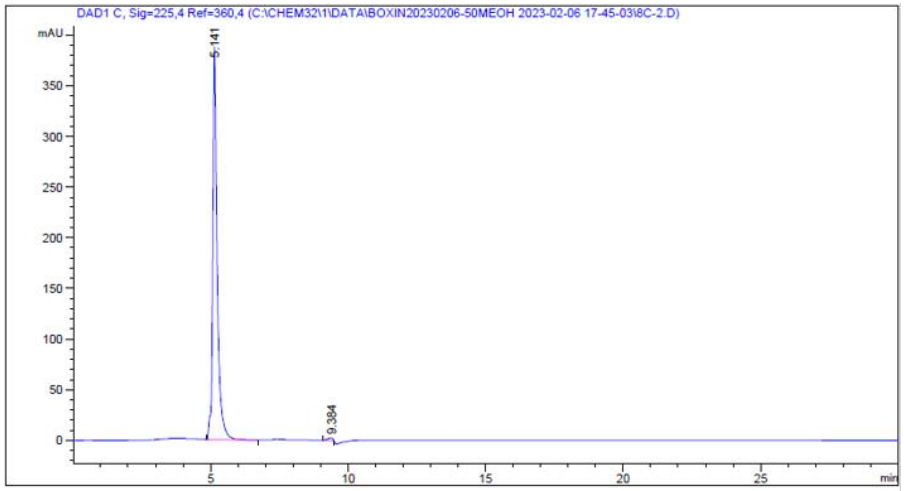


```
=====================================================================
                    Area Percent Report
=====================================================================

Sorted By             :      Signal
Multiplier            :      1.0000
Dilution              :      1.0000
Do not use Multiplier & Dilution Factor with ISTDs


Signal 1: DAD1 C, Sig=225,4 Ref=360,4

Peak RetTime Type  Width     Area      Height     Area
  #   [min]       [min]   [mAU*s]     [mAU]       %
----|-------|----|-------|----------|----------|--------|
   1   5.141 BB    0.1603 4335.92188  388.35629  99.0763
   2   9.384 MM R  0.2335   40.42500    2.88498   0.9237

Totals :                  4376.34688  391.24127
```

Figure S9. ^{1}H NMR (DMSO-d_6), ^{13}C NMR (DMSO-d_6), HRMS and HPLC analysis of ligand **2**.

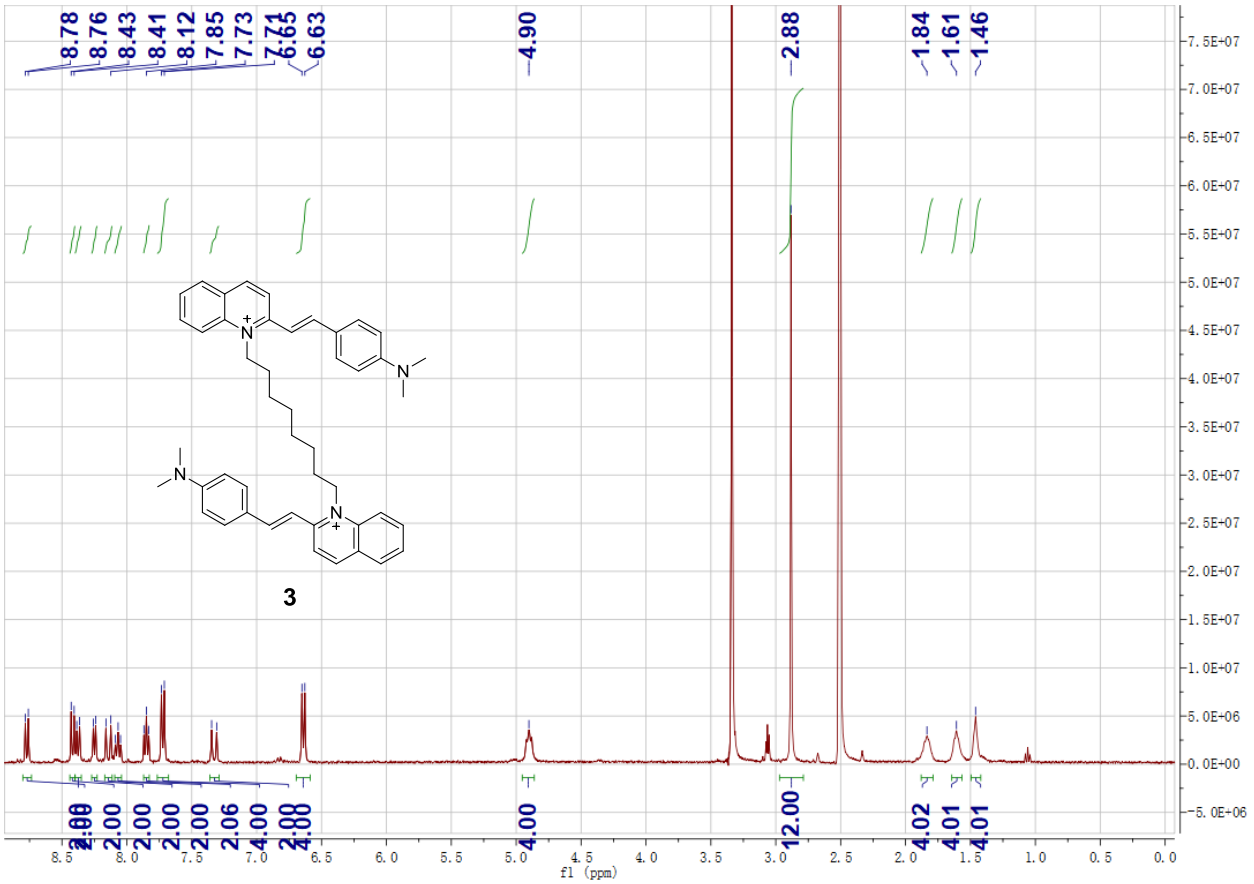
8.78
8.76
8.43
8.41
8.12
7.85
7.73
7.71
7.65
6.63
4.90
2.88
1.84
1.61
1.46
3
f1 (ppm)

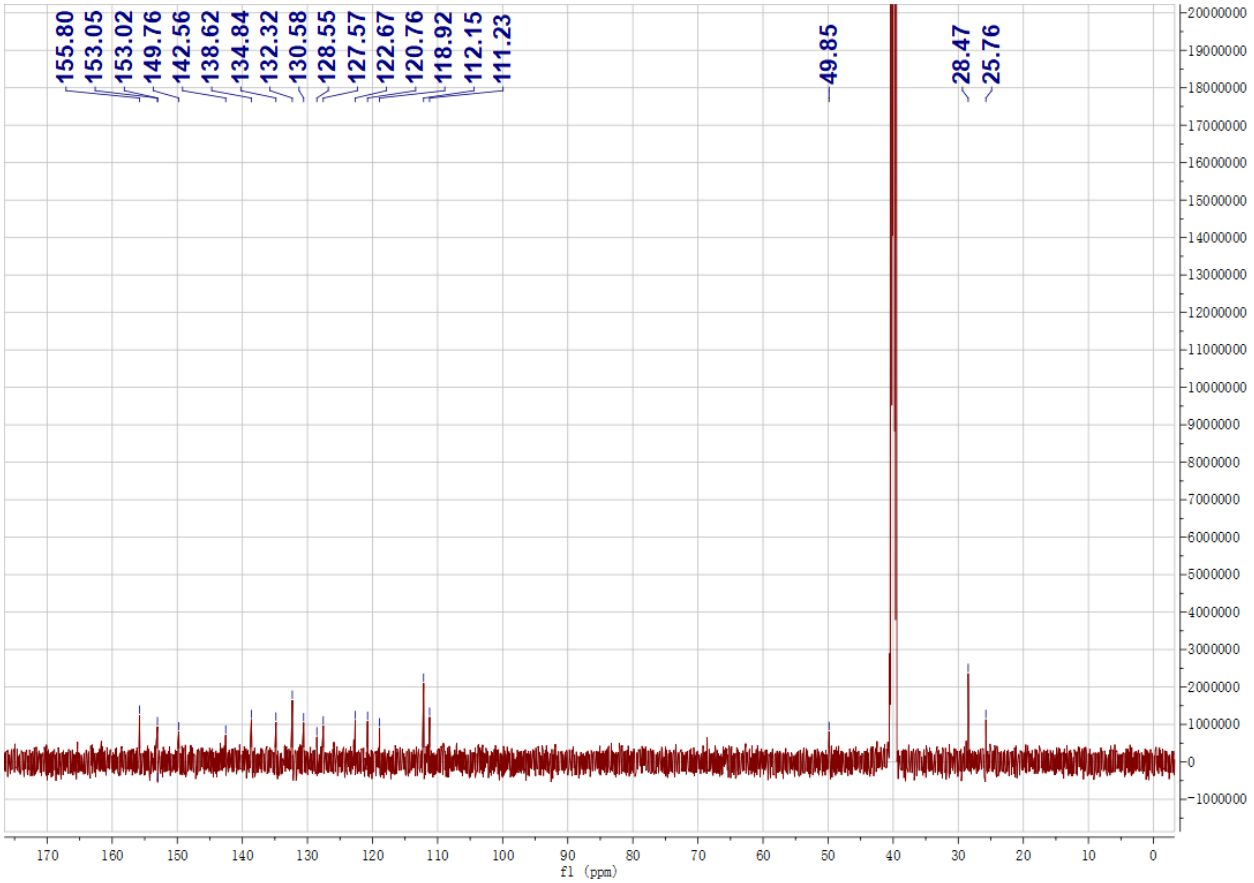
155.80
153.05
153.02
149.76
142.56
138.62
134.84
132.32
130.58
128.55
127.57
122.67
120.76
118.92
112.15
111.23
49.85
28.47
25.76
f1 (ppm)

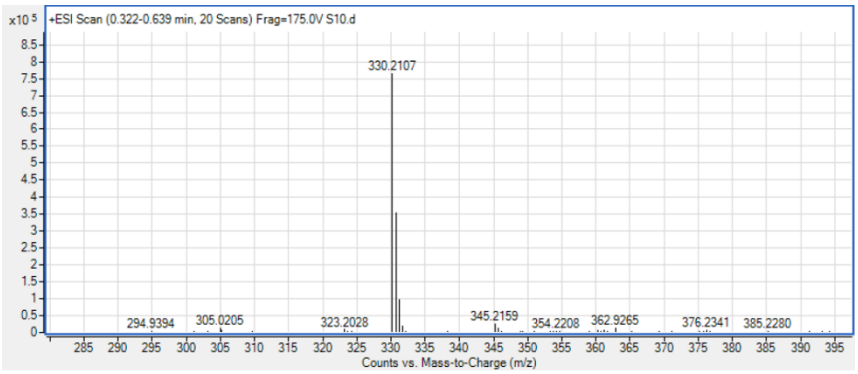

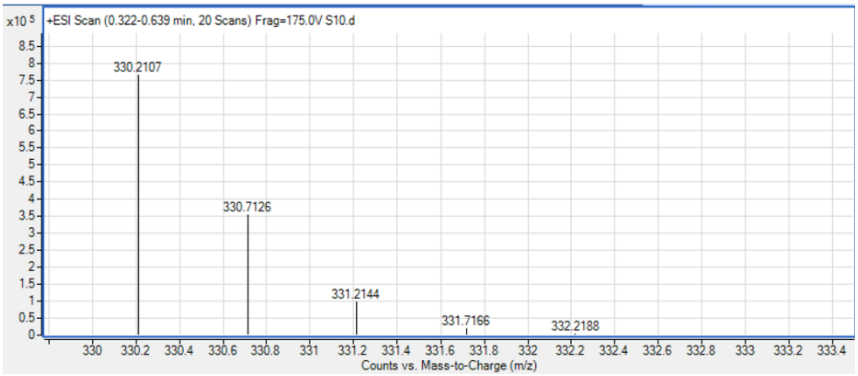

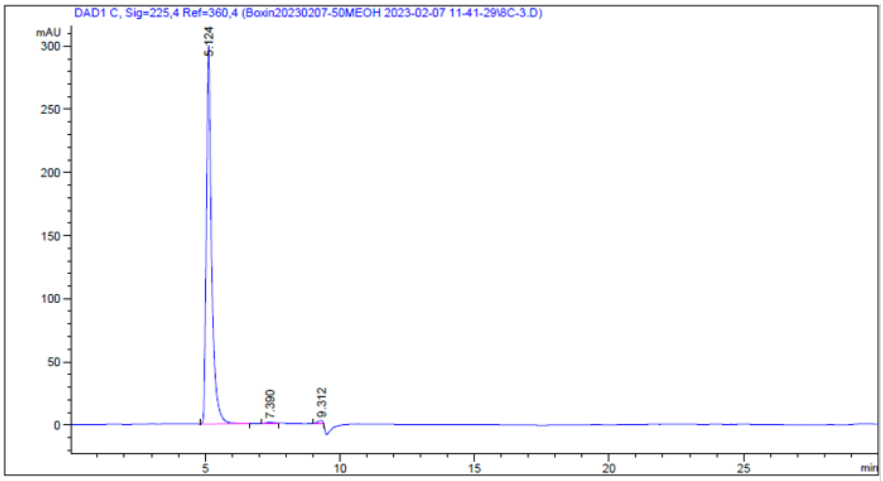


```
=====================================================================
                    Area Percent Report
=====================================================================

Sorted By             :      Signal
Multiplier            :      1.0000
Dilution              :      1.0000
Do not use Multiplier & Dilution Factor with ISTDs


Signal 1: DAD1 C, Sig=225,4 Ref=360,4

Peak RetTime Type  Width     Area      Height     Area
  #   [min]       [min]   [mAU*s]     [mAU]       %
----|-------|----|-------|----------|----------|--------|
   1   5.124 BB    0.1932 4089.43018  299.64417  98.4757
   2   7.390 MM R  0.4329   29.94305    1.15273   0.7210
   3   9.312 MM R  0.2112   33.35563    2.63207   0.8032

Totals :                  4152.72885  303.42897
```

Figure S10. ^{1}H NMR (DMSO-d_6), ^{13}C NMR (DMSO-d_6), HRMS and HPLC analysis of ligand **3**.

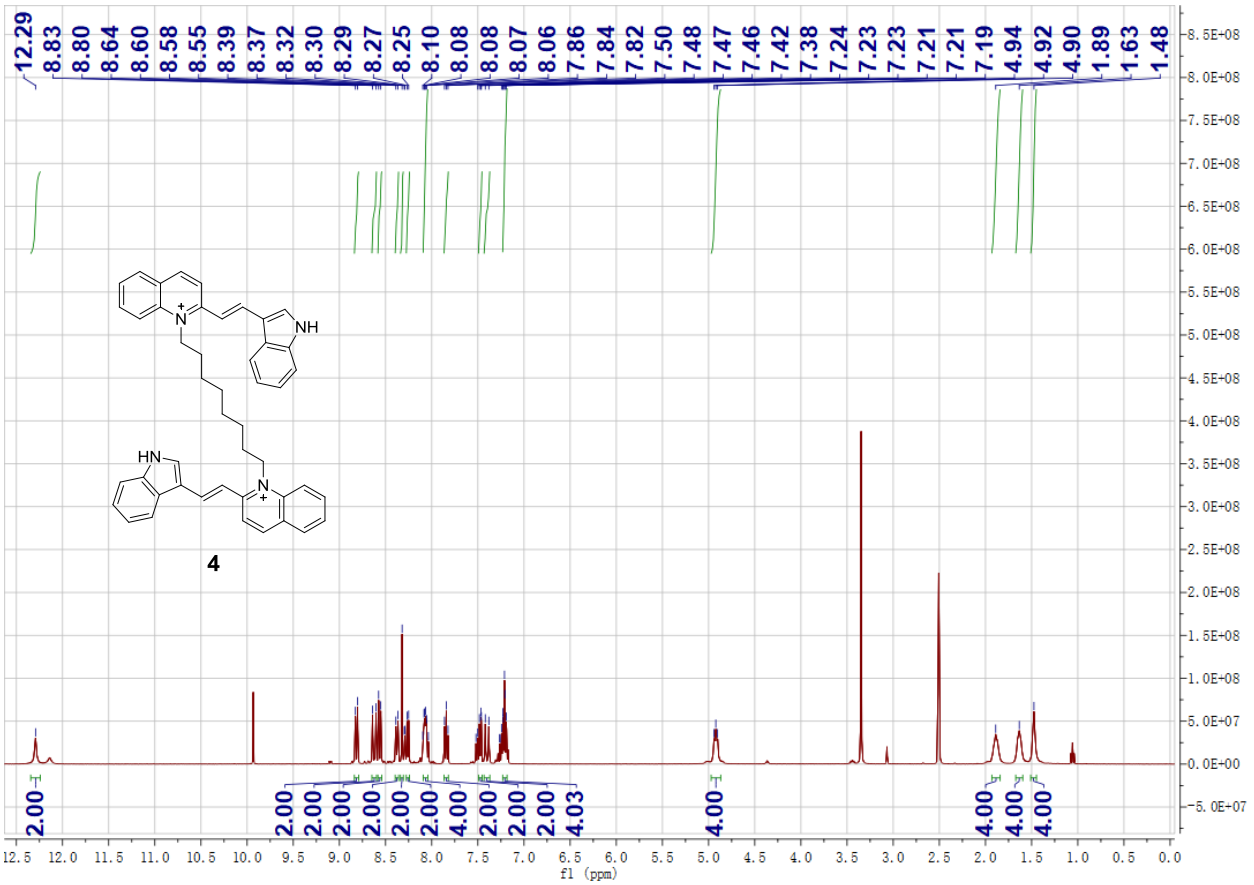
12.29
8.83
8.80
8.64
8.60
8.58
8.55
8.39
8.37
8.32
8.30
8.29
8.27
8.25
8.10
8.08
8.08
8.07
8.06
7.86
7.84
7.82
7.50
7.48
7.47
7.46
7.42
7.38
7.24
7.23
7.23
7.21
7.21
7.19
4.94
4.92
4.90
1.89
1.63
1.48
NH
HN
N
N
4
2.00
2.00
2.00
2.00
2.00
2.00
4.00
2.00
2.00
2.00
4.03
4.00
4.00
4.00
4.00
f1 (ppm)

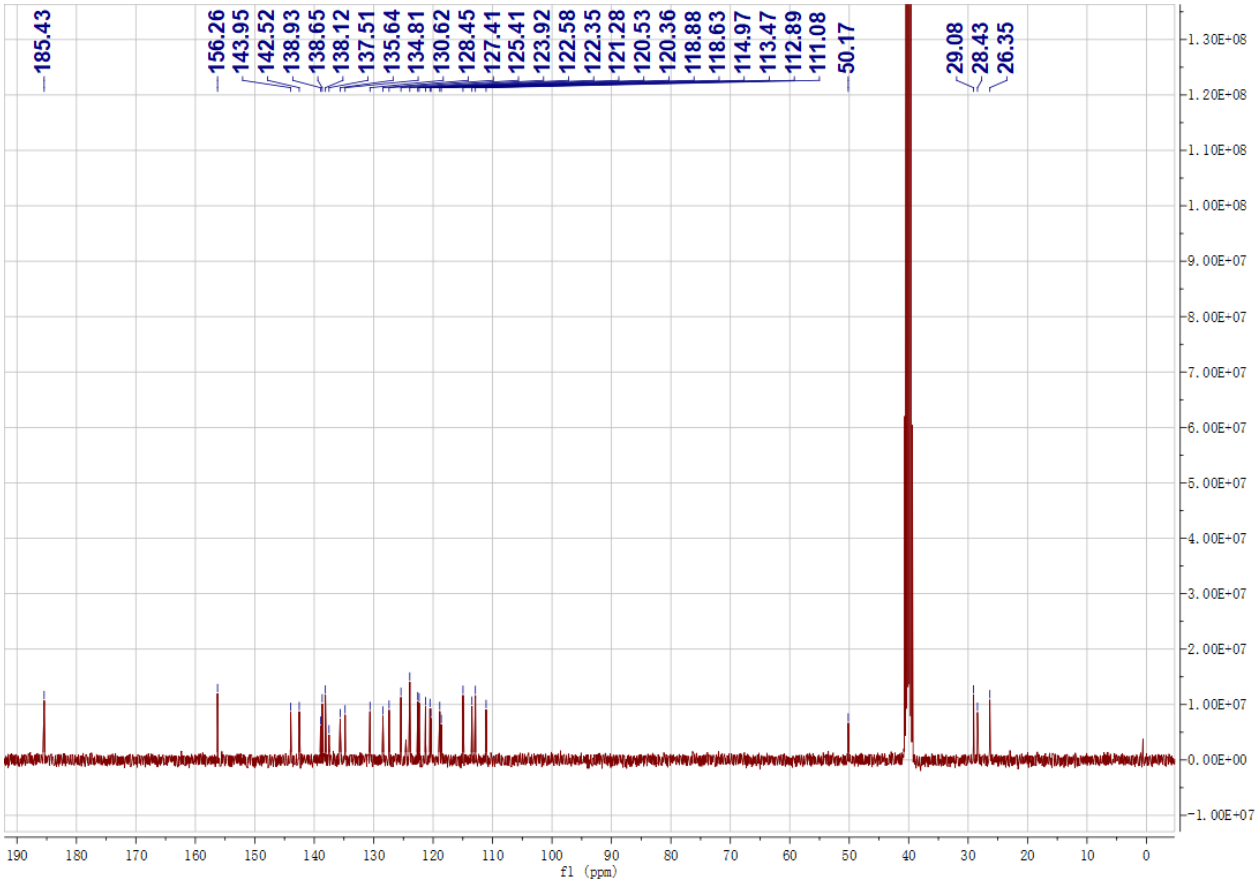
185.43
156.26
143.95
142.52
138.93
138.65
138.12
137.51
135.64
134.81
130.62
128.45
127.41
125.41
123.92
122.58
122.35
121.28
120.53
120.36
118.88
118.63
114.97
113.47
112.89
111.08
50.17
29.08
28.43
26.35
f1 (ppm)

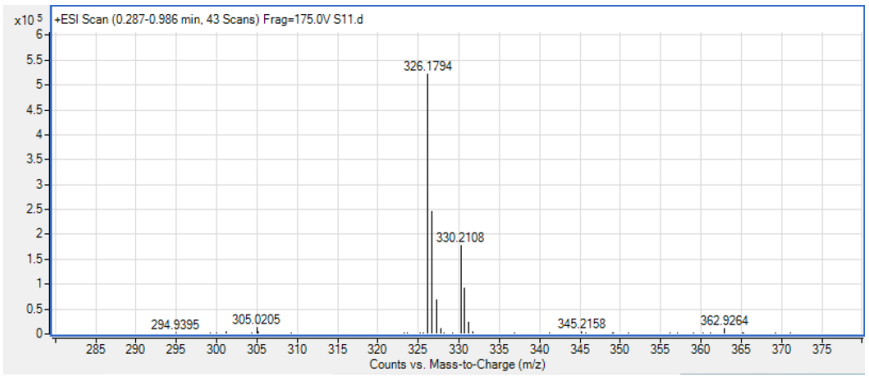

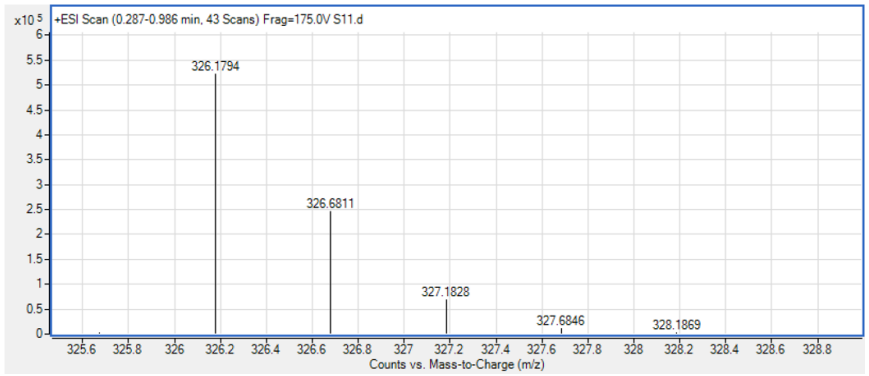

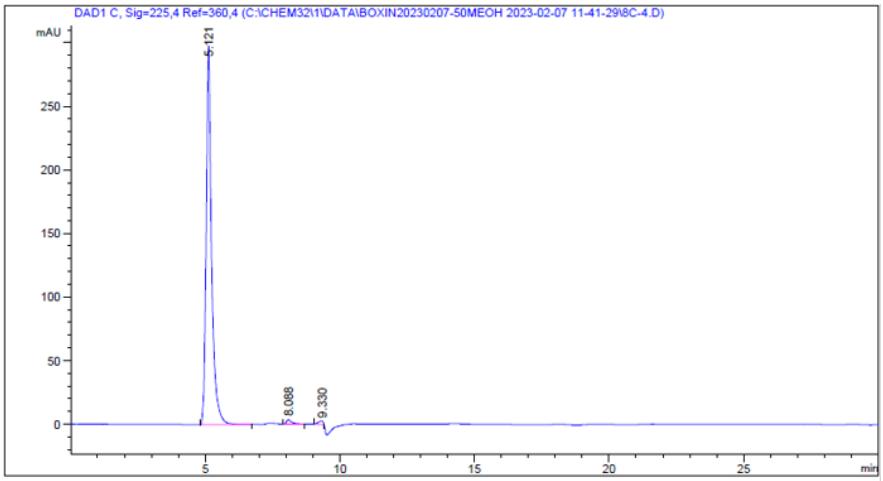


```
=====================================================================
                    Area Percent Report
=====================================================================

Sorted By             :      Signal
Multiplier            :      1.0000
Dilution              :      1.0000
Do not use Multiplier & Dilution Factor with ISTDs


Signal 1: DAD1 C, Sig=225,4 Ref=360,4

Peak RetTime Type  Width     Area      Height     Area
  #   [min]       [min]   [mAU*s]     [mAU]       %
----|-------|----|-------|----------|----------|--------|
   1   5.121 BB    0.1975 4180.91650  298.38602  98.0663
   2   8.088 BB    0.1977   46.41065    3.39021   1.0886
   3   9.330 MM R  0.2091   36.02980    2.87171   0.8451

Totals :                  4263.35696  304.64794
```

Figure S11. ^{1}H NMR (DMSO-d_6), ^{13}C NMR (DMSO-d_6), HRMS and HPLC analysis of ligand **4**.

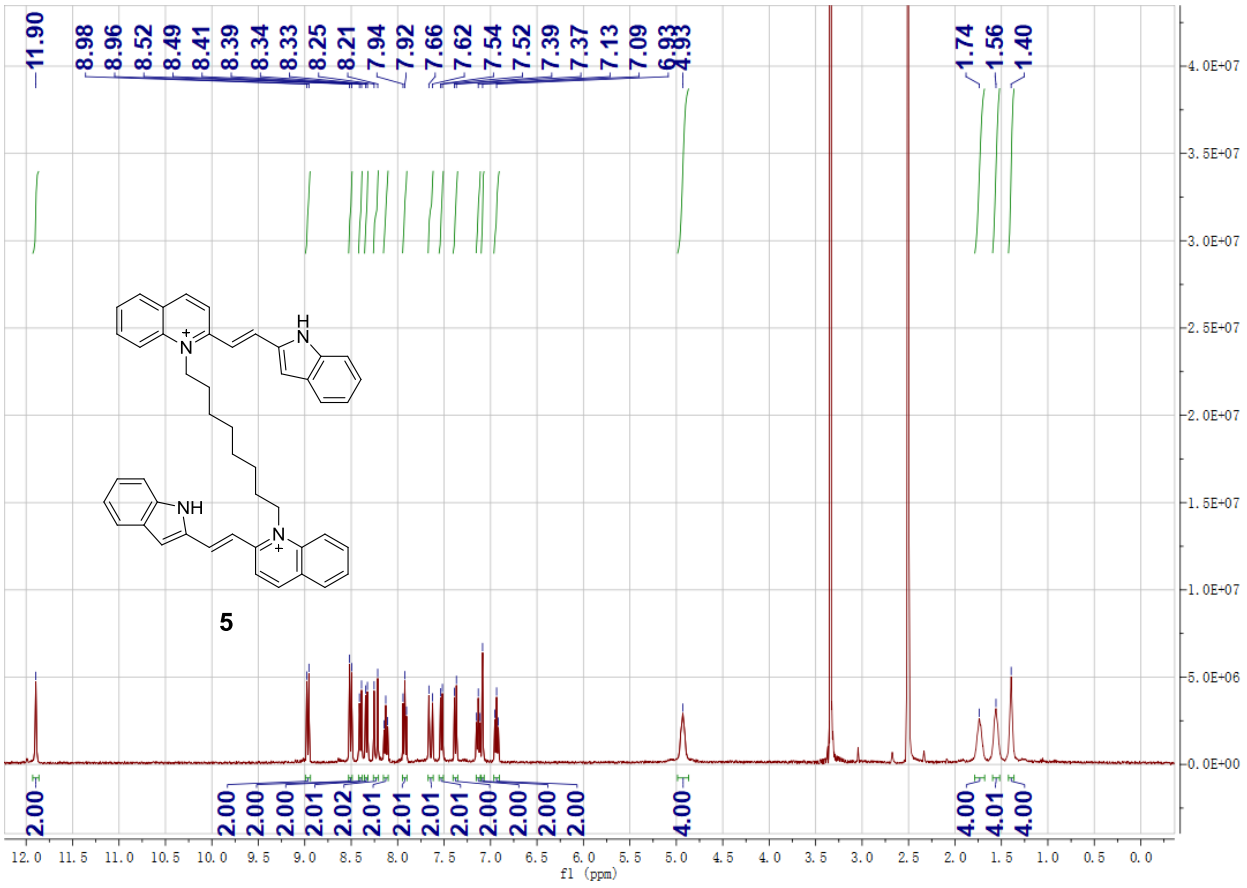
11.90
8.98
8.96
8.52
8.49
8.41
8.39
8.34
8.33
8.25
8.21
7.94
7.92
7.66
7.62
7.54
7.52
7.39
7.37
7.13
7.09
6.93
4.93
1.74
1.56
1.40
H
N
+
N
NH
N
+
5
2.00
2.00
2.00
2.00
2.02
2.01
2.01
2.01
2.01
2.00
2.00
2.00
2.00
4.00
4.00
4.01
4.00
f1 (ppm)

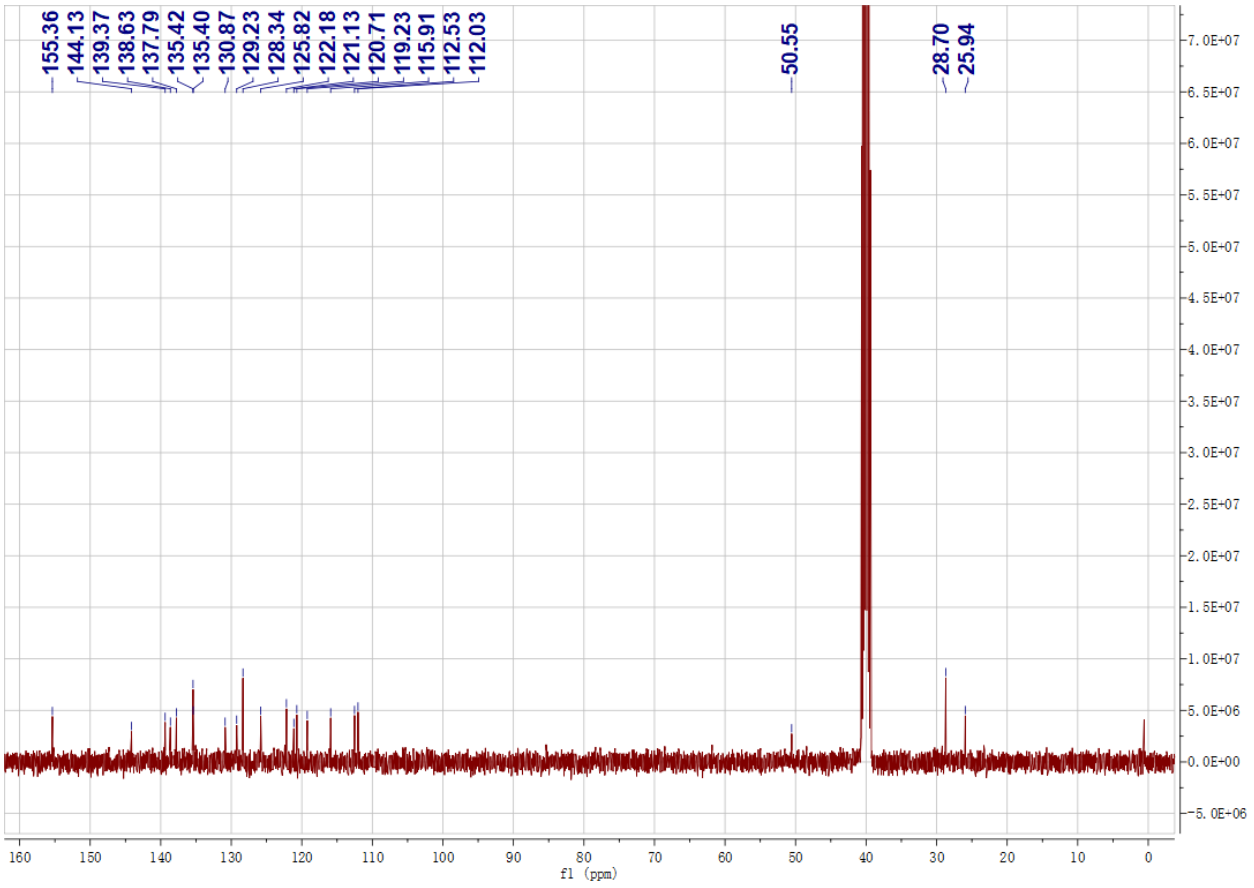
155.36
144.13
139.37
138.63
137.79
135.42
135.40
130.87
129.23
128.34
125.82
122.18
121.13
120.71
119.23
115.91
112.53
112.03
50.55
28.70
25.94
f1 (ppm)

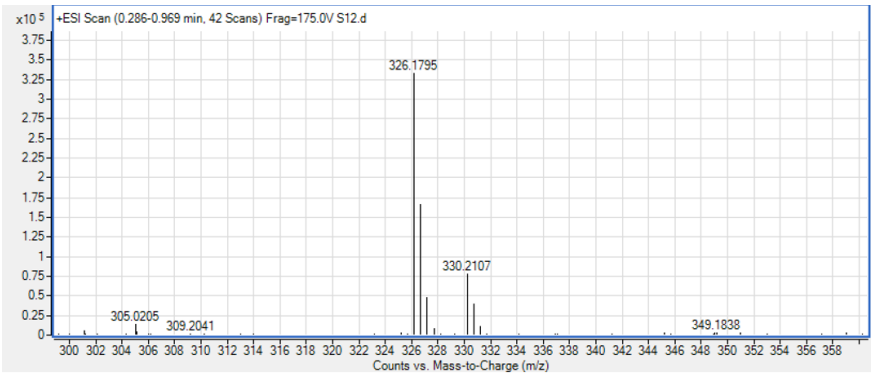

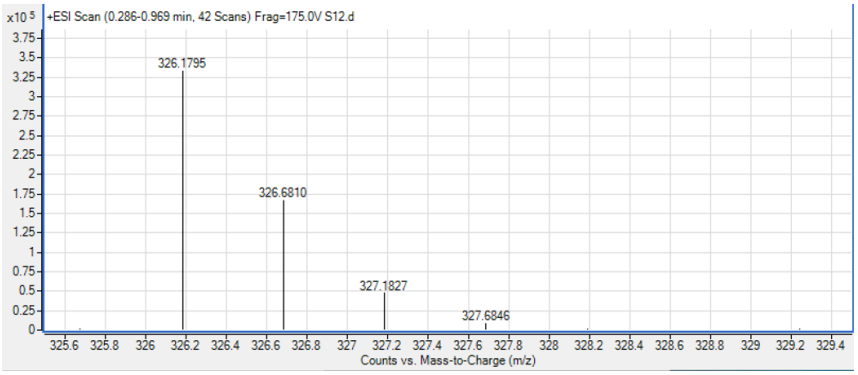

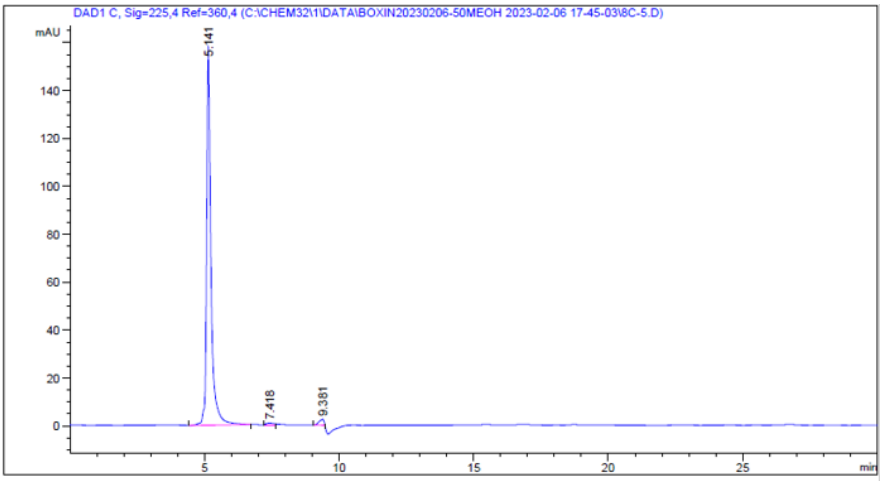


```
=====================================================================
                    Area Percent Report
=====================================================================

Sorted By             :      Signal
Multiplier            :      1.0000
Dilution              :      1.0000
Do not use Multiplier & Dilution Factor with ISTDs


Signal 1: DAD1 C, Sig=225,4 Ref=360,4

Peak RetTime Type  Width     Area      Height     Area
  #   [min]       [min]   [mAU*s]     [mAU]       %
----|-------|----|-------|----------|----------|--------|
   1   5.141 BB    0.1596 1787.25952  158.47443  97.5619
   2   7.418 MM R  0.3307   15.62454 7.87329e-1   0.8529
   3   9.381 MM R  0.2049   29.03983    2.36226   1.5852

Totals :                  1831.92389  161.62402
```

Figure S12. ^{1}H NMR (DMSO-d_6), ^{13}C NMR (DMSO-d_6), HRMS and HPLC analysis of ligand **5**.

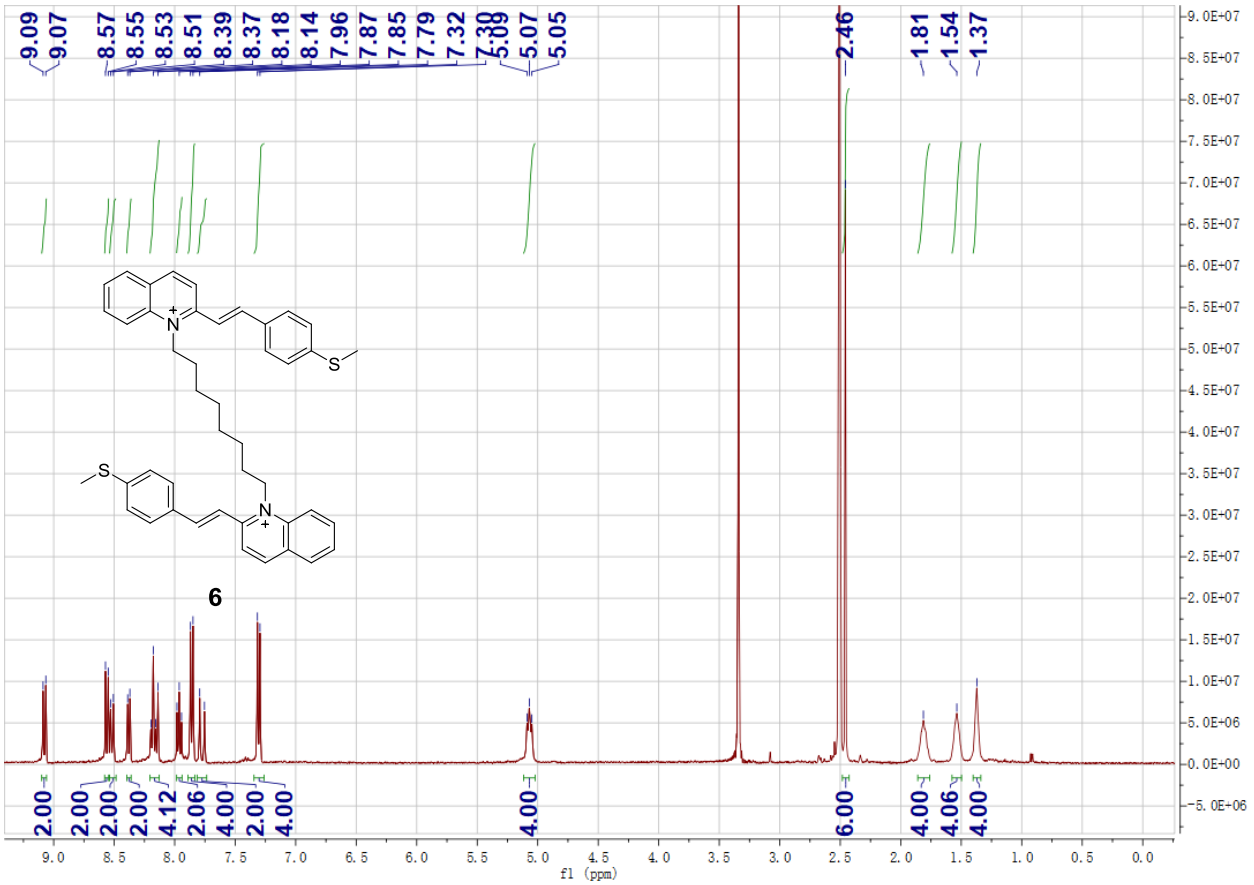
9.09
9.07
8.57
8.55
8.53
8.51
8.39
8.37
8.18
8.14
7.96
7.87
7.85
7.79
7.32
7.30
5.09
5.07
5.05
2.46
1.81
1.54
1.37
6
2.00
2.00
2.00
2.00
4.12
2.06
4.00
2.00
4.00
4.00
6.00
4.00
4.06
4.00
f1 (ppm)

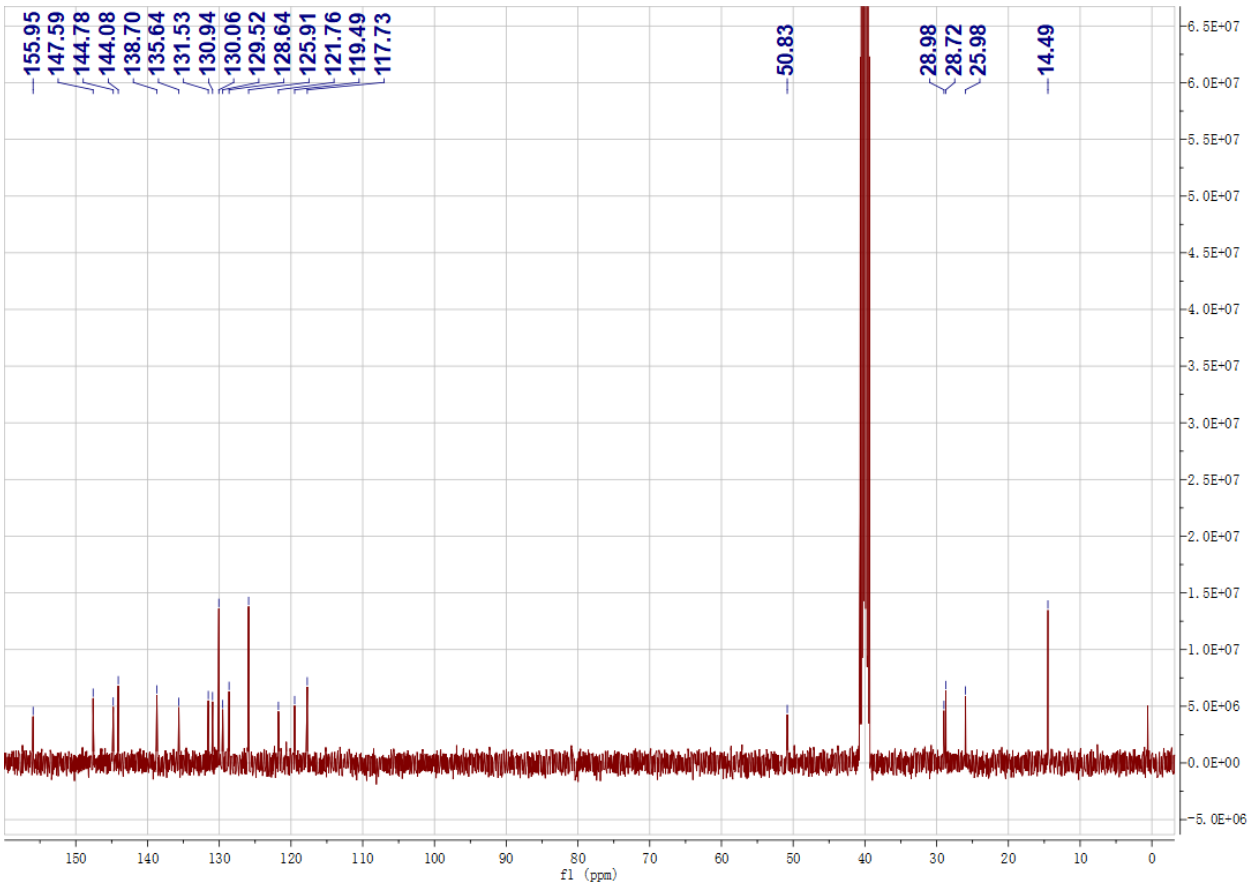
155.95
147.59
144.78
144.08
138.70
135.64
131.53
130.94
130.06
129.52
128.64
125.91
121.76
119.49
117.73
50.83
28.98
28.72
25.98
14.49
f1 (ppm)

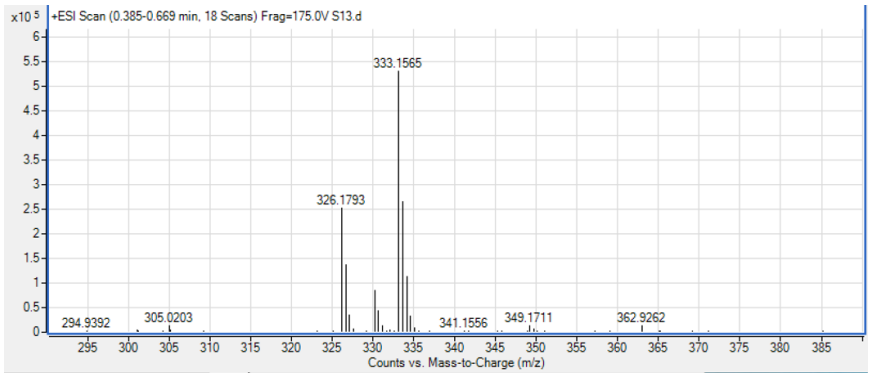

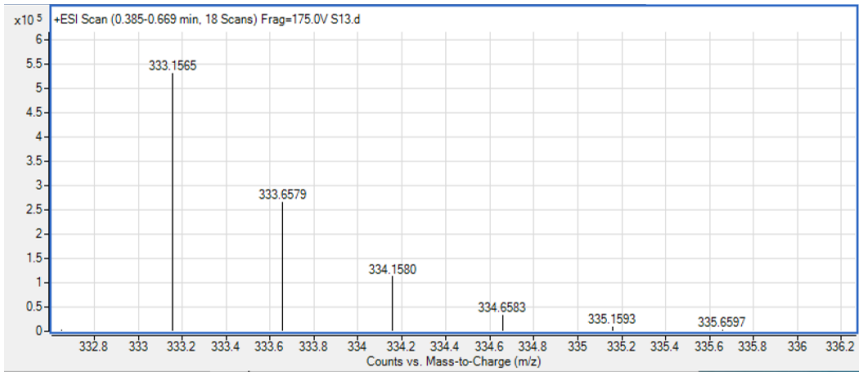

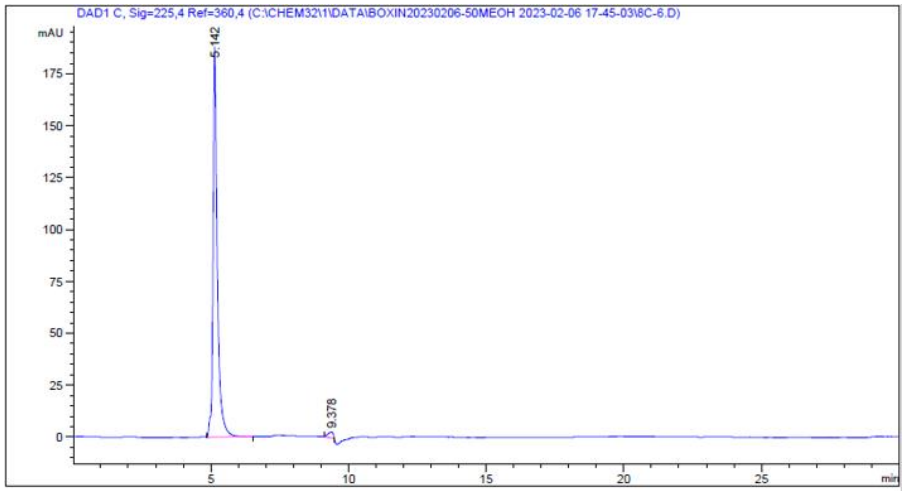


```
=====================================================================
                        Area Percent Report
=====================================================================

Sorted By             :      Signal
Multiplier            :      1.0000
Dilution              :      1.0000
Do not use Multiplier & Dilution Factor with ISTDs


Signal 1: DAD1 C, Sig=225,4 Ref=360,4

Peak RetTime Type  Width     Area      Height     Area
  #   [min]        [min]   [mAU*s]     [mAU]       %
----|-------|----|-------|----------|----------|--------|
   1   5.142 BB    0.1573 2054.52173  188.26871  98.1864
   2   9.378 MM R  0.2168   37.94823    2.91689   1.8136

Totals :                  2092.46996  191.18560
```

Figure S13. ^{1}H NMR (DMSO-d_6), ^{13}C NMR (DMSO-d_6), HRMS and HPLC analysis of ligand **6**.

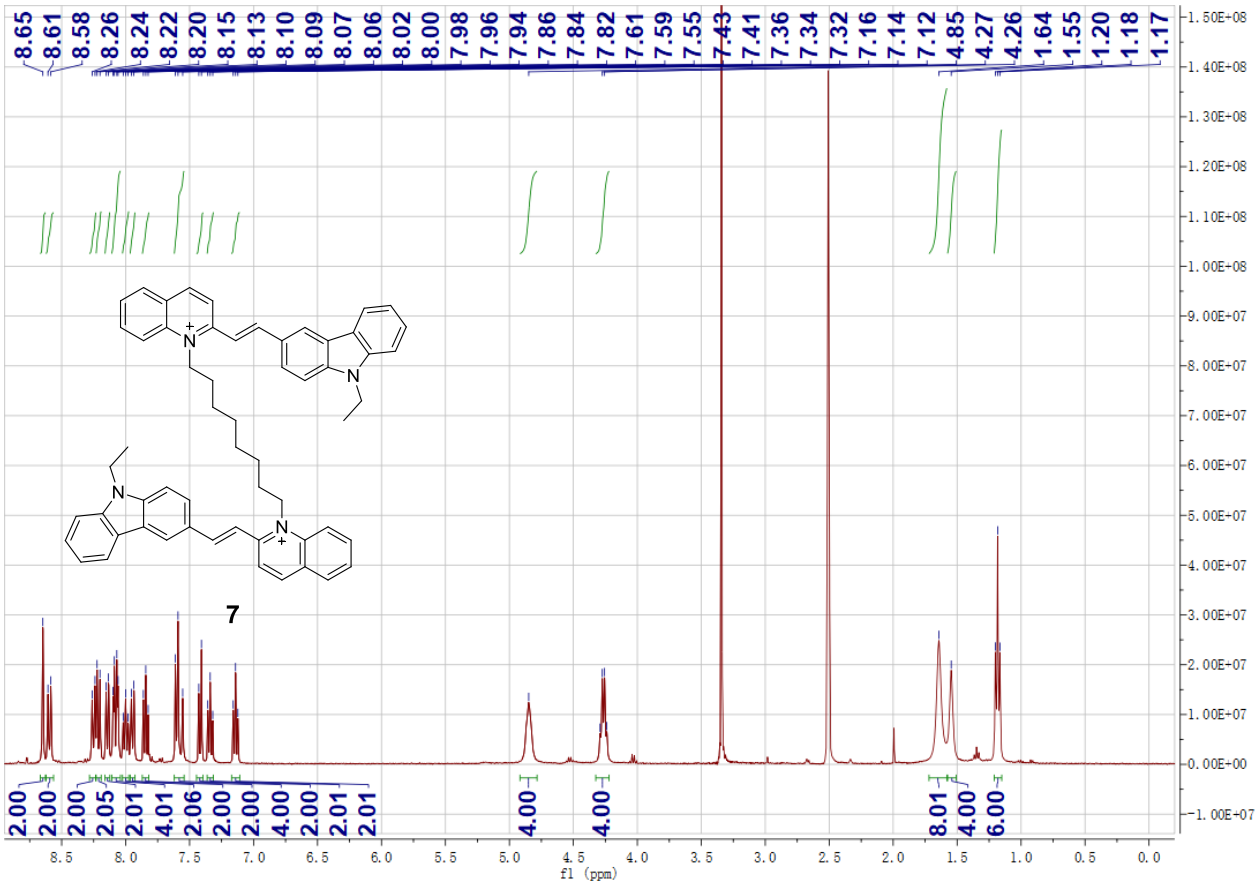
8.65 8.61 8.58 8.26 8.24 8.22 8.20 8.15 8.13 8.10 8.09 8.07 8.06 8.02 8.00 7.98 7.96 7.94 7.86 7.84 7.82 7.61 7.59 7.55 7.43 7.41 7.36 7.34 7.32 7.16 7.14 7.12 4.85 4.27 4.26 1.64 1.55 1.20 1.18 1.17
7
2.00 2.00 2.00 2.05 2.01 4.01 2.06 2.00 2.00 4.00 2.00 2.01 2.01
4.00 4.00
8.01 4.00 6.00
f1 (ppm)

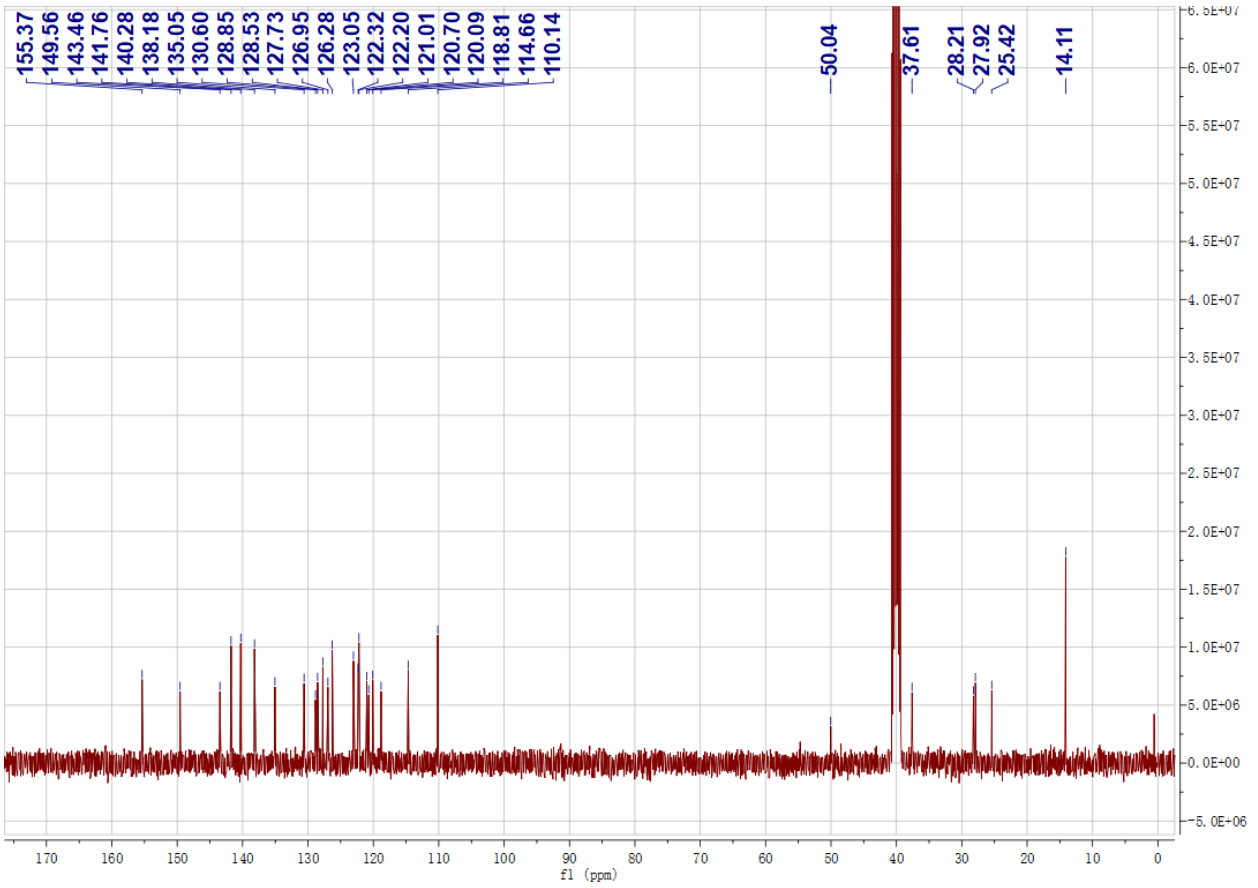
155.37 149.56 143.46 141.76 140.28 138.18 135.05 130.60 128.85 128.53 127.73 126.95 126.28 123.05 122.32 122.20 121.01 120.70 120.09 118.81 114.66 110.14
50.04
37.61
28.21 27.92 25.42
14.11
f1 (ppm)

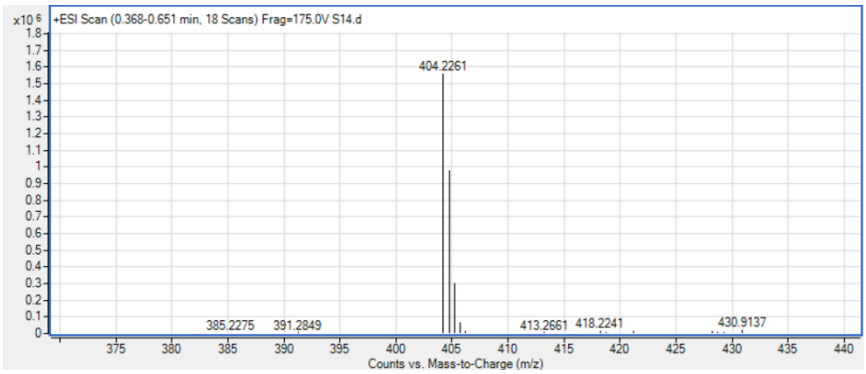

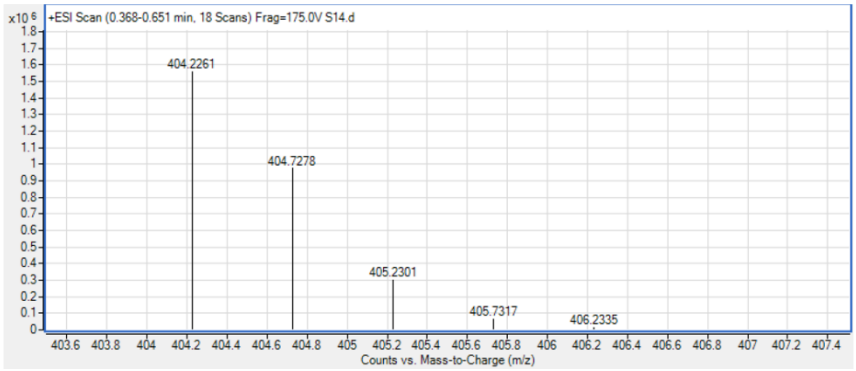

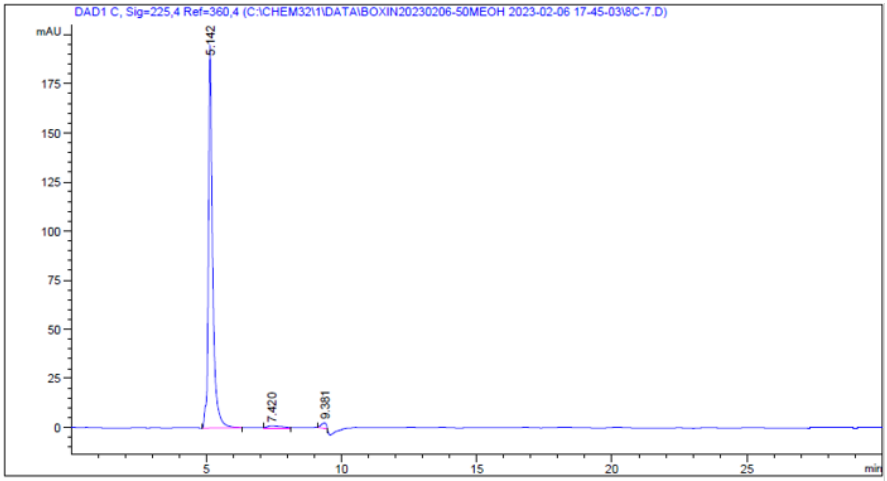


```
=====================================================================
                    Area Percent Report
=====================================================================

Sorted By             :      Signal
Multiplier            :      1.0000
Dilution              :      1.0000
Do not use Multiplier & Dilution Factor with ISTDs


Signal 1: DAD1 C, Sig=225,4 Ref=360,4

Peak RetTime Type  Width     Area      Height     Area
  #   [min]        [min]   [mAU*s]     [mAU]       %
----|-------|----|-------|----------|----------|--------|
   1   5.142 BB    0.1561 2140.64600  195.01607  96.5533
   2   7.420 MM R  0.6002   42.78769    1.18820   1.9299
   3   9.381 MM R  0.2071   33.62852    2.70690   1.5168

Totals :                  2217.06221  198.91117
```

Figure S14. ^{1}H NMR (DMSO-d_6), ^{13}C NMR (DMSO-d_6), HRMS and HPLC analysis of ligand **7**.

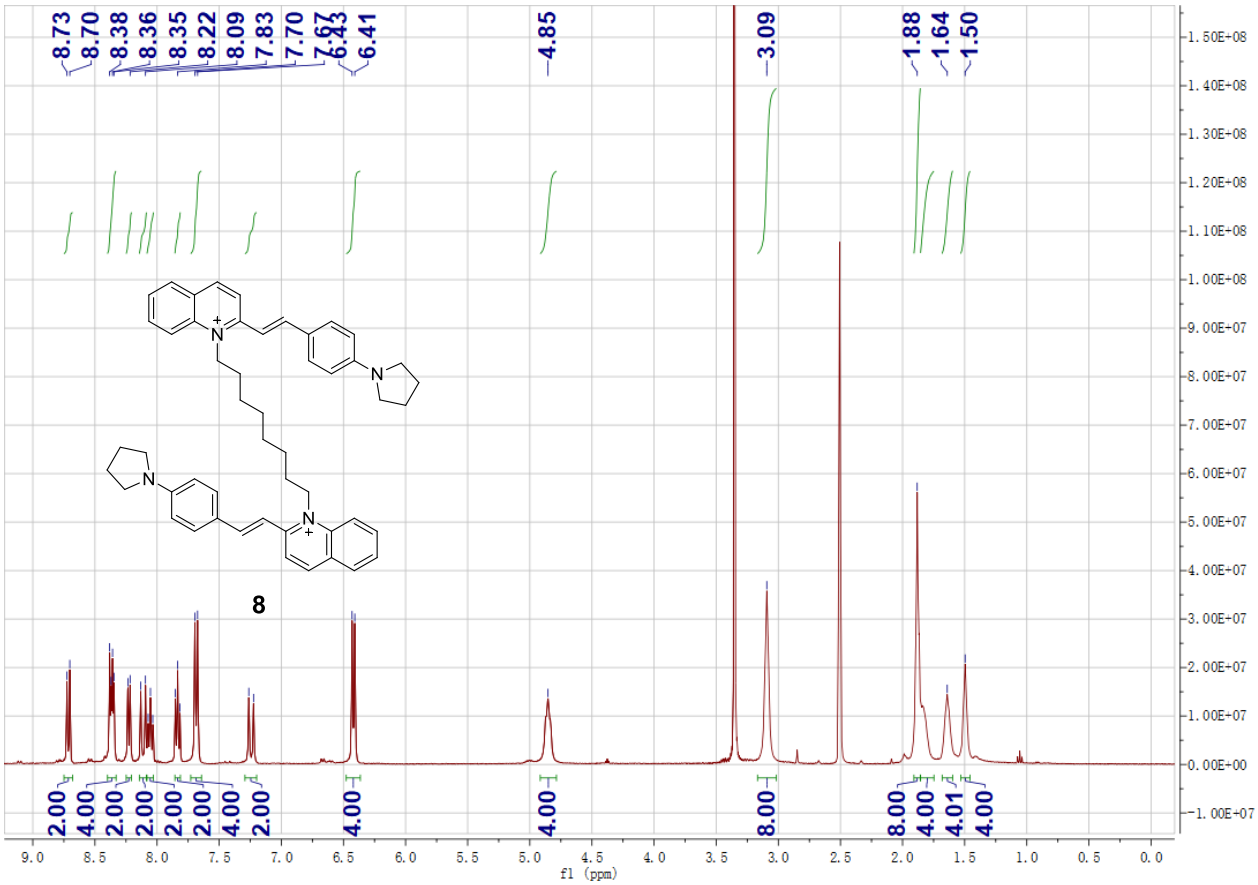
8.73
8.70
8.38
8.36
8.35
8.22
8.09
7.83
7.70
7.67
7.43
6.41
4.85
3.09
1.88
1.64
1.50
2.00
4.00
2.00
2.00
2.00
2.00
4.00
2.00
4.00
4.00
8.00
8.00
4.00
4.01
4.00
f1 (ppm)

8

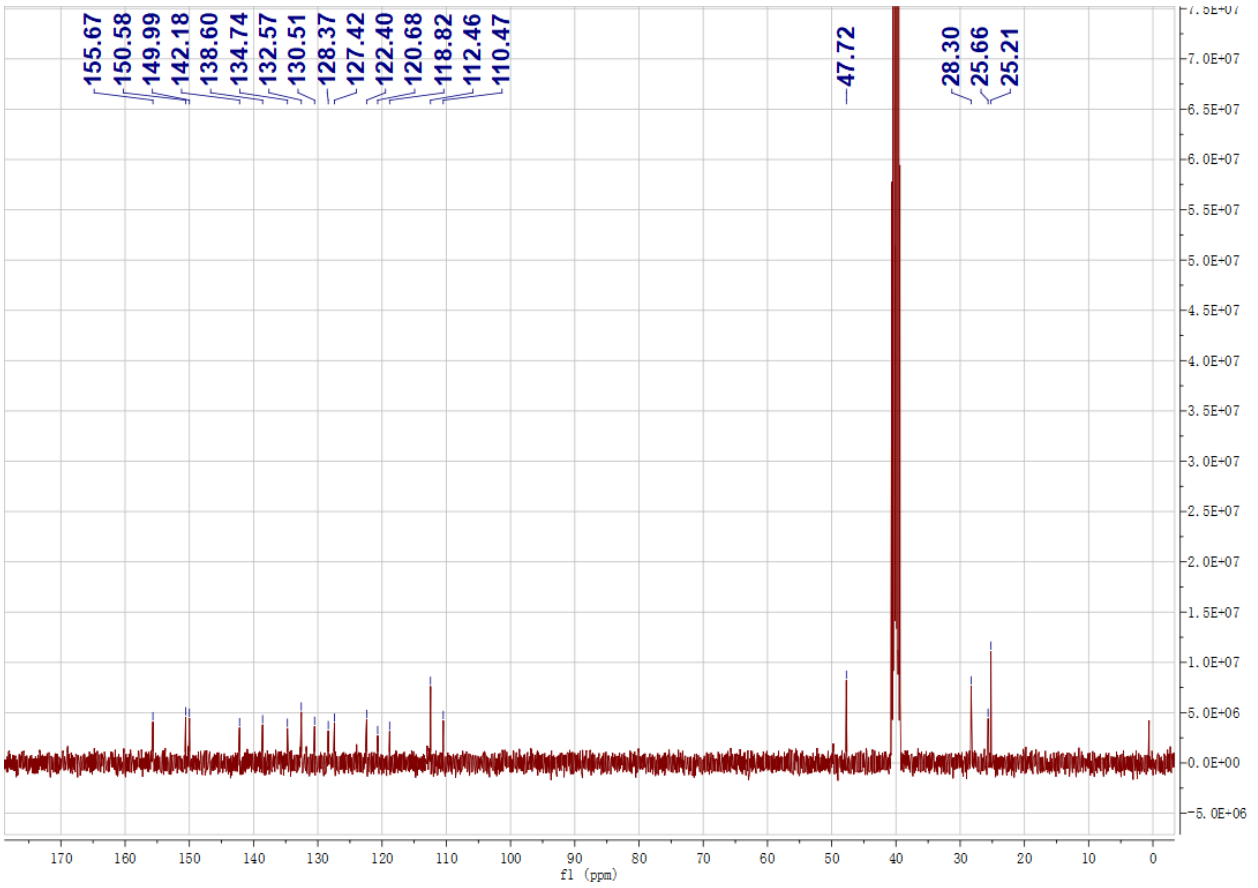
155.67
150.58
149.99
142.18
138.60
134.74
132.57
130.51
128.37
127.42
122.40
120.68
118.82
112.46
110.47
47.72
28.30
25.66
25.21
f1 (ppm)

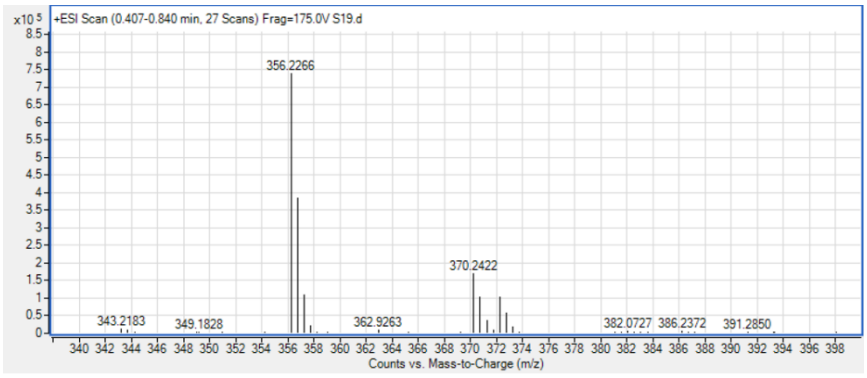

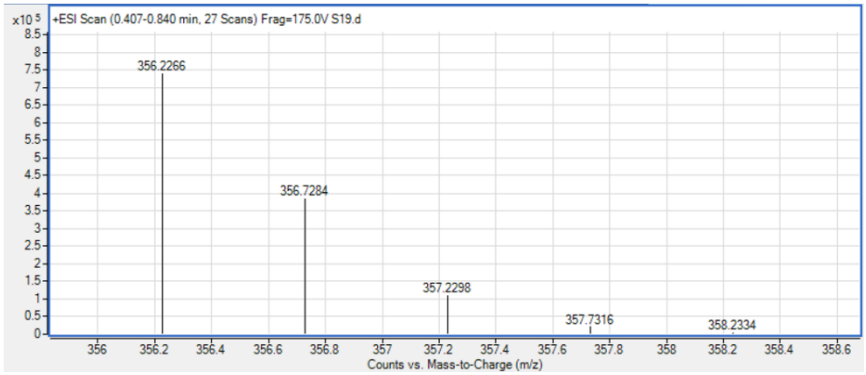

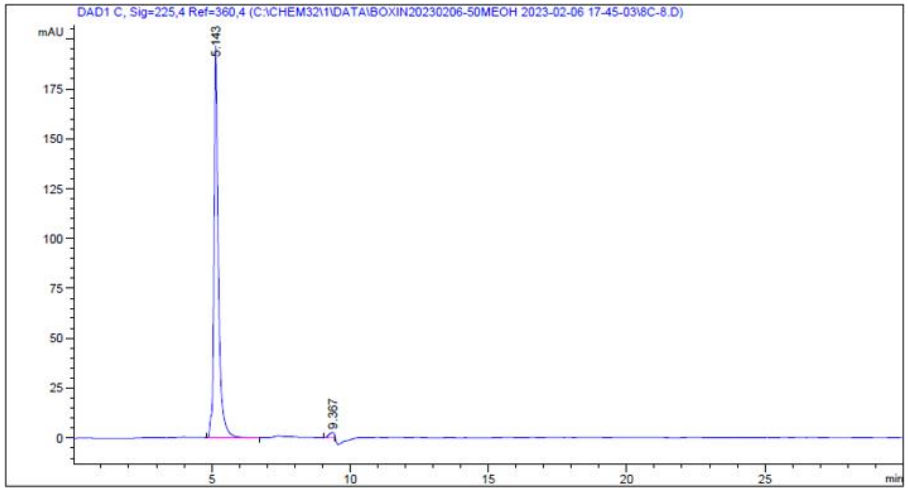


```
=====================================================================
                      Area Percent Report
=====================================================================

Sorted By             :      Signal
Multiplier            :      1.0000
Dilution              :      1.0000
Do not use Multiplier & Dilution Factor with ISTDs


Signal 1: DAD1 C, Sig=225,4 Ref=360,4

Peak RetTime Type  Width     Area      Height     Area
  #   [min]        [min]   [mAU*s]     [mAU]       %
----|-------|----|-------|----------|----------|--------|
   1   5.143 BB    0.1562 2158.70020  196.52516  98.5553
   2   9.367 MM R  0.2106   31.64436    2.50379   1.4447

Totals :                  2190.34456  199.02895
```

Figure S15. ^{1}H NMR (DMSO-d_6), ^{13}C NMR (DMSO-d_6), HRMS and HPLC analysis of ligand **8**.

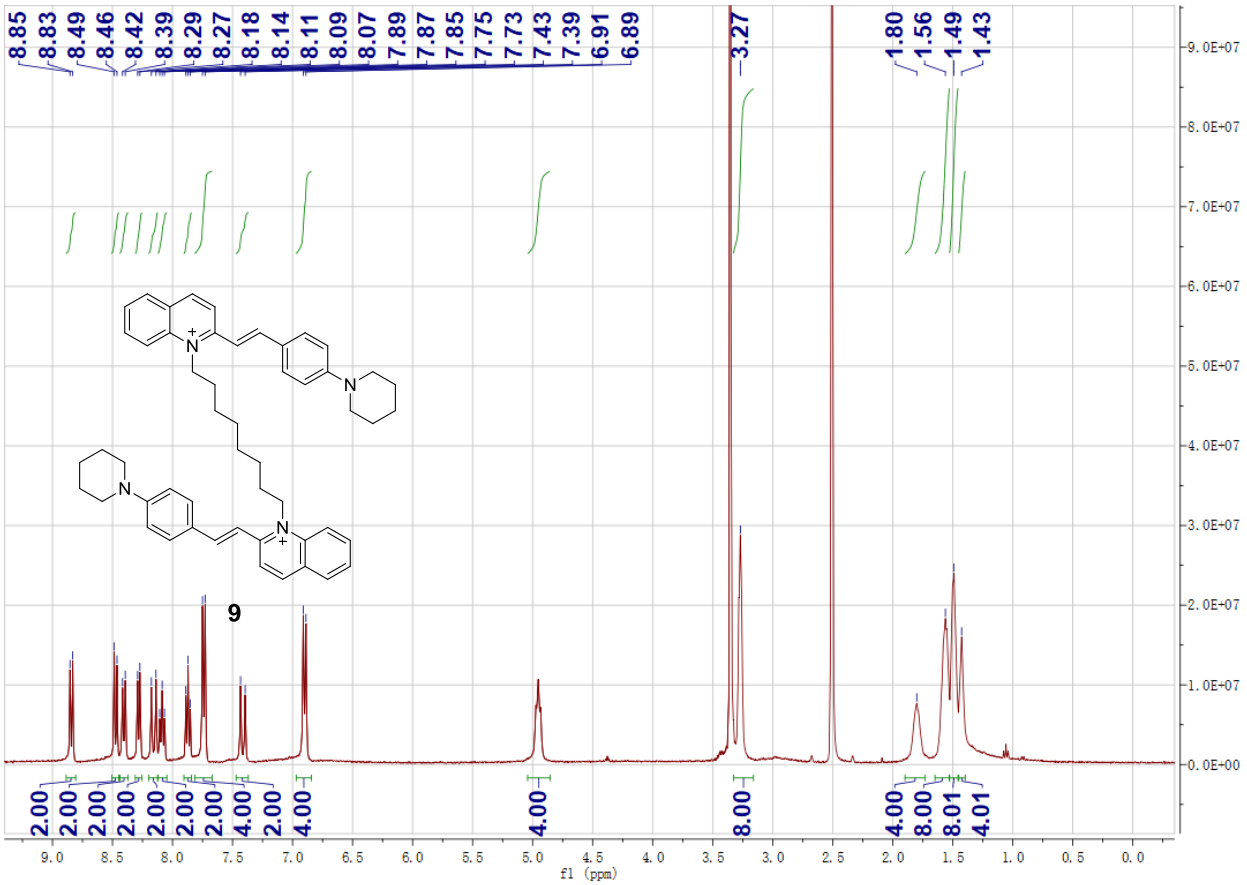
8.85
8.83
8.49
8.46
8.42
8.39
8.29
8.27
8.18
8.14
8.11
8.09
8.07
7.89
7.87
7.85
7.75
7.73
7.43
7.39
6.91
6.89
3.27
1.80
1.56
1.49
1.43
9
2.00
2.00
2.00
2.00
2.00
2.00
2.00
4.00
2.00
4.00
4.00
8.00
4.00
8.00
8.01
4.01
f1 (ppm)

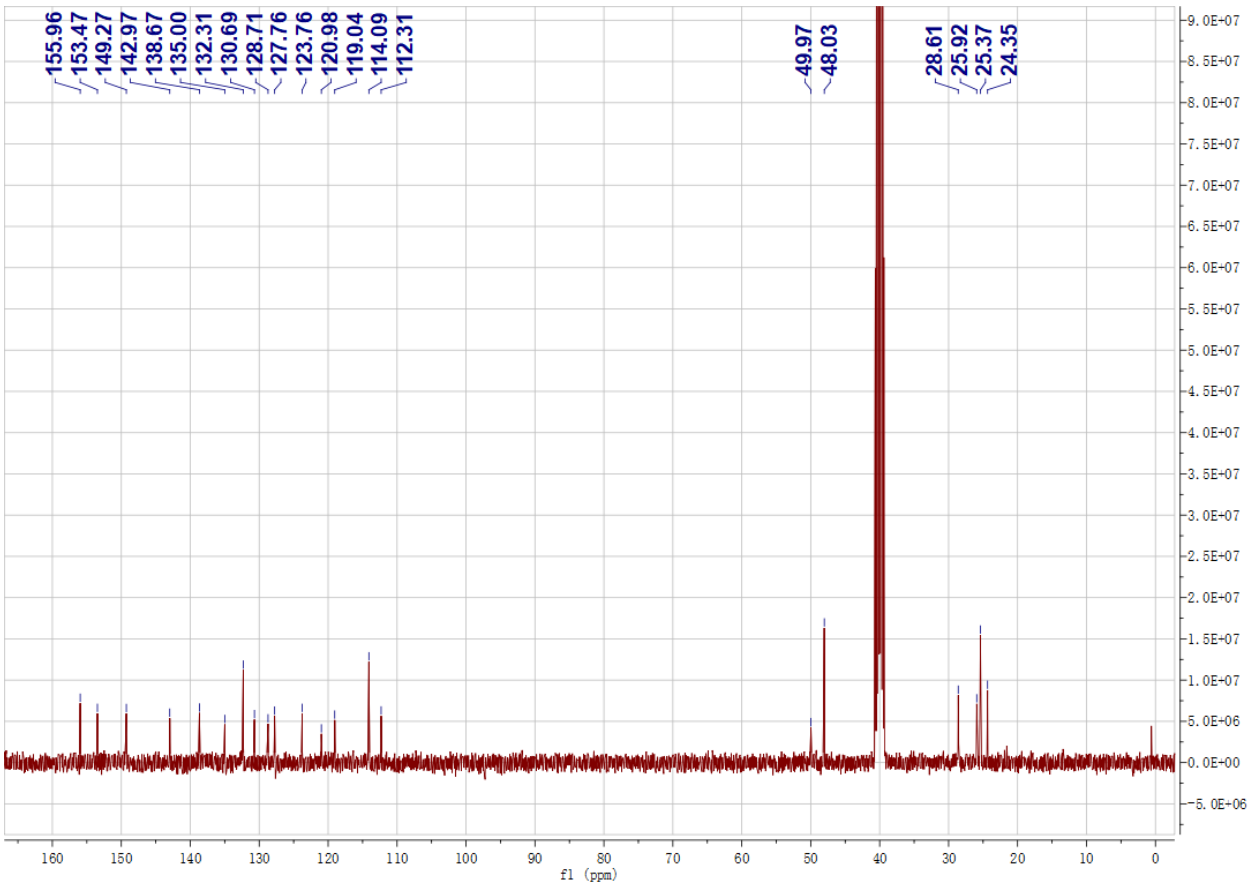
155.96
153.47
149.27
142.97
138.67
135.00
132.31
130.69
128.71
127.76
123.76
120.98
119.04
114.09
112.31
49.97
48.03
28.61
25.92
25.37
24.35
f1 (ppm)

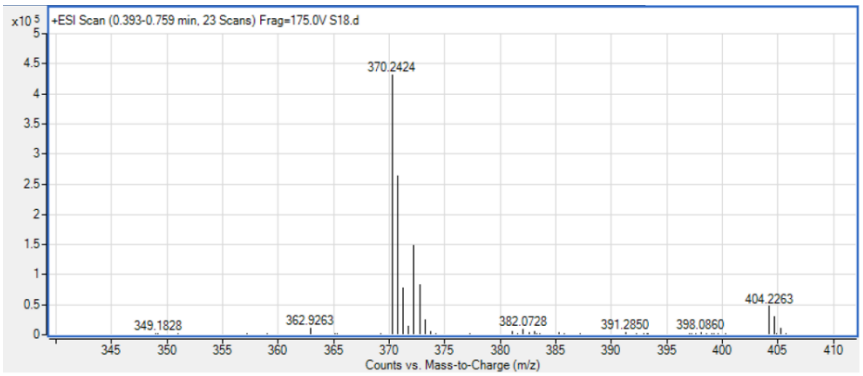

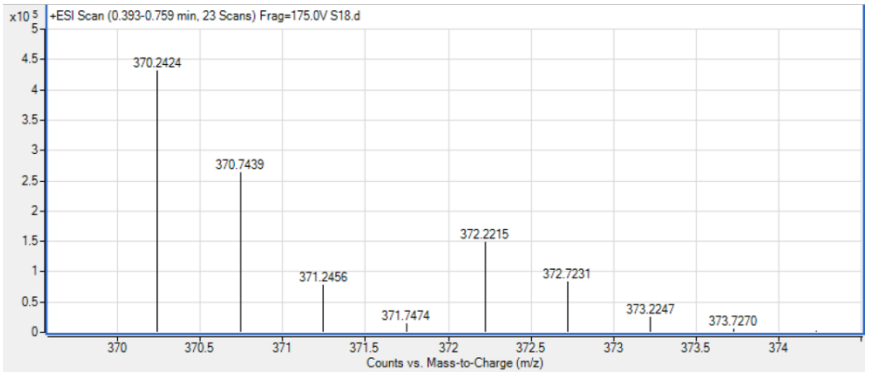

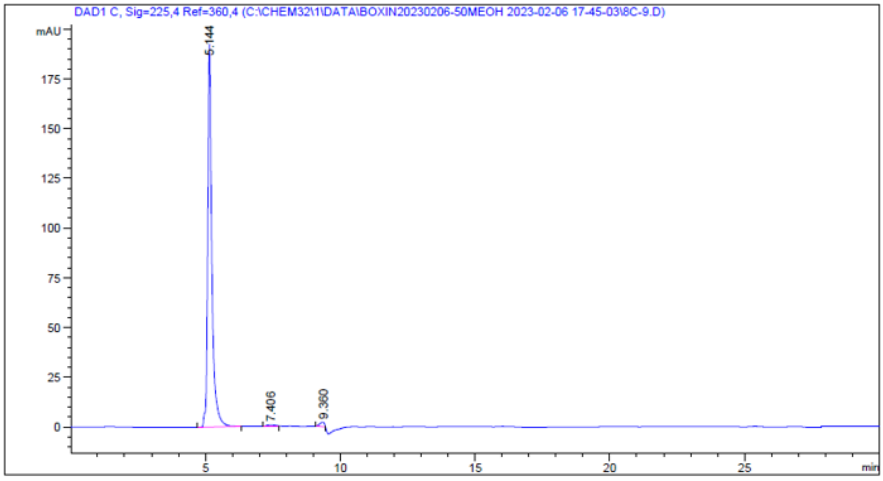


```
=====================================================================
                    Area Percent Report
=====================================================================

Sorted By             :      Signal
Multiplier            :      1.0000
Dilution              :      1.0000
Do not use Multiplier & Dilution Factor with ISTDs


Signal 1: DAD1 C, Sig=225,4 Ref=360,4

Peak RetTime Type  Width     Area      Height     Area
  #   [min]        [min]   [mAU*s]     [mAU]       %
----|-------|----|-------|----------|----------|--------|
   1   5.144 BB    0.1557 2073.72241  192.44838  97.8496
   2   7.406 MM R  0.3635   17.73536 8.13251e-1   0.8369
   3   9.360 MM R  0.1985   27.83755    2.33746   1.3135

Totals :                  2119.29532  195.59909
```

Figure S16. ^{1}H NMR (DMSO-d_6), ^{13}C NMR (DMSO-d_6), HRMS and HPLC analysis of ligand **9**.

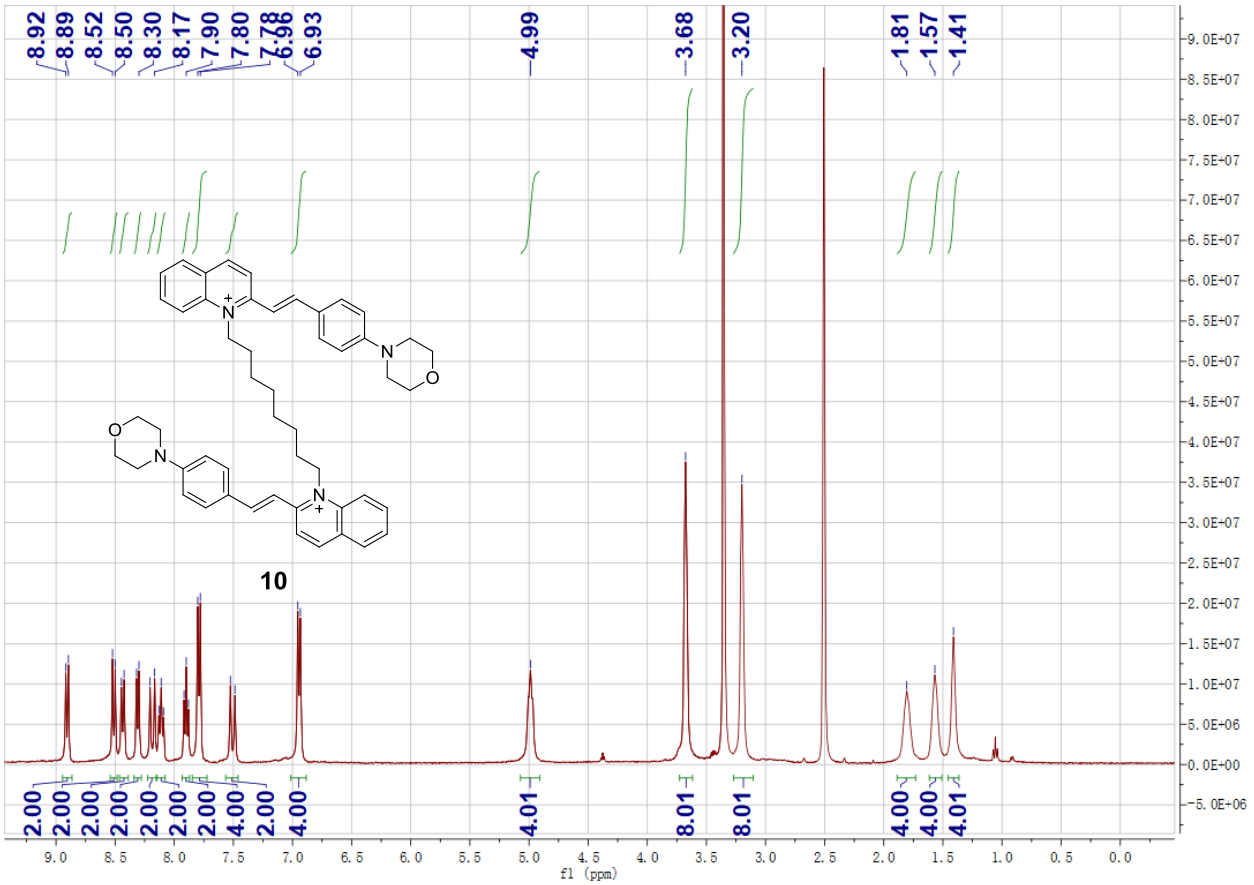
8.92
8.89
8.52
8.50
8.30
8.17
7.90
7.80
7.78
7.66
6.93
4.99
3.68
3.20
1.81
1.57
1.41
10
2.00
2.00
2.00
2.00
2.00
2.00
2.00
4.00
2.00
4.00
4.01
8.01
8.01
4.00
4.00
4.01
f1 (ppm)

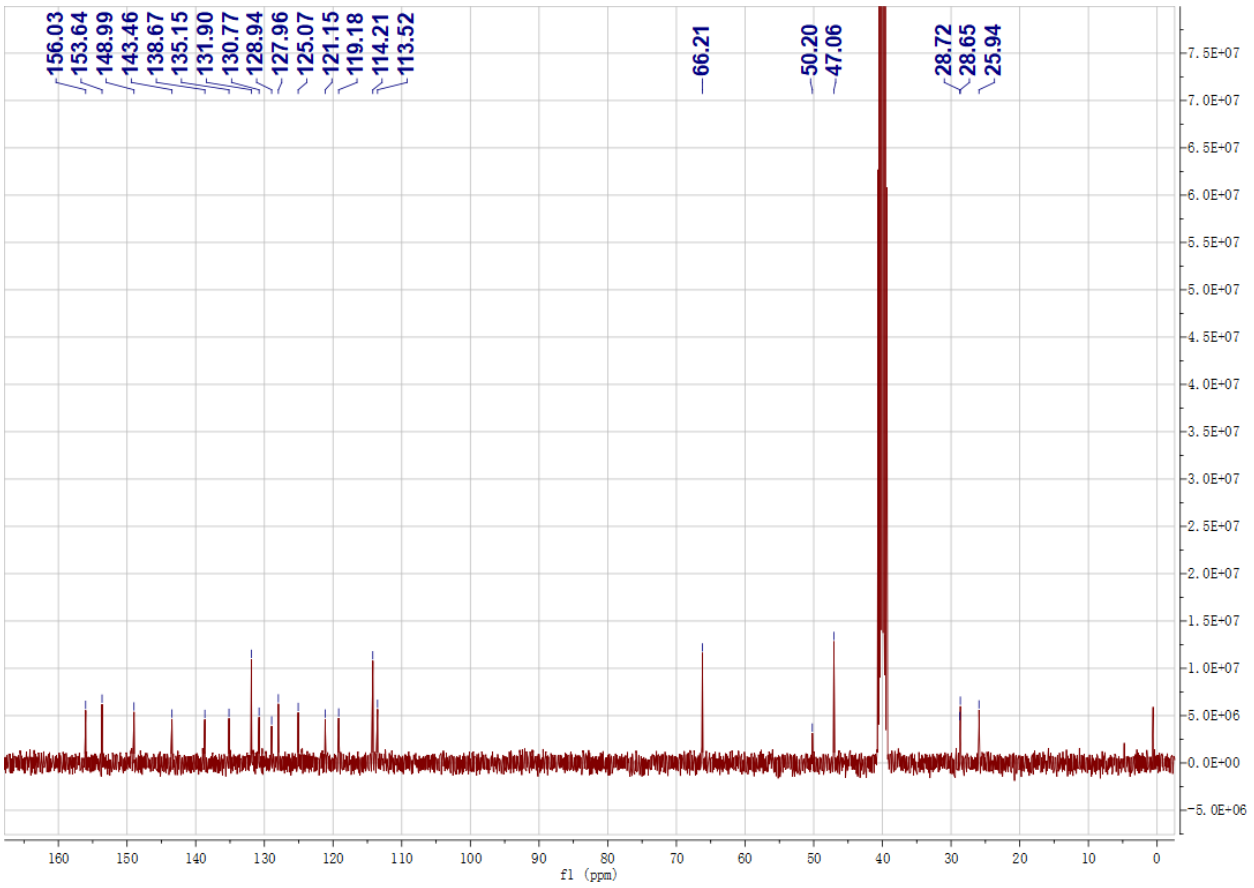
156.03
153.64
148.99
143.46
138.67
135.15
131.90
130.77
128.94
127.96
125.07
121.15
119.18
114.21
113.52
66.21
50.20
47.06
28.72
28.65
25.94
f1 (ppm)

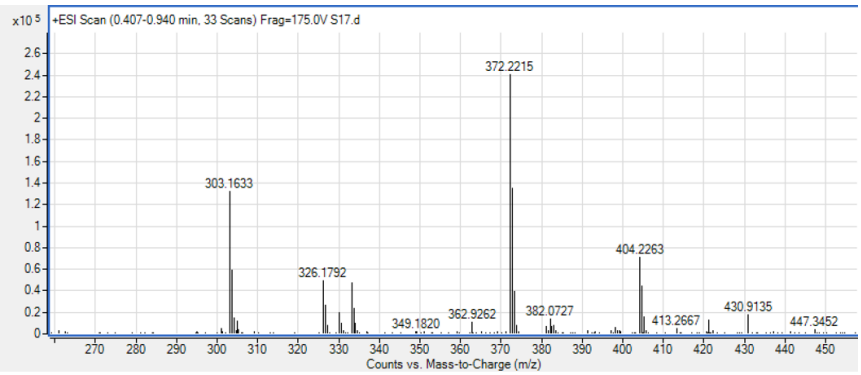

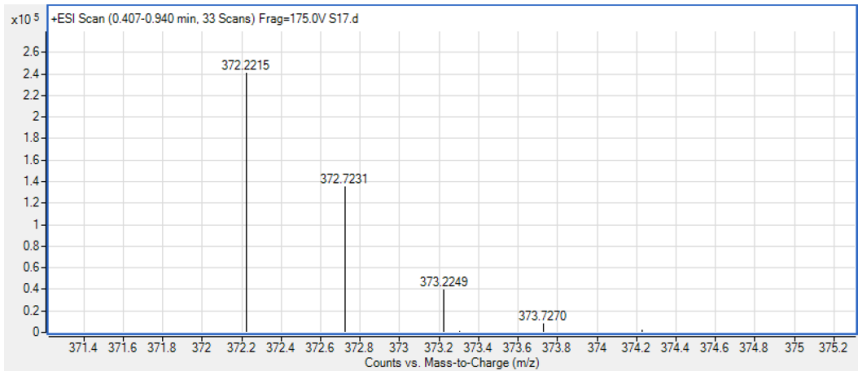

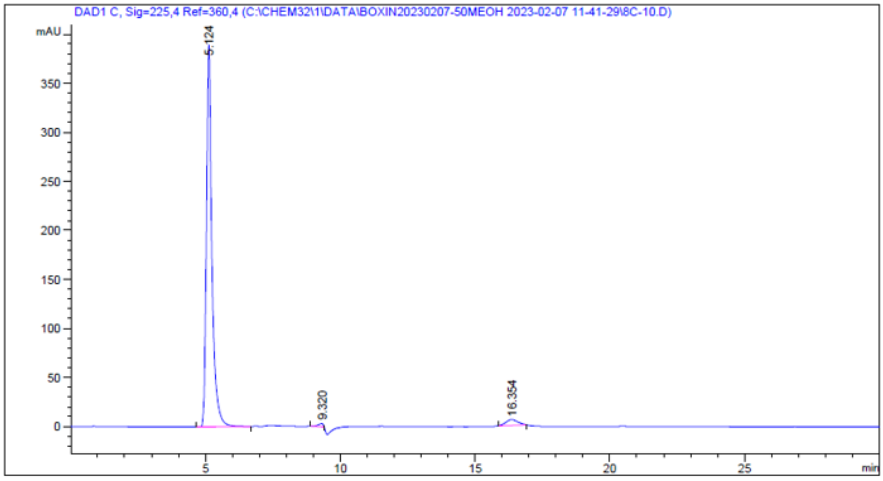


```
=====================================================================
                    Area Percent Report
=====================================================================

Sorted By             :      Signal
Multiplier            :      1.0000
Dilution              :      1.0000
Do not use Multiplier & Dilution Factor with ISTDs


Signal 1: DAD1 C, Sig=225,4 Ref=360,4

Peak RetTime Type  Width     Area      Height     Area
  #   [min]        [min]   [mAU*s]     [mAU]       %
----|-------|----|-------|----------|----------|--------|
   1   5.124 BB    0.1999 5478.77832  389.90942  95.8771
   2   9.320 MM R  0.2232   42.91117    3.20459   0.7509
   3  16.354 MM R  0.5145  192.68622    6.24175   3.3720

Totals :                  5714.37571  399.35576
```

Figure S17. ^{1}H NMR (DMSO-d_6), ^{13}C NMR (DMSO-d_6), HRMS and HPLC analysis of ligand **10**.

References

[1] W.C. Huang, T.Y. Tseng, Y.T. Chen, C.C. Chang, Z.F. Wang, C.L. Wang, T.N. Hsu, P.T. Li, C.T. Chen, J.J. Lin, P.J. Lou, T.C. Chang, Direct evidence of mitochondrial G-quadruplex DNA by using fluorescent anti-cancer agents, Nucleic Acids Res 43(21) (2015) 10102-13.

[2] A. Bedrat, L. Lacroix, J.L. Mergny, Re-evaluation of G-quadruplex propensity with G4Hunter, Nucleic Acids Res 44(4) (2016) 1746-59.

[3] B.-X. Zheng, Indole-benzothiazole derivatives as mitochondrial and c-MYC G-quadruplex ligands, Guangdong University of Technology (2021).